TsAGI, MGATU

Composite panel postbuckling behavior and general model of joints in composite structures

Prepared by

G.N.Zamula
V.F.Kut'inov
V.V.Vasil'yev
V.I.Grishin
K.M.Ierusalimsky
N.S.Azikov
T.K.Begeyev

1996

Abstract

The present paper is a final technical report on the research programme NCCW-73 accomplished within co-operation between NASA of the USA and GOSKOMOBORONPROM of Russia in the field of aeronautics. The report contains basic results of studies in two areas, "Analysis of postbuckling behavior of composite panels" and "Development of general model of joints in composite structures"; these results were obtained in conformity with requirements of NCCW-73.

In addition, consideration is given to some related issues, and proposals for further studies are formulated.

Table of Contents

1. Introduction

Implementing the composite structures is regarded as one of the most important areas of improving the state-of-the-art aircraft and space technologies. Of current interest here are insufficiently explored problems of stability and postbuckling behavior of thin-walled composite structures, as well as the evaluation of stresses in, and strength of, joints in the composite structures. The Russian/American joint working group on aeronautics established within the limits of co-operation between GOSKOMOBORONPROM and NASA has selected these problems as high priority for co-operation in the period 1995 - 1996; they are the core of the NCCW-73 joint research programme.

In accordance with the requirements of NCCW-73 the present report provides major results of studies accomplished by specialists of TsAGI and MGATU. The results are grouped into two large parts: "Postbuckling behavior of composite panels" and "General model of joints of composite structures"; these are presented in the report sections 2 and 3, respectively.

The paper is devoted mainly to theories, but, with the aim to validate the computational models, contains in some areas comparison with test results. Problem formulation, basic assumptions and the underlying relationships are exposed for each of the parts at the beginning of the corresponding sections. Both parts contain not only the computational algorithms but also examples of concrete analyses and some recommendations.

Concluding remarks on the work as a whole, the lists of references used, and Appendices are provided in sections 4, 5, and 6 of the report.

Authors wish to thank Dr. D.Starnes of NASA Langley Research Center for close collaboration in formulation and discussion of the work, and make excuses for the unavoidable brevity of presentation -- and for some imperfection in the document design.

2. Part 1. Postbuckling behavior of composite panels

It is generally known that a cover skin in a stiffened panels of a thin-walled aerospace structure can buckle locally under compression, shear and multiaxial stresses when loads are less than the limit values. There arises the problem to evaluate the load-carrying capability of such structures, taking into account the nonlinear postbuckling behavior of skins. In this case, one is required, firstly, describe rather adequately the stress-strain state (SSS) of buckled skin cells between the stiffeners; secondly, the loss in stiffnesses of the buckled skin should be allowed for in the global analysis of the built-up structure. As applied to metal structures, these two aspects of the problem were studied analytically, by experiment and numerically in a large number of papers, starting from the classical works of Bubnov, Karman, Papkovich, Timoshenko, Marguerre, and Wagner [1 - 9].

For structures with composite materials similar studies were conducted in the recent years only (for example, see writings by NASA Langley Research Center specialists M.Stein, D.Starnes, and M.Nemeth [10 - 12]), chiefly in the first of the above aspects. Taken into consideration are important features of the composite structures such as anisotropy, multiple layers, brittleness; these are known to substantially complicate the problem and make the composite panel postbuckling behavior notably differing from behavior of metal parts.

The present paper attempts an engineering approach to the problem for multiaxially (compression and shear) loaded flat stiffened panels, paying attention to determination of both postbuckling behavior of an individual cell (a plate) in the composite skin and stiffnesses/strengths of the panel as a whole which is composed of rectilinear ribs and the buckled skin that interact. The work is assumed to be continued, first of all, towards complication of both the structure geometry and the load conditions.

2.1. Problem formulation and principal relationships for orthotropic panels and plates

A panel is assumed to be an orthotropic, symmetric-layup composite plate uniformly stiffened with ribs (with the step sizes a and b) with no eccentricity in the two mutually perpendicular directions, see Fig. 2.1. The plate thickness and stiffnesses are uniform; the orthotropy axes coincide with directions of longitudinal and transverse ribs. All ribs of a particular direction are made of a unidirectional composite or a metal; their characteristics are identical in the two directions. The panel is loaded in plane by uniform compression or tension along the two axes and by shear. In both prebuckling and postbuckling stages of skin deformation every periodically repeated fragment (consisting of the rectangular skin cell and the adjacent rib portions) is in identical conditions, and its ribs and edges $\{x=0,\ x=a,\ y=0,\ y=b\}$ of cell (which is plate with dimensions a and b) remain rectilinear. If the rib torsional stiffness is insignificant and the buckled panel has the out-of-plane displacement $w(x,y)$, for this displacement we have simple support boundary conditions at these edges.

Thus, the postbuckling behavior of the panel after skin buckling, is characterized by an identical multiaxial bending stress-strain state in each cell; it is described by nonlinear equations of Karman type with the corresponding boundary conditions. In this connection the longitudinal forces redistribute between the ribs and the skin, and the cells behave as panels with lowered (reduced) stiffnesses. Subsequently, the panel can fail in certain areas of the skin/ribs or because of global buckling of the panel as a whole (i.e., as an inseparable combination of ribs and the skin with reduced characteristics).

Below, in 2.2 - 2.4, we provide the analytical solution to the problem on stability and postbuckling behavior of the simply supported orthotropic panel, the solution being valid for both a cell of the skin in the panel above and the separate unstiffened composite plate. This solution is the basis for us to consider in 2.4 more thoroughly

- strength and stiffnesses of a buckled skin and
- aspects of its interaction with ribs in the stiffened fiber reinforced laminate.

The major goal here is to derive rather simple formulae for calculating the reduction coefficients that are included in the general analysis and including (in particular cases of compression/shear loaded metal panels) the classical results by von Karman and Marguerre.

Let us adopt the assumptions (traditional for multilayer composites) about quasihomogeneity and orthotropy of the layers and their being elastic; with this, stresses and strains in a k-th layer are interrelated by the generalized Hooke's law [13, 14]

$$\begin{Bmatrix} \sigma_x \\ \sigma_y \\ \tau_{xy} \end{Bmatrix}^K = \left[C_{ij}\right]^K \begin{Bmatrix} \varepsilon_x \\ \varepsilon_y \\ \gamma_{xy} \end{Bmatrix}, \qquad i,j = 1,2,3. \tag{2.1}$$

Here C_{ij} are layer stiffnesses referred to the x and y axes; sigma and epsilon are the stresses and the strains in the layer. In accordance with the Kirchhoff-Love hypothesis, the strains are

$$\begin{Bmatrix} \varepsilon_x \\ \varepsilon_y \\ \gamma_{xy} \end{Bmatrix} = \begin{Bmatrix} \varepsilon_{x0} \\ \varepsilon_{y0} \\ \gamma_{xy0} \end{Bmatrix} + z \begin{Bmatrix} \chi_x \\ \chi_y \\ \chi_{xy} \end{Bmatrix}, \tag{2.2}$$

(the z coordinate is measured from the panel mid-surface along the normal thereto), and the strains and curvatures of the mid-surface $\{\varepsilon_0\}$, $\{\chi\}$ are related to its displacements u, v, w as follows:

$$\varepsilon_{x0} = \frac{\partial u}{\partial x} + \frac{1}{2}\left(\frac{\partial w}{\partial x}\right)^2, \quad \varepsilon_{y0} = \frac{\partial v}{\partial y} + \frac{1}{2}\left(\frac{\partial w}{\partial y}\right)^2, \quad \gamma_{xy0} = \frac{\partial u}{\partial y} + \frac{\partial v}{\partial x} + \frac{\partial w}{\partial x}\frac{\partial w}{\partial y},$$

$$\chi_x = -\frac{\partial^2 w}{\partial x^2}, \qquad \chi_y = -\frac{\partial^2 w}{\partial y^2}, \qquad \chi_{xy} = -2\frac{\partial^2 w}{\partial x \partial y}. \tag{2.3}$$

Assume that the multilayer composite panel fails when any of the layers reaches its limiting state at any point. The limiting state is determined by using an appropriate polynomial strength criteria based on stresses along the layer orthotropy axes.

Adopting these assumptions, the following relationships are valid for the panel as a whole:

- elasticity:

$$\begin{Bmatrix} N \\ M \end{Bmatrix} = \begin{bmatrix} B & 0 \\ 0 & D \end{bmatrix} \begin{Bmatrix} \varepsilon_0 \\ \chi \end{Bmatrix}, \tag{2.4}$$

$$\text{where } \begin{bmatrix} B & 0 \\ 0 & D \end{bmatrix} = \begin{bmatrix} B_{11} & B_{12} & 0 & 0 & 0 & 0 \\ B_{21} & B_{22} & 0 & 0 & 0 & 0 \\ 0 & 0 & B_{33} & 0 & 0 & 0 \\ 0 & 0 & 0 & D_{11} & D_{12} & 0 \\ 0 & 0 & 0 & D_{21} & D_{22} & 0 \\ 0 & 0 & 0 & 0 & 0 & D_{33} \end{bmatrix},$$

- equilibrium equations in terms of displacements:

$$B_{11}\frac{\partial^2 u}{\partial x^2} + B_{33}\frac{\partial^2 u}{\partial y^2} + (B_{12}+B_{33})\frac{\partial^2 v}{\partial x \partial y} + B_{11}\frac{\partial w}{\partial x}\frac{\partial^2 w}{\partial x^2} + (B_{12}+B_{33})\frac{\partial w}{\partial y}\frac{\partial^2 w}{\partial x \partial y} + B_{33}\frac{\partial w}{\partial x}\frac{\partial^2 w}{\partial y^2} = 0,$$

(2.5)

$$(B_{12}+B_{33})\frac{\partial^2 u}{\partial x \partial y} + B_{33}\frac{\partial^2 v}{\partial x^2} + B_{22}\frac{\partial^2 v}{\partial y^2} + (B_{12}+B_{33})\frac{\partial w}{\partial x}\frac{\partial^2 w}{\partial x \partial y} + B_{22}\frac{\partial w}{\partial y}\frac{\partial^2 w}{\partial y^2} + B_{33}\frac{\partial w}{\partial y}\frac{\partial^2 w}{\partial x^2} = 0$$

;

$$D_{11}\frac{\partial^4 w}{\partial x^4} + 2(D_{12}+2D_{33})\frac{\partial^4 w}{\partial x^2 \partial y^2} + D_{22}\frac{\partial^4 w}{\partial y^4} - N_x\frac{\partial^2 w}{\partial x^2} - N_y\frac{\partial^2 w}{\partial y^2} - 2N_{xy}\frac{\partial^2 w}{\partial x \partial y} = 0,$$

(2.6)

- expression for the total potential energy:

$$Э = \frac{1}{2}\int_0^a\int_0^b \left\{ B_{11}\left[\frac{\partial u}{\partial x} + \frac{1}{2}\left(\frac{\partial w}{\partial x}\right)^2\right]^2 + 2B_{12}\left[\frac{\partial u}{\partial x} + \frac{1}{2}\left(\frac{\partial w}{\partial x}\right)^2\right]\left[\frac{\partial v}{\partial y} + \frac{1}{2}\left(\frac{\partial w}{\partial y}\right)^2\right] + \right. \tag{2.7}$$

$$+B_{22}\left[\frac{\partial v}{\partial y} + \frac{1}{2}\left(\frac{\partial w}{\partial y}\right)^2\right]^2 + B_{33}\left(\frac{\partial u}{\partial y} + \frac{\partial v}{\partial x} + \frac{\partial w}{\partial x}\frac{\partial w}{\partial y}\right)^2 + D_{11}\left(\frac{\partial^2 w}{\partial x^2}\right)^2 +$$

$$\left. +2D_{12}\frac{\partial^2 w}{\partial x^2}\frac{\partial^2 w}{\partial y^2} + D_{22}\left(\frac{\partial^2 w}{\partial y^2}\right)^2 + 4D_{33}\left(\frac{\partial^2 w}{\partial x \partial y}\right)^2 + 2T_x\frac{\partial u}{\partial x} + 2T_y\frac{\partial v}{\partial y} + 2T_{xy}\left(\frac{\partial u}{\partial y} + \frac{\partial v}{\partial x}\right)\right\} dxdy.$$

Here, $\{N\}=[N_x N_y N_{xy}]^T$, $\{M\}=[M_x M_y M_{xy}]^T$ are the stress resultants and the moments in the plate; T_x, T_y, T_{xy} (refer to Fig. 2.1) are the external loads; B_{ij} and D_{ij} are panel stiffnesses to be determined on the basis of $[C_{ij}]^K$ by using the usual equations from [14, 15].

When analyzing behavior of the skin and ribs in a panel, use is made of

- conventional conditions of equilibrium and their joint deformation and
- the relations of the elastic bar theory.

2.2. Stability of orthotropic plates

Following the suggested applied method for analyzing the load-bearing capacity of composite panels, the first stage is to determine eigenvalues and the corresponding proper functions of the boundary value problem that describes stability of an orthotropic panel under compression, shear, and multiaxial load. Write the out-of-plane displacement of the simply supported panel as the double trigonometric series:

$$w = \sum_{m=1}^{\infty}\sum_{n=1}^{\infty} A_{mn} \sin\lambda_m x \sin\lambda_n y \ , \qquad \lambda_m = m\pi/a \ , \qquad \lambda_n = n\pi/b \ , \tag{2.8}$$

where a and b are the length and the width of the panel.

Substitute the expansion (2.8) into the equilibrium equation (2.6) in which the stress resultants in nonlinear terms should be replaced by their subcritical values, i.e., $N_x=-T_x$, $N_y=-T_y$,. $N_{xy}=-T_{xy}$. Applying the Bubnov-Galerkin procedure, obtain the infinite homogeneous system of linear algebraic equations for the vector $\{A\}$:

$$[M]\ \{A\} = 0, \tag{2.9}$$

where [M] is a square matrix whose diagonal coefficients are of form

$$M_{dd} = \frac{\pi^2}{b^2}\sqrt{D_{11}D_{22}}\left(m^4\alpha + 2m^2n^2\beta + n^4/\alpha\right) - T_x m^2 - T_y n^2 a^2/b^2 \ .$$

Off-diagonal coefficients of the matrix [M] are written as

$$M_{\substack{dl \\ (d\neq l)}} = \begin{cases} \dfrac{32}{\pi^2}\dfrac{a}{b} T_{xy} \dfrac{mnij}{\left(m^2-i^2\right)\left(n^2-j^2\right)} & \text{при} \quad \begin{matrix} m\pm i = 1,3,5,\ldots, \\ n\pm j = 1,3,5,\ldots; \end{matrix} \\ 0 \qquad \text{при} \quad m\pm i = 2,4,6,\ldots; \quad n\pm j = 2,4,6,\ldots & \end{cases} ,$$

$$\alpha = \frac{b^2}{a^2}\sqrt{\frac{D_{11}}{D_{22}}} \qquad , \qquad \beta = \frac{D_{12}+2D_{33}}{\sqrt{D_{11}D_{22}}} .$$

Critical stress resultants of compression (T_x^* and T_y^*) and shear (T_{xy}^*) are sought in the following form:

$$T_x^* = \frac{\pi^2}{b^2}\sqrt{D_{11}D_{22}}\ k_x^*, \qquad T_y^* = \frac{\pi^2}{b^2}\sqrt{D_{11}D_{22}}\ k_y^*, \qquad T_{xy}^* = \frac{\pi^2}{b^2}\sqrt{D_{11}D_{22}}\ k_{xy}^*.$$

(2.10)

Transform the set of simultaneous equations (2.9) taking into account (2.10):

$$[M]\ \{A\} = \frac{\pi^2}{b^2}\sqrt{D_{11}D_{22}}\ [\overline{M}]\ \{A\} = 0,$$

where $[\overline{M}]$ is a matrix whose elements depend on coefficients k_x, k_y, and k_{xy}:

$$\overline{M}_{dd} = m^2n^2k_{mn} - k_xm^2 - k_yn^2a^2/b^2\ ,$$

$$\overline{M}_{\substack{dl\\(d\neq l)}} = \begin{cases} \dfrac{32}{\pi^2}\dfrac{a}{b}k_{xy}\dfrac{mnij}{(m^2-i^2)(n^2-j^2)} & \text{for} \quad \begin{matrix} m \pm i = 1,3,5,\ldots, \\ n \pm j = 1,3,5,\ldots; \end{matrix} \\ 0 \qquad \text{for} \quad m \pm i = 2,4,6,\ldots; \quad n \pm j = 2,4,6,\ldots \end{cases},$$

$$k_{mn} = m^2\alpha / n^2 + 2\beta + n^2/(\alpha m^2).$$

For the particular loading cases we will find eigenvalues and their proper vectors of the matrix $[\overline{M}]$ and study the influence of the stack orthotropy on panel stability.

2.2.1. Compression

In the case of uniaxial compression the set of equations (2.9) breaks down into individual equations for the coefficients k_x :

$$k_x = k_{mn}n^2\ .$$

Each value of k_x is corresponded to by an eigen vector $\{q\}=[0, 0, .., q_{mn}=1, 0, ...]^T$ and a natural shape $\overline{w} = \sin\lambda_m x\ \sin\lambda_n y$. The stability coefficient k_x^* is found from the condition $k_x^*= \min(k_x)$; the numbers of half-waves, m and n, at which k_x becomes minimum, are hereafter identified by m_0 and n_0 ($n_0 =1$ for uniaxial compression). The stability coefficient k_x^* is corresponded to by the natural shape $\overline{w}^* = \sin(m_0\pi x/a)\ \sin(\pi y/b)$. The critical compression stress resultant T_x^* is found by using (2.10).

Study the influence of the fiber orientation angle on stability of orthotropic panels made from carbon fiber reinforced plastic. Assume that the stack consists of alternating layers with fiber orientation angles $+\varphi$ and $-\varphi$; the total thickness of the layers $h=1.1 \cdot 10^{-3}$m; characteristics of an elementary layer: E_1 = 180 GPa, E_2 = 6.2 GPa, G_{12} = 5.0 GPa, μ_{21} = 0.26; panel dimensions, a=b=0.4 m. Figure 2.2 shows the function $T_x^*(\pm\varphi)$ (line 1). For a square panel the critical stress resultant reaches its maximum at the fiber orientation angle $\varphi= \pm 45°$.

This solution conforms to the case of free lateral displacement of longitudinal edges. It is known that airframes usually incorporate multispan panels. Displacements of longitudinal edges of such a panel (being a skin supported by stringers) can be restrained or not allowed at all. In this case the plate compression loaded in a particular direction may experience biaxial compression due to the Poisson effect, see [16]. Let us consider two types of boundary conditions:

- panel edges can freely displace in plane (configuration 1);
- longitudinal edges of the panel cannot displace laterally (configuration 2).

In the first case, $T_y = 0$ over the longitudinal edges. In the second case, a mutual displacement of longitudinal edges along the OY axis is absent, i.e., $\Delta v = v(y=b) - v(y=0) = 0$. Solution of the two-dimensional problem provides $T_y = T_x B_{12}/B_{11}$. Thus, the plate is subjected to biaxial compression. Combine the homogeneous systems of linear algebraic equations corresponding to the two types of panel boundary conditions. In this case the only change will be in diagonal components of the matrix [M]:

$$M_{dd} = \frac{\pi^2}{b^2}\sqrt{D_{11}D_{22}}\,\left(m^4\alpha + 2m^2n^2\beta + n^4/\alpha\right) - T_x(m^2 + f_x n^2 a^2/b^2)\ .$$

Here f_x is a coefficient depending on the conditions posed on the edge displacements; $f_x=0$ for the configuration 1, and $f_x=B_{12}/B_{11}$ for the configuration 2. The curve 2 in Fig. 2.2 corresponds to the case of uniaxial compression of a panel with fixed longitudinal edges. For a square panel the criical compression stress resultant reaches its maximum at the fiber orientation angle ±35°.

Let now the plate whose edges can displace freely, is subject to compressive stress resultants T_x and T_y. Determine the critical compression stress resultants T_x^* and T_y^*. The generic homogeneous system of linear algebraic equations (2.9) breaks down into individual equations for the coefficients k_x and k_y:

$$k_x + k_y(na)^2/(mb)^2 = n^2 k_{mn}\ . \qquad (2.11)$$

From (2.11) we establish coefficients k_{x0} and k_{y0} for the panel loaded with "isolated" stress resultants T_x and T_y. If $T_y=0$ then $k_{x0}=n^2k_{mn}$, and $k_{y0}=m^2k_{mn}(b/a)^2$ for $T_x=0$. By minimizing k_{x0} and k_{y0} with respect to the numbers m and n we determine the stability coefficients: $k_{x0}^*=\min(n^2k_{mn})$ and $k_{y0}^*=\min[m^2k_{mn}(b/a)^2]$. Return now to the case of biaxial compression and determine the stability coefficients k_x^* and k_y^*. Let the stress resultant T_y is varied in proportion to the stress resultant T_x: $T_y = \psi T_x$. From (2.11) (after simple transformations) one can find

$$k_x = \frac{k_{mn}n^2}{1+\psi(na/mb)^2}\ , \qquad k_y = \frac{\psi k_{mn}n^2}{1+\psi(na/mb)^2}\ .$$

By minimizing k_x and k_y with respect to the numbers of half-waves, find the stability coefficients for the proportional loading:

$$k_x^* = \min\left[\frac{k_{mn}n^2}{1+\psi(na/mb)^2}\right]\ , \qquad k_y^* = \psi k_x^*.$$

The pair { k_x^*, k_y^* } is corresponded to by the natural shape

$$\bar{w}^* = \sin(m_0 \pi x / a) \ \sin(n_0 \pi y / b) \ .$$

Use now (2.10) to determine the critical compression stress resultants T_x^* and T_y^* and study the effect of the fiber orientation angle fi on stability of panels made from carbon fiber reinforced plastic. Figure 2.2 shows the function $T_x^*(\pm\varphi)$ for a square panel (line 3) and a rectangular panel (a/b=3, line 4) under the proportional loading (ψ = 0.3). Applying a biaxial compression, the critical stress resultants in the square plate are maximum at $\varphi = \pm 45°$, and those in the rectangular plate, at $\varphi = \pm 55°$.

2.2.2. Shear

Assume that the orthotropic plate is loaded with a shear flow T_{xy} only. Elements of the matrix $[\overline{M}]$ in this case are

$\overline{M}_{dd} = m^2 n^2 k_{mn}$;

$$\overline{M}_{\substack{dI \\ (d \neq I)}} = \begin{cases} \dfrac{32}{\pi^2} \dfrac{a}{b} k_{xy} \dfrac{mnij}{\left(m^2 - i^2\right)\left(n^2 - j^2\right)} & \text{for} \quad m \pm i = 1,3,5,\ldots, n \pm j = 1,3,5,\ldots; \\ 0 & \text{for} \quad m \pm i = 2,4,6,\ldots, n \pm j = 2,4,6,\ldots. \end{cases}$$

Transform the homogeneous system (2.9) of linear algebraic equations into

$$[S] \{A\} - \lambda \{A\} = 0 \ . \qquad (2.12)$$

Here [S] is a square matrix whose components include

$$S_{\substack{dI \\ (d \neq I)}} = \begin{cases} r_{mn} \dfrac{mnij}{\left(m^2 - i^2\right)\left(n^2 - j^2\right)} & \text{for} \quad m \pm i = 1,3,5,\ldots, n \pm j = 1,3,5,\ldots; \\ 0 & \text{for} \quad m \pm i = 2,4,6,\ldots; n \pm j = 2,4,6,\ldots, \end{cases}$$

$$S_{dd} = 1, \quad r_{mn} = -\frac{32a}{\pi^2 b(m^4 \alpha + 2m^2 n^2 + n^4 / \alpha)} .$$

The eigenvalues λ are related to the coefficients k_{xy} via the equality $k_{xy} = 1/(\lambda - 1)$. The matrix [S] for our problem is asymmetrical and may be transformed into an upper (or lower) Hessenberg matrix; thereafter the QR-factorization or QL-factorization may be employed to compute eigenvalues λ and eigen vectors {q}, refer to [17]. The stability coefficient k^*_{xy} is found from the condition $k^*_{xy} = \min[1/(\lambda - 1)] = 1/[\max(\lambda) - 1]$. It has the eigen vectors $\{q^*\}$ and the natural mode

$$\overline{w}^* = \sum_{m=1}^{\infty}\sum_{n=1}^{\infty} q_{mn}^* \sin\lambda_m x \ \sin\lambda_n y.$$

Consider the effect of the fiber orientation angle φ on critical shear stress resultant T^*_{xy}, derived from (2.10) for the abovesaid orthotropic panel out of carbon fiber reinforced plastic: laminate thickness $h=1.1\ 10^{-3}$ m; width b=0.4 m; length a=(0.4; 0.8; 1.2; 2.0) m. The results are presented in Fig. 2.3. It is usual to assume that the structures loaded in shear should have fibers laid at an angle of ±45°. Examination of $T^*_{xy}(\pm\varphi, a/b)$ suggests that such a layup is effective for square panels only. As to rectangular panels, a maximum value of critical shear stress resultants is achieved with different fiber orientation angles. In particular, for a panel with the aspect ratio a/b=3 the maximum value of T^*_{xy} is achieved at $\varphi=\pm59°$. The difference between $T^*_{xy}(\pm45°)=3.2$ kN/m and $T^*_{xy}(\pm59°)=3.8$ kN/m is 18.7%, i.e., the critical shear stress resultant reduces notably, and the structure gets less effective in respect of weight. The computation was based on 30 terms of the series.

The results of computation of critical shear stress resultants were validated experimentally by using a plate out of CFRP reinforced at an angle of ±45° and having the following characteristics: a=0.196 m; b=0.096 m; $D_{11}=D_{22}=0.685$ Nm; $D_{12}=0.548$ Nm; $D_{33}=0.585$ Nm. The experimental value of the stability coefficient is $k^*_{xy}=9.67$, see [18]; the theoretical value is $k^*_{xy}=9.79$, i.e., the computed results satisfactorily correlate with the experiment. Figure 2.4 demonstrates the shape of the panel surface after buckling, and Fig. 2.5 shows the natural mode of the experimental panel. The comparison of the natural mode with the postbuckling shape of the surface shows that there exists similarity between them.

2.2.3. Multiaxial load

Address the stability of a plate under axial compression and shear ($T_x \neq 0$, $T_{xy} \neq 0$). Make use of the earlier obtained values of the critical stress resultant of compression, T^*_{x0}, and shear, T^*_{xy0}, (for the cases of the loads being applied separately) and establish dependence between T_x and T_{xy} at instant of buckling. Assume that T_x is varied in proportion to the critical compression stress resultant T^*_{x0}: $T_x=\psi T^*_{x0}$. Matrix $[\overline{M}]$ elements will be of form

$$\overline{M}_{dd} = m^2n^2k_{mn} - \psi\, k^*_{x0}(m^2 + f_x n^2 a^2/b^2)\ ;$$

$$\overline{M}_{\substack{dI\\(d\neq I)}} = \begin{cases} \dfrac{32}{\pi^2}\dfrac{a}{b}k_{xy}\dfrac{mnij}{\left(m^2-i^2\right)\left(n^2-j^2\right)} & \text{for} \quad m\pm i = 1,3,5,\ldots, n\pm j = 1,3,5,\ldots; \\ 0 & \text{for} \quad m\pm i = 2,4,6,\ldots, n\pm j = 2,4,6,\ldots. \end{cases}$$

Transform the matrix $[\overline{M}]$ by analogy with transformations carried out for the problem on stability under shear.

From the set of simultaneous equations of (2.12) type, by using the technique described in 2.2.2 and specifying a series of values of ψ, one can establish the function $k^*_{xy}=f(\psi k^*_{x0})$. Figure 2.6 shows examples of the relations for

- the CFRP plate above ((a/b=1, φ=±45°)) with free edges (∗) and
- a plate with longitudinal edges not moving laterally (+).

Curves in Fig. 2.6 correspond to the equation

$$\frac{T_x}{T^*_{x0}} + \left(\frac{T_{xy}}{T^*_{xy0}}\right)^2 = 1 \ . \tag{2.13}$$

From this Figure it follows that the results can well be described by formula (2.13); the latter allows analysts to use the values of critical stress resultants T^*_{x0} and T^*_{xy0} to determine the stress resultants T_x and T_{xy} at which the plate buckles.

2.3. Postbuckling behavior of plates

Let us make use of the previous section's natural modes to approximately determine postbuckling out-of-plane displacement of a plate. Express the buckling out-of-plane displacement w_o in the form of a product of an unknown amplitude A_o and a natural mode $\bar{w}$:

$$w_o = A_o \bar{w} = A_o \sum_m \sum_n q_{mn} \sin\lambda_m x \ \sin\lambda_n y. \tag{2.14}$$

Let us assume that, under the proportionally increasing loads $[T_x T_y T_{xy}]^T \geq [T^*_x T^*_y T^*_{xy}]^T$ (not far in excess of the critical stress resultants) the plate out-of-plane displacement shape is similar to the natural mode $\bar{w}^*$ corresponding to the minimum eigenvalue. The subsequent loading can change the out-of-plane displacement - a jump to the shape corresponding to the second eigenvalue etc. From the first two differential equations of equilibrium (2.5), taking into account (2.14), we write mid-surface displacements

$$\begin{aligned} u &= C_1 x + C_2 y + \frac{A_0^2}{16} \sum_m \sum_n q_{mn} (q_{mn} \bar{u}_1 + 2\sum_i \sum_j q_{ij} \bar{u}_2) \ , \\ v &= C_3 x + C_4 y + \frac{A_0^2}{16} \sum_m \sum_n q_{mn} (q_{mn} \bar{v}_1 + 2\sum_i \sum_j q_{ij} \bar{v}_2). \end{aligned} \tag{2.15}$$

Here

$$\bar{u}_1 = -\lambda_m \left(1 - \frac{\lambda_n^2}{\lambda_m^2} \frac{B_{12}}{B_{11}}\right) \sin 2\lambda_m x + \lambda_m r_1 \sin 2\lambda_m x \cos 2\lambda_n y,$$

$$\bar{v}_1 = -\lambda_n \left(1 - \frac{\lambda_m^2}{\lambda_n^2} \frac{B_{12}}{B_{22}}\right) \sin 2\lambda_n y + \lambda_n r_{11} \cos 2\lambda_m x \sin 2\lambda_n y,$$

$$\bar{u}_2 = \lambda_m\left[r_3 \sin(\lambda_m - \lambda_i)x \ \cos(\lambda_n - \lambda_j)y + r_5 \sin(\lambda_m + \lambda_i)x \ \cos(\lambda_n + \lambda_j)y + \right.$$
$$\left. + r_7 \sin(\lambda_m - \lambda_i)x \ \cos(\lambda_n + \lambda_j)y + r_9 \sin(\lambda_m + \lambda_i)x \ \cos(\lambda_n - \lambda_j)y\right] ,$$

$$\bar{v}_2 = \lambda_n\left[r_{13} \cos(\lambda_m - \lambda_i)x \ \sin(\lambda_n - \lambda_j)y + r_{15} \cos(\lambda_m + \lambda_i)x \ \sin(\lambda_n + \lambda_j)y + \right.$$
$$\left. + r_{17} \cos(\lambda_m - \lambda_i)x \ \sin(\lambda_n + \lambda_j)y + r_{19} \cos(\lambda_m + \lambda_i)x \ \sin(\lambda_n - \lambda_j)y\right] ;$$

m, n, i, and j are numbers of half-waves ($m \neq i$, $n \neq j$);

$r_1, r_3, r_5, r_7, r_9, r_{11}, r_{13}, r_{15}, r_{17}, r_{19}$ - are coefficients to be evaluated in pairs from systems of linear algebraic equations

$$[L]\{r\}=\{B\},$$

where [L] is a 2x2 (square) matrix, {B} is the right-hand side column.

For an orthotropic plate we have $r_1=r_{11}=1$, and the matrix [L] and the vector {B} for determining coefficients $[r_3 r_{13}]^T$, $[r_5 r_{15}]^T$, $[r_7 r_{17}]^T$, $[r_9 r_{19}]^T$ are of form

$$[L] = \begin{bmatrix} B_{11}t_1^2 + B_{33}t_2^2 & (B_{12} + B_{33})t_1 t_2 \\ (B_{12} + B_{33})t_1 t_2 & B_{33}t_1^2 + B_{22}t_2^2 \end{bmatrix} ,$$

$$\{B\} = \begin{Bmatrix} (B_{11}\lambda_i\delta_1 + B_{12}\lambda_n\lambda_j\delta_2 / \lambda_m)t_1 + 2B_{33}\lambda_j t_2 \delta_2 \\ 2B_{33}\lambda_j t_1 \delta_2 + (B_{12}\lambda_i\delta_2 + B_{22}\lambda_n\lambda_j\delta_1 / \lambda_m)t_2 \end{Bmatrix} ,$$

where the values t_1, t_2, δ_1, δ_2 should be

$t_1 = \lambda_m - \lambda_i$, $t_2 = \lambda_n - \lambda_j$, $\delta_1 = \delta_2 = 1$;
$t_1 = \lambda_m + \lambda_i$, $t_2 = \lambda_n + \lambda_j$, $\delta_1 = \delta_2 = -1$;
$t_1 = \lambda_m - \lambda_i$, $t_2 = \lambda_n + \lambda_j$, $\delta_1 = -1$, $\delta_2 = 1$;
$t_1 = \lambda_m + \lambda_i$, $t_2 = \lambda_n - \lambda_j$, $\delta_1 = 1$, $\delta_2 = -1$.

The constants C_1, C_2, C_3, C_4 for (2.15) are determined from the integral boundary conditions over the plate contour. In the case of a plate with freely moving longitudinal edges these conditions are

$$\int_0^b N_x dy = -T_x b \quad \text{при} \quad x = 0, a; \quad \int_0^a N_y dx = -T_y a \quad \text{при} \quad y = 0, b;$$

$$\int_0^a N_{xy} dx = -T_{xy} a \quad \text{при} \quad y = 0, b \ . \tag{2.16}$$

For a plate with fixed longitudinal edges the boundary conditions are written as

$$\int_0^b N_x dy = -T_x b \quad \text{при} \quad x = 0, a; \quad \Delta v = v(y=b) - v(y=0) = 0 \ ;$$

$$\int_0^a N_{xy} dx = -T_{xy} a \quad \text{при} \quad y = 0, b \ . \tag{2.17}$$

We should determine stress resultants N_x, N_y, N_{xy} by means of equations (2.3), (2.4), (2.14), and (2.15) and substitute these into the boundary conditions (2.16) or (2.17). Proceeding in this way, find

$$C_1 = -\beta_1 T_x + \beta_2 T_y - A_0^2 \sum_m \sum_n q_{mn}^2 (\lambda_m^2 + \beta_6 \lambda_n^2)/8, \qquad C_2 + C_3 = -\beta_8 T_{xy} \ ,$$

$$C_4 = -\beta_2 T_x - \beta_3 T_y - A_0^2 \sum_m \sum_n q_{mn}^2 \beta_7 \lambda_n^2 / 8 \ .$$

If the edges of a plate can displace freely, then

$\beta_1 = B_{22}/B$, $\beta_2 = B_{12}/B$, $\beta_3 = B_{11}/B$, $\beta_6 = 0$, $\beta_7 = 1$, $\beta_8 = 1/B_{33}$, $B = B_{11}B_{22} - B^2_{12}$.

If it is not the case, then $\beta_1 = 1/B_{11}$, $\beta_2 = \beta_3 = \beta_7 = 0$, $\beta_6 = B_{12}/B_{11}$, $\beta_8 = 1/B_{33}$.

Having fixed A_0 the out-of-plane displacement (2.14) and displacements (2.15) are employed to find deformations, stress resultants, and moments in the plate after buckling:

$$\varepsilon_{x0} = -\beta_1 T_x + \beta_2 T_y + A_0^2 \bar{\varepsilon}_x / 8 \ , \ \varepsilon_{y0} = -\beta_3 T_y + \beta_2 T_x + A_0^2 \bar{\varepsilon}_y / 8 \ ,$$

$$\gamma_{xy0} = -\beta_8 T_{xy} + A_0^2 \bar{\gamma}_{xy} / 8 \ ; \tag{2.18}$$

$$N_x = -T_x + A_0^2 (B_{11} \bar{\varepsilon}_x + B_{12} \bar{\varepsilon}_y)/8 \ , \qquad N_y = -T_y + A_0^2 (B_{12} \bar{\varepsilon}_x + B_{22} \hat{\bar{\varepsilon}}_y)/8 \ ,$$

$$N_{xy} = -T_{xy} + A_0^2 B_{33} \bar{\gamma}_{xy} / 8 \ ; \tag{2.19}$$

$$M_x = A_0 \sum_m \sum_n q_{mn} (D_{11} \lambda_m^2 + D_{12} \lambda_n^2) \sin \lambda_m x \ \sin \lambda_n y \ ,$$

$$M_y = A_0 \sum_m \sum_n q_{mn} (D_{12} \lambda_m^2 + D_{22} \lambda_n^2) \sin \lambda_m x \ \sin \lambda_n y \ , \tag{2.20}$$

$$M_{xy} = -2A_0 \sum_m \sum_n q_{mn} D_{33} \lambda_m \ \lambda_n \cos \lambda_m x \ \cos \lambda_n y \ .$$

Here, the following notation is introduced:

$$\bar{\varepsilon}_x = \sum_m \sum_n \Big\{ q_{mn}^2 (-\beta_6 \lambda_n^2 + B_{12} \lambda_n^2 \cos 2\lambda_m x / B_{11} - \lambda_m^2 \cos 2\lambda_n y) +$$

$$+ q_{mn} \lambda_m \sum_i \sum_j q_{ij} \lambda_i \Big[\ f_1 \cos(\lambda_m - \lambda_i)x \ \cos(\lambda_n - \lambda_j)y \ + f_3 \cos(\lambda_m + \lambda_i)x \ \cos(\lambda_n + \lambda_j)y +$$

$$+ f_5 \cos(\lambda_m - \lambda_i)x \ \cos(\lambda_n + \lambda_j)y + f_7 \cos(\lambda_m + \lambda_i)x \ \cos(\lambda_n - \lambda_j)y \ \Big] \Big\} \ ,$$

$$\bar{\varepsilon}_y = \sum_m \sum_n \Big\{ q_{mn}^2 \big[(1-\beta_7)\lambda_n^2 + B_{12}\lambda_m^2 \cos 2\lambda_n y / B_{22} - \lambda_n^2 \cos 2\lambda_m x) \big] +$$

$$+ q_{mn}\lambda_n \sum_i \sum_j q_{ij}\lambda_j \Big[f_{11}\cos(\lambda_m - \lambda_i)x \ \cos(\lambda_n - \lambda_j)y + f_{13}\cos(\lambda_m + \lambda_i)x \ \cos(\lambda_n + \lambda_j)y \ +$$

$$+ f_{15}\cos(\lambda_m - \lambda_i)x \ \cos(\lambda_n + \lambda_j)y + f_{17}\cos(\lambda_m + \lambda_i)x \ \cos(\lambda_n - \lambda_j)y \ \Big] \Big\} ,$$

$$\bar{\gamma}_{xy} = -\sum_m \sum_n q_{mn}\lambda_n \sum_i \sum_j q_{ij}\lambda_j \Big[f_{22}\sin(\lambda_m - \lambda_i)x \ \sin(\lambda_n - \lambda_j)y + f_{24}\sin(\lambda_m + \lambda_i)x \ \sin(\lambda_n$$

$$+ f_{26}\sin(\lambda_m - \lambda_i)x \ \sin(\lambda_n + \lambda_j)y \ + f_{28}\sin(\lambda_m + \lambda_i)x \ \sin(\lambda_n - \lambda_j)y \ \Big] ,$$

$$\hat{T}_y = \begin{cases} T_y & \text{for plate with freely moving edges,} \\ T_x B_{12}/B_{11} & \text{for plate with fixed longitudinal edges.} \end{cases}$$

Coefficients $f_1, f_3, \ldots, f_{28}$ of series for strains $\bar{\varepsilon}_x$, $\bar{\varepsilon}_y$, $\bar{\gamma}_{xy}$ are:

$f_1 = 1 + r_3(\lambda_m - \lambda_i)/\lambda_i$, $f_{11} = 1 + r_{13}\lambda_m(\lambda_n - \lambda_j)/(\lambda_n \lambda_j)$,
$f_3 = -1 + r_5(\lambda_m + \lambda_i)/\lambda_i$, $f_{13} = -1 + r_{15}\lambda_m(\lambda_n + \lambda_j)/(\lambda_n \lambda_j)$,
$f_5 = -1 + r_7(\lambda_m - \lambda_i)/\lambda_i$, $f_{15} = 1 + r_{17}\lambda_m(\lambda_n + \lambda_j)/(\lambda_n \lambda_j)$,
$f_7 = 1 + r_9(\lambda_m + \lambda_i)/\lambda_i$, $f_{17} = -1 + r_{19}\lambda_m(\lambda_n - \lambda_j)/(\lambda_n \lambda_j)$,
$f_{22} = r_3(\lambda_n - \lambda_j)/\lambda_j + r_{13}\lambda_m(\lambda_m - \lambda_i)/\lambda_j + 2$,
$f_{24} = r_5(\lambda_n + \lambda_j)/\lambda_j + r_{15}\lambda_m(\lambda_m + \lambda_i)/\lambda_j - 2$,
$f_{26} = r_7(\lambda_n - \lambda_j)/\lambda_j + r_{17}\lambda_m(\lambda_m - \lambda_i)/\lambda_j + 2$,
$f_{28} = r_9(\lambda_n - \lambda_j)/\lambda_j + r_{19}\lambda_m(\lambda_m + \lambda_i)/\lambda_j - 2$.

Relations (2.14) and (2.19) do not make it possible to accurately satisfy the third equilibrium equation (2.6). To construct an approximate solution, make use of the energy functional (2.7). Substitute in (2.7) the mid-surface displacements (2.14) and (2.15) to obtain after integration:

$$\begin{aligned} \mathrm{Э}_0 = &-\frac{ab}{2}\Big[T_x(\beta_1 T_x - \beta_2 T_y) + T_y(\beta_3 T_y - \beta_2 T_x) + T_{xy}^2\beta_8\Big] + \\ &+ A_0^2 \frac{\pi^2}{8}\frac{a}{b}\Big(\bar{N} - T_x\alpha_x - T_y\alpha_y - T_{xy}\alpha_{xy}\Big) + A_0^4 \frac{I_0}{128} , \end{aligned} \tag{2.21}$$

Here

$$\bar{N} = \frac{\pi^2}{a^2}\sqrt{D_{11}D_{22}} \sum_m \sum_n q_{mn}^2 m^2 n^2 k_{mn} ,$$

$$\alpha_x = \sum_m \sum_n q_{mn}^2 m^2 \left(\frac{b^2}{a^2} + f_x \frac{n^2}{m^2} \right) , \quad \alpha_y = \sum_m \sum_n q_{mn}^2 n^2 ;$$

$$\alpha_{xy} = \frac{32}{\pi^2}\frac{b}{a}\sum_m\sum_n q_{mn} mn \sum_\xi\sum_\eta q_{\xi\eta}\frac{\xi\eta}{(m^2-\xi^2)(n^2-\eta^2)}\ , \quad \begin{matrix} m \pm \xi = 1,3,5,\ldots, \\ n \pm \eta = 1,3,5,\ldots; \end{matrix}$$

$$I_0 = \int_0^a\int_0^b \left(B_{11}\bar{\varepsilon}_x^2 + 2B_{12}\bar{\varepsilon}_x\bar{\varepsilon}_y + B_{22}\bar{\varepsilon}_y^2 + B_{33}\bar{\gamma}_{xy}^2 \right) dxdy\ .$$

Let us use the minimum total potential energy principle: minimize the functional (2.21) as a function of A_0. This provides $A_0=f(T_x,T_y,T_{xy})$ for the postbuckling out-of-plane displacement:

$$A_0 \frac{\pi^2 a}{4b}\left(\overline{N} - T_x\alpha_x - T_y\alpha_y - T_{xy}\alpha_{xy} + A_0^2\frac{bI_0}{8\pi^2 a} \right) = 0\ , \qquad (2.22)$$

Hence

$$A_0^{(1)} = 0\ ; \qquad A_0^{(2,3)} = \pm 2\pi\sqrt{2a(T_x\alpha_x + T_y\alpha_y + T_{xy}\alpha_{xy} - \overline{N})/(bI_0)}\ .$$

Equation (2.22) has three roots; the first of them ($A_0^{(1)}$) corresponds to plate deformation without bending; and the other two roots, to a plate deformation with out-of-plane displacement. From (2.22) it follows that if the stress resultants are less than critical (i.e., if $T_x\ \alpha_x+T_y\ \alpha_y+T_{xy}\ \alpha_{xy} < \overline{N}^*$) then roots $A_0^{(2,3)}$ are imaginary, and the plate can have a flat equilibrium shape only. If stress resultants exceed critical values (i.e., if $T_x\ \alpha_x+T_y\ \alpha_y+T_{xy}\ \alpha_{xy} > \overline{N}^*$) then roots $A_0^{(2,3)}$ are real and non-zero, which means that the plate can show a bending equilibrium shape.

Relations (2.18) - (2.20) should be complemented with a procedure describing changeover of the buckling shapes. To achieve this, transform the energy functional (2.21) taking into account formulas (2.22) for the out-of-plane displacement amplitude A_0:

$$Э_0 = -\frac{ab}{2}(T_x^2\beta_1 + T_y^2\beta_3 - 2T_xT_y\beta_2 + T_{xy}^2\beta_8) - \frac{\pi^4 a^2}{2I_0 b^2}(T_x\alpha_x + T_y\alpha_y + T_{xy}\alpha_{xy} - \overline{N})^2 . (2.23)$$

Let us analyze variation of $Э_0$ for three likely postbuckling states. The first state corresponds to a flat plate and is associated with energy $Э_0^{(0)}$:

$$Э_0^{(0)} = -\frac{ab}{2}(T_x^2\beta_1 + T_y^2\beta_3 - 2T_xT_y\beta_2 + T_{xy}^2\beta_8)\ .$$

The second state corresponds to a bending equilibrium shape similar to the first natural mode $\overline{w}^*$ and has the associated energy $Э_0^{(1)}$

$$Э_0^{(1)} = -\frac{ab}{2}(T_x^2\beta_1 + T_y^2\beta_3 - 2T_xT_y\beta_2 + T_{xy}^2\beta_8) - \frac{\pi^4 a^2}{2I_0^* b^2}(T_x\alpha_x^* + T_y\alpha_y^* + T_{xy}\alpha_{xy}^* - \overline{N^*}\ )^2.$$

The third state corresponds to a bending equilibrium shape similar to the second natural mode $\overline{w}^{(2)}$ and has the associated energy $Э_0^{(2)}$

$$\acute{Y}_0^{(2)} = -\frac{ab}{2}(T_x^2\beta_1 + T_y^2\beta_3 - 2T_xT_y\beta_2 + T_{xy}^2\beta_8) - \frac{\pi^4 a^2}{2I_0^{(2)}b^2}(T_x\alpha_x^{(2)} + T_y\alpha_y^{(2)} + T_{xy}\alpha_{xy}^{(2)} - \overline{N}^{(2)})^2.$$

Figure 2.7 shows the variation of energy of every state in the course of proportional loading with generalized stress resultants $\{T\}^T=T[T'_xT'_yT'_{xy}]^T$. The real postbuckling equilibrium shape depends on a loading level T. At an initial stage of loading, when $T \le T^*$ (T^* is the first eigenvalue), the equation (2.22) produces the result $A_0=0$; consequently, the plate remains flat. In further loading, when $T > T^*$, two equilibrium modes are possible: planar and curved, with a surface shape similar to the first natural mode. We can assume that the plate takes the equilibrium mode which corresponds to minimum generalized stress resultant and a minimum total potential energy. If $T > T^*$ the real equilibrium mode is the one with a surface shape similar to the first natural mode. At the bifurcation point, the total potential energies of two equilibrium states, $Э_0^{(0)}$ and $Э_0^{(1)}$, must satisfy the condition $Э_0^{(0)}=Э_0^{(1)}$; from this the following equality appears:

$$T_x\alpha_x^* + T_y\alpha_y^* + T_{xy}\alpha_{xy}^* - \overline{N}^* = 0 .$$

It allows us to find the value T^* and the stress resultant $\{T_xT_yT_{xy}\}^T$ at which the equilibrium shape changes over. Of course, the first of such change-overs occurs at a force equal to the critical value. Determine the real equilibrium mode in the postbuckling stage at stress resultants $T>>T^*$. We shall compare now the energy levels of the plate with

- the shape of the surface similar to the first natural mode and
- the shape of the surface similar to the second natural mode,

i.e., $Э_0^{(1)}$ and $Э_0^{(2)}$. Refer to Fig. 2.7. The first equilibrium mode has energy $Э_0^{(1)}$ (T_1) (line 2), and the second has energy $Э_0^{(2)}$ (T_2) (line 3). If the accumulated energy levels are identical $Э_0^{(1)}=Э_0^{(2)}$ and the load level $T_1,T_2<T_S$ then the first equilibrium mode takes place, whereas the second one appears at $T_1,T_2>T_S$. The value T_S can be called the stress resultant of secondary bifurcation. Use the condition $Э_0^{(1)}=Э_0^{(2)}$ to determine the value T_S. After simple transformations we obtain the following equation:

$$T_x\gamma_x + T_y\gamma_y + T_{xy}\gamma_{xy} = \overline{N}^* - \overline{N}^{(2)}\sqrt{I_0^*/I_0^{(2)}} ,$$

where

$$\gamma_x = \alpha_x^* - \alpha_x^{(2)}\sqrt{I_0^*/I_0^{(2)}} , \qquad \gamma_y = \alpha_y^* - \alpha_y^{(2)}\sqrt{I_0^*/I_0^{(2)}} , \; \gamma_{xy} = \alpha_{xy}^* - \alpha_{xy}^{(2)}\sqrt{I_0^*/I_0^{(2)}} .$$

With the relation between stress resultants T_x,T_y,T_{xy} known, it is an easy task to evaluate each of them. If a plate is rather thin and a load level $T>T_S$ does not cause failure, a further change of the plate surface shape in the postbuckling stage is possible. To determine a level of the next bifurcation, one must compare total potential energies $Э^{(2)}_0$ and $Э^{(3)}_0$ etc.

With the equilibrium shape known, we may determine the out-of-plane displacement amplitude (2.22) and plate state characteristics (2.19) and (2.20) for each point. Use mid-surface strains (2.3) to find strains of every layer, (2.2), and layer stresses (σ_1, σ_2, τ_{12}) referred to layer orthotropy axes:

$$\sigma_1 = \bar{E}_1\Big[\,(\varepsilon_{x0} + z\chi_x)(\cos^2\varphi + \mu_{12}\sin^2\varphi) + (\varepsilon_{y0} + z\chi_y)(\sin^2\varphi + \mu_{12}\cos^2\varphi) +$$
$$+(\gamma_{xy0} + z\chi_{xy})(1-\mu_{12})\sin\varphi\,\cos\varphi\,\Big]\,,$$

$$\sigma_2 = \bar{E}_2\Big[\,(\varepsilon_{x0} + z\chi_x)(\sin^2\varphi + \mu_{21}\cos^2\varphi) + (\varepsilon_{y0} + z\chi_y)(\cos^2\varphi + \mu_{21}\sin^2\varphi) -$$
$$-(\gamma_{xy0} + z\chi_{xy})(1-\mu_{21})\sin\varphi\,\cos\varphi\,\Big]\,,$$

$$\tau_{12} = G_{12}[(\varepsilon_{y0} - \varepsilon_{x0} + z\chi_y - z\chi_x)\sin 2\varphi + (\gamma_{xy0} + z\chi_{xy})\cos 2\varphi]\,,$$

where

$$\chi_x = A_0\sum_m\sum_n q_{mn}\lambda_m^2\sin\lambda_m x\,\sin\lambda_n y\,,\quad \bar{E}_1 = \frac{E_1}{1-\mu_{12}\mu_{21}}\,,$$

$$\chi_y = A_0\sum_m\sum_n q_{mn}\lambda_n^2\sin\lambda_m x\,\sin\lambda_n y\,,\quad \bar{E}_2 = \frac{E_2}{1-\mu_{12}\mu_{21}}\,,$$

$$\chi_{xy} = -2A_0\sum_m\sum_n q_{mn}\lambda_m\lambda_n\cos\lambda_m x\,\cos\lambda_n y\,,\quad \mu_{12} = \mu_{21}\frac{E_2}{E_1}\,;$$

E_1, E_2, G_{12}, μ_{21} are conventional elastic characteristics of a layer. The stresses in every elementary layer should be compared with fracture stresses $\bar{\sigma}_1, \bar{\sigma}_2, \bar{\tau}_{12}$ to determine the plate limiting state after buckling.

Let us study the postbuckling behavior and load-carrying capability of composite plates for particular cases of compression, shear, and multiaxial load.

2.3.1. Compression

For this type of loadings (when $T_{xy} = 0$) the natural mode is of form

$$\bar{w} = \sin(m\pi x/a)\sin(n\pi y/b)$$

and relations (2.15), (2.18) - (2.20), (2.22) and (2.23) become significantly simpler.
A postbuckling out-of-plane displacement is described by the equation

$$w=A_0\sin\lambda_m x\ \sin\lambda_n y\ .$$

For a plate with freely moving edges we have the following relations:
- mid-surface displacements

$$u=\left(-\beta_1 T_x-A_0^2\lambda_m^2/8\right)x-\frac{A_0^2}{16}\left[(\lambda_m^2-B_{12}\lambda_n^2/B_{11})\lambda_m^{-1}\sin 2\lambda_m x-\lambda_m\sin 2\lambda_m x\cos 2\lambda_n y\right],$$

$$(2.25)$$

$$v=\left(-\beta_2 T_x-A_0^2\beta_7\lambda_n^2/8\right)y-\frac{A_0^2}{16}\left[(\lambda_n^2-B_{12}\lambda_m^2/B_{22})\lambda_n^{-1}\sin 2\lambda_n y-\lambda_n\cos 2\lambda_m x\sin 2\lambda_n y\right];$$

-the strains

$$\varepsilon_{x0}=-\beta_1 T_x+A_0^2(B_{12}\lambda_n^2\cos 2\lambda_m x/B_{11}-\lambda_m^2\cos 2\lambda_n y)/8\ ,$$

$$(2.26)$$

$$\varepsilon_{y0}=-\beta_2 T_x+A_0^2(B_{12}\lambda_m^2\cos 2\lambda_n y/B_{22}-\lambda_n^2\cos 2\lambda_m x)/8\ ,\quad \gamma_{xy0}=0\ ;$$

- stress resultants

$$N_x=-T_x-A_0^2B\ (8B_{22})^{-1}\lambda_m^2\cos 2\lambda_n y\ ,$$

$$(2.27)$$

$$N_y=-A_0^2B\ (8B_{11})^{-1}\lambda_n^2\cos 2\lambda_m x\ ,\quad N_{xy}=0\ ;$$

- moments

$$M_x=A_0\left(D_{11}\lambda_m^2+D_{12}\lambda_n^2\right)\sin\lambda_m x\ \sin\lambda_n y\ ,$$
$$M_y=A_0\left(D_{12}\lambda_m^2+D_{22}\lambda_n^2\right)\sin\lambda_m x\ \sin\lambda_n y\ ,\quad M_{xy}=-2A_0D_{33}\lambda_m\lambda_n\cos\lambda_m x\ \cos\lambda_n y\ .$$

Layer stresses could be determined using the following formulas:

$$\sigma_1=-\bar{E}_1T_x\left[\ \beta_1\left(\cos^2\varphi+\mu_{12}\sin^2\varphi\right)-\beta_2(\sin^2\varphi+\mu_{12}\cos^2\varphi)\ \right]+$$
$$+\bar{E}_1A_0^2\left[\left(B_{12}\lambda_n^2\cos 2\lambda_m x/B_{11}-\lambda_m^2\cos 2\lambda_n y\right)\ (\cos^2\varphi+\mu_{12}\sin^2\varphi)+\right.$$
$$\left.+\left(B_{12}\lambda_m^2\cos 2\lambda_n y/B_{22}-\lambda_n^2\cos 2\lambda_m x\right)\ (\sin^2\varphi+\mu_{12}\cos^2\varphi)\ \right]/8+$$
$$+A_0z\bar{E}_1\left\{\left[\lambda_m^2(\cos^2\varphi+\mu_{12}\sin^2\varphi)+\lambda_n^2(\sin^2\varphi+\mu_{12}\cos^2\varphi)\right]\sin\lambda_m x\sin\lambda_n y-\right.$$
$$\left.-2\lambda_m\lambda_n(1-\mu_{12})\sin\varphi\cos\varphi\cos\lambda_m x\cos\lambda_n y\ \right\}\ ,$$

$$\sigma_2=-\bar{E}_2T_x\left[\beta_1\left(\sin^2\varphi+\mu_{21}\cos^2\varphi\right)-\beta_2(\cos^2\varphi+\mu_{21}\sin^2\varphi)\ \right]+$$

$$+\bar{E}_2 A_0^2\Big[\Big(B_{12}\lambda_n^2 \cos 2\lambda_m x / B_{11} - \lambda_m^2 \cos 2\lambda_n y\Big)\ (\sin^2\varphi + \mu_{21}\cos^2\varphi) +$$

$$+\Big(B_{12}\lambda_m^2 \cos 2\lambda_n y / B_{22} - \lambda_n^2 \cos 2\lambda_m x\Big)\ (\cos^2\varphi + \mu_{21}\sin^2\varphi)\ \Big] / 8 + \qquad (2.28)$$

$$+A_0 z \bar{E}_2\Big\{\Big[\lambda_m^2(\sin^2\varphi + \mu_{21}\cos^2\varphi) + \lambda_n^2(\cos^2\varphi + \mu_{21}\sin^2\varphi)\Big]\sin\lambda_m x\ \ \sin\lambda_n y +$$

$$+2\lambda_m\lambda_n(1-\mu_{21})\sin\varphi\ \ \cos\varphi\ \ \cos\lambda_m x\ \ \cos\lambda_n y\ \Big\}\ ,$$

$$\tau_{12} = G_{12}\Big\{\ T_x(\beta_1+\beta_2)\sin 2\varphi + A_0^2\Big[\lambda_m^2(1+\frac{B_{12}}{B_{22}})\cos 2\lambda_n y -$$

$$-\frac{\lambda_n^2}{8}(1+B_{12}/B_{11})\cos 2\lambda_m x\ \Big]\sin 2\varphi + A_0 z\Big[(\lambda_n^2-\lambda_m^2)\sin 2\varphi\ \ \sin\lambda_m x\ \ \sin\lambda_n y -$$

$$-2\lambda_m\lambda_n\cos 2\varphi\ \ \cos\lambda_m x\ \ \cos\lambda_n y\ \Big]\Big\}\ .$$

The plate out-of-plane displacement amplitude is of form

$$A_0^2 = \frac{16}{\lambda_n^2}\left(T_x - T_{mn}\right)\left(\frac{\lambda_n^2 B}{\lambda_m^2 B_{11}} + \frac{\lambda_m^2 B}{\lambda_n^2 B_{22}}\right)^{-1}, \qquad (2.29)$$

where $T_{mn} = \lambda_n^2\sqrt{D_{11}D_{22}}\ k_{mn}$. The total potential energy of the compression loaded plate can be presented as follows:

$$Э_0 = -\frac{ab}{2}T_x^2\ \beta_1 - ab(T_x - T_{mn})^2\left(\frac{B}{B_{22}} - \frac{\lambda_n^4}{\lambda_m^4}\frac{B}{B_{11}}\right)^{-1}. \qquad (2.30)$$

Complement the relations (2.25) - (2.30) with a procedure for searching the real equilibrium mode in postbuckling stage of loading. The total potential energy of compression of a flat plate is $Э_0^{(0)} = -T_x^2\ \beta_1\ ab/2$.

The total potential energy of compression of a curved plate with a surface shape similar to the first and second natural modes will be of form

$$Э_0^{(1)} = -\frac{ab}{2}T_x^2\ \beta_1 - ab(T_x - T_x^*)^2\left(\frac{B}{B_{22}} - \frac{\lambda_{n0}^4}{\lambda_{m0}^4}\frac{B}{B_{11}}\right)^{-1},$$

$$Э_0^{(2)} = -\frac{ab}{2}T_x^2\ \beta_1 - ab(T_x - T_x^{(2)})^2\left(\frac{B}{B_{22}} - \frac{n_0^4\ a^4}{(m_0+1)b^4}\frac{B}{B_{11}}\right)^{-1},$$

and so on. At the initial stage of loadings, when $T_x \le T^*_x$ a plane state of equilibrium is implemented, and the plate total potential energy is a function on $\ni^{(0)}{}_0$. With a load level $T_x > T^*_x$ two equilibrium modes are likely: a planar mode and a curved mode with a surface shape similar to the first natural mode. To identify the real equilibrium mode, compare compressive stress resultants at identical levels of energy accumulation ($\ni^{(0)}{}_0 = \ni^{(1)}{}_0$), i.e.,

$$-\frac{ab}{2}T_0^2\,\beta_1 = -\frac{ab}{2}T_1^2\,\beta_1 - ab(T_1 - T_x^*)^2\left(\frac{B}{B_{22}} - \frac{\lambda_{n0}^4}{\lambda_{m0}^4}\frac{B}{B_{11}}\right)^{-1}.$$

The equality holds if $T_0 > T_1$. Let us assume that the real equilibrium mode is the one which corresponds to lower stress resultants. Consequently, at $T_x > T^*_x$ the plate takes the equilibrium mode whose surface shape is similar to the first natural mode. Study now the plate equilibrium mode for stress resultants $T_x >> T^*_x$; total potential energies $\ni^{(1)}{}_0$ and $\ni^{(2)}{}_0$ should be compared. For identical levels of accumulated energy ($\ni^{(1)}{}_0 = \ni^{(2)}{}_0$) compare the stress resultants T_1 and T_2; for this purpose we write the equation:

$$-\frac{ab}{2}T_1^2\,\beta_1 - ab(T_1 - T_x^*)^2\left(\frac{B}{B_{22}} - \frac{\lambda_{n0}^4}{\lambda_{m0}^4}\frac{B}{B_{11}}\right)^{-1} =$$

$$= -\frac{ab}{2}T_2^2\,\beta_1 - ab(T_2 - T_x^{(2)})^2\left(\frac{B}{B_{22}} - \frac{n_0^4\,a^4}{(m_0+1)^4 b^4}\frac{B}{B_{11}}\right)^{-1}.$$

After simple transformations we can establish the load level T_S at which $\ni^{(1)}{}_0 = \ni^{(2)}{}_0$ and $T_1 = T_2$. It is from the relation

$$T_S = (T^*_x - T_x^{(2)} f_S) / (1 - f_S)\,,$$

$$\text{where}\quad f_s = \sqrt{\left(\frac{B}{B_{22}} - \frac{\lambda_{n0}^4}{\lambda_{m0}^4}\frac{B}{B_{11}}\right)\left[\frac{B}{B_{22}} - \frac{n_0^4 a^4}{(m_0+1)^4 b^4}\frac{B}{B_{11}}\right]^{-1}}\,.$$

The stress resultant T_S is the secondary bifurcation stress resultant. If $T^*_x < T_x < T_S$ the plate is in the equilibrium mode with the surface shape similar to the first natural mode (since $T_1 < T_2$), whereas if $T_x > T_S$ then the plate is in the equilibrium mode with the surface shape similar to the second natural mode ($T_1 > T_2$ in this case).

To exemplify determination of secondary bifurcation stress resultants, a plate may be considered whose stiffnesses and geometric characteristics are given in [19]. For such a plate the above procedure for identifying secondary bifurcation points gives $T_S = 3.08T^*_x$. In [19], a finite difference technique is employed to find the stress resultant $T_S = 3.28T^*$. A difference between the results is 6.5%.

For a plate with fixed longitudinal edges we have the following relations describing the displacements, strains, stress resultants, and stresses:

$$u = \left(-\beta_1 T_x - A_0^2(\lambda_m^2 + B_{12}\lambda_n^2 / B_{11}) / 8\right)x -$$

$$-\frac{A_0^2}{16}\left[(\lambda_m^2 - B_{12}\lambda_n^2 / B_{11})\lambda_m^{-1} \sin 2\lambda_m x - \lambda_m \sin 2\lambda_m x \;\; \cos 2\lambda_n y\right] ,$$

$$v = -A_0^2\beta_7\lambda_n^2 y / 8 - \frac{A_0^2}{16}\left[(\lambda_n^2 - B_{12}\lambda_m^2 / B_{22})\lambda_n^{-1} \sin 2\lambda_n y - \lambda_n \cos 2\lambda_m x \;\; \sin 2\lambda_n y\right] ;$$

$$\varepsilon_{x0} = -\beta_1 T_x + A_0^2(-\lambda_n^2 B_{12} / B_{11} + B_{12}\lambda_n^2 \cos 2\lambda_m x / B_{11} - \lambda_m^2 \cos 2\lambda_n y) / 8 ,$$

$$\varepsilon_{y0} = A_0^2(\lambda_n^2 + B_{12}\lambda_m^2 \cos 2\lambda_n y / B_{22} - \lambda_n^2 \cos 2\lambda_m x) / 8 , \quad \gamma_{xy0} = 0 ;$$

$$N_x = -T_x - A_0^2 B(8B_{22})^{-1}\lambda_m^2 \cos 2\lambda_n y ,$$

$$N_y = -T_x B_{12} / B_{11} - A_0^2 B(8B_{11})^{-1}\lambda_n^2 \cos 2\lambda_m x , \quad N_{xy} = 0 ;$$

$$\sigma_1 = -\bar{E}_1 T_x(\cos^2\varphi + \mu_{12}\sin^2\varphi) / B_{11} + \bar{E}_1 A_0^2\big[\varepsilon_{x0}(\cos^2\varphi + \mu_{12}\sin^2\varphi) +$$

$$+\varepsilon_{y0}(\sin^2\varphi + \mu_{12}\cos^2\varphi) \;\big] / 8 +$$

$$+A_0 z\bar{E}_1\Big\{\Big[\lambda_m^2(\cos^2\varphi + \mu_{12}\sin^2\varphi) + \lambda_n^2(\sin^2\varphi + \mu_{12}\cos^2\varphi)\Big]\sin\lambda_m x \sin\lambda_n y -$$

$$-2\lambda_m\lambda_n(1 - \mu_{12})\sin\varphi\cos\varphi\cos\lambda_m x\cos\lambda_n y \;\Big\} ,$$

$$\sigma_2 = -\bar{E}_2 T_x(\cos^2\varphi + \mu_{21}\sin^2\varphi) / B_{11} + \bar{E}_2 A_0^2\Big[\varepsilon_{x0}\Big(\sin^2\varphi + \mu_{21}\cos^2\varphi\Big) +$$

$$+\varepsilon_{y0}(\cos^2\varphi + \mu_{21}\sin^2\varphi) \;\Big] / 8 +$$

$$+A_0 z\bar{E}_2\Big\{\Big[\lambda_m^2(\sin^2\varphi + \mu_{21}\cos^2\varphi) + \lambda_n^2(\cos^2\varphi + \mu_{21}\sin^2\varphi)\Big]\sin\lambda_m x \;\; \sin\lambda_n y +$$

$$+2\lambda_m\lambda_n(1 - \mu_{21})\sin\varphi \;\; \cos\varphi \;\; \cos\lambda_m x \;\; \cos\lambda_n y \;\Big\} ,$$

$$\tau_{12} = G_{12}\Big\{ \; T_x \sin 2\varphi / B_{11} + \frac{A_0^2}{8}\Big[\; \lambda_n^2(1 + \frac{B_{12}}{B_{11}}) + \lambda_m^2(1 + \frac{B_{12}}{B_{22}})\cos 2\lambda_n y -$$

$$-\lambda_n^2(1 + \frac{B_{12}}{B_{11}})\cos 2\lambda_m x\Big]\sin 2\varphi + A_0 z \;\Big[(\lambda_n^2 - \lambda_m^2)\sin 2\varphi \;\; \sin\lambda_m x \;\; \sin\lambda_n y -$$

$$-2\lambda_m\lambda_n \cos 2\varphi \;\; \cos\lambda_m x \;\; \cos\lambda_n y \;\Big]\Big\} .$$

The amplitude of out-of-plane displacements of such plate is defined by the equation:

$$A_0^2 = \frac{16}{\lambda_n^2}\left[T_x\left(1 + \frac{B_{12}}{B_{11}}\frac{\lambda_n^2}{\lambda_m^2}\right) - T_{mn}\right]\left(\frac{\lambda_n^2}{\lambda_m^2}\frac{B}{B_{11}} + \frac{\lambda_m^2}{\lambda_n^2}\frac{B}{B_{22}}\right)^{-1} .$$

Compare theoretical results with test data from [20] dealing with postbuckling behavior of homogeneous orthotropic plates with the freely moving edges. Experimental plates had the following characteristics:

plate N1: $h=2.506 \cdot 10^{-3}$ m, $B/hB_{22}=E_x=28.06$ GPa,
$B/hB_{11}=E_y=5.3$ GPa, $B_{33}/h=G_{xy}=2.15$ GPa, $B_{12}/B_{22}=\mu_{yx}=0.33$;
plate N2: $E_x=27.38$ GPa, $E_y=8.06$ GPa, $G_{xy}=2.71$ GPa, $\mu_{yx}=0.33$.

The dotted line in Fig. 2.8 shows the "relative load - relative displacement of loaded edges" relation based on (2.25) for the first plate. Points are from experiments. Figure 2.9 provides stress distribution $\sigma_x = N_x/h$ across the width of the plate N2, as found from (2.27) (dotted line). Points here also show test data. From these plots it follows that the solution satisfactorily describes behavior of buckled composite plates and may be used to estimate their load-carrying capability.

Address a CFRP plate with thickness $h=1.1 \cdot 10^{-3}$ m, dimensions a=b=0.4 m and the following mechanical characteristics of a layer: $E_1=180$ Gpa, $E_2=6.2$ GPa, $G_{12}=5.0$ GPa, $\mu_{21}=0.26$, $\bar{\sigma}_1=(+1000, -450)$ MPa, $\bar{\sigma}_2=(+33, -100)$ MPa, $\bar{\tau}_{12}=27$ MPa. Determine limit loads for various versions of reinforcement. The results of computation based on the Tsai criterion from [14] are depicted in Fig. 2.10; here, the solid line is for the plate with freely moving edges, whereas the dotted line, for the plate whose longitudinal edges do not displace transversely. From Fig. 2.10 it follows that the maximum load-bearing capability is ensured by plates with longitudinal stacking. When determining $\bar{T}_X$, account was taken of the change in the number of longitudinal half-waves in the course of loading. The load-carrying capacity of the plate with fixed longitudinal edges is slightly higher than that of the plate with free edges.

Compare critical stress resultants T^*_x with ultimate stress resultants $\bar{T}_X$.

We have: $\bar{T}_X/T^*_x = 104.3$ (109.1) at $\varphi = 0°$,
$\bar{T}_X/T^*_x = 9.29$ (16.4) at $\varphi = \pm 45°$.

The results between the brackets are for a plate with longitudinal edges not moving laterally. These results evidence that a buckled composite plate is able to carry considerable loads.

Traditionally, the load-carrying capability of a stiffened thin-walled panel with a buckled skin under compression is estimated by means of the reduction coefficient defined as the ratio of a mean compressive stress resultant $N_s = -\int_0^b N_x dy / b$ to a stress resultant N_p at the longitudinal edge of the skin: $\varphi_E = N_s / N_p$. Determination of reduction coefficients for metal uniaxially stiffened panels is dealt with in a large number of works, for example [1 - 5]. When analyzing aircraft structures, use is widely made of the notorious equation by von Karman [3]: $\varphi_E = \sqrt{T^*_x / N_p}$.

Let us employ the relation (2.27) for stress resultants in order to establish the reduction coefficient for compression loaded composite panels. We have

$$\varphi_E = \frac{1 + B_{22}(na/mb)^4 / B_{11}}{3 + B_{22}(na/mb)^4 / B_{11}} + \frac{T_x^*}{N_p}\,\frac{2}{3 + B_{22}(na/mb)^4 / B_{11}},$$

$$N_p = -T_x - A^2_0\,\lambda^2_m\,B/(8B_{22}). \tag{2.31}$$

The monograph [1] by A.S.Vol'mir presents experimental values of the reduction coefficients for traditional materials. These are shown by points in Fig. 2.11. The solid line shows the theoretical relation for φ_E at $a/b = 1$, taking into account changes in the skin buckling shape. One may see satisfactory coincidence of the results for metal panels at $N_p / T^*_x \leq 12 \div 16$.

However, application of the traditional reduction coefficient method to evaluation of load-carrying capabilities of composite panels is not always justified. As is generally known, it assumes that (1) a skin area with the width $b_{pr} = \varphi_E b$ is reduced to a stringer and (2) the likely final condition of the panels is reached as a result of general or local buckling of the stringer or its failure under compression. In this case, in accordance with the experience available, the skin is normally assumed not to fail. Some composites (in particular, carbon fiber reinforced plastics most widely utilized in thin-walled airframes) feature the brittle fracture at strains of 0.5 - 1.0%. This implies the compression loaded composite panels becoming broken, as a rule, due to skin failure from compression and bending that follows buckling. This is just the failure mode of the plate in the example above. That issue is studied in more detail in 2.4 below.

2.3.2. Shear

Consider postbuckling behavior of an orthotropic plate under shear. In this case the postbuckling out-of-plane displacement is governed by the general equation (2.14), whereas formulas (2.15) - (2.24) remained unchanged, taking into account that $T_x = T_y = 0$, $C_2 = C_3 = \beta_8 T_{yx} / 2$.

The out-of-plane displacement amplitude is

$$A_0 = 2\pi\sqrt{2a(T_{xy}\alpha_{xy} - \overline{N})/(bI_0)} \tag{2.32}$$

Stresses in layers are:

$$\sigma_1 = \overline{E}_1\Big\{-T_{xy}\beta_8(1-\mu_{12})\ \sin\varphi\ \cos\varphi + \frac{A_0^2}{8}\Big[\ \overline{\varepsilon}_x(\cos^2\varphi + \mu_{12}\sin^2\varphi) +$$

$$+\overline{\varepsilon}_y(\sin^2\varphi + \mu_{12}\cos^2\varphi) + \overline{\gamma}_{xy}(1-\mu_{12})\sin\varphi\ \cos\varphi\ \Big]\Big\} +$$

$$+A_0 z\overline{E}_1\sum_m\sum_n q_{mn}\Big\{\Big[\ \lambda_m^2(\cos^2\varphi + \mu_{12}\sin^2\varphi) + \lambda_n^2(\sin^2\varphi +$$

$$+\mu_{12}\cos^2\varphi)\ \Big]\sin\lambda_m x\ \sin\lambda_n y - 2\lambda_m\lambda_n(1-\mu_{12})\sin\varphi\ \cos\varphi\ \cos\lambda_m x\ \cos\lambda_n y\ \Big\},$$

$$\sigma_2 = \bar{E}_2\Big\{T_{xy}\beta_8(1-\mu_{21})\ \sin\varphi\ \cos\varphi + \frac{A_0^2}{8}\Big[\ \bar{\varepsilon}_x(\sin^2\varphi + \mu_{21}\cos^2\varphi) +$$
$$+\bar{\varepsilon}_y(\cos^2\varphi + \mu_{21}\sin^2\varphi) - \bar{\gamma}_{xy}(1-\mu_{21})\sin\varphi\ \cos\varphi\ \Big] + \tag{2.33}$$
$$+A_0 z\bar{E}_2\sum_m\sum_n q_{mn}\Big[\lambda_m^2\Big(\sin^2\varphi + \mu_{21}\cos^2\varphi\Big) + \lambda_n^2\Big(\cos^2\varphi +$$
$$+\mu_{21}\sin^2\varphi)\ \Big]\sin\lambda_m x\ \ \sin\lambda_n y + 2\lambda_m\lambda_n(1-\mu_{21})\sin\varphi\ \ \cos\varphi\ \ \cos\lambda_m x\ \ \cos\lambda_n y\ \Big\}\ ,$$

$$\tau_{12} = G_{12}\Big\{-T_{xy}\beta_8\cos 2\varphi + \frac{A_0^2}{8}\Big[(\bar{\varepsilon}_y - \bar{\varepsilon}_x)\sin 2\varphi + \bar{\gamma}_{xy}\cos 2\varphi\Big] +$$
$$+A_0 z\sum_m\sum_n q_{mn}\Big[(\lambda_n^2 - \lambda_m^2)\sin 2\varphi\ \ \sin\lambda_m x\ \ \sin\lambda_n y -$$
$$-2\lambda_m\lambda_n\cos 2\varphi\cos\lambda_m x\cos\lambda_n y\ \Big]\Big\}\ .$$

Values $\bar{\varepsilon}_x$, $\bar{\varepsilon}_y$, $\bar{\gamma}_{xy}$, $\bar{N}$, α_{xy} and I_0 have been defined earlier.

Address the stress state and load-carrying capacity of various commonly used plates out of CFRP under identical loads T_{xy} =11.5 kN/m ($T_{xy} = 2T^*_{xy}(\pm 45°)$). The plates with dimensions a=b=0.4 m and thickness h=1.3_10^{-3} m had the following layups: φ = 0° (plate 1), ±30° (plate 2), ±45° (plate 3), ±60° (plate 4), and 90°(plate 5). Figures 2.12 - 2.16 show distributions of stress resultants (N_x, N_y, N_{xy}), moments (M_x, M_y, M_{xy}) and stresses (σ_1, σ_2, τ_{12}) over the section $\bar{x} = x/a = 0.5$ of every plate. Stresses are presented for the layer whose mid-surface coincides with the plate mid-surface. Identification numbers of lines are identical to numbers of the plates, i.e., the line 1 is for the plate with the longitudinal stacking (φ = 0°) etc.

Of interest is dependence of the out-of-plane displacement amplitude on the applied load for differing layups. Figure 2.17 provides a plot of the "relative stress resultant (T_{xy}/T^*_{xy}) - relative out-of-plane displacement (w/h)" relation for plates 1, 2, and 3. The load-carrying capability of plates after buckling under shear substantially depends on layups and geometries. Figure 2.18 shows $\bar{T}_{xy}$ ($\pm\varphi$) for three plates with the aspect ratio a/b=1, 2, 3. In the case of the square plate the maximum load-carrying capability under shear is ensured by a plate with fiber orientation angles φ = ±45°; in the case of the plate with the aspect ratio a/b=2, the plate with angles φ = ±63°; in the case of the plate with the aspect ratio a/b=3, the plate with angles φ = ±67°. As well as under compression, composite plates after buckling under shear are capable of carrying the load. Employing this property in thin-walled structures of flight vehicles will make it possible to increase the effectiveness of composites. For the above plates the ratio of ultimate critical stress resultants $\bar{T}_{xy}$ / T^*_{xy} is (at φ = ±45°):

- 12.1 for the square plate;
- 10.5 for the plate with the aspect ratio a/b = 2;
- 5.2 for the plate with the aspect ratio a/b = 3.

It is usual that load-carrying capabilities of stiffened metal skin panels and spar webs under shear are estimated by using the theory of complete and partial diagonal tension fields [6,9]. Applicability of such an approach to composite structures was studied experimentally and theoretically by determining the load-carrying capability of a traditional thin-walled beam with (1) steel flanges and battens and (2) the web out of CFRP with fiber orientation angles ±45°. A buckling mode shape of the web subjected to a shear load Q is shown in Fig. 2.4; it well conforms to the first natural mode obtained by computation. Here, the failure mode of the web in the postbuckling stage is also shown.

The panel was analyzed by means of the diagonal field theory. In this case the measured slope of the wave, $\alpha=43°$, in the final condition was in a good agreement with the theoretical value, $\alpha=43.3°$. Initiation of several parallel waves at plate corners was also observed. However, failure of the web was not in correspondence with the model used in the diagonal field theory: failure from tension along the line 1-2 in Fig. 2.4 was preceded by advent of cracks along the line 0-2 in the vicinity of the point 2. This crack is caused by web bending along the hump of the wave due to buckling. Thus, the load-carrying capability of a thin-walled beam with a web out of a brittle composite (a typical example of which is the carbon fiber reinforced plastic) cannot be predicted on the basis of the diagonal field theory. More detailed information on web stress state in the postbuckling stage is required; it cannot be derived from this theory.

2.3.3. Multiaxial load

Assume that a composite plate is buckled under axial (T_x) and shear (T_{xy}) stress resultants. The plate stress-strain state is defined by relations (2.14) - (2.20), whereas the "stress resultant - out-of-plane displacement amplitude" relation may be established with the help of equation (2.22). Consider the loading model in which the stress resultants T_x and T_{xy} are varied in proportion to one parameter. Determine the load-carrying capability of a square plate out of CFRP loaded with identical stress resultants T_x and T_{xy} (T_x:T_{xy}=1:1). Fibres are laid at angles of ±45°. The computation predicts the breaking stress resultants $\overline{T}_x=\overline{T}_{xy}=11.5$ kN/m. Figure 2.19 shows stress distributions (σ_1, σ_2, τ_{12}) in three sections with relative coordinates $\overline{x}$ =(0; 0.25; 0.5). Change the relation between stress resultants T_x and T_{xy} and generate the plate strength surface for the multiaxial load. Figure 2.20(a) represents such a surface for the square CFRP plate with angles φ = ±45°. Figure 2.20(b) shows the same surface in relative coordinates ($\overline{T}_x/\overline{T}_{x0}$, $\overline{T}_{xy}/\overline{T}_{xy0}$), where $\overline{T}_{x0}$, $\overline{T}_{xy0}$ are breaking stress resultants for isolated action of axial compression and shear, respectively. Points are from computation, and lines are approximations thereof by means of the relation

$$\frac{\overline{T}_x}{\overline{T}_{x0}}+\left(\frac{\overline{T}_{xy}}{\overline{T}_{xy0}}\right)^2=1\ . \tag{2.34}$$

Comparison of the results shows that the load-carrying capability of orthotropic composite plates under multiaxial load may in many instances be estimated via the simplified equation (2.34).

2.4. Stiffness and strength of panel with buckled skin

For analysis of postbuckling composite skin deformation, let us consider the behavior of rectangular plate stiffened by mutually perpendicular ribs, Fig.2.1.

Each typical part of plate with adjoining parts of ribs in biaxial compression and shear behave similar to the others retaining the rectilinearity of ribs and edges $x=0$, $x=a$, $y=0$, $y=b$ of plate cell. Prior to buckling, the uniform flat stress state is realized in the plate with average stresses $p_x=T_x/h$, $p_y=T_y/h$, $\tau=S/h$. After buckling, the plate get the deflection $w(x,y)$; the distribution of membrane forces balancing external loads T_x, T_y, S becomes nonuniform. Let us consider that the ribs are simply supported; the plate is orthotropic with symmetrical layup arrangement. Postbuckling plate behavior is described by nonlinear differential equations of von Karman type

$$L_1(\Phi)+\frac{1}{2}L_3(w,w)=0, \quad L_2(w)-L_3(\Phi,w)=0, \tag{2.35}$$

where Φ is force function,

$$\begin{gathered}
L_1=A_{22}\frac{\partial^4}{\partial x^4}+2A_3\frac{\partial^4}{\partial x^2\partial y^2}+A_{11}\frac{\partial^4}{\partial y^4}, \quad A_3=A_{12}+A_{33}/2, \\
L_2=D_{11}\frac{\partial^4}{\partial x^4}+2D_3\frac{\partial^4}{\partial x^2\partial y^2}+D_{22}\frac{\partial^4}{\partial y^4}, \quad D_3=D_{12}+2D_{33}, \\
L_3=\frac{\partial^2}{\partial x^2}\frac{\partial^2}{\partial y^2}+\frac{\partial^2}{\partial y^2}\frac{\partial^2}{\partial x^2}-\frac{\partial^2}{\partial x\partial y}\frac{\partial^2}{\partial x\partial y}, \quad [A]=[A_{ij}]=[B]^{-1}, \\
\frac{\partial^2\Phi}{\partial y^2}=N_x, \quad \frac{\partial^2\Phi}{\partial x^2}=N_y, \quad \frac{\partial^2\Phi}{\partial x\partial y}=N_{xy}, \quad \{\varepsilon_0\}=[A]\{N\}.
\end{gathered} \tag{2.36}$$

Plate midsurface strains are coupled with its displacements $u(x,y)$, $v(x,y)$, and deflection $w(x,y)$ by relationships (2.3), so that for relative mutual displacements of plate cell edges the following is valid:

$$\begin{gathered}
e_x=-\frac{1}{a}\int_0^a\frac{\partial u}{\partial x}dx=-\frac{1}{a}\int_0^a\left[A_{11}\frac{\partial^2\Phi}{\partial y^2}+A_{12}\frac{\partial^2\Phi}{\partial x^2}-\frac{1}{2}\left(\frac{\partial w}{\partial x}\right)^2\right]dx=Const\ , \\
e_x=-\frac{1}{b}\int_0^b\frac{\partial v}{\partial y}dy=-\frac{1}{b}\int_0^b\left[A_{12}\frac{\partial^2\Phi}{\partial y^2}+A_{22}\frac{\partial^2\Phi}{\partial x^2}-\frac{1}{2}\left(\frac{\partial w}{\partial y}\right)^2\right]dy=Const\ .
\end{gathered} \tag{2.37}$$

We will give the approximate solution of the problem by using the assumption that the postbuckling deflection pattern is close to that for buckling pattern and by solving the latter from the equations (2.35) using Bubnov-Galerkin's method.

2.4.1. Biaxial compression

In this case we shall follow the solution scheme proposed by K. Marquerre [5] in application to metal plates. According to (2.37), we consider the relative mutual displacements e_x, e_y as given ones (by defining the absolute displacements of edges). The plate deflection we represent as

$$w(x,y) = f_0 \sin\frac{m\pi x}{a} \sin\frac{n\pi y}{b}, \qquad m,n = 1,2,3,..., \tag{2.38}$$

that corresponds to all possible buckling modes of simply supported plate

$$w|_{x=0,a} = \frac{\partial^2 w}{\partial x^2}|_{x=0,a} = 0, \; w|_{y=0,b} = \frac{\partial^2 w}{\partial y^2}|_{x=0,b} = 0. \tag{2.39}$$

Boundary conditions (2.39) are satisfied only in postbuckling phase of deforming at any amplitude of deflection f_0. Substituting equation (2.38) into first equation (2.35), the solution of the latter can be expressed as

$$\Phi(x,y) = -\frac{T_x y^2}{2} - \frac{T_y x^2}{2} + \frac{f_0^2}{32}\left(\frac{a^2 n^2}{b^2 m^2 A_{22}} Cos\frac{2m\pi x}{a} + \frac{b^2 m^2}{a^2 n^2 A_{11}} Cos\frac{2n\pi y}{b} \right). \tag{2.40}$$

Hence the loads in plate are expressed as

$$\begin{aligned} N_x(x,y) &= -T_x - \frac{\pi^2 m^2}{8a^2 A_{11}} f_0^2 Cos\frac{2n\pi y}{b}, \\ N_y(x,y) &= -T_y - \frac{\pi^2 n^2}{8b^2 A_{22}} f_0^2 Cos\frac{2m\pi x}{a}, \quad N_{xy}(x,y) = 0. \end{aligned} \tag{2.41}$$

Here T_x, T_y = averaged compressive plate loads in x and y directions. They should satisfy the conditions

$$\begin{aligned} T_x &= -\frac{1}{b}\int_0^b N_x(x,y)\,dy = -\frac{1}{b}\int_0^b \frac{\partial^2 \Phi}{\partial y^2} dy = Const, \\ T_y &= -\frac{1}{a}\int_0^a N_y(x,y)\,dx = -\frac{1}{a}\int_0^a \frac{\partial^2 \Phi}{\partial x^2} dx = Const. \end{aligned} \tag{2.42}$$

It is obvious that T_x, T_y are independent on coordinates x,y. Substituting equations (2.38), (2.40) into conditions (2.37) together with simultaneous using the average laminate stresses p_x, p_y result in relationships

$$e_x=\frac{p_x}{E_x}-\mu_{xy}\frac{p_y}{E_y}+\frac{\pi^2m^2}{8a^2}f_0^2,\quad e_y=\frac{p_y}{E_y}-\mu_{yx}\frac{p_x}{E_x}+\frac{\pi^2n^2}{8b^2}f_0^2, \tag{2.43}$$

where

$$E_x=\frac{1}{A_{11}h},E_y=\frac{1}{A_{22}h},\mu_{yx}=-\frac{A_{12}}{A_{11}}=\frac{B_{12}}{B_{22}},\mu_{xy}=-\frac{A_{12}}{A_{22}}=\mu_{yx}\frac{E_y}{E_x} \tag{2.44}$$

are laminate elastic moduli and Poisson ratios (average of lamina moduli and ratios [14]). According to (2.36)

$$A_{11}=\frac{B_{22}}{B},\ A_{22}=\frac{B_{11}}{B},\ A_{12}=-\frac{B_{12}}{B},\ A_{33}=\frac{1}{B_{33}},\ B=B_{11}B_{22}-B_{12}^2.$$

For f_o determination we use the approximate solution of second equation (2.35) by Bubnov-Galerkin's method. According to it

$$\int_0^a\int_0^b[L_2(w)-L_3(\Phi,w)]\sin\frac{m\pi x}{a}\sin\frac{n\pi y}{b}dxdy=0$$

Substituting equations (2.38), (2.40) into this equation, for $f_0\neq 0$, the following relation can be obtained after some transformations

$$D(m,n)-p_x\frac{m^2}{4a^2}-p_y\frac{n^2}{4b^2}+E(m,n)f_0^2=0, \tag{2.45}$$

where

$$D(m,n)=\frac{\pi^2}{4h}\left(D_{11}\frac{m^4}{a^4}+2D_3\frac{m^2n^2}{a^2b^2}+D_{22}\frac{n^4}{b^4}\right),$$
$$E(m,n)=\frac{\pi^2}{64}\left(E_x\frac{m^4}{a^4}+E_y\frac{n^4}{b^4}\right).$$

Critical state of the plate is determined from the condition of nontrivial solution $f_0\neq 0$ of equation (2.45). For proportional loading $p_y=\psi p_x$, we can find

$$p_x^*=\min_{m,n}p_x(m,n)=p_x(m_0,n_0),\ p_y^*=\psi p_x^*$$
$$p_x(m,n)=\frac{D(m,n)}{\dfrac{m^2}{4a^2}+\psi\dfrac{n^2}{4b^2}}, \tag{2.46}$$

where m_0, n_0 = numbers of half-waves in buckle pattern of plate cell. Fixing these numbers for postbuckling plate deformation phase at $p_x > p_x^*$, we can obtain from (2.45) the following dependency of f_o^2 on p_x, p_y

$$f_0^2=\frac{D_0}{E_0}\left(\frac{p_x}{p_x^*}-1\right)=\frac{D_0}{E_0}(\bar{p}-1), \tag{2.47}$$

where

$$\begin{aligned}
&\bar{p}=\bar{p}_x+\bar{p}_y, \quad \bar{p}_x=\frac{p_x}{p_{x0}}, \quad \bar{p}_y=\frac{p_y}{p_{y0}},\\
&D_0=D(m_0,n_0), \quad E_0=E(m_0,n_0),\\
&p_{x0}=\frac{4a^2}{m_0^2}D_0, \quad p_{y0}=\frac{4b^2}{n_0^2}D_0.
\end{aligned} \tag{2.48}$$

Substituting equation (2.47) into equation (2.43) at $m=m_0$, $n=n_0$, $\bar{p} \geq 1$ result in two relations between e_x, e_y and p_x, p_y similar to that for prebuckling deformation phase $\bar{p} \leq 1$, when at $f_0=0$, $e_x = \epsilon_x$, $e_y = \epsilon_y$, the usual relations (2.36) of prebuckling plane stress state of plate are valid

$$\varepsilon_{x0}=\frac{p_x}{E_x}-\mu_{xy}\frac{p_y}{E_y}, \quad \varepsilon_{y0}=\frac{p_y}{E_y}-\mu_{yx}\frac{p_x}{E_x}. \tag{2.49}$$

So the postbuckling state of representative plate cell is fully determined including its deflections and bending stress-strain state; the boundary conditions could be determined by mutual relative displacements e_x, e_y, by external forces $T_x=p_xh$, $T_y=p_yh$ or by their combinations e_x, T_y and e_y, T_x.

The characteristic features of obtained solution are that the shear forces are equal to zero including the forces on the edges of plate cell as well as the nonlinear variation of contour tangent displacements along the edge. This result in inaccurate satisfaction of compatibility conditions for displacements of the plate and ribs in the direction along rib, when these conditions are satisfied integrally (the so-called edge slipping). Marquerre [5] has shown that this has no appreciable effect on the SSS of plate and ribs and all the more on reduction factors.

Reduction factors

As far as stiffness characteristics of buckled composite plate are concerned, let us consider the most interesting case of uniaxial longitudinal compression of elongated plate with $a>>b$. We will use usual nondimensional parameters of the theory of orthotropic plates

$$\alpha=\frac{b^2}{a^2}\sqrt{\frac{D_{11}}{D_{22}}}, \qquad \beta=\frac{D_3}{\sqrt{D_{11}D_{22}}}, \qquad \kappa_x^*=\frac{b^2hp_x}{\pi^2\sqrt{D_{11}D_{22}}}. \tag{2.50}$$

The solution of instability problem (2.46) for $\psi=0$, $1/\sqrt{\alpha} \geq 3$ can be expressed by known relations

$$n_0=1, \quad m_0=\frac{1}{\sqrt{\alpha}}, \quad p_x^*=\frac{\pi^2\sqrt{D_{11}D_{22}}}{b^2h}\kappa_x^*, \quad \kappa_x^*=2(1+\beta). \tag{2.51}$$

For the amplitude of postbuckling deflection f_0 from (2.47) we can obtain

$$\frac{f_0}{\sqrt{A_{11}D_{11}}}=f_0\sqrt{\frac{E_xh}{D_{11}}}=4\sqrt{2}\sqrt{\frac{(1+\beta)}{(1+\gamma)}\left(\frac{p_x}{p_x^*}-1\right)}. \tag{2.52}$$

Here an additional nondimensional stiffness parameter is introduced

$$\gamma=\frac{A_{11}D_{11}}{A_{22}D_{22}}=\frac{B_{22}D_{11}}{B_{11}D_{22}}=\frac{E_yD_{11}}{E_xD_{22}}, \tag{2.53}$$

influencing the postbuckling behavior of plate.

Substitution of equation (2.52) at $p_y=0$ into relations (2.43) results in the following relationships

$$e_x=\frac{p_x\left(3+\gamma-2\dfrac{p_x^*}{p_x}\right)}{E_x(1+\gamma)}=\frac{p_x}{E_x^s}, \quad p_x=\frac{E_xe_x(1+\gamma)}{(3+\gamma)}\left[1+\frac{2e_x^*/e_x}{(1+\gamma)}\right]=E_x^se_x,$$
$$e_y=-\frac{p_x}{E_x}\left[\mu_{yx}-\frac{2\sqrt{D_{11}/D_{22}}}{(1+\gamma)}\left(1-\frac{p_x^*}{p_x}\right)\right]=-\mu_{yx}^s\frac{p_x}{E_x^s}, \quad (e_x^*=p_x^*/E_x) \tag{2.54}$$

As we can see from the comparison of relations (2.54) and (2.49), the buckled skin behave like non-buckled plate made of nonlinear elastic material exhibiting the reduced averaged elastic modulus $E_x^s=1/A_{11}^sh=\varphi_x^s E_x$ and corresponding reduced stiffness characteristic $A_{11}^s=A_{11}/\varphi_x^s$. From equations (2.54) changing e_x by ϵ_{x0} we can obtain two equivalent expressions for secant reduction factor $\varphi_x^s=E_x^s/E_x \leq 1$

$$\varphi_x^s=\frac{(1+\gamma)}{\left(3+\gamma-2\dfrac{p_x^*}{p_x}\right)}=\frac{(1+\gamma)}{(3+\gamma)}\left[1+\frac{2\varepsilon_{x0}^*/\varepsilon_{x0}}{(1+\gamma)}\right], \tag{2.55}$$

where $\varphi_x^s=1$ at $p_x=p_x^*$, $\varepsilon_{x0}=\varepsilon_{x0}^*$ and prior to buckling. In particular case of isotropic plate when $\gamma=1$, this expression can be transformed into the following one

$$\varphi_x^s = \frac{1}{2 - \frac{p_x^*}{p_x}} = \frac{1}{2}\left(1 + \frac{\varepsilon_{x0}^*}{\varepsilon_{x0}}\right), \tag{2.56}$$

which corresponds to the solution [5]. Thus the unique parameter determining the distinctions of reduction factors for orthotropic and isotropic plate is the nondimesional parameter γ. In accordance with equation (2.53) for homogeneous and quasi-homogeneous plates, the parameter γ is also equal to unit because the following is valid

$$D_{11} = \frac{E_x h^3}{12(1 - \mu_{xy}\mu_{yx})}, \; D_{22} = \frac{E_y h^3}{12(1 - \mu_{xy}\mu_{yx})}.$$

Thus we obtain an important result, that such plates behave like the isotropic metal plate with respect to the longitudinal stiffness.

In addition, we obtain from the second relation (2.54), that the Poisson ratio is also reduced according to relationship

$$\mu_{yx}^s = \varphi_x^s\left[\mu_{yx} - \frac{2d}{(1+\gamma)}(1 - p_x^*/p_x)\right] = \varphi_x^s\mu_{yx} - (1 - \varphi_x^s)d, \tag{2.57}$$

where the additional parameter $d = \sqrt{D_{11}/D_{22}}$ has appeared. In particular case of homogeneous material, this parameter may be replaced by $d = \sqrt{E_x/E_y}$. For isotropic skin we can obtain

$$\mu_{yx}^s = \varphi_x^s(\mu - 1 + p_x^*/p_x) = \varphi_x^s(1 + \mu) - 1.$$

It is obvious that the value of reduced Poisson ratio can be expressed through the reduction factor φ_x^s, which in its turn depends upon the extent of critical state exceedance p_x/p_x^* or $\varepsilon_{x0}/\varepsilon_{x0}^*$.

Fig. 2.21a shows the typical generalized dependence of p_x/p_x^* upon $\varepsilon_{x0}/\varepsilon_{x0}^*$ obtained from equation (2.54). These functions do not depend on parameter β; they are piecewize linear. The obtained solution gives the constant slopes of these curves in postbuckling region. The tangent modulus $E_x^t = 1/A_{11}^t h = \varphi_x^t E_x$ and reduction factor

$$\varphi_x^t = \frac{E_x^t}{E_x} = \frac{1}{E_x}\frac{dp_x}{d\varepsilon_{x0}} = \frac{1+\gamma}{3+\gamma}, \; (\varphi_x^t|_{\gamma=1} = 0.5) \tag{2.58}$$

are independent upon p_x/p_x^* or $\varepsilon_{x0}/\varepsilon_{x0}^*$

These results qualitatively correspond to the results of numerical solution of the problem under consideration given by Stein [10]; they coincide for the initial phase of postbuckling deforming. The dotted curve in Fig. 2.21 shows the particular case of isotropic plate, which correspond to the relationship (2.59) reliably verified by tests (see [1], [5] and Fig. 2.11):

$$\varphi_x^s=\sqrt{\frac{p_x^*}{p_x}}=\sqrt[3]{\frac{\varepsilon_{x0}^*}{\varepsilon_{x0}}},\quad \varphi_x^t=\frac{2}{3}\varphi_x^s. \tag{2.59}$$

The obtained solution is rather accurate in the region of "moderate postbuckling" when the conditions $\epsilon_{x0}/\epsilon_{x0}^*\leq 7$, $p_x/p_x^*\leq 4$ are satisfied. If buckling state is exceeded more than in these conditions, the value of φ_x^s appreciably differs from the numerical result [10] and results of calculation by equations (2.59). In accordance with equation (2.55), this value approaches

$(1+\gamma)/(3+\gamma)=\varphi_x^t$ as $p_x/p_x^*\to\infty$, while the tests and equation (2.59) give considerably smaller

values $\varphi_x^s\to 0$. The reason of this discrepancy is certainly the constant representation of plate deflection mode (2.38), while the real mode modifies during the plate loading up to the possible full change of wave pattern [1]. For quasi-homogeneous plates in this case, the relationships (2.55), (2.58) can be changed by relationships (2.59). It should be noted that for uniaxial loading, the introduction of elastic modulus reduction factor φ_x^s with respect to the longitudinal stiffness of skin is the same as the introduction of effective skin width by von Karman $b_x=\varphi_x^s b$ at the same E_x, because $E_x^s b=E_x b_x=\varphi_x^s(E_x b)$.

In case of biaxial loading, after substituting equation (2.47) into equation (2.43) and taking into account, that $e_x=\varepsilon_{x0}$, $e_y=\varepsilon_{y0}$, we can go over the usual relations (2.49) with reduced stiffness characteristics

$$\varepsilon_{x0}=\frac{p_x}{E_x^s}-\mu_{xy}^s\frac{p_y}{E_y^s},\quad \varepsilon_{y0}=\frac{p_y}{E_y^s}-\mu_{yx}^s\frac{p_x}{E_x^s}, \tag{2.60}$$

where

$$\begin{gathered}E_x^s=\varphi_x^s E_x=\frac{1}{A_{11}^s h},\quad E_y^s=\varphi_y^s E_y=\frac{1}{A_{22}^s h},\quad \mu_{yx}^s=-\frac{A_{12}^s}{A_{11}^s},\\ \mu_{xy}^s=-\frac{A_{12}^s}{A_{22}^s}=\mu_{yx}^s\frac{A_{11}^s}{A_{22}^s}=\mu_{ys}^s\frac{E_y^s}{E_x^s},\end{gathered} \tag{2.61}$$

and the secant reduction factors φ_x^s, φ_y^s, Poisson ratios μ_{xy}^s, μ_{yx}^s can be expressed by the following way

$$\begin{gathered}\varphi_x^s=\frac{1+\bar\gamma}{3+\bar\gamma-2/\bar p},\quad \varphi_y^s=\frac{1+\bar\gamma}{1+3\bar\gamma-2\bar\gamma/\bar p},\\ \mu_{xy}^s=\varphi_y^s\left[\mu_{xy}-\frac{2\bar\gamma}{\bar d+(1+\bar\gamma)}\left(1-\frac{1}{\bar p}\right)\right]=\varphi_y^s\mu_{xy}-\frac{1-\varphi_y^s}{\bar d},\\ \mu_{yx}^s=\varphi_x^s\left[\mu_{yx}-\frac{2\bar d}{(1+\bar\gamma)}\left(1-\frac{1}{\bar p}\right)\right]=\varphi_x^s\mu_{yx}-(1-\varphi_x^s)\bar d.\end{gathered} \tag{2.62}$$

The following notation are introduced in (2.62)

$$\bar{\gamma} = \bar{d}^2 \frac{E_y}{E_x} = \frac{l_x^4 E_y}{l_y^4 E_x}, \quad \bar{d} = \frac{l_x^2}{l_y^2} = \sqrt{\bar{\gamma}\frac{E_x}{E_y}}, \quad l_x = \frac{a}{m_0}, \quad l_y = \frac{b}{n_0}.$$

The latter two depend on the direction of loading (ψ). Thus, as in case of uniaxial loading, the buckled plate can be replaced by the stiffness-equivalent nonbuckled plate made of nonlinear elastic material with characteristics (2.61),(2.62). The extent of critical state exceedance under biaxial compression is characterized by the load index $\bar{p}$ becoming equal to unit in critical state. In particular case of uniaxially loaded elongated plate, when $\bar{\gamma}=\gamma$, $\bar{d}=d$, $p_{x0}=p_x^*$, the relations (2.62) result in the above mentioned relations (2.55), (2.57). The important inverse statement is also true, that the general expressions (2.62) can be simply obtained from (2.55), (2.57) by substituting $\bar{p}$, $\bar{\gamma}$, $\bar{d}$ for p_x/p_x^*, γ, d respectively. After that φ_y^s, μ_{xy}^s can be obtained from φ_x^s, μ_{yx}^s by the simple change of variables $x \to y$, $y \to x$, $\bar{\gamma} \to 1/\bar{\gamma}$, $\bar{d} \to 1/\bar{d}$. . Stain-stress relations (2.60) in the obtained solution are piecewize linear with constant secant elastic characteristics

$$E_x^t = \varphi_x^t E_x = \frac{1}{\dfrac{\partial \varepsilon_{x0}}{\partial p_x}} = \frac{1+\bar{\gamma}}{3+\bar{\gamma}} E_x, \quad A_{11}^t = E_x^t h,$$

$$E_y^t = \varphi_y^t E_y = \frac{1}{\dfrac{\partial \varepsilon_{y0}}{\partial p_y}} = \frac{1+\bar{\gamma}}{1+3\bar{\gamma}} E_y, \quad A_{22}^t = E_y^t h,$$

$$\mu_{xy}^t = -E_y^t \frac{\partial \varepsilon_{x0}}{\partial p_y} = \varphi_y^t \left[\mu_{xy} - \frac{2\bar{\gamma}}{\bar{d}(1+\bar{\gamma})} \right] = \varphi_y^t \mu_{xy} - \frac{1-\varphi_y^t}{\bar{d}}, \tag{2.63}$$

$$\mu_{yx}^t = -E_x^t \frac{\partial \varepsilon_{y0}}{\partial p_x} = \varphi_x^t \left[\mu_{yx} - \frac{2\bar{d}}{1+\bar{\gamma}} \right] = \varphi_x^t \mu_{yx} - (1-\varphi_x^t)\bar{d},$$

$$A_{12}^t = -\mu_{yx}^t A_{11}^t = -\mu_{xy}^t A_{22}^t, \quad \mu_{xy}^t = \mu_{yx}^t \frac{E_y^t}{E_x^t}.$$

It should be noted that all stiffness matrixes of the buckled skin $[\mathbf{A}_{ij}^s]$, $[\mathbf{A}_{ij}^t]$, $[\mathbf{B}_{ij}^s] = [\mathbf{A}_{ij}^s]^{-1}$, $[\mathbf{B}_{ij}^t] = [\mathbf{A}_{ij}^t]^{-1}$ can be uniquely determined by the introduced secant and tangent reduction factors and other elastic characteristics of material (2.62), (2.63).

If numbers m_0, n_0 are fixed, all the reduced stiffness characteristics depend on the loads identically. The character of these functions is determined by the index $\bar{p}$; it is independent on the load path. Since in accordance with equation (2.46) in general case m_0, n_0 depend on nondimensional plate parameters α, β, a/b and they discretely change as ψ changes, the relations (2.62), (2.63) behave similarly. The boundary of stability $\bar{p}=1$ in p_x, p_y-frame of reference is the piecewize linear function; these pieces are created by the straight lines corresponding to m_0, n_0 = Const. For the constant values of $\bar{p}>1$, the similar piecewize boundaries with discrete change of m_0, n_0 and relations (2.62), (2.63) at corresponding values of ψ (see Fig. 2.22).

In each rectilinear piece of this boundary, the reduced plate stiffness characteristics are constant and independent on the load direction. For the plate which form is close to the square when m_0, n_0 are independent on ψ and equal to unit, we obtain unique relations of reduction factors and loading index $\bar{p}$ for all possible load spectra. These relations (2.62), (2.63) are the same for all load paths including the case of uniaxial compression in x or y directions.

2.4.2. Shear consideration in compact plates

The plate is considered to be "compact" if α parameter satisfies the inequality

$$0.5\le\alpha\le 2. \tag{2.64}$$

If such plate is loaded by the loads T_x, T_y, S, its deflections at the moment of buckling can be approximated by the expression [1]:

$$w=f_{11}\sin\frac{\pi x}{a}\sin\frac{\pi y}{b}+f_{22}\sin\frac{2\pi x}{a}\sin\frac{2\pi y}{b}, \tag{2.65}$$

which satisfies the simply supported edge conditions (2.39). The solution of the first equation (2.35) in this case is:

$$\begin{aligned}\Phi(x,y)=&-\frac{T_x y^2}{2}-\frac{T_y x^2}{2}-Sxy+C_1\cos\frac{2\pi x}{a}+C_2\cos\frac{2\pi y}{b}+C_3\cos\frac{4\pi x}{a}+\\&+C_4\cos\frac{4\pi y}{b}+C_5\cos\frac{\pi x}{a}\cos\frac{3\pi y}{b}+C_6\cos\frac{3\pi x}{a}\cos\frac{\pi y}{b},\end{aligned} \tag{2.66}$$

where

$$\begin{aligned}&C_1=\frac{1}{32}\frac{a^2}{b^2}\frac{1}{A_{22}}f_{11}^2,\quad C_2=\frac{1}{32}\frac{b^2}{a^2}\frac{1}{A_{11}}f_{11}^2,\quad C_3=\frac{1}{32}\frac{a^2}{b^2}\frac{1}{A_{22}}f_{22}^2,\\&C_4=\frac{1}{32}\frac{b^2}{a^2}\frac{1}{A_{11}}f_{22}^2,\quad C_5=\frac{1}{25}\frac{1}{A_5}f_{11}f_{22},\quad C_6=\frac{1}{25}\frac{1}{A_6}f_{11}f_{22},\end{aligned} \tag{2.67}$$

and

$$A_5=0.01\frac{b^2}{a^2}A_{22}+0.81\frac{a^2}{b^2}A_{11}+0.18A_3\ ,\ A_6=0.01\frac{a^2}{b^2}A_{11}+0.81\frac{b^2}{a^2}A_{22}+0.18A_3. \tag{2.68}$$

The membrane forces in the plate are defined by the following expressions

$$N_x(x,y)=-T_x-C_2\frac{4\pi^2}{b^2}\cos\frac{2\pi y}{b}-C_4\frac{16\pi^2}{b^2}\cos\frac{4\pi y}{b}-C_5\frac{9\pi^2}{b^2}\cos\frac{\pi x}{a}\cos\frac{3\pi y}{b}-C_6\frac{\pi^2}{b^2}\cos\frac{3\pi x}{a}\cos\frac{\pi y}{b},$$

$$N_y(x,y)=-T_y-C_1\frac{4\pi^2}{a^2}\cos\frac{2\pi x}{a}-C_3\frac{16\pi^2}{a^2}\cos\frac{4\pi x}{a}-C_5\frac{\pi^2}{a^2}\cos\frac{\pi x}{a}\cos\frac{3\pi y}{b}- \tag{2.69}$$

$$-C_6\frac{9\pi^2}{a^2}\cos\frac{3\pi x}{a}\cos\frac{\pi y}{b},$$

$$N_{xy}(x,y)=S-C_5\frac{3\pi^2}{ab}\sin\frac{\pi x}{a}\sin\frac{3\pi y}{b}-C_6\frac{3\pi^2}{ab}\sin\frac{3\pi x}{a}\sin\frac{\pi y}{b}.$$

For the relative mutual displacements of plate edges, the following expressions are obtained:

$$e_x=\frac{p_x}{E_x}-\mu_{xy}\frac{p_y}{E_y}+B_e,\quad e_y=\frac{p_y}{E_y}-\mu_{yx}\frac{p_x}{E_x}+\frac{a^2}{b^2}B_e,$$
$$B_e=\frac{\pi^2}{8a^2}f_{11}^2+\frac{\pi^2}{2a^2}f_{22}^2. \tag{2.70}$$

The elastic moduli and Poisson ratios used in equations (2.70) are determined by equations (2.44).
The plate average shear deformation can be expressed by the relationship

$$\theta=\frac{1}{b}(\bar{u}|_{y=b}-\bar{u}|_{y=0})+\frac{1}{a}(\bar{v}|_{y=a}-\bar{v}|_{x=0}), \tag{2.71}$$

where

$$\bar{u}|_{y=b}=\frac{1}{a}\int_0^a u|_{y=b}dx,\quad \bar{u}|_{y=0}=\frac{1}{a}\int_0^a u|_{y=0}dx,$$
$$\bar{v}|_{x=a}=\frac{1}{b}\int_0^b v|_{y=a}dy,\quad \bar{v}|_{x=0}=\frac{1}{b}\int_0^b v|_{y=0}dy \tag{2.72}$$

are the displacements $\bar{u}$ and $\bar{v}$ averaged over the plate edges.

For determination of functions $u(x,y)$, $v(x,y)$ the expressions (2.3), (2.49), (2.65), (2.69) as well as relation $\gamma_{xy0}=N_{xy}/G_{xy}h$ where $G_{xy}=1/A_{33}h=B_{33}/h$.

After performing the integration (2.72), we substitute the result into equation (2.71)

$$\theta = \frac{\tau}{G_{xy}} + B_\theta, \tag{2.73}$$

where

$$B_\theta = \frac{2}{ab} f_{11} f_{22} \left[\frac{1}{9}(g_1 + g_3 - 2) - (g_2 + g_4 - 2) \right],$$

$$g_1 = 1 + \frac{2}{25}\frac{a^2}{b^2}\frac{1}{A_6 E_x h} - \frac{18}{25}\frac{1}{A_6 E_y h}\mu_{xy}, \quad g_2 = 1 - \frac{18}{25}\frac{a^2}{b^2}\frac{1}{A_5 E_x h} + \frac{2}{25}\frac{1}{A_5 E_y h}\mu_{xy},$$

$$g_3 = 1 + \frac{2}{25}\frac{b^2}{a^2}\frac{1}{A_5 E_y h} - \frac{18}{25}\frac{1}{A_5 E_x h}\mu_{yx}, \quad g_4 = 1 - \frac{18}{25}\frac{b^2}{a^2}\frac{1}{A_6 E_y h} + \frac{2}{25}\frac{1}{A_6 E_x h}\mu_{yx}.$$

For determination of f_{11} and f_{22} we will use the solution of the second equation (2.35) by Bubnov-Galerkin's method. Transformations yield two cubic equations with respect to desired parameters

$$\begin{aligned} &\frac{C_7}{16}\bar{f}_{11}^3 + C_8 \bar{f}_{11} \bar{f}_{22}^2 + \bar{f}_{11}(1 - \bar{p}) - 4\bar{\tau}\bar{f}_{22} = 0, \\ &C_7 \bar{f}_{22}^3 + C_8 \bar{f}_{11}^2 \bar{f}_{22} + \bar{f}_{22}(16 - 4\bar{p}) - 4\bar{\tau}\bar{f}_{11} = 0, \end{aligned} \tag{2.74}$$

where $\bar{p}$ is determined in accordance with equation (2.48) at $m_0 = n_0 = 1$ and

$$\begin{aligned} &C_7 = \frac{h^3}{K\sqrt{D_{11}D_{22}}}\left(\frac{a^2}{b^2}E_y + \frac{b^2}{a^2}E_x\right), \quad C_8 = \frac{4}{25}\frac{h^2}{K\sqrt{D_{11}D_{22}}}\left(\frac{1}{A_5} + \frac{1}{A_6}\right), \quad K = \alpha + 2\beta + \frac{1}{\alpha}, \\ &\bar{\tau} = \frac{\tau}{\tau_0}, \quad \tau_0 = \frac{9}{32}\frac{\pi^4 K}{abh}\sqrt{D_{11}D_{22}}, \quad \bar{f}_{11} = \frac{f_{11}}{h}, \quad \bar{f}_{22} = \frac{f_{22}}{h}. \end{aligned} \tag{2.75}$$

The stability boundary is determined from equation (2.74) assuming the smallness of amplitudes f_{11}, f_{22}

$$\bar{p}_* + \frac{4\bar{\tau}_*^2}{4 - \bar{p}_*} = 1, \quad (\bar{p}_* < 4). \tag{2.76}$$

The buckling mode is determined by expression.(2.65) in which

$$f_{22} = \frac{\bar{\tau}_*}{4 - \bar{p}_*} f_{11},$$

and $\bar{p}_*, \bar{\tau}_*$ is a critical combination of forces $\bar{p}, \bar{\tau}$.

In the postbuckling region, when

$$\bar{p}=\bar{p}_* q, \quad \bar{\tau}=\bar{\tau}_* q, \quad q \geq 1, \tag{2.77}$$

the amplitudes $\bar{f}_{11}, \bar{f}_{22}$ are determined by the following way:

It follows from (2.74) that

$$\bar{f}_{11}^2=\frac{\bar{p}-1+4(4-\bar{p})\xi^2}{\left(\frac{1}{16}-\xi^4\right)C_7}, \tag{2.78}$$

where $\xi=\bar{f}_{11}/\bar{f}_{22}$ and $\frac{\bar{\tau}_*}{4-\bar{p}_*}<\xi<0.5$.

The relationship for q determination is obtained by using the equations (2.74)

$$q=\frac{C_9(1-\xi^2)-1}{\bar{p}_*(C_9-4\xi^2 C_9-1)-4\xi\bar{\tau}_*}, \tag{2.79}$$

where $C_9=\dfrac{1+16\xi^2\dfrac{C_8}{C_7}}{1-16\xi^2}$.

Consequently, the determined values of q and $\bar{f}_{11}^2$ correspond to each value of ξ according to (2.79) and (2.78) respectively. So the one-to-one relation between amplitudes f_{11}, f_{22} and $\bar{p}, \bar{\tau}$ is established. If q is given, the corresponding values of ξ, f_{11}, f_{22} can be obtained by iterations.

Expressions (2.70) can be reduced to the form (2.60), (2.61), which is valid for the orthotropic plate with variable elastic parameters and Poisson ratios depending on extent of critical state exceedance q at proportional loading. The expressions (2.73) can be reduced to the form:

$$\gamma_{xy}=\frac{\tau}{G_{xy}^s}, \quad G_{xy}^s=\varphi_\gamma^s G_{xy}. \tag{2.80}$$

By setting for buckled plate

$$e_x=\varepsilon_{x0}, \quad e_y=\varepsilon_{y0}, \quad \theta=\gamma_{xy},$$

we obtain

$$\bar{p}_x\left(\frac{1}{\varphi_x^s}-1\right)+\bar{p}_y\frac{b^2}{a^2}\left(\mu_{yx}-\frac{\mu_{yx}^s}{\varphi_x^s}\right)=\bar{B}\ ,\quad \bar{p}_y\left(\frac{1}{\varphi_y^s}-1\right)\frac{b^2}{a^2}\frac{E_x}{E_y}+\bar{p}_x\left(\mu_{yx}-\frac{\mu_{yx}^s}{\varphi_x^s}\right)=\frac{a^2}{b^2}\bar{B},$$

$$\bar{\tau}\left(\frac{1}{\varphi_\gamma^s}-1\right)=\bar{B}_\theta\ ,\quad \mu_{xy}^s=\mu_{yx}^s\frac{E_y^s}{E_x^s}. \tag{2.81}$$

Reduction factors φ_x^s, φ_y^s, φ_γ^s, Poisson ratios μ_{xy}^s, μ_{yx}^s are expressed from equations (2.81) by the following way:

$$\varphi_x^s=\frac{1}{1+\bar{B}/\bar{p}},\quad \mu_{yx}^s=\varphi_x^s\left(\mu_{yx}-\frac{a^2}{b^2}\frac{\bar{B}}{\bar{p}}\right),\ \varphi_y^s=\frac{1}{1+\dfrac{a^4}{b^4}\dfrac{E_x}{E_y}\dfrac{\bar{B}}{\bar{p}}},\quad \mu_{xy}^s=\mu_{yx}^s\frac{E_y}{E_x}\frac{\varphi_y^s}{\varphi_x^s},\ \varphi_\gamma^s=\frac{\bar{\tau}}{1+\bar{B}_\theta/\bar{\tau}}\cdot \tag{2.82}$$

In equations (2.81) and (2.82) the following is denoted:

$$\bar{B}=B_e\frac{E_x}{p_{x0}},\quad \bar{B}_\theta=B_\theta\frac{G_{xy}}{\tau_0}$$

If $S=0$, relationships (2.82) are converted into relations (2.62) at $m_0=n_0=1$.

Figure 2.23 shows the factors φ_x^s, φ_γ^s versus q according to equation (2.82) at different ratios $\bar{p}/\bar{\tau}$, $\bar{\tau}/\bar{p}$ for the plate with $\alpha=1$.

Tangent reduction factors in presence of shear are calculated numerically on the increments of $\bar{p}$, $\bar{\tau}$ at the reached level of critical state exceedance. They are shown in Figure 2.24 for the plate with $\alpha=1$.

2.4.3. Analysis of stiffened composite panels with the local skin buckling

It is known that the skin of thin-walled aerospace structures often buckle locally under load which is much less than the general failure load. The nonlinear problem arises to determine the general stress state and load-carrying capability of such structures with buckled skin.

For example, the static bending failure of wing box is usually caused by the general instability of upper stringer-stiffened panel. After skin buckling, the panel is considered as the structurally orthotropic panel with reduced skin elastic characteristics which depend on the load level. These characteristics enter into the known expressions for stiffness **[B]**, **[D]** of structurally-orthotropic panel.

Thus, two different problems should be solved. First, the prebuckling stress state in the structure with buckled skin is determined for the increased load (***t*** parameter) by using some method, e.g. engineering "beam" method or finite element method. The stress resultants (membrane forces) are determined which nonlinearly depend on the external load ($P_t(t)$ in case of wing box bending). These resultants are necessary to solve the general instability problem for each t value.

The numerical method for thin-walled structural stress state determination in application to the metal structures was reported by the authors on the Second World Congress on the Computational Mechanics in Stuttgart [21]. With the help of special methods of reduction [22] and special finite elements, the problem is reduced in essence to classical iteration methods of variable elasticity parameters and the others which are applied for the stress analysis of the structures made of nonlinear elastic materials. The specific character of composite skin is only in the necessity of calculation of its secant reduced elastic characteristics in postbuckling phase by using the relatively simple relationships obtained above. Thus, the method of analysis proposed in paper [21] can be applied to the structures comprising composite elements.

The second problem of general instability of both separate structurally-orthotropic panel and cylindrical structure as the whole can be solved for each load level by the different method. However, in contrast to the SSS-problem, the tangential stiffness should be used in stability equations, which characterize the relations between the increments of generalized forces and the deformations of elements. This result in the necessity of calculation of above mentioned tangent elastic characteristics for buckled composite skin, in particular according to relationships (2.63). Naturally, further theoretical and experimental investigations are necessary to refine both secant and tangential reduction factors for locally buckled composite elements . This specially concerns with nonplanar, nonrectangular elements with complicated boundary conditions.

The panel in Fig. 2.1 is a regularly stiffened panel. Its stresses and strength may be evaluated through the theory taking into account local skin buckling and the skin/stiffener interaction. Let us limit ourselves to the case of biaxial compression loading and involve the approximate solution derived in 2.4.1 for a plate cell. The following notation will be utilized hereinafter:

P_1 and P_2, the loads applied to a portion of the panel;

EF_1 and EF_2, the longitudinal stiffness characteristics of uniaxially loaded stiffeners (webs) for the x axis and the y axis, respectively.

The composite-skin stress resultants (T_x and T_y) and the stiffener forces (N_1 and N_2) are unknown values depending on a ratio of stiffnesses of webs and the skin, the out-of-plane deflection and stiffnesses of the skin at the postbuckling stage depending, in turn, on $p_x = T_x/h$ and $p_y = T_y/h$, see (2.47) and (2.62).

The solution and the relations (2.38) - (2.45) for the plate keep their form but should be complemented with skin/web deformation compatibility equations:

$$e_x = N_1/EF_1, \qquad e_y = N_2/EF_2$$

and panel portion equilibrium equations:

$$P_1 = 2N_1 + p_x hb, \qquad P_2 = 2N_2 + p_y hb,$$

This produces:

$$e_x = \frac{P_1}{2EF_1} - p_x \frac{hb}{2EF_1}, \qquad e_y = \frac{P_2}{2EF_2} - p_y \frac{hb}{2EF_2} . \qquad (2.83)$$

Relations (2.43), (2.45) and (2.83) are a closed system of 5 linear algebraic equations for 5 unknowns p_x, p_y, f_0^2, e_x and e_y. Equating the right-hand side expressions in (2.43) and (2.83), we derive the following relations (depending on f_0) for p_x and p_y:

$$p_x = p'_x - \frac{\pi^2 f_0^2}{8k} E_x \left(k_y \frac{m^2}{a^2} + \mu_{xy} \frac{n^2}{b^2} \right),$$

$$p_y = p'_y - \frac{\pi^2 f_0^2}{8k} E_y \left(k_x \frac{n^2}{b^2} + \mu_{yx} \frac{m^2}{a^2} \right), \tag{2.84}$$

where

$$p'_x = p_x\big|_{f_0=0} = \frac{E_x}{k} \left(\frac{P_1}{2EF_1} k_y + \frac{P_2}{2EF_2} \mu_{xy} \right),$$

$$p'_y = p_y\big|_{f_0=0} = \frac{E_y}{k} \left(\frac{P_2}{2EF_2} k_x + \frac{P_1}{2EF_1} \mu_{yx} \right) \tag{2.85}$$

are thickness-average stresses obtained for the case of a flat (not buckled) plate (i.e., $f_0=0$); additional symbols here are

$$k_x = 1 + \frac{E_x hb}{2EF_1}, \qquad k_y = 1 + \frac{E_y ha}{2EF_2}, \qquad k = k_x k_y - \mu_{xy}\mu_{yx}.$$

Note that $f_0 = 0$ for a flat plate, so relations $p_x = p'_x$ and $p_y = p'_y$ hold according to (2.84). In addition, if stiffeners are "weak" (so that $EF_1 \to 0$, $EF_2 \to 0$) the relations (2.84) and (2.85) provide

$$p_x = p'_x = \frac{P_1}{hb} \left(T_x = \frac{P_1}{b} \right), \qquad p_y = p'_y = \frac{P_2}{ha} \left(T_y = \frac{P_2}{a} \right),$$

i.e., we turn again to the case of specified skin loading not depending on f_0, as considered in 2.4.1.

Substituting p_x and p_y from (2.84) into (2.45) at $f_0 \neq 0$ results in the following equation for the displacement amplitude:

$$D(m,n) - p'_x \frac{m^4}{4a^2} - p'_y \frac{n^4}{4b^2} + E'(m,n) f_0^2 = 0, \tag{2.45'}$$

where $E'(m,n) = E(m,n) + \dfrac{\pi^2}{32k} \left(E_x k_y \dfrac{m^4}{a^4} + E_y k_x \dfrac{n^4}{b^4} + 2E_x \mu_{xy} \dfrac{m^2 n^2}{a^2 b^2} \right).$

When determining critical state of the skin from (2.45') and (2.85) the relations (2.46) hold; therefore, (2.45') is the basis for us to write for postbuckling of the skin:

$$f_0^2 = \frac{1}{E'_0} \left(p'_x \frac{m_0^2}{4a^2} + p'_y \frac{n_0^2}{4b^2} - D_0 \right) = \frac{D_0}{E'_0} (\bar{p}' - 1), \tag{2.86}$$

where $E'_0 = E'(m_0, n_0)$, $\quad \bar{p}' = \bar{p}'_x + \bar{p}'_y$, $\quad \bar{p}'_x = \dfrac{p'_x m_0^2}{4a^2 D_0}$, $\quad \bar{p}'_y = \dfrac{p'_y n_0^2}{4b^2 D_0}$.

Now, stresses in the panel are determined completely: p_x and p_y ($T_x = p_x h$, $T_y = p_y h$) are described by (2.84), e_x, e_y are from (2.43), $N_x(x,y)$, $N_y(x,y)$ are written in (2.41), forces in webs are $N_1 = EF_1 e_x = (P_1 - p_x hb)/2$ and $N_2 = EF_2 e_y = (P_2 - p_y hb)/2$, and the strain field is from (2.2):

$$\varepsilon_x(x,y,z) = A_{11}N_x(x,y) + A_{12}N_y(x,y) + z\frac{m_0^2\pi^2}{a^2}w(x,y),$$

$$\varepsilon_y(x,y,z) = A_{12}N_x(x,y) + A_{22}N_y(x,y) + z\frac{n_0^2\pi^2}{b^2}w(x,y), \qquad (2.87)$$

$$\gamma_{xy}(x,y,z) = -2z\frac{m_0 n_0 \pi^2}{ab}w'(x,y).$$

Here, $w(x,y)$ are defined by the formula (2.38), and

$$w'(x,y) = f_0 \cos\frac{m\pi x}{a}\ \cos\frac{n\pi y}{b}.$$

To evaluate the composite skin strength, we can assume that strains are uniform through the thickness of a layer and equal to the layer midsurface strains. In this case the expressions (2.87) define the plate layer strain components, with z being a coordinate of the midsurface of a *k*-th layer. The plate is assumed to break down if at least one point in some layer reaches its limiting state. Used as the limiting state criterion is the layer strength polynomial criterion written with reference to the layer orthotropy axes:

$$\frac{\sigma_1^2}{\bar{\sigma}_1^2} - \frac{\sigma_1\sigma_2}{\bar{\sigma}_1^2} + \frac{\sigma_2^2}{\bar{\sigma}_2^2} + \frac{\tau_{12}^2}{\bar{\tau}_{12}^2} = 1, \qquad (2.88)$$

where $\bar{\tau}_{12}$, $\bar{\sigma}_1^+$, $\bar{\sigma}_1^-$, $\bar{\sigma}_2^+$, $\bar{\sigma}_2^-$ are respective ultimate stresses for shear, tension (+) and compression (—) along and across fibers. Stresses $\{\sigma\} = [\sigma_1\ \sigma_2\ \tau_{12}]^T$ in each layer are described as

$$\{\sigma\} = [E]\{\varepsilon\}, \qquad (2.89)$$

where $\quad \{\varepsilon\} = [\varepsilon_1\ \varepsilon_2\ \gamma_{12}]^T = [R]\{\bar{\varepsilon}\},$

$$[E]=\begin{bmatrix}\bar{E}_1 & \mu_{12}\bar{E}_1 & 0\\ \mu_{21}\bar{E}_2 & \bar{E}_2 & 0\\ 0 & 0 & G_{12}\end{bmatrix}, \qquad [R]=\begin{bmatrix}m^2 & n^2 & mn\\ n^2 & m^2 & -mn\\ -2mn & 2mn & m^2-n^2\end{bmatrix}$$

$$\{\bar{\varepsilon}\}=\left[\varepsilon_x\ \varepsilon_y\ \gamma_{xy}\right]^T, \qquad m=\cos\varphi, \qquad n=\sin\varphi .$$

The panel strength is determined by proportionally increasing the loads P_1 and P_2 in increments from an initial vector at which the skin is flat. In this process we find critical (buckling) stresses p_x^* and p_y^* (from (2.46)) and their respective loads P_1^* and P_2^* (according to (2.85)), thereafter the stress field, the failure loads $\bar{P}_1$ and $\bar{P}_2$, and the fracture point (by using (2.88)).

At each load level a check is made of web strength:

$$N_1 / F_1\bar{\sigma}_x = E\varepsilon_x / \bar{\sigma}_x = 1, \qquad N_2 / F_2\bar{\sigma}_y = E\varepsilon_y / \bar{\sigma}_y = 1, \tag{2.90}$$

where $\bar{\sigma}_x, \bar{\sigma}_y$ are ultimate stresses of web materials.

Of particular interest is the case of uniaxial loading of axially stiffened long plate; here, we should adopt $P_2 = 0$ and $EF_2 \to 0$ and, following (2.84), assume that $p_y = 0$, $p_y' = 0$, $\psi = 0$. In addition, relations (2.51) are valid for skin buckling. Upon some transformations the equation (2.86) produces the following out-of-plane displacement amplitude formula that generalizes (2.52):

$$f_0\sqrt{\frac{E_x h}{D_{11}}} = 4\sqrt{2}\sqrt{\frac{k_x(1+\beta)}{(k_x + k_x\gamma + 2)}\left(\frac{p_x'}{p_x^*} - 1\right)} \tag{2.91}$$

where $p_x' = E_x P_1/2k_x EF_1$. Equation (2.91) becomes relation (2.52) when $EF_1 \to 0$, $k_x \to \infty$ and $p_x' = p_x = P_1/hb$. Similarly (with due account of (2.91)), the first relation in (2.84) produces the mean skin stresses:

$$p_x = p_x' - \frac{\pi^2 E_x f_0^2 m_0^2}{8k_x a^2} = p_x' \frac{k_x + k_x\gamma + 2p_x^*/p_x'}{k_x + k_x\gamma + 2} \tag{2.92}$$

With this, the force in the longitudinal webs is

$$2N_1 = P_1 - p_x hb = \frac{P_1\left[3k_x + k_x\gamma - 2(k_x - 1)p_x^*/p_x'\right]}{k_x(k_x + k_x\gamma + 2)} \tag{2.93}$$

If the panel load severity factor ($p_x' / p_x^* = P_1 / P_1^*$) grows (and the skin deflection increases, according to (2.91)), it is easily seen that skin/stiffener load distribution does change so that a skin load decreases and a stiffener force increases. Asymptotically (as $P_1 / P_1^* \to \infty$) this leads to the values below:

$$p_{x\infty} = p_x' \frac{k_x(1+\gamma)}{k_x(1+\gamma)+2}, \qquad 2N_{1\infty} = P_1 \frac{3+\gamma}{k_x(1+\gamma)+2} \quad . \tag{2.94}$$

These same loads corresponding to the case of no skin buckling do not depend on the panel load severity factor and are constant:

$$p_x = P_1E_x/2k_xEF_1 , \qquad 2N_1 = P_1/k_x . \tag{2.95}$$

It may be readily demonstrated that the same solution (2.92) - (2.94) can be derived by employing the general method with reduction coefficients if we consider joint deformation of two flat elements, of which one (the skin) has a variable modulus of elasticity depending on stresses: $E_x^s = \varphi_x^s E_x$. To do so, it suffices to transform equations (2.95) by substituting

E_x for E_x^s and
k_x for $k_x^s = 1+E_x^s\, hb / 2EF_1$

and, thereafter, to solve these equations by either iterations or explicitly, through the use of (2.55) for the reduction coefficient φ_x^s.

If compression is biaxial, the panel stress field and skin/stiffener interaction are governed not only by the nondimensional parameters introduced earlier but also by complementary parameters $k_x \geq 1$ and $k_y \geq 1$ that characterize a ratio of stiffnesses of the skin and webs; also significant become the skin layup sequence and the skin-layer/web strength limit ratio.

Let us demonstrate this with some examples.

A stiffened rectangular plate with the length of 300 mm and the 100-mm width is loaded longitudinally by a compressive force P_1. The graphite/epoxy skin has a $(\pm 45/90/0)_S$ layup, ply thickness of 0.11 mm, and the following ply characteristics:

E_1 = 12000 kg/sq.mm, E_2 = 850 kg/sq.mm, G_{12} = 650 kg/sq.mm,
μ_{21} = 0.27, $\bar{\sigma}_1^+$ = 100 kg/sq.mm, $\bar{\sigma}_1^-$ = 100 kg/sq.mm, $\bar{\sigma}_2^+$ = 2.4 kg/sq.mm,
$\bar{\sigma}_2^-$ = 9.5 kg/sq.mm, $\bar{\tau}_{12}$ = 8 kg/sq.mm.

Web cross-sectional areas F_1 and F_2 are 5 sq.mm, the elasticity modulus E is equal to 18,000 kg/sq.mm, and strength limits $\bar{\sigma}_x$ and $\bar{\sigma}_y$ are equal to 100 kg/sq.mm.

Results of computations using the above relations are represented in Figs. 2.25 through 2.28. Middle curves in Figs. 2.25 and 2.26 show the influence of the panel load severity factor on the postbuckling deflection relative amplitude f_0 / h and the reduction coefficient $\varphi_x^s = p_x / e_xE_x$. Figure 2.27 represents distributions of N_x in the skin transverse direction at various values of P_1/P_1^*; note that m_0=3 and n_0=1. Figure 2.28 depicts the effect of P_1/P_1^* on a mean stress N_1/F_1 in longitudinal webs. The panel fails due to web failure in accordance with the condition (2.90).

Also, Figs. 2.25, 2.26 and 2.28 demonstrate the calculated results for various web stiffnesses — when $F_1(=F_2)$ is increased and decreased by a factor of 10 from the initial value 5 sq.mm (and the parameter k_x varies from 1.23 to 24.55, respectively). In many cases the first to break are longitudinal webs; however, if we raise the web ultimate stress, the sequence of failures in the skin and webs gets changed.

For instance, when $F_1=F_2=5$ sq.mm and $\overline{\sigma}_x = \overline{\sigma}_y$ is increased from 100 to 120 kg/sq.mm (see Fig. 2.28) the first to break is the composite skin. The limiting state appears in the 45-degree layer at z=0.385 mm at the plate center (x=a/2, y=b/2).

3. Part 2. General model of joints in composite structures

3.1. Problem statement

When designing a composite structure, one should try to reduce the amount of joints and attachment elements and to develop the structure as a unit. However, no one designer could eliminate joints, therefore the analysis and design of joints remain an important problem in the process of introduction of composites in complex built-up airframes.

To attach composite structures to one another or to metal structures, perspectives are with adhesive bond as the most suitable in view of the features of composite materials. These joints can appropriately transfer the distributed loads between plates of intermediate thickness. In this case the joint is a regular continual part, and analyses may be based on the theory of elasticity.

Low ultimate compressive stresses; the presence of weak polymer layers; low ultimate in-plane shear stresses; all this notably reduces the load-bearing capability of the mechanical joints. Boundary effects around holes and/or other discontinuities in materials may both result in local interply failures and notably change the effective stress concentration factors.

These problems are solved by using the computational models based on the finite-element method alone or in combination with other means (such as structural mechanics and the theory of elasticity).

Section 3.2 presents an algorithm for analyzing adhesive bonds of various types. The theory makes it possible to determine stresses σ_x, τ_{xy}, and σ_y for all components of the joint; this is a necessary condition for estimating the strength, taking into account that the shear and flatwise tension ultimate stresses of composite plates are comparable to those of the adhesive layer.

The problem is solved by employing the Papkovich method that assumes the stress field to be decomposed into a fundamental state and a correction. The fundamental solution is the one satisfying the equilibrium equations and boundary conditions for the surface. If deformation compatibility condition is not met, corrections are introduced, each of which corresponding to a self-equilibrium stress field.

The corrections are determined by utilizing the strain energy; true stresses in an elastic body correspond to minimum strain energy.

Section 3.3 considers some models supporting the analysis of joints in stress concentration zones and load application areas:

- a model for analyzing the mechanical joint,
- a model for analyzing adhesive joints near stress concentrations,
- an analytical model accounting for three-dimensionality of joints.

The first two model are applicable to study of two-dimensional joints and are employed to evaluate adhesive and fastener joints around stress concentration areas (in particular, to analyze repairs with in-service damages).

The third model is for analyzing stresses and strength of joints that transfer great concentrated loads. It can be used to study a wide range of joints in composite structures. The model has been validated by comparing the computed values with the analytical, numerical and experimental data available for some types of joints.

The model and related computational techniques can be employed to determine stresses in very diverse joints and to reasonably select parameters of joints of composite elements in structures.

3.2. Engineering analysis of commonly used adhesive joints in composite thin-walled structures

Consideration is given to theoretical analysis of stresses in an adhesive joint of two sheets. The sheets are assumed to be made of polymer filamentary composites. A feature of such joints is that the shear strength and the flatwise tension ultimate stress of composites are comparable with the same characteristics of the adhesive layer, therefore the analysts need stress components in all structural elements – not only in the adhesive layer as the analysis of adhesive bonds in metallic structures assumes.

Below, variational analysis is provided as a basis for determining stresses in the sheets and the adhesive layer. Sheets are assumed to be loaded in tension, but the method may easily be generalized to cover the problem of stress state of components under pressure.

3.2.1. Computational model of symmetric and asymmetrical adhesive joints

In real structures the width of sheets is much larger than the total thickness, therefore the stress state may be analyzed by using a strip with a unit width (Fig. 3.1a) that is under plane strain conditions.

At edges of the sheets the elastic axis of the bar has jumps with magnitudes Δy_i. The latter is defined as a difference between the sheet neutral line and the neutral line of the section including the adhesive joint. If the bar is loaded with a tensile force P, then the elastic axis deforms and extra bending moments and transverse shear forces appear, added to the tensile load. We should start with estimation of the forces/moments over the bar.

Evaluation of forces and moments over a bar cross-section

Consider tension of a continuous bar whose elastic axis looks like that in Fig. 3.1b. Types of joints that could be transformed thereto are represented in Table 3.1.

To compute strains, bending moments and shear stress resultants, we can employ the general equation (written in terms of initial parameters, see [1]) for the elastic line of a tension-loaded and bent bar. The co-ordinate system origin and the positive directions of axes, strains and stresses are identified in Fig. 3.1c. After the necessary transformations, we obtain the following relations for computing the initial parameters:

$$Q_0 = \overline{Q_0} = -P\ \frac{\overline{Y_L} + Y_R}{L_L + L_R};$$

(3.1)

$$M_0 = -\overline{M_0} = P\ \frac{\overline{\Delta y_L}\, A_R \,\mathrm{Ch}\nu_{1R} - \Delta y_R\, A_L\, \mathrm{Ch}\nu_{1L} - \Delta y_0\, A_L\, B_R\, \mathrm{Ch}\nu_{1R}\, \mathrm{Ch}\nu_{1L}}{\left(A_R B_L + A_L B_R\right)\mathrm{Ch}\nu_{1R}\, \mathrm{Ch}\nu_{1L}};$$

$$\varphi_0 = \overline{\varphi_0} = -\frac{Q_0}{P} - \frac{\overline{\Delta y_L}\, B_R\, \mathrm{Ch}\nu_{1R} + \Delta y_R\, B_L\, \mathrm{Ch}\nu_{1L} + \Delta y_0\, B_L\, B_R\, \mathrm{Ch}\nu_{1R}\, \mathrm{Ch}\nu_{1L}}{\left(A_R B_L + A_L B_R\right)\mathrm{Ch}\nu_{1R}\, \mathrm{Ch}\nu_{1L}};$$

$$y_0 = -\overline{y_0} = \frac{M_0}{P} - \frac{\overline{Y_L}\, L_R - Y_R\, L_L}{L_L + L_R};$$

where

$$A_j = \frac{1}{K_{1j}}\,\mathrm{th}\nu_{1j} + \frac{1}{K_{2j}}\,\mathrm{th}\nu_{2j},$$

$$B_j = 1 + \frac{K_{1j}}{K_{2j}}\,\mathrm{th}\nu_{1j}\,\mathrm{th}\nu_{2j},$$

$$K_{ij} = \sqrt{\frac{P}{\left(\overline{EJ}\right)_{ij}}}\,, \qquad \nu_{ij} = K_{ij}\, l_{ij}$$

$i = 1,\ 2;$ $\qquad$ $j = L\ ,\ R$

$\left(\overline{EJ}\right)_{ij}$ is a reduced stiffness of an i-j portion.

Other components present in (3.1) are identified in Fig. 3.1.
Adopt the common x0y system and take into account that

$\overline{Y_L} = -Y_L,\ \ \overline{\Delta y_L} = -\Delta y_L,\ \ \overline{M_{1L}} = -M_{1L},\ \ \overline{x} = -x.$

Then equations for bending moments and shear forces over the portions of the joint may be written as follows:

Portion 1L $\quad (-l_{1L} \le x \le 0)$:

$$M_{1L}(x) = \left(\varphi_0 P + Q_0\right)\frac{\mathrm{Sh}(K_{1L}x)}{K_{1L}} + M_0 \mathrm{Ch}(K_{1L}x),$$

$$Q_{1L}(x) = (\varphi_0 P + Q_0)\mathrm{Ch}(K_{1L}x) + M_0 K_{1L} \mathrm{Sh}(K_{1L}x). \qquad (3.2a)$$

Portion 1R $(0 \le x \le l_{1R})$:

$$M_{1R}(x) = \left(\varphi_0 P + Q_0\right)\frac{\mathrm{Sh}(K_{1R}x)}{K_{1R}} + \left(\Delta y_0 P + M_0\right)\mathrm{Ch}(K_{1R}x),$$

$$Q_{1R}(x) = (\varphi_0 P + Q_0)Ch(K_{1R}x) + (\Delta y_0 P + M_0)K_{1R}Sh(K_{1R}x). \qquad (3.2b)$$

Thus, the joint is considered to be subdivided into portions that are between the cross sections with free edges of the sheets. A loading pattern for the adhesive joint is shown in Fig.3.2.

Idealized bar model for analyzing the stresses

The real joint may be transformed into the model that is an idealized bar (Fig. 3.3a) composed of a finite number of longitudinal elements that are mutually bonded by webs. The longitudinal elements (whose total cross-sectional area is equal to the cross-sectional area of the original object) carry the normal stress σ_x only. A cross-sectional area of an *i*-th longitudinal elements is

$$f_i = \left(\frac{\delta_{i-1}}{2} + \frac{\delta_i}{2}\right)$$

where δ_{i-1} and δ_i are depths of adjacent webs.

The webs are assumed to be two-layered components (Fig. 3.3b):

- one of them carries the shear stresses only; its shear modulus is assumed to be equal to the modulus of the real structural portion substituted;

- the second layer is a set of distributed struts that carry the normal stresses σ_y only; its modulus of elasticity is assumed to be equal to the modulus E_y of the real structural portion substituted.

A web depth is determined as

$$\delta_i = y_{i+1} - y_i$$

where y_i and y_{i+1} are co-ordinates of the center of gravity of adjacent longitudinal elements in co-ordinate system adopted.

3.2.2. Hypothesis of local corrections

The solution of the adhesive joint stress problem relies upon the Papkovich method [2, 3] that suggests the stress state being decomposed into the basic state and the correction state. The basic solution is obtained by analyzing the joint as a tension-loaded and bent bar which has discontinuity in the elastic line. The effects of free edges are allowed for by introducing corrections that are some fast-fading exponential functions. In real adhesive joints the distances between sections containing the free edges are rather long; this enables us to adopt the assumption of no interaction between the correction functions introduced in neighboring sections.

The hypothesis of local corrections makes it possible to transform the original "adhesive joint problem" into

- search for the basic solution for the adhesive joint as a whole and
- independent determination of corrections that are local for the portions.

The basic solution is obtained from the analysis of the adhesive joint as a tension-loaded and bent bar which has discontinuity in the elastic line. The local correction stresses are determined by solving the problem on gradual loading of a sheet through a semi-infinite bar (with one end being free).

3.2.3. Analysis method

The Papkovich method assumes that the stress state is decomposed into the basic state and the correction. The basic state is from the solution that satisfies the equilibrium equations and boundary conditions over the surface; for the basic solution we use symbols $\overline{\sigma}_x$, $\overline{\tau}_{x,y}$, $\overline{\sigma}_y$.

If strain compatibility conditions are not met, the correction solutions are introduced; they also satisfy the equilibrium equations and the surface boundary conditions. Each of the correction functions corresponds to a self-equilibrium stress field. We denoted these functions by using $\sigma_x^{(i)}$, $\tau_{x,y}^{(i)}$, $\sigma_y^{(i)}$, i=0, 1, 2, ..., n.

The true solution is written as

$$\sigma_x = \overline{\sigma}_x + \sum_{i=1}^{n} \sigma_x^{(i)} , \quad \tau_{xy} = \overline{\tau}_{xy} + \sum_{i=1}^{n} \tau_{xy}^{(i)} , \quad \sigma_y = \overline{\sigma}_y + \sum_{i=1}^{n} \sigma_y^{(i)} .$$

By varying the correction functions, we can change the stress field while not violating the equilibrium equations and boundary conditions.

When solving this problem, the basic solution is the one from the beam theory. It provides a practically valuable solution for almost all span of the bar, and correction is only necessary for a vicinity of sheet edges.

We may limit ourselves to introduction of one correction written as a product of two functions, one depending on X, and the other one, on Y. Accuracy of such "truncated" solution depends on qualities of the correction function.

Basic solution

Adopted as the basic solution is the solution provided by the beam theory with the flat cross-section hypothesis. Equations (3.2) are used to determine the loads M_z and Q_y applied to a particular section of the tension-loaded bar; the beam theory suggests the following relations:

$$\bar{\sigma}_{xi} = \frac{\psi_i}{\bar{F}} P(x) - \frac{\psi_i y_i}{\bar{J}_z} M_z(x);$$

$$\bar{\tau}_{xy} = Q(x) \frac{\bar{S}_{z,i}}{\bar{J}_z}; \qquad \bar{\sigma}_{y,i} = 0; \tag{3.3}$$

where $\bar{F} = \sum_{i=1}^{n} \psi_i f_i$, $\bar{J}_z = \sum_{i=1}^{n} \psi_i y_i^2 f_i$, $\bar{S}_{z,i} = \sum_{k=1}^{i} \psi_k y_k f_k$, $\psi_i = \frac{E_{x,i}}{E_f}$,

y_i is a distance from an *i*-th longitudinal element to the neutral axis,
E_f is the modulus of the material to which the cross section is reduced.

Correction function

Within the analytical model adopted the correction part of normal stresses in any longitudinal element is described as

$$\sigma^0_{x,i}(x,y) = \chi(x)\sigma^0_{x,i} \qquad \text{where } i=1, 2, ..., n. \tag{3.4}$$

Separate a bar element that is at a distance X from the co-ordinate system origin, as shown in Fig. 3.4a. The equilibrium equations are then employed to find the corrective shear stress applied to an *i*-th web:

$$\tau_{xy,i} = \chi'(x)\tau^0_{xy,i} \tag{3.5}$$

where $\tau^0_{xy,i} = \sum_{k=1}^{i} \sigma^0_{x,k} f_k$; $\qquad$ i=1, 2, ..., n-1.

The equilibrium equations for an infinitesimal element cut out of the *i*-th web (Fig. 3.4b) produces the differential equation relating the normal $\sigma_{y,i}$ stress to the shear $\tau_{xy,i}$ stress:

$$\frac{\partial \sigma_{y,i}}{\partial y} + \frac{\partial \tau_{xy,i}}{\partial x} = 0.$$

Substitute the function $\tau_{xy,i}$ and take into account that $\sigma_{y,1}=0$; then integration provides

$$\sigma_{y,i}(x,y) = \chi''(x)\ \sigma^0_{y,i}(y), \tag{3.6}$$

where $\sigma^0_{y,i}(y) = \sigma^0_{y,i} + \tau^0_{xy,i}(y - y_i)$, $\qquad$ i=1, 2, 3, ..., n-1,

$\sigma^0_{y,i} = \sum_{k=1}^{i-1} \tau^0_{xy,k}\delta_k$ is the stress in the vicinity of the i-th element.

Thus, the stress tensor components for each element of the adhesive joint may be established using

$$\begin{aligned}
\sigma_{x,i} &= \overline{\sigma}_{x,i} + \chi(x)\sigma^0_{x,i}\,; \\
\tau_{xy,i} &= \overline{\tau}_{xy,i} + \chi'(x)\tau^0_{xy,i}\,; \\
\sigma_{y,i} &= \chi''(x)\sigma^0_{y,i}(y)
\end{aligned} \tag{3.7}$$

where $\overline{\sigma}_{x,i}$ and $\overline{\tau}_{xy,i}$ are from formulas (3.3), and $\sigma^0_{x,i}$, $\tau^0_{xy,i}$ and $\sigma^0_{y,i}(y)$ are from (3.4), (3.5), and (3.6), respectively.

Selecting the correction function σ^0_x

The correction function should eliminate normal stress over free edges of the sheets, so it is reasonable to assume that the function $\sigma^0_x(y)$ is piecewise linear. The self-equilibrium corrective function may be written as follows:

* upper sheet broken

$$\sigma^0_{x,i} = \begin{cases} \beta_I + \omega_I y_i & i = 1 \div k \\ \beta_{II} + \omega_{II} y_i & i = k+1 \div n \end{cases}$$

* lower sheet broken

$$\sigma^0_{x,i} = \begin{cases} \beta_{II} + \omega_{II} y_i & i = 1 \div k \\ \beta_I + \omega_I y_i & i = k+1 \div n \end{cases} \tag{3.8}$$

Here, the index I is for the broken sheet, and II, for the continuous sheet.
Use the self-equilibrium conditions:

$$\sum_{i=1}^{n} \sigma^0_{x,i} f_i = 0 \qquad \sum_{i=1}^{n} y_i \sigma^0_{x,i} f_i = 0 \tag{3.9}$$

to derive

$$\begin{aligned}
\beta_{II} &= \frac{(F_I J_{II} - S_I S_{II})\beta_I + (S_I J_{II} - J_I S_{II})\omega_I}{S^2_{II} - F_{II} J_{II}} \\
\omega_{II} &= \frac{-(F_I S_{II} - S_I F_{II})\beta_I - (S_I S_{II} - J_I F_{II})\omega_I}{S^2_{II} - F_{II} J_{II}}
\end{aligned} \tag{3.10a}$$

where $F_I = \sum_k f_i$; $F_{II} = \sum_{n-k} f_i$;

$$S_I = \sum_k y_i f_i \; ; \qquad S_{II} = \sum_{n-k} y_i f_i \; ;$$

$$J_I = \sum y_i^2 f_i \; ; \qquad J_{II} = \sum_{n-k} y_i^2 f_i \; ;$$

f_i the area of the *i*-th element,
y_i the distance from the *i*-th element to the neutral axis,
k the total number of longitudinal elements in the broken sheet,
n the total number of longitudinal elements.

In a section $x = x_n$ at the end face of the broken sheet (index I) the normal stress σ_x is zero, so the following equality holds:

$$\overline{\sigma}_{x,i} + \chi(x_n)\sigma^0_{x,i} = 0 .$$

Substituting the stresses from (3.3) and (3.8), obtain

$$\Psi_i \frac{P}{\overline{\overline{F}}} - \Psi_i \frac{M_Z(x_n)}{\overline{J}} y_i + \chi(x_n)(\beta_I + \omega_I y_i) = 0 .$$

Assuming

$$\chi(x_n) = 1 , \tag{3.11}$$

we can derive the following relations for coefficients β_I and ω_I :

$$\beta_I = -\Psi_i \frac{P}{\overline{\overline{F}}}, \qquad \omega_I = \Psi_i \frac{M_Z(x_n)}{\overline{J}} . \tag{3.10b}$$

With the function $\sigma^0_x(y)$ determined, formulas (3.5) and (3.6) are utilized to determine the corrective stress functions τ^0_{xy} and σ^0_y. Figure 3.5 graphically represents the components of the basic and correction functions in the section where the free end is.

With the function $\chi(x)$ found, the relations (3.8) and (3.3) - (3.6) are employed to compute all stress components applied in elements of the adhesive joint.

The sought-for function $\chi(x)$ is determined from the minimal potential strain energy condition; the energy may be written in the form,

$$U = \int_V U_0 dV = U_1 + U_2 + U_3 = \frac{1}{2}\int_0^l \left[\sum_{i=1}^{n} \frac{(\sigma_{x,i})^2 f_i}{E_{x,i}} + \sum_{i=1}^{n-1} \frac{(\tau_{xy,i})^2 \delta_i}{G_{xy,i}} + \sum_{i=1}^{n-1} \frac{(\sigma_{y,i})^2 \delta_i}{E_{y,i}} \right] dx$$

where U_1, U_2 and U_3 are strain energies, respectively, of longitudinal elements, shear-carrying webs, and struts transferring normal stresses σ_y; l is the length of the structure.

In longitudinal elements, all stresses, except for σ_x, are zero; σ_x stress is described by (3.7); with this, the potential energy of all longitudinal elements is

$$U_1 = \frac{1}{2}\int_0^l \sum_{i=1}^{n} \frac{\left(\bar{\sigma}_{x,i} + \chi\sigma_{x,i}^0\right)^2 f_i}{E_{x,i}} dx = \frac{1}{2}\int_0^l \left(A_0 + 2A_1\chi + A\chi^2\right) dx \qquad (3.12)$$

where $A_0 = \sum_{i=1}^{n} \frac{1}{E_{x,i}} f_i \bar{\sigma}_{x,i}^2$, $A_1 = \sum_{i=1}^{n} \frac{1}{E_{x,i}} f_i \bar{\sigma}_{x,i} \sigma_{x,i}^0$, $A = \sum_{i=1}^{n} \frac{1}{E_{x,i}} f_i \left(\sigma_{x,i}^0\right)^2$.

Substitute in the equation for A_1 the value of $\bar{\sigma}_{x,i}$ from (3.3); taking into account relations (3.9), we have

$$A_1 = \frac{P}{E_f \bar{F}} \sum_{i=1}^{n} f_i \sigma_{x,i}^0 + \frac{M}{E_f \bar{J}} \sum_{i=1}^{n} f_i y_i \sigma_{x,i}^0 = 0 .$$

Thus, the formula for strain energy of longitudinal elements becomes

$$U_1 = \frac{1}{2}\int_0^l \left(A_0 + A\chi^2\right) dx .$$

In the *i*-th shear-carrying web the only stress component is shear, eq. (3.7). Strain energy of all shear-carrying webs is

$$U_2 = \frac{1}{2}\int_0^l \left[B_0 + 2B_1\chi' Q_y + B(\chi')^2\right] dx , \qquad (3.13)$$

$$B_0 = \frac{1}{\left(\bar{J}_z\right)^2} \sum_{i=1}^{n-1} \frac{\delta_i \left(\bar{S}_{z,i}\right)^2}{G_{xy,i}} \; ; \quad B_1 = \frac{1}{\bar{J}_z} \sum_{i=1}^{n-1} \frac{\delta_i}{G_{xy,i}} \bar{S}_{z,i} \tau^0_{xy,i} \; ; \quad B = \sum_{i=1}^{n-1} \frac{\delta_i}{G_{xy,i}} \left(\tau^0_{xy,i}\right)^2 .$$

For the i-th web transferring the normal stress σ_y the strain energy is expressed by

$$U_{3,i} = \frac{1}{2} \int_0^l \sum_{i=1}^{n-1} \frac{(\chi'')^2}{E_{y,i}} \left[\int_0^{\delta_i} \left(\sigma^0_{y,i} - \tau^0_{xy,i} s \right)^2 ds \right] dx$$

where $s = y - y_i$ and $\delta_i = y_{i+1} - y_i$.

After conducting the necessary manipulations, we arrive at the final expression for strain energy of a web transferring the normal stresses σ_y:

$$U_3 = \frac{1}{2} \int_0^l C(\chi'')^2 dx \tag{3.14}$$

where $C = \sum_{i=1}^{n-1} \frac{\delta_i}{E_{y,i}} \left[\frac{1}{3} \left(\tau^0_{xy,i} \delta_i \right)^2 - \sigma^0_{y,i} \left(\tau^0_{xy,i} \delta_i \right) + \left(\sigma^0_{y,i} \right)^2 \right]$.

The potential energy of the entire joint is a sum of potential energies of all elements as described by (3.12), (3.13), and (3.14).

After summation we obtain the following expression for potential energy as a functional that depends on the χ function and its derivatives:

$$U = U_1 + U_2 + U_3 = \frac{1}{2} \int_0^l R(\chi, \chi', \chi'', x) dx \tag{3.15}$$

where $R(\chi, \chi', \chi'', x) = A_0 + A\chi^2 + B_0 + 2B_1\chi' + B(\chi')^2 + C(\chi'')^2$.

For a function $\chi(x)$ to deliver minimum to the functional (3.15), the Euler variational equation must be satisfied:

$$\frac{\partial R}{\partial \chi} - \frac{d}{dx}\left(\frac{\partial R}{\partial \chi'}\right) + \frac{d^2}{dx^2}\left(\frac{\partial R}{\partial \chi''}\right) = 0 . \tag{3.16}$$

After the necessary transformations, we obtain the differential equation for the unknown $\chi(x)$ function:

$$C\chi^{IV} - B\chi'' + A\chi = B_1 Q^I_y . \tag{3.17}$$

Coefficients A, B, B_1, and C are described by (3.12), (3.13), and (3.14).

Equation (3.17) is a linear differential equation with constant coefficients. Its solution can be presented as

$$\chi(x) = \sum_{i=1}^{4} D_i \varphi_i(x) + \varphi_0(x), \tag{3.18}$$

where D_i are arbitrary constants,
$\varphi_i(x)$ are solutions to the homogeneous equation for (3.17),
$\varphi_0(x)$ is a particular solution to the inhomogeneous equation.

To find $\varphi_i(x)$, we should determine roots of the characteristic equation which is biquadratic in the case under consideration:

$$Cr^4 - Br^2 + A = 0. \tag{3.19}$$

If roots r_i of (3.19) are real and distinct, the solutions are

$$\varphi_i(x) = \exp\,(r_i\, x)\ . \tag{3.20}$$

If there exist repeated roots – for example, if $r_1 = r_2$, – then

$$\varphi_1(x) = \exp\,(r_1 x)\ , \quad \varphi_2(x) = x\,\exp\,(r_1 x)\ . \tag{3.21}$$

If eq. (3.19) has complex roots, these could be conjugate pairs – for example, $\pm(r_1 + r_2 i)$ and $\pm(r_1 - r_2 i)$. The corresponding solutions appear:

$$\varphi_1(x) = \cos\,(r_2 x)\,\exp\,(r_1 x) \quad \text{and} \quad \varphi_2(x) = \sin\,(r_2 x)\,\exp\,(r_1 x)\ . \tag{3.22}$$

For the shear force $Q_y(x)$ established in accordance with (3.2) we have the particular solution:

$$\varphi_0(x) = m_{1i}\,\mathrm{Ch}(K_{1,i}x) + m_{2i}\mathrm{Sh}(K_{1,i}x)\ , \qquad i = L,\ R\ , \tag{3.23}$$

where $m_{1R} = \dfrac{B_{1R}K_{1R}^2(M_0 + \Delta y_0 P)}{C_R K_{1R}^4 - B_R K_{1R}^2 + A_R}$; $\qquad m_{1L} = \dfrac{B_{1L}K_{1L}^2 M_0}{C_L K_{1L}^4 - B_L K_{1L}^2 + A_L}$;

$$m_{1R} = \frac{B_{1R}K_{1R}(\varphi_0 P + Q_0)}{C_R K_{1R}^4 - B_R K_{1R}^2 + A_R}\ ; \qquad m_{1L} = \frac{B_{1L}K_{1L}(\varphi_0 P + Q_0)}{C_L K_{1L}^4 - B_L K_{1L}^2 + A_L}\ .$$

The four arbitrary constants D_i are determined from boundary conditions.

Two boundary conditions are implied by the local correction hypothesis: the function and its derivative are limited at a distance from the sheet free end,

$$\chi(x)\big|_{x=L\to\infty} = \chi'(x)\big|_{x=L\to\infty} = 0\ . \tag{3.24}$$

The other two boundary conditions are written for the section where the sheet free end is located. Normal stresses at the sheet free end are zero according to (3.4); this produces

$$\chi(x_n) = 1. \tag{3.25}$$

By assuming a shear stress resultant at the sheet free end to be approximately zero, obtain:

$$\sum_i \tau_{xy,i}(x_n)\ \delta_i = 0\ ,$$

Here, summation covers all webs of the free end and the adhesive layer.

Utilize relations (3.7), (3.8), and (3.2) to re-write the boundary condition:

$$\chi'(x_n) = -\frac{Q_y(x_n)}{\bar{J}} \frac{\sum_i \bar{S}_{z,i}\delta_i}{\sum_i \tau^0_{xy,i}\delta_i}. \tag{3.26}$$

3.2.4. Computational examination of adhesive joints

Stresses in adhesive joint of a tension-loaded sheet with symmetric doublers made of the same material

A schematic of the joint is depicted in Fig. 3.6a; initial data for analyses are reported in Table 3.2. In this case we have $\Delta y_0 = \overline{\Delta y}_L = \Delta y_R = 0$ and, therefore, $y_0 = \varphi_0 = M_0 = Q_0 = 0$.

The correction (see Fig. 3.6a) is defined by formulas (3.8) and (3.10):

$$\sigma^0_{x,i} = \begin{cases} -\dfrac{P}{\bar{\bar{F}}} & \text{for doublers;} \\[2ex] \dfrac{F_I}{F_{II}}\dfrac{P}{\bar{\bar{F}}} & \text{for the sheet.} \end{cases}$$

Relevant expressions are utilized to evaluate $\tau^0_{xy,i}$ and $\sigma^0_{y,i}$ and to determine the coefficients A, B, and C of the differential equation (3.17). Owing to symmetry of the structure, consideration is given to an analytical model comprising the doubler and a half-thickness sheet, which are each modeled by 11 longitudinal elements (strips).

Differential equations for the $\chi(x)$ function is of the form

$$0.576\ \chi^{IV} - 0.769\ \chi'' + 0.214\ \chi = 0\ .$$

The solution to this equation (taking into account limitedness of the $\chi(x)$ function and its derivative at a distance from the doubler free end) may be written as

$$\chi(x) = D_2 \exp(-r_1 x) + D_4 \exp(-r_2 x).$$

Use the boundary conditions (3.25) and (3.26) to establish the remaining arbitrary constants:

$$D_2 = \frac{r_2}{r_2 - r_1} \quad ; \qquad D = -\frac{r_1}{r_2 - r_1} \ .$$

Thus, the solution to the differential equation appears:

$$\chi(x) = -1.852 \exp(-0.969x) + 2.852 \exp(-0.629x) \ .$$

Figure 3.6b represents plots of normal (σ_y) and shear stresses in the adhesive layer; variation of the stresses over the vertical extent of the section where the maximum stresses exist is also shown – Fig. 3.6c.

The differential equation (3.17) may by transition to a limiting state be transformed to the previously known simplified solution that is utilized in many articles devoted to behavior of adhesive joints.

Assume that the sheets have a rather high shear stiffness ($G_{xy,I} = G_{xy,II} \rightarrow \infty$) and that no displacement is allowed through the vertical extent of the joint (for example, if there is a rigid clamp): $E_{y,I} = E_{y,II} = E_{y,a} \rightarrow \infty$.

By transition to a limiting state we obtain the well-known equation:

$$\tau'' - \lambda^2 \tau = 0, \qquad (3.27)$$

where $\lambda^2 = \dfrac{G_{xy,a}(1+\Delta)}{\delta_a E_{xII} F_{II}}$; $\qquad \Delta = \dfrac{E_{xII} F_{II}}{E_{xI} F_I}$.

The solution to this equation is of the form

$$\tau = \frac{P\lambda}{1+\Delta} \exp(-\lambda x).$$

Figure 3.6d demonstrates the function $\tau_{xy,a}$, as computed by means of (3.27) (line I); for comparison's sake, a curve taking into account the real properties of the materials is also depicted – line III. The line II in Fig. 3.6d corresponds to an analysis in which $G_{xy,I}=G_{xy,II} \rightarrow \infty$, $E_{y,I} = E_{y,II} \rightarrow \infty$, and the adhesive layer has its real properties.

The allowance for real properties of all elements in the adhesive joint does notably change both the profile shape and magnitude of shear stresses; there appears the possibility to predict ultimate flatwise tensile stresses for both the adhesive layer and the sheets.

Sheet with a one-sided patch

A schematic of the joint is demonstrated in Fig. 3.7, and Table 3.3 provides the initial data for calculation. The model of the joint contains 11 strips in the sheet and 11 strips in the patch.

Having chosen a corrective function in accordance with (3.8), we determine functions $\tau^0_{xy,i}$ and $\sigma^0_{y,i}$ and compute coefficients A, B, C, B_1 of the differential equation (3.17). The differential equation is of the form

$$0.0428\ \chi^{IV} - 0.2066\ \chi'' + 0.1955\ \chi = Q^I_y B_1\ .$$

Roots of the characteristic equation (3.19) are real, and the solution is provided by the relation (3.18).

Let the free end of the patch be at the section $x=x_n$; having satisfied the boundary conditions (3.24) - (3.26) we write the solution:

$$\chi(x) = D_2 \exp[\alpha r_1(x-x_n)] + D_4 \exp[\alpha r_2(x-x_n)] + m_1 \mathrm{Ch}K_1x + m_2 \mathrm{Sh}K_1x\ , \tag{3.28}$$

where $D_2 = \dfrac{(r_2 - \alpha æ) - (r_2 m_1 - \alpha m_2 K_1)\ \mathrm{Ch}(K_1 x_n) - (r_2 m_2 - \alpha m_1 K_1)\ \mathrm{Sh}(K_1 x_n)}{r_2 - r_1}$;

$$D_4 = -\frac{(r_1 - \alpha æ) - (r_1 m_1 - \alpha m_2 K_1)\ \mathrm{Ch}(K_1 x_n) - (r_1 m_2 - \alpha m_1 K_1)\ \mathrm{Sh}(K_1 x_n)}{r_2 - r_1}\ ;$$

$\alpha=-1$ for $x > x_n$,

$\alpha=1$ for $x < x_n$,

r_1 and r_2 are roots of the characteristic equation (3.19),

$$m_1 = \frac{B_1 K_1^2 (\Delta y_0 P + M_0)}{C K_1^4 - B K_1^2 + A}\ ;\quad m_2 = \frac{B_1 K_1 (\varphi_0 P + Q_0)}{C K_1^4 - B K_1^2 + A};\quad æ = -\frac{Q_y(x_n) \sum_i \delta_i \bar{S}_{z,i}}{\bar{J}_z \sum_i \delta_i \tau^0_{xy}}\ .$$

Summation covers the webs at the free end and the adhesive layer.

The results are represented in Fig. 3.7:

- variation of normal ($\sigma_{y,a}$) and shear ($\tau_{xy,a}$) stresses in the adhesive layer around the free end of the patch (Fig. 3.7b) and

- distributions of stresses τ_{xy} and σ_y throughout the vertical extent of the stack in the sections where the stresses reach their maximum values (Fig. 3.7c).

The work [4] solves this problem via a continual model and the variational principle of the theory of elasticity. Computation results are almost coincident. Figure 3.7d represents differences between stresses in the adhesive layer:

$$\Delta\tau_{xy,a} = \frac{\left(\tau_{xy,a}\right)_k - \left(\tau_{xy,a}\right)_d}{\left(\tau_{xy,a}\right)_k}\ 100\%\ ; \qquad \Delta\sigma_{y,a} = \frac{\left(\sigma_{y,a}\right)_k - \left(\sigma_{y,a}\right)_d}{\left(\sigma_{y,a}\right)_k}\ 100\%\ ,$$

the index k corresponding to the continual model and the index d, to the discrete model.

The present model with an adequate total number of discrete elements provides a practically sufficient accuracy of determining stresses in adhesive bonds.

Choosing the appropriate total number of discrete elements in model of joint

When establishing a model of a joint, the question appears, how many discrete elements do we need to model the sheets bonded with adhesives?

To clarify the influence of the discretization degree on the analysis accuracy, the maximum stresses in an adhesive joint of sheets were computed for various numbers of discrete elements.

The joint discussed in the previous example was analyzed by using models in which every sheet was modeled by 4, 6, 8, 12, and 15 strips. Figure 3.8 shows difference of stresses in the continual model and the discrete model in which the total number of discrete elements is *i*:

$$\Delta N(i) = \frac{N_k - N_{d,i}}{N_k}\ 100\ \%\ ,$$

where $N_{d,i}$ is a value for the discrete model in which the total number of discrete elements is *i*,

N_K is the value for the continual model.

The graphical representation evidences that the model with an insufficient total number of longitudinal elements has greater maximum stresses as compared with the data from the continual model; the higher the discretization degree, the less the difference in stresses.

Replacing the sheet with 6 to 8 discrete elements ensures a practically sufficient accuracy of the analysis based on the discrete model.

Inserted adhesive joint of a composite sheet and an aluminum sheet

Consider a symmetric joint of two sheets (Fig. 3.9). Initial data may be seen in Table 3.4.

Due to the symmetry we have $\Delta y_0 = \Delta y_k = \overline{\Delta y_L} = 0$ and $y_0 = \varphi_0 = M_0 = Q_0 = 0$. The self-equilibrium correction from (3.8) and (3.10) can be written as

$$\sigma^0_{x,i} = \begin{cases} 1 & \text{for the composite sheet} \\ -\dfrac{F_I}{F_{II}} & \text{for the aluminum sheet} \end{cases} \qquad (3.29)$$

Here, F_I is the area of the composite portion in the joint and F_{II} is the area of the aluminum portion in the joint.

Equations (3.5) and (3.6) are utilized to compute other components of the correction, and equations (3.12) - (3.14) are employed to calculate coefficients A, B, and C. The result is the following differential equation for determining the function $\chi(x)$:

$$\chi^{IV} - 2\times 0.515\,\chi'' + 0.0543\,\chi = 0 .$$

Roots of the characteristic equation are real: $r_1=-r_2=0.987$, $r_3=-r_4=0.237$.
The general solution to the differential equation looks like this:

$$\chi(x) = D_1\,Ch(r_1x) + D_2\,Sh(r_1x) + D_3\,Ch(r_2x) + D_4\,Sh(r_2x) .$$

D_i are arbitrary constants to be determined on the basis of boundary conditions.

Boundary values of the function $\chi(x)$ and its derivative are established by nullifying the stresses σ_x and τ_{xy} at the free edge of the composite sheet (x=-1) and the aluminum sheet (x=1):

$$\chi(-1) = -\psi_I \frac{P}{\bar{F}}, \qquad \chi'(-1) = 0 ;$$

$$\chi(1) = \psi_{II} \frac{F_{II}}{F_I}\frac{P}{\bar{F}}, \qquad \chi'(1) = 0 . \qquad (3.30)$$

After substitution of values of the function and its derivative into boundary conditions we obtain the following expressions for the constants:

$$D_1 = \frac{P}{2\bar{F}}\left(\frac{F_{II}}{F_I}\psi_{II} - \psi_I\right)\frac{Sh\nu_2}{Sh\nu_2\ Ch\nu_1 - \frac{r_1}{r_2}Sh\nu_1\ Ch\nu_2}$$

$$D_2 = \frac{P}{2\bar{F}}\left(\frac{F_{II}}{F_I}\psi_{II} - \psi_I\right)\frac{Ch\nu_2}{Sh\nu_1\ Ch\nu_2 - \frac{r_1}{r_2}Sh\nu_2\ Ch\nu_1}$$

$$D_3 = -\frac{P}{2\bar{F}}\left(\frac{F_{II}}{F_I}\psi_{II} - \psi_I\right)\frac{r_1}{r_2}\frac{Sh\nu_1}{Sh\nu_2\ Ch\nu_1 - \frac{r_1}{r_2}Sh\nu_1\ Ch\nu_2}$$

$$D_4 = -\frac{P}{2\overline{F}}\left(\frac{F_{II}}{F_I}\psi_{II} - \psi_I\right)\frac{r_1}{r_2}\,\frac{Ch\nu_1}{Sh\nu_1\ Ch\nu_2 - \frac{r_1}{r_2}\,Sh\nu_2\ Ch\nu_1}$$

where $\nu_1=r_1 l$, $\nu_2=r_2 l$.

Having the $\chi(x)$ function determined from equations (3.7), all components of the stress tensor can be found. Figure 3.9 shows profiles of shear and normal stresses in the adhesive layer for joints with differing lengths.

Increasing the length of an adhesive joint is feasible to a certain limit only, since stresses in adhesive do not decrease in too a long joint.

If stiffnesses of sheets in a joint differ ($E_I F_I \neq E_{II} F_{II}$) then stresses in the adhesive at opposite free edges also differ; the higher the stiffness of an element, the higher the maximum stress in adhesive at the end of the element.

Inserted multilayered adhesive joint

The method developed for analyzing the simple inserted adhesive joint is well applicable to analysis of the multilayered adhesive joint.

Consider stresses in a multilayered symmetric joint of sheets made from composites and aluminum. A schematic of the joint is demonstrated in Fig. 3.10a; Table 3.5 provides initial data for calculation.

The model includes 24 strips, a corrective function is adopted in accordance with (3.29). Figure 3.10b represents stresses $\sigma^0{}_x$, $\tau^0{}_{xy}$ and $\sigma^0{}_y$. Further, equations (3.12) - (3.14) are involved to determine coefficients A, B, and C.

The differential equation for the function $\chi(x)$ in this example is of the form

$$\chi^{IV} - 2 \cdot 0.0782\ \chi'' + 0.0152\chi = 0.$$

Roots of the characteristic equation are a complex conjugate pair, $\pm(r_1 \pm r_2 i)$; here, $r_1=0.318$, $r_2=0.15$.

The solution to the differential equation is

$$\chi(x) = D_1 Ch(r_1x)\ Cos(r_2x) + D_2 Sh(r_1x)\ Cos(r_2x) + D_3 Ch(r_1x)\ Sh(r_2x) + D_4 Sh(r_1x)\ Sin(r_2x).$$

Boundary conditions for establishing the arbitrary constants coincide with relations (3.30); introducing therein the function $\chi(x)$ and its derivative, we obtain formulas for establishing the arbitrary constants.

Shown in Figure 3.10c is variation of shear stresses along the most severely loaded adhesive layer (web 5); Fig. 3.10d presents distribution of shear stresses τ_{xy} over the vertical extent of the section where the stresses are at maximum. For comparison, these plots are having the profiles (refer to dashed lines) of stresses in the adhesive joint with the same sheets but made as a "simple inserted joint."

The inserted multilayered adhesive joints enables decreasing the stress level for elements in adhesive joints, thus shortening the joint.

Distribution of stress resultants between the adhesive layers in multilayered adhesive joints is not uniform; the present analysis method makes it possible to determine real stress fields in adhesive joints.

Adhesive lap joint with two identical sheets

A lap joint may be modeled by a bar whose elastic axis has discontinuity at sheet ends. Consider an adhesive joint of two composite sheets; a schematic of the joint is demonstrated in Fig. 3.11a, and Table 3.6 provides initial data for calculation.

Locate the co-ordinate system origin at the central point of the lap area. Assume $\Delta y_0=0$. Equations (3.1) may be utilized to determine initial parameters; thereafter we can compute strains and forces/moments in the joint (Fig. 3.11b).

The analytical model incorporates 6 longitudinal elements for each sheet. Having determined the correction functions and coefficients A, B, C, and B_1, we arrive at the following differential equation for determining the function $\chi(x)$:

$$1.246\ \chi^{IV} - 15.497\ \chi'' + 3.866\ \chi = 0.009\ \mathrm{Sh}(0.0285x)\ .$$

The joint is asymmetric, therefore $\chi(x) = -\chi(-x)$; so the general solution to the equation may be written as

$$\chi(x) = D_2\ \mathrm{Sh}(r_1x) + D_4\ \mathrm{Sh}(r_2x) + D_0\ \mathrm{Sh}(K_1x)\ .$$

Arbitrary constants D_2 and D_4 are determined on the basis of boundary conditions for the free end ($x=l_c$) that correspond to relations (3.25) and (3.26).

Figure 3.11 represents diagrams of shear and normal stresses in adhesive joints with various lengths.

If an overlap area is short, the total bond area is insufficient, and shear stress is high throughout; increasing the overlap length decreases the shear stress, and stress distribution becomes nonuniform, with stresses showing peaks near the free ends. Increasing further the overlap length makes the shear/normal stress peaks get notably lower, thereafter intensity of reduction of maximum stresses in the adhesive layer gets slower; lastly, in rather long overlap areas, the maximum stresses do not always depend on the overlap area length.

Adhesive lap joint with two arbitrary sheets

Assume that the overlap area length enables employing the local correction hypothesis.

To determine the basic solution, the structure may be modeled by a bar whose elastic axis has two discontinuity points: the left-hand end ($x = -x_L$) and the right-hand end ($x = x_R$) (Fig. 3.12).

Making use of (3.1) and (3.2), we determine initial parameters and forces/moments applied to the ends. Thereafter, two correction functions are introduced and, in accordance with the local correction hypothesis, the problem is solved twice – for left-hand and right-hand parts in separation.

After the relevant transformations, we obtain two independent differential equations for left-hand and right-hand parts of the joint:

$$C_L \chi_L^{IV} - B_L \chi''_L + A_L \chi_L = Q^I_{Y,L} B_{1L}, \qquad -x_L \le x \le 0;$$
$$C_R \chi_R^{IV} - B_R \chi''_R + A_R \chi_R = Q^I_{Y,R} B_{1R}, \qquad 0 \le x \le x_R. \qquad (3.31)$$

Solutions to these equations with boundary conditions (3.24) - (3.26) are provided by (3.28). With functions χ_L and χ_R established, the corresponding relations are employed to determine stress components for any point in the joint.

Considered as an illustration may be an overlap joint of sheets made from carbon fiber reinforced plastic (CFRP) and aluminum. Data necessary for the analysis are in Table 3.7.

Determine co-ordinates of the neutral layer for each portion of the structure and establish the jumps of the elastic axis:

$$\overline{\Delta y_L} = 0.8535 \text{ м}, \qquad \Delta y_v = 0, \qquad \Delta y_R = 0.7465.$$

Equations (3.1) and (3.2) are source of initial parameters and end forces/moments necessary for subsequent calculations. Thereafter the correction stresses are computed for left-hand and right-hand parts of the joint in separation.

Figure 3.12 shows variation of normal and shear stresses in the adhesive layer, as well as diagrams of stresses σ_x, σ_y and τ_{xy} for certain cross sections.

If an adhesive joint incorporates several sections with free ends of sheets, each section introduces a correction function. In a general case we should allow for interaction of the correction solutions; this noticeably complicates the overall problem. In certain cases the situation may be simplified by using the local correction hypothesis. The latter is valid in the case that a distance $\Delta L_{i,i+1}$ between neighboring sections with free ends is rather long; in practice the "interaction" of the ends can be neglected if

$$\Delta L_{i,i+1} = x_{i+1} - x_i \ge \frac{5}{r_{min}}, \qquad (3.32)$$

where r_{min} is the minimum root of the characteristic equation (3.19).

The relation (3.32) is also a criterion for specifying a rational overlap length in an adhesive joint.

3.3. Finite-element model for analyzing the irregular adhesive and mechanical joints between composite parts

In recent years a considerable progress has been achieved in computing technologies and analysis methods. However, the variety of joints is very large due to differences in structural shapes and manufacturing processes; therefore the immediate analysis by means of elasticity/plasticity theories and fracture mechanics is a notable difficulty. So the effective method for analyzing the joints is to combine these methods and the engineering methods of structural mechanics.

The present model (Fig. 3.13) includes

a) an analytical model of discrete joints,

b) an analytical model of adhesive joints, and

c) an analytical model of three-dimensional joints.

The first two models are for estimating the two-dimensional objects and may be used to analyze thin-walled wing/fuselage components at the design stage, for estimating the repair after in-service damage, or when bonding the reinforcement doublers (whose edges are attached by bolts or metal needles). The bolt force allocation derived may be utilized in boundary conditions for analyzing the most severely loaded area by means of the three-dimensional model (see item c) above). In addition, the three-dimensional model can be employed independently, to analyze stress-strain states (and estimate the strength) of composite joints transferring large concentrated forces.

3.3.1. Joints with discrete bonds

Resolving a structure into components results in appearance of additional parts, an increase in weight, and a decrease in structure service life due to tendency to failure from fatigue under variable loads. The aircraft industry undertakes attempts to decrease the number of joints by introducing extruded panels, one-piece forged units, etc. However, this cannot "eradicate" joints because these are required due to many circumstances. On one hand, we must attach members made of diverse materials, envisage convenient installation/maintenance of assemblies; on the other hand, reasonable articulation simplifies production, makes a structure "more workable", and reduces manufacture costs.

There are a number of papers dealing with calculation of force distributions in bolted/rivetted joints, see, for example, contributions by P.A.Stepin [5], L.E.Jarfall [6]. Both elastic and elastoplastic formulations were studied. These investigations are usually to joints that may be considered as one-dimensional. In sophisticated assemblies such approach may prove not to be acceptable at all. Therefore, to analyze complex 3D bolted/rivetted joints, we suggest a method based on the following assumptions:

1) a structural material is elastic;

2) friction between parts is neglected;

3) in small-size areas various solutions may be superposed.

Of course, this approach at present has some disadvantages, since it does not "see" friction between sheets in a stack, does not account elastoplastic behavior of materials. None the less, it is quite suitable for strength evaluation and can be used to predict the service life.

In estimation of load-bearing capability of a joint, an important stage is determination of local stresses near fasteners; tensors may be computed by solving immediately the three-dimensional contact problem with correction for friction and plasticity -- this is a very difficult problem. However, the local stresses around fasteners may be assessed using the superposition principle. In so doing (see [6]), the local stresses are resolved into - stresses caused by a force "going around" a fastenerand - stresses transferred by a fastener (Fig. 3.14):

$$\sigma_{loc} = \alpha \ \beta \left(K_1 \frac{\Delta P}{dt} \theta_\sigma + K_2 \frac{P}{Wt} \right)$$

where K_1 the factor of concentration with respect to the nominal bearing stress from the force P, K_2 the concentration factor for a gross section loaded by the stress resultant getting around the fastener, d the hole diameter, t the sheet thickness, θ_σ the coefficient for taking into account the local increase in stresses that is due to deformation of the fastener, α the coefficient accounting for the hole condition (including the surface roughness, residual stresses from cold-work hardening, etc.), β the factor introduced to correct the result for interference between the fastener and the hole.

Values of coefficients K_1 and K_2 are to be taken from plots in [7]; the coefficients θ_σ, α, and β are usually obtained by experiment. When performing a qualitative estimation of a joint's concept, these coefficients may be set to 1.

Point-like links, such as rivets, bolts, and welding spots, are modelled by springs. In such an approach, various relations (within a general assumption of elasticity) between displacements of fastener points δ_p and the shear force P are used:

$$\delta_p = C \ P$$

C is a fastener compliance coefficient.

A large amount of theoretical and experimental studies were performed to evaluate the fastener compliance coefficients [9-11]. According to Rosenfeld [11], the compliance of a double-shear joint should be evaluated on the basis of a sum of displacements due to

- bearing of a stack (δ_{bs}),
- bending of a fastener (δ_{bf}), and
- shear of a fastener (δ_s):

$$\begin{aligned} \delta_{bs} &= P \left(\frac{1}{2 \ t_d E_b} + \frac{1}{t_p E_b} + \frac{1}{2 \ t_d E_d} + \frac{1}{t_p E_p} \right); \\ \delta_{bf} &= P \left(8t_d^3 + 16t_d^2 t_p + 8t_d t_p^2 + t_p^3 \right) / \left(192 E_b I_b \right); \\ \delta_s &= P \left(2t_d + t_p \right) / 6 G_b F_b . \end{aligned} \qquad (3.33)$$

Here, F_b is a fastener cross-sectional area, I_b is a fastener cross section moment of inertia, t denotes thicknesses of components; subscripts d, p and b are respectively for the side plate, the central plate, and the fastener.

Table 3.8 compares analytical compliances C_{an} and experimentally obtained values C_{ex}. The first group of three lines is for joints of steel parts. The fourth line is the joint in which a plate is made out of aluminum alloy [9]. The fifth line of Table 3.8 reports the theoretical compliance C_{an} and experimental data for a double-shear structure whose parts are made from acrylic plastic. Relative difference between analytical and experimental results evidences that these equations for computing the compliances can be recommended for practical analyses.

Note that this problem statement assumes that the bolt is represented by a single node in a finite-element mesh of each part in the build-up structure. This can lead to differing solutions to the problem on meshes with different numbers of nodes.

These circumstances have been a reason to conduct additional studies to evaluate how much the components of the main stress state (the forces transferred by bolts) are influenced by the singularity at the load application point when the bolt bond is approximated as a single point. The main stress state of a three-row bolted joint (Fig. 3.15a) was obtained on meshes differing in the discretization degree. Figure 3.15b demonstrates the results. Solid lines depict variation of the relative value of the force in the edge bolt, assuming zero compliance (**C**=0, rigid fasteners) and a real compliance (**C**$\neq$0, elastic fasteners); the finite-element meshes differ in a relative cell size l/d around the loaded point (here, l is the mesh step length). Shaded bands contain solutions obtained from finite-element meshes with n×n division with a multiple-point approximation of the bolt (nodes falling into the circle with a diameter equal to the bolt hole diameter approximate the bolt). From Fig. 3.15 it is seen that scatter in relative values of the force transferred by the edge bolt does not exceed 5%. If the fastener is approximated by a single point a solution with the same accuracy may be obtained by using a ratio l/d>1.8.

The present relations have been implemented in the FITING program package [12] for automatically computing the bolt/rivet compliance. The compliance calculation techniques are known to be subject to further improvement, therefore FITING incorporates options for immediately specifying the compliances C (for example, those obtained by means of [10]). The relation (3.33) has been derived assuming that a load distribution along a bolt in a double-shear joint is uniform. Nonuniformity of the load distribution for some types of joints is taken into account in formulas of [10]. The above superposition and the calculated general stress-strain states and force distributions were used to compute local stresses in the joint of Fig.3.16.

The structure is a butt joint of two aluminum wing panels reinforced by a quasi-isotropic composite doubler attached by steel screws to the panels and the internal flange. Due to symmetry the analysis covered a fourth part of the structure, including the left-hand half of the scheme in Fig. 16a. Bolt rows are numbered successively from 1 to 3 (Fig. 3.16f); relative forces P of the bolts are shown in Fig. 3.16b. Table 3.9 represents computed stresses at bolt holes in the skin and the doubler. It follows from the Table that maximum local stresses in the fastener zone are around screws 1-1 and 2-1. It has been in these areas that cracks appeared during fatigue testing.

Stress concentration factors are computed as

$$K_\sigma = {(\sigma_{loc})_{max}} / {\sigma_{gross}}$$

Here, **w** is a structural width, **d** is a screw diameter, **t** is a thickness; indices **s** and **d** are to the skin and the doubler.

Thus, the results of analyses of bolted/rivetted joints by the present technique are validated by experimental data from fatigue tests in respect of prediction of both the points and sequence of crack formation; hence, the technique is currently suitable for qualitative estimation, and further development is anticipated to improve it to quantitatively evaluate joints.

3.3.2. Joints with continuous bond

With advent of high performance adhesives and the corresponding assembly procedures the adhesive joints are more and more widely used in airframes. Perspectives are seen to utilize adhesives to mount high strength doubler for mitigating stress concentration in structures with cutouts; this undertaking may be envisaged both at a design stage and for strengthening the existing structures. However, the doublers can hamper visual inspection of main parts, thus not allowing operators to detect microcracks; therefore the analysis procedure is required to be accurate. The information available from the up-to-date literature is mainly to stresses in vertical cross sections, and stress profiles over horizontal planes are left without attention.

The present Section is an attempt to provide a tool for estimating the influence of an adhesive bonded doubler on elastic stresses along an edge of a circular cutout. Both a main plate and a doubler are assumed to be manufactured out of thin sheets and comply with plane stress state hypotheses of the theory of elasticity. In addition, we assume that the structure is subjected to inplane loads and does not buckle.

Let us subdivide the structure into substructures so that either the doubler as a whole or a part thereof be one substructure and the panel or a part thereof attached to the doubler be the other substructure. Each substructure is further resolved into finite elements.

Interaction of the plate with the bonded doubler may be accounted for by introducing the shear-tie elements shown in Fig. 3.17; these include compliances of both the adhesive and the flat components in the vertical section. By analogy with a tension rod the relation of nodal forces $\{T_{xi}, T_{xj}\}$ to Ox displacements $\{u_i, u_j\}$ may be written as

$$\begin{Bmatrix} T_{xi} \\ T_{xj} \end{Bmatrix} = C \begin{bmatrix} 1 & -1 \\ -1 & 1 \end{bmatrix} \begin{Bmatrix} u_i \\ u_j \end{Bmatrix} \tag{3.34}$$

In (3.34) the $1/C_i$ is a compliance coefficient which is meant as a mutual displacement of points in midplanes of panels and the doubler under the force T_j=1. The displacement of the doubler with respect to a panel may be described by the equation

$$u_j - u_i = \int_{a_n}^{a_3} \frac{\tau_{xz}}{G_p} dz + \int_{a_3}^{a_4} \frac{\tau_{xz}}{G_a} dz + \int_{a_4}^{a_5} \frac{\tau_{xz}}{G_d} dz ,$$

where $\tau_{xz} = T_{xz}/F_i$; a_n=a_1 for two-sided doublers, and a_n=a_2 for a doubler bonded on one surface; G_p, G_a, and G_d are shear moduli of the plate, the adhesive, and the doubler, respectively; F_i is the shear-tie element cross-section area (in the OXY plane).

We are allowed to assume that the shear stresses are maximum in the adhesive and vanish at free surfaces and at a plate symmetry plane in the case of two-sided doublers [12].

This shear stress distribution may be approximated by parabolas (Fig. 3.17) to give an estimate of the stiffness coefficient C_i:

$$C_i = \frac{F_i}{\frac{1}{3}\cdot\frac{t_p}{G_p} + \frac{t_a}{G_a} + \frac{11}{24}\cdot\frac{t_d}{G_d}}$$

for the two-sided reinforcement and

$$C_i = \frac{F_i}{\frac{t_a}{G_a} + \frac{11}{24}\cdot(\frac{t_p}{G_p} + \frac{t_d}{G_d})}$$

for the one-sided reinforcement. Here t_p , t_a and t_d are thicknesses of the plate, the adhesive, and the doubler, respectively. Shear in the OYZ plane can be accounted for in a similar way.

Summing the stiffnesses (3.34) up with the coefficients of the plate stiffness matrix and taking account of boundary displacement conditions, we derive a linear system of constitutive equations

$$\{R\} = [K^*]\{\delta\} \tag{3.35}$$

for the joint; $\{R\}$ and $\{\delta\}$ are vectors of nodal forces and displacements, respectively; $[K]$ is the stiffness matrix.

Thereafter the shear stresses in the adhesive layer are

$$\tau_a = \sqrt{\tau_{xz}^2 + \tau_{yz}^2}$$

where

$$\tau_{xz} = \frac{C_i}{F_i}(u_j - u_i), \qquad \tau_{yz} = \frac{C_i}{F_i}(v_j - v_i),$$

u_i and v_i are displacement of the plate and the doubler along the OX and OY axis.

Figure 3.18 shows a finite-element model of a plate with adhesive bonded doublers and a central transverse crack. Due to symmetry with respect to the OX axis the analysis addressed a half of the structure. The plate, doubler and adhesive layer have meshes with quadrilateral elements with linear approximation of displacements. The plate is assumed to be manufactured out of a 3.2 mm thick aluminum material. The composite doubler is from 0.1 mm dia. boron fibers with epoxy resin binder. The adhesive thickness is 0.1 mm. Elastic constants for the aluminum alloy are the elastic modulus E of 68.4 GPa and the Poisson's ratio μ=0.318; boron fibers: E_1=197, E_2=14.5, G=5.22 GPa, μ_1=0.168, μ_2=0.0124; adhesive: E=1.9 GPa, μ=0.35.

Figure 3.19 represents distribution of strain ε_x along the line {y=0} in the plate and the doubler; data from strain gauges bonded to the external surfaces of the plate and doubler are given for comparison's sake. The results evidence the rather high accuracy of the computation method for determining strain fields in similar structures and estimating the stress intensity factor.

Figure 3.20 demonstrates the influence of the composite doubler thickness and layup pattern on the stress intensity factor K_I in the plate with a central transverse crack. The fracture mechanics solves problems with arbitrarily oriented through cracks by using the virtual growth method [13]; according thereto, the mode I (opening mode) and II (sliding mode) stress intensity factors K_I and K_{II}, respectively, are computed as

$$\frac{1}{E}\left(\left(K_I^2 + K_{II}^2\right)\cos\theta - 2K_I K_{II}\sin\theta\right) = -\frac{1}{2}\{\delta\}^T \frac{\partial[K]}{\partial s}\{\delta\} \qquad (3.36)$$

by changing the crack tip position (along the crack path) by a length s and turning the tip through the angle θ. In (3.36) E is an elastic modulus, [K] is the structure stiffness matrix, $\{\delta\}$ is the nodal displacement vector. The structure is modeled with triangular simplex elements; errors depend on element size, see estimates in [13]. From Fig. 3.20 it is clear that the doubler notably affects the stress intensity factor K_I: the doubler with a relative thickness of 0.0625 reduces K_I by a factor of almost three.

Generally, a composite doubler may comprise several layers, each with its own direction of orthogonal principal axes; elastic constants of a doubler can be determined from relations of [8]. Various layups (see Fig. 3.20) provide almost identical effects. But the $\left[0/\pm 45^\circ\right]\|$ and $\left[0/\pm 90^\circ\right]\|$ layups have better characteristics in the transverse direction, so these patterns are recommended for use. It is known that layers in composite materials may delaminate; therefore, such repair on an aircraft should for reliability be finished with riveting a doubler. Figure 3.21a shows how the stress intensity factor K_I in a transversely cracked plate reinforced with a composite doubler depends on the doubler thickness. Three types of joint are considered: adhesive, riveted, and riveted with adhesive. A rivet diameter of 3 mm is selected so as to ensure an equally strong joint. Rivets are shown by circles. From the Figure it is clear that a riveted joint is less efficient than adhesive bond; rivets in addition to adhesive do not almost reduce the stress intensity factor. Figure 3.21b compares efficiencies of doublers made of a composite material, aluminum, and steel. The most notable reduction of the stress intensity factor is attained with the steel doubler. The composite doubler is slightly less efficient, and the aluminum one greatly weaker. Dashed lines demonstrate variation of the doubler mass M as a function of a doubler thickness. As to the structural weight saving concern, the composite doublers should be preferred.

3.3.3. Allowance for three-dimensional features in joints

Applicability of theory of elasticity methods to investigation into structural behavior was significantly augmented recent years due to development in numerical analysis techniques which allow geometry of structures to be described quite fairly; also, increased memory/FLOPS capabilities of computers allow researchers to effectively employ the FEM when concerning with contact problems in 2D and 3D.

The constitutive equation of the assumed displacement method for a discretized domain ω, based on minimization of the Lagrangian functional, is

$$[K]\{\delta\} = \{R\} \tag{3.37}$$

using a nodal displacement vector $\{\delta\}$, an external load vector $\{R\}$, and a structure stiffness matrix $[K]$. For solving system (3.37), one should specify for a part of the domain ω the boundary displacement conditions (or "kinematic" boundary conditions)

$$\delta = U_0 \tag{3.38}$$

Let us consider two bodies of arbitrary shapes (i and j are indices to identify the bodies) in Cartesian coordinate system XOY (Fig. 3.22).

Let S_{ic} and S_{jc} be assumed surfaces of contact, i.e. those portions of the bodies i and j which are close to each other and have points which can interact. Assume that the surface S_{ic} at every point C_{ik} (k is a point number, k=1, 2, ...) has an outward normal n_{ik} which intercepts the surface S_{jc} at the point C_{jk}. Such points C_{ik} and C_{jk} will be referred to as conjugate points. As noted in [14], conjugation of points can only be determined with a fair degree of accuracy before solving the problem in case of an obvious pattern of contact deformation. Otherwise, the contact area will be outlined after operation of an algorithm based on criteria of mutual non-penetration of bodies. Introduce radius vectors $r_{ik}$and r_{jk} to identify initial positions of the points C_{ik} and C_{jk}, respectively (Fig. 3.14). After loading, the positions of these points in the plane will be defined by the relations

$$\begin{aligned} \{r_{ik}\} &= \{r_{oi}\} + \{\delta_{ik}\} \\ \{r_{jk}\} &= \{r_{oj}\} + \{\delta_{jk}\} \end{aligned} \tag{3.39}$$

where $\{\delta_{ik}\}$ and $\{\delta_{jk}\}$ are displacement vectors of the conjugate points.

The criterion of contact of the points C_{ik} and C_{jk} can be written as

$$(\{r_{ik}\} - \{r_{jk}\}) \cdot \{n_k\} = 0 \big|_{C_{ik} \in S_{ic}} \tag{3.40}$$

where S_c is a contact surface.

Considering eqs. (3.39), from relations (3.40) we obtain a compatibility condition:

$$(\{r_{ik}\} - \{r_{jk}\}) \cdot \{n_k\} = (\{\delta_{jk}\} - \{\delta_{ik}\}) \cdot \{n_k\} \big|_{C_{ik} \in S_c} \tag{3.41}$$

For conjugate non-contacting points the following condition should hold:

$$(\{r_{ik}\} - \{r_{jk}\}) \cdot \{n_k\} =< 0 \big|_{C_{ik} \in S_c} \tag{3.42}$$

which, in essence, expresses the condition of mutual non-penetration of bodies. In the projection on the normal n_{ik} the condition (3) will be written as

$$\delta_{ik}^{(n)} + \delta_{o}^{(n)} = \delta_{jk}^{(n)} \tag{3.43}$$

where $\delta_{ik}^{(n)}$ and $\delta_{jk}^{(n)}$ are displacements of conjugate points of the bodies i and j along the outward normal; $\delta_{o}^{(n)}$ is the initial interference (the minus sign in (3.43), or gap, the plus sign) between conjugate points as measured along the normal n_{ik}.

The equations of equilibrium of isolated bodies i and j (with no contact between them) in the matrix notation are

$$\begin{bmatrix} K_{i11} & K_{i12} \\ K_{i21} & K_{i22} \end{bmatrix} \begin{Bmatrix} \delta_{i1} \\ \delta_{i2} \end{Bmatrix} = \begin{Bmatrix} P_i \\ Q_i \end{Bmatrix}$$

$$\begin{bmatrix} K_{j11} & K_{j12} \\ K_{j21} & K_{j22} \end{bmatrix} \begin{Bmatrix} \delta_{j1} \\ \delta_{j2} \end{Bmatrix} = \begin{Bmatrix} P_j \\ Q_j \end{Bmatrix} \tag{3.44}$$

where δ_{i1} and δ_{j1} are displacements of the nodes that do not touch each other; δ_{i2} and δ_{j2} are displacements of the conjugate nodes; P_i and P_j are prescribed external forces; Q_i and Q_j are contact interaction forces to be sought for. We may perform the Gaussian elimination to write eq. (3.44) in terms of the unknown displacements of the contacting nodes:

$$\left[K_i^*\right]\{\delta_i\} = \{R_i\}$$

$$\left[K_j^*\right]\{\delta_j\} = \{R_j\} \tag{3.45}$$

where

$$\left[K_i^*\right] = \left[K_{i22} - K_{i21}K_{i11}^{-1}K_{i12}\right]$$

$$\left[K_j^*\right] = \left[K_{j22} - K_{j21}K_{j11}^{-1}K_{j12}\right]$$

$$\left[R_i^*\right] = \left[Q_i - K_{i12}K_{i11}^{-1}P_i\right]$$

$$\left[R_j^*\right] = \left[Q_j - K_{j12}K_{j11}^{-1}P_j\right] \tag{3.46}$$

Assume that between *k*-th conjugate nodes of the *i*-th and *j*-th substructures a link exists that, in a local coordinate system, may be expressed as

$$[\gamma]\begin{Bmatrix} \delta_{ik} \\ \delta_{jk} \end{Bmatrix} = \begin{Bmatrix} Q_{ik} \\ Q_{jk} \end{Bmatrix} \tag{3.47}$$

where

$$\{\gamma\} = \begin{bmatrix} [C] & -[C] \\ -[C] & [C] \end{bmatrix} \tag{3.48}$$

δ_{ik} and δ_{jk} are displacements, Q_{ik} and Q_{jk} are contact forces acting on these conjugate nodes.

In two-dimensional problems,

$$[C] = \begin{bmatrix} C_n & 0 \\ 0 & C_\xi \end{bmatrix}$$

and in 3D ones,

$$[C] = \begin{bmatrix} C_n & 0 & 0 \\ 0 & C_\xi & 0 \\ 0 & 0 & C_\eta \end{bmatrix} \tag{3.49}$$

where C_n, C_ξ and C_η are stiffnesses of the links as considered in the local system.

Let $[\lambda]$ be a direction cosine matrix that relates the local system $\{n, \xi, \eta\}$ to the global one {x, y, z}.

By summing eqs. (3.45) and (3.46), obtain equilibrium equations for the bodies:

$$\begin{bmatrix} [K_i^*] + [\gamma^o] & -[\gamma^o] \\ -[\gamma^o] & [K_j^*] + [\gamma^o] \end{bmatrix} \begin{Bmatrix} \delta_i \\ \delta_j \end{Bmatrix} = \begin{Bmatrix} R_i \\ R_j \end{Bmatrix} \tag{3.50}$$

Coefficients of the matrix $[\gamma^0]$ characterize the link stiffnesses in the global coordinate system; they are

$$[\gamma_{kij}] = [\lambda]^T [C][\lambda] \tag{3.51}$$

If the structure is subjected to interference (quantified by a vector $\{\delta_o\}$), one should add to the right-hand side of eq. (3.45) the component

$$\{R_o\} = [K_i]\{\delta_o\} \tag{3.52}$$

If the bodies under study do not touch each other ($[\gamma^o]=0$) the relations (3.50) transform:

$$\begin{bmatrix} [K_i^*] & 0 \\ 0 & [K_j^*] \end{bmatrix} \begin{Bmatrix} \delta_i \\ \delta_j \end{Bmatrix} = \begin{Bmatrix} -[K_{i11}]^{-1}\{P_i\} \\ -[K_{j11}]^{-1}\{P_{ji}\} \end{Bmatrix} \tag{3.53}$$

They can be resolved with respect to unknowns $\{\delta_i\}$ and $\{\delta_j\}$.

Of course, we assume here the general case – the body i is in contact with the body j. The set of simultaneous equations (3.50) would be solved using the following algorithm:

1. Specify preliminarily the contact nodes, assign the stiffness matrix $[C_{ik}]$.
2. Prepare the direction cosine matrix $[\lambda]$.
3. Compute the stiffness matrices for substructures and the right-hand side vectors according to (3.44).
4. Transform eqs. (3.44) to equilibrium equations for contact nodes by using the Gaussian elimination procedure.
5. Employ (3.43) to determine the interference δ_R (along the normal)

$$\delta_R = \delta_j^n - \delta_i^n - \delta_o$$

6. Compute the forces R applied to the substructure i because of the interference δ_R:

$R=[Ki]\{\delta_R\}$;

this vector must then be added to the prescribed external load vector of the substructure under consideration.

7. Use relations (3.51) to transform the link stiffness matrices to the global coordinate system; add these matrices to the structure stiffness matrix (3.50).
8. Use (3.50) to determine displacements of contact nodes $\{\delta_i\}$ and $\{\delta_j\}$.
9. Determine the contact forces along normals by using relations (3.52):

$$Q_k = C_k \lambda(\delta_{kj} - \delta_{kj}) \tag{3.54}$$

10. Analyze the non-penetration criterion (3.42). Go to the item 11 below if eq. (3.42) is satisfied, otherwise repeat the solution from the item 5.
11. Finish evaluating the displacements of contact nodes; carry on with usual procedures of the Finite Element Method.

The above algorithm is not difficult to use to take account of friction forces Q_{fr} on the contacting surfaces: after the item 9 these forces may be estimated by

$$Q_{fr} = -\mu_f \times \text{sign}|\delta_\xi| Q_k \tag{3.55}$$

(here μ_f is a friction coefficient, δ_ξ is a displacement along a ξ axis), then added to the load vector. However, such approach need be validated by treating realistic problems.

The present technique for contact problems is a simplified means, since the constitutive equations (3.50) incorporate complementary stiffnesses described by eqs. (3.49). The normal component C_n models a contact layer. Tangential components C_ξ and C_η seem to be useful for modelling the friction forces and/or for simulating behavior of adhesives, etc.

It is clear from eq. (3.54) that the C_n should be specified at a relatively high level, so that the difference of displacements be small as compared to each of the displacements. On the other hand, after specifying too large a C_n, we will suffer from the round-off errors not allowing the contact forces Q_{ic} to be determined accurately. The required value of C_n was estimated by means of parametric studies. Consideration was given to interaction of two clamped plates of uniform thickness t=1 made of a material with a Young modulus E=1 and Poisson's ratio μ=0.3 (Fig. 3.23). The geometric size of the plate i along the 0X axis exceeds that of the plate j by a magnitude of interference δ_0=2. For simplicity's sake the example involves dimensionless characteristics. The interference above causes uniform stresses $\sigma_{x,exact}$=-0.1. In the present analysis each of the plates is modelled with simplex finite elements with type 5x5 meshes. The parameter C_n is parameterized by the equation $C_n=E\times10^N$ where N is assumed to be varied from 1 to 12. Figure 3.23 represents the calculated stresses as a function of the parameter N. This plot shows that two true digits in stresses are ensured by N equal to 2 thru 8, with the best results corresponding to N from 4 to 6.

3.3.4. Some results of computational analyses

Figure 3.24a depicts a mesh of a cylinder with two pistons which apply a force P=60 kN; this combination models a power cylinder of a commonly used booster (Fig. 3.24b). The model is composed of simplex axisymmetric triangular elements. The total number of unknown displacements is 1298; the contact problem is limited to investigation of 44 displacements of nodes on the contact surface. Axial stresses σ_x on the internal and external surfaces of the cylinder are shown in Fig. 3.24c; they are compared to the test data got from strain gauges of 5 mm gauge length.

Consider interaction of a usual lug with a bolt (Fig. 3.25). Both the bolt and the lug are modelled by tetrahedrons. Symmetry allows us to treat a one-fourth of the global model; the lug is covered by 500 nodes, and the bolt, by 684 nodes. The total number of displacements to be found is 3552. The load σ=74 MPa is applied to a lug section at X=0 and is transferred to the bolt that outstands from the lug as far as half a lug thickness. We assume that the bolt is separated from the lug by a gap $\delta=0.05(1-\cos\theta)$. Figure 3.25 represents the contact stresses as a function of the angle θ in the lug sections at Z=0 (a "middle section") and Z=40 mm (a "limiting section"). These stresses are compared to the results of [3.15] for a two-dimensional problem. It is seen that the data differ not only in values but in trends. The minimum contact-stresses are in the middle section, and the maximum ones are seen on edges of the lug hole; this indicates the bolt being deformed in the 0XZ plane.

The other example is the propfan blade root loaded with stresses due to inertia of a blade. Currently, our design bureaus develop spar-based constructions (Fig. 3.26). Such a concept provide weight savings and is very reliable in service. It includes a structurally significant item — the root where a polymer matrix composite is coupled with a metallic fitting. A schematic of the model is depicted in Fig. 3.27.

The fitting is made of 40KhNMA steel with E=210000 MPa and μ=0.3. The VPS-20 composite utilized in the blade has a radial Young modulus E_1=20000 MPa, an axial modulus E_2=46000 MPa and a tangential modulus E_3=12000 MPa; the shear modulus is G=3600 MPa, and Poisson's ratios are μ_{12}=0.27, μ_{23}=0.25 and μ_{31}=0.25.

The model in Fig. 3.28 comprises 11 substructures with a total number of unknown displacements of 2556. The structure was subjected to axial tension caused by the blade body forces. In the course of analyses the load was incremented by steps of 100000 N from 100000 to 400000 N, and the domain of contact between the root fitting and the composite part was outlined; the interaction force was evaluated. Friction between the parts was assumed not to exist. Analyses showed that the contact domain does not alter over the whole of the load range; the number of iterations for outlining the contact domain (with a load fixed) was 4 at the first step and 2 at the last step.

Figure 3.29 compares radial interferences (a solid line) with test data (Table 3.10) received from dial indicators (Fig. 3.30) measuring the diameters of certain cross sections under the applied load of 200000 N.

For an article with a thin rubber layer the results agree well. The dashed line in Fig. 3.29 depicts the radial interferences obtained by analysis for an article where the composite and the fitting are assumed to be adhesive bonded. Figure 3.31 shows axial profiles of internal longitudinal forces in the two structural components.

Table 3.11 represents verification of equilibrium conditions for contact force projections on the main axis:

$$P = \sum_{i=1}^{n} N_i \sin\alpha_i$$

where P the axial load applied to the unit, n the number of contact nodes, N_i the contact interaction force in a node i, α_i the angle of slope of a collar at a node i (measured from the main axis).

The maximum tensile stresses in the composite part are seen on the external surface near the fourth collar of the fitting. At a root of this collar, but in the fitting, one can see significant axial normal stresses of 200 MPa.

Structural concepts of joints with composite parts are very diverse, depending on both the application area and the manufacturing process. In particular, concentrated loads from metal parts may be transferred to composite panels by means of joints demonstrated in Fig. 3.32.

The concentrated load P is transferred via a steel bolt (4) with the aid of the metal bushing (2) to the composite panel (1). The bushing (2) comprises two parts that are screwed and cemented to the panel at the outer surface.

The bolt and the bushing are made out of steel with the Young's modulus E=2000 GPa and the Poisson's ratio μ=0.3. The panel material has the following characteristics:

E_x=50 GPa, E_y=16 GPa, E_z=20 GPa, G_{xy}=5.2 GPa, G_{yz}=0.8 GPa, G_{zx}=0.8 GPa, μ_{xy}=0.27, μ_{yx}=0.23, μ_{zx}=0.23.

The analysis of the symmetric structure was limited to two octants: XOYZ and (-X)OYZ (Fig. 3.32). Kinematic boundary conditions relevant to the symmetry were specified; in addition, the left-hand edge of the panel was fixed. The load P/2 was applied as a distributed shear stress τ=P/2F at the upper plane of the bolt (F is the bolt sectional area). The analytical model comprised five substructures with the total number of unknown displacement being equal to 5961. Three versions were considered. In the first, the panel hole and the bushing were assumed not to be bonded with adhesive, so their surfaces contact freely, with no friction. In the second version, the bushing was assumed to be cemented to the panel by a no more than 0.1 mm thick adhesive layer whose elastic modulus is 2.5 GPa. In the third version a steel panel (E=200 GPa and μ=0.3) with no adhesive was addressed.

The contact area was outlined, and the negative pressure condition met, for 5 iterations in the first and third cases and for four in the second case.

Figure 3.33 presents tangential stresses over the internal surface of the bolt hole; these are referred to the bearing stress σ_b=P/td (where t is the panel thickness and d is a hole diameter) and compared to stresses in a similar structure in which all parts are made of steel. The external load is such that σ_b=200 MPa. From the pressure profiles it is seen that orthotropy of the composite material makes the stresses more nonuniform along both the circumference and the bushing axis (sections A and B); the circumferential stresses in the composite part are increased by a factor of 1.65 as compared with metal. If the bushing and the composite part are coupled with an adhesive with high elastic properties (the shear modulus G_a=2500 MPa) then the circumferential stresses over the composite surface get notably reduced (versions 1 and 2 in Fig. 3.33).

Consider a plate loaded with two tension forces P applied via two bolts (Fig.3.34). The real structure is a 180 by 48 by 2 mm plate made out of KMU-4E composite with the [0/45/90] layup. It has two 12-mm holes wherein the steel bolts are inserted to apply the external forces P.

The bolts are torqued (via nuts laid on washers) to a moment M that generates an internal tension force Q. In experiments, three cases of fracture of the specimen loaded with Q=0, Q=17500 N, and Q=35000 N were considered. Bolts were made of 30KhGSA steel with the modulus of elasticity E=200 GPa and the Poisson's ratio μ=0.3. The plate is composite:

E_1=60 GPa, E_2=60 GPa, E_3=60 GPa, G_{12}=14 GPa, G_{23}=14 GPa, G_{31}=14 GPa, μ_{12}=0.35, μ_{23}=0.35, μ_{31}=0.15.

The analytical model, due to symmetry, was 1/8 of the entire structureand consisted of three substructures: one modeled the bolt and the other two substructures represented the composite plate. The total number of nodes was 800; the number of displacements, 2400; and in contact were 204 nodes.

Figure 3.34 shows dependence of the maximum plate tangential stress σ_θ on the force P at the friction coefficient μ_f=0.15. It is easily seen that increasing the clamp-up force Q reduces the stress σ_θ. If one knows the allowable stress [σ] (from Fig.3.34) then Fig.3.35 may be used to determine the ultimate tensile force [P].

Taking into account instability of properties of composites, the ultimate forces in Fig. 3.35 are given for two values of allowable stresses: [σ]=333 MPa and [σ]=400 MPa. Also, ultimate forces P obtained in experiments are shown. The experimental values in Fig. 3.35 are seen to be in good agreement with stresses computed at [σ]=400 MPa.

Figure 3.36 demonstrates variation of the maximum tangential stress σ_θ as a function of the friction coefficient at fixed values of the clamp-up force Q (17,500 N) and the external load P (11,250 N). Increasing the friction coefficient reduces the stress, and the maximum value turns out to be at deeper points of the plate.

4. Conclusion

In compliance with NCCW-73 specifications the TsAGI and MGATU have fulfilled a research work in two areas: "Analysis of postbuckling behavior of composite panels" and "Development of general model of joints in composite structures".

The following major results have been provided:

- a theoretical solution to the problem on postbuckling behavior of a composite plate under multiaxial load in the case when a wave type can change over in the course of postbuckling deformation;
- relations that describe (1) stiffness reduction coefficients for a buckled skin in a stiffened composite panel and (2) load-bearing capability of the panel under biaxial compression and shear;
- a method to analyze the commonly used types of adhesive bond areas in composite structures, assuming that the adhesive layer behaves linearly;
- a model for analyzing irregular adhesive/fastener joints in composite structures; some joints were analyzed by using finite element methods.

Proceeding from objectives of the Cooperative Agreement NCCW-73, work status and technical appropriateness, we propose the research to be extended to cover the following problem areas:

- allowance for temperature difference between stiffeners and skin; estimating the influence of the difference and the related thermal strains and stresses on postbuckling behavior, skin reduction factors and load-carrying capability of stiffened composite panels;
- account of thermal effects and a real nonlinear stress-strain relation for an adhesive layer -- analytical and finite-element models of joints in composite structures;
- parametric analyses of composite structures and their joints — comparing various methods to estimate the accuracy and applicability areas thereof and the structural parameters.

A schematic and the assumed dates of the new work package are represented in Fig.3.37. Researchers (i.e., TsAGI and MGATU) and the general direction of the studies are as before.

5. References

For part 1.

1. Vol'mir A.S. Flexible plates and shells. - GITTL, Moscow, 1956.

2. Bubnov I.G. Ship skin stresses under the water pressure. - 1902.

3. Karman Th., Sechler E.E., Donnel L.H., The strength of thin plates in compression, Trans. ASME no.54, 1932.

4. Timoschenko S., Theory of elastic stability, N.-Y., 1936.

5. Marguerre K., Die mittragende Breite der gedruckten Platte, Luftfahrtforschung, 14, Nr.3, 1937.

6. Lahde R., Wagner H., Versuche zur Ermittlung des Spannungszustandes von Zugfeldern, Luftfahrtforschung, 13, Nr.8, 1936.

7. Papkovich P.F. Ship structural mechanics, Part 2. - Sudpromgiz, Leningrad, 1939.

8. Bleich F., Buckling strength of metal structures, N.-Y., McGraw-Hill Book Company, 1952.

9. Kuhn P., Stresses in aircraft and shell structures, N.-Y., McGraw-Hill Book Company, 1956.

10. Stein M., Postbuckling of orthotropic composite plates loaded in compression, AIAA Journal, Vol.21, no.12, 1983.

11. Starnes J.H., Dickson J.N., Rouse M., Postbuckling behavior of graphite-epoxy panels, ACEE composite structures technology conference, Seattle, USA, 1984.

12. Nemeth M.P., Importance of anisotropy in buckling of compression-loaded symmetric composite plates, AIAA Journal, Vol.24, no.11, 1986.

13. Lekhnitsky S.G. Anisotropic plates. - Gostekhizdat, Moscow, 1947.

14. Vasiliev V.V., Mechanics of Composite Structures, Washington, Tailor and Francis, 1993.

15. Alfutov N.A., Zinov'yev P.A., Popov B.G. Analysis of multilayered plates and shells made out of composite materials. Mashinostroyeniye, 1984.

16. Vasiliev V.V., Voytkov N.I. Stability of laminated orthotropic plates loaded in compression along one and two axes. - In: "Design, analysis and testing of composite structures", issue VIII, TsAGI, 1981.

17. Voyevodin V.V., Kuznetsov Yu.A. Matrices and computation. - Nauka, Moscow, 1984.

18. Vasiliev V.V., Azikov N.S., Salov V.A., Thin-walled composite panels - applied theory, Experiments, 33rd International SAMPE symposium and Exhibition, Anaheim, California, USA, 7 - 10 March 1988.

19. Yevstratov A.A. On finite-difference study of behaviour of flexible plates. - Izvestiya Vysshikh Uchebnykh Zavedeniy, "Building and architecture", no. 5, 1977.

20. Banks W.M., Harvey J.M., Experimental study of stability problems in composite materials, Stab. Probl. Eng. Struct. and Components, London, 1979.

21. Zamula G.N. Numerical analysis of thin-walled structure with a buckled skin. - WCCM-II Lecture, Stuttgart, 27 - 31 August, 1990.

22. Zamula G.N., Ierusalimsky K.M. Method for reducing the buckled skin under multiaxial loads. - Uchenyye Zapiski TsAGI, vol. 20, no. 6, 1989.

For part 2.

1. N.K.Snitko, Structural Mechanics. - Vysshaya Shkola, Moscow, 1972.

2. P.F.Papkovich, Theory of Elasticity. - Oborongiz, Moscow, 1939.

3. N.I.Bezukhov, Theory of Elasticity and Plasticity. - Gostekhizdat, Moscow, 1953.

4. V.F.Kut'inov, Stresses in adhesive-bonded built-up plate. - Trudy TsAGI, no. 2063, 1980.

5. Stepin P.V. On Analysis of Shear Stresses in Assemblies with Continuous Joints. - Vestnik inzhenerov i tekhnikov, no. 4, 1951.

6. Jarfall L. Optimum Design of Joints: the Stress Severity Factor Concept. - In: Aircraft Fatigue, Design, Operational and Economic Aspects, pp. 49 - 63, 1972.

7. Peterson R.E. Stress Concentrasion Factors. J.Wiley & Sons, Ney York . London . Sydey . Toronto, 1974.

8. Lekhnitsky S.G. Theory of Elasticity for Anisotropic Bodies. Nauka, Moscow, 1977.

9. Fayerberg I.I., Rubina A.L. Distribution of Forces Across Bolts in a Butt Joint with Inelastic Stresses. - Trudy TsAGI, 25 p., 1950.

10. Barrois W. Stresses and Displacements due to Load Transfer by Fasteners in Structural Assemblies. - Engng Fract. Mech., v. 10, no. 1, 1978.

11. Rosenfeld S. Analytical and Experimental Investigation of Bolted Joints. - NACA TN 1458, 1947.

12. Grishin V.I., Begeyev T.K. Stress Intensity Factors for a Plate with a Central Transverse Crack Reinforced with Composite Doublers. - Mekhanika kompozitnykh materialov, Riga, no. 4, pp. 696 - 700, 1986.

13. Grishin V.I., Donchenko V.Yu. On Study of Stress Intensity Factors for Structures with Curved Cracks. - Uchenyye Zapiski TsAGI, vol. 14, no. 2, pp. 105 - 112, 1983.

14. Iosilevich G.B. Concentration of Stresses and Strains in Machine Parts. - Mashinostroyeniye, Moscow, 1981.

15. Lee B.C., Kwak B.M. A Computational Method for Elastic-Plastic Contact Problems. - Int. J. Computers and Structures, vol. 18, No. 5, 1984.

APPENDIX

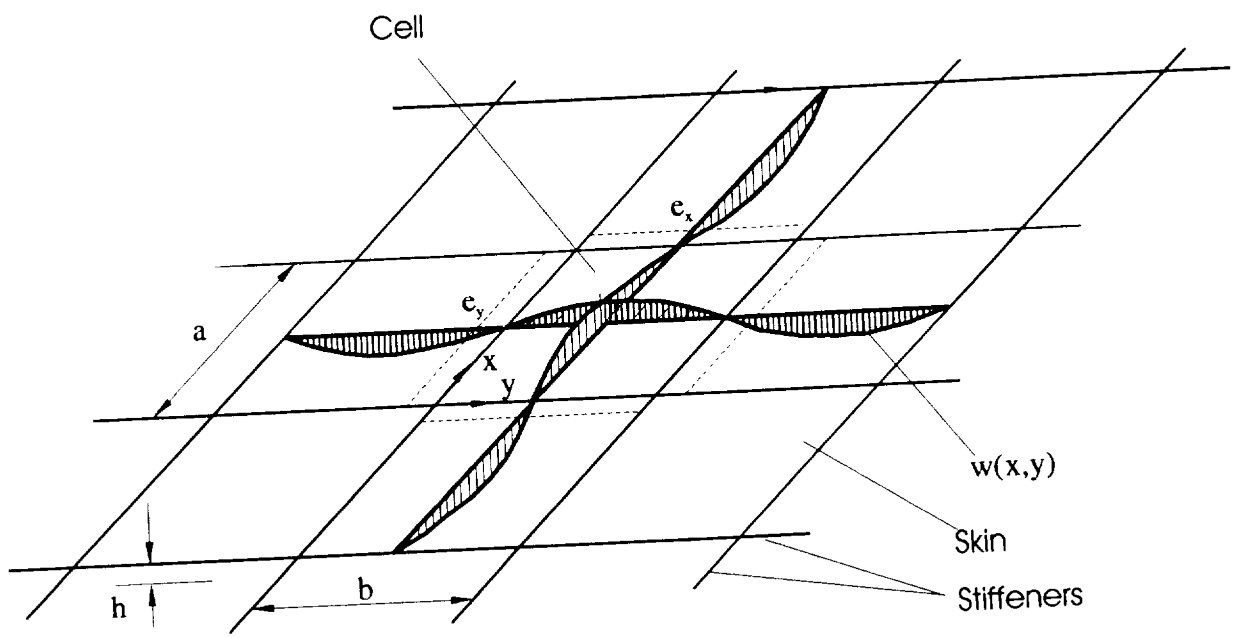

Figure 2.1. Stiffened composite panel

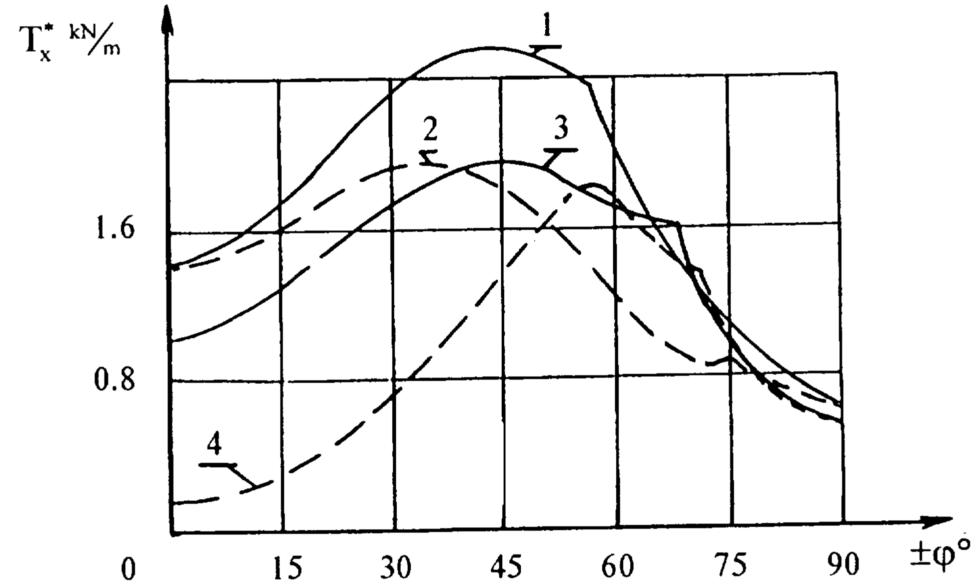

Figure 2.2. Critical stress resultants for compression-loaded composite plate with freely moving and fixed edges 1 and 2; critical stress resultants in the case of proportional loading 3 and 4

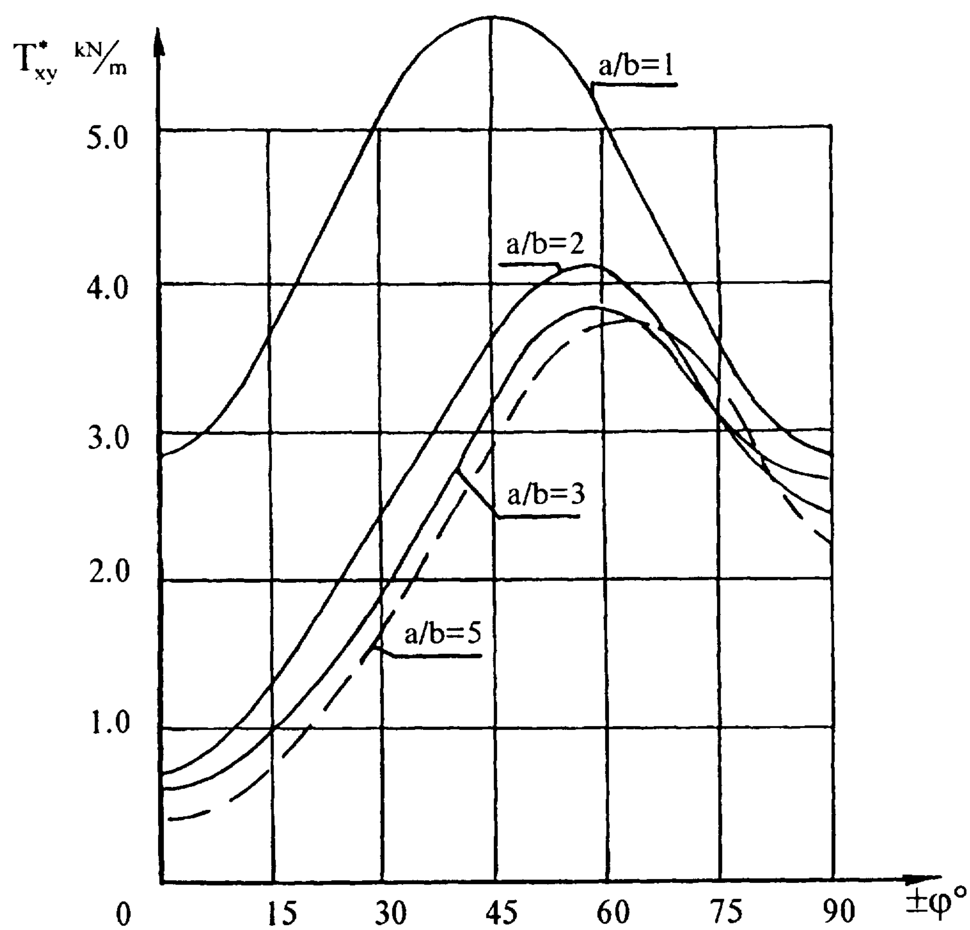

Figure 2.3. Critical shear stress resultants for CFRP plate

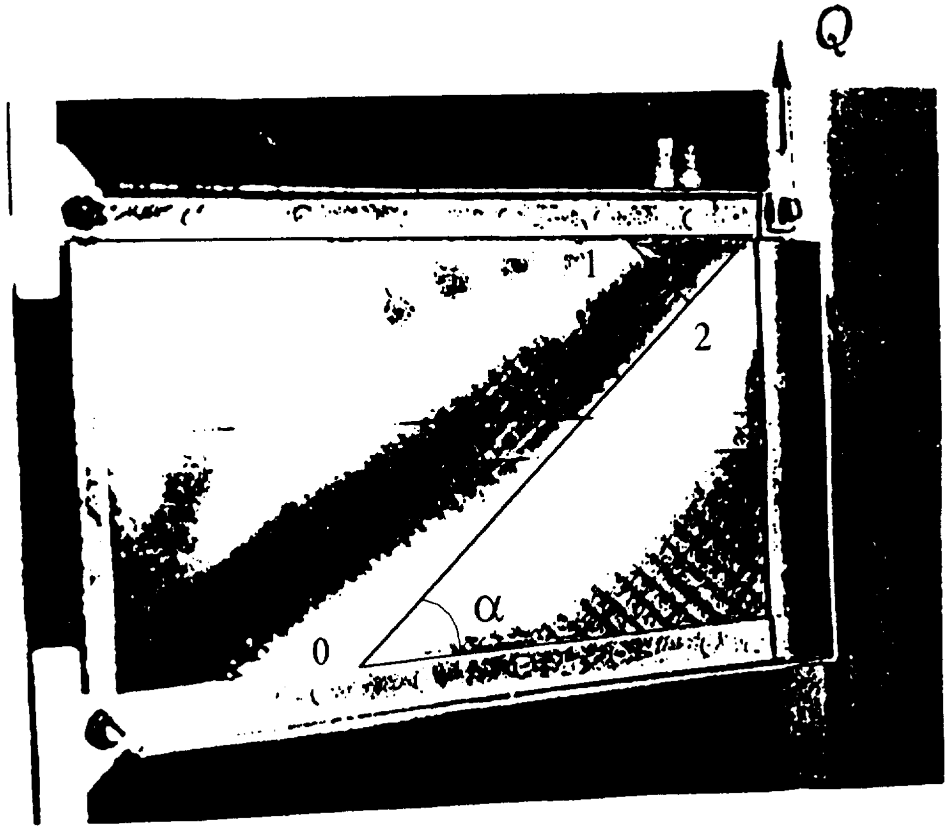

Figure 2.4. Postbuckling plate surface shape

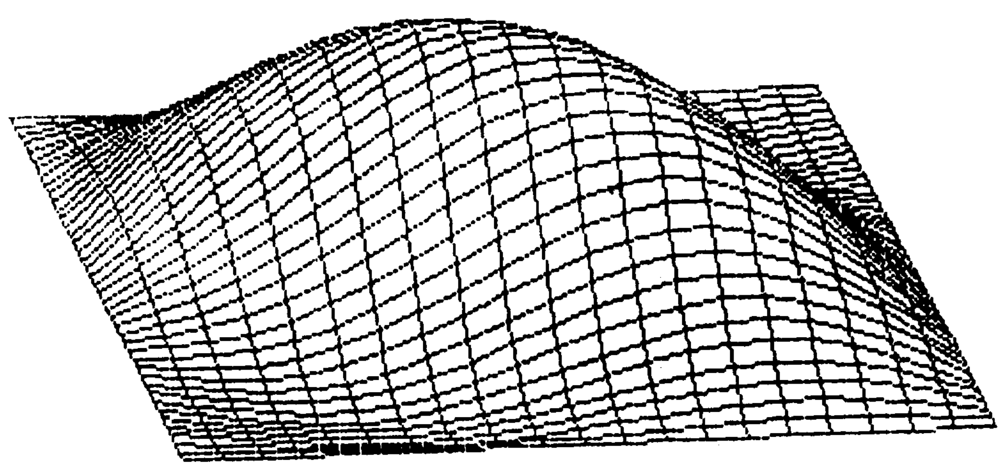

Figure 2.5. Natural mode shape of CFRP plate

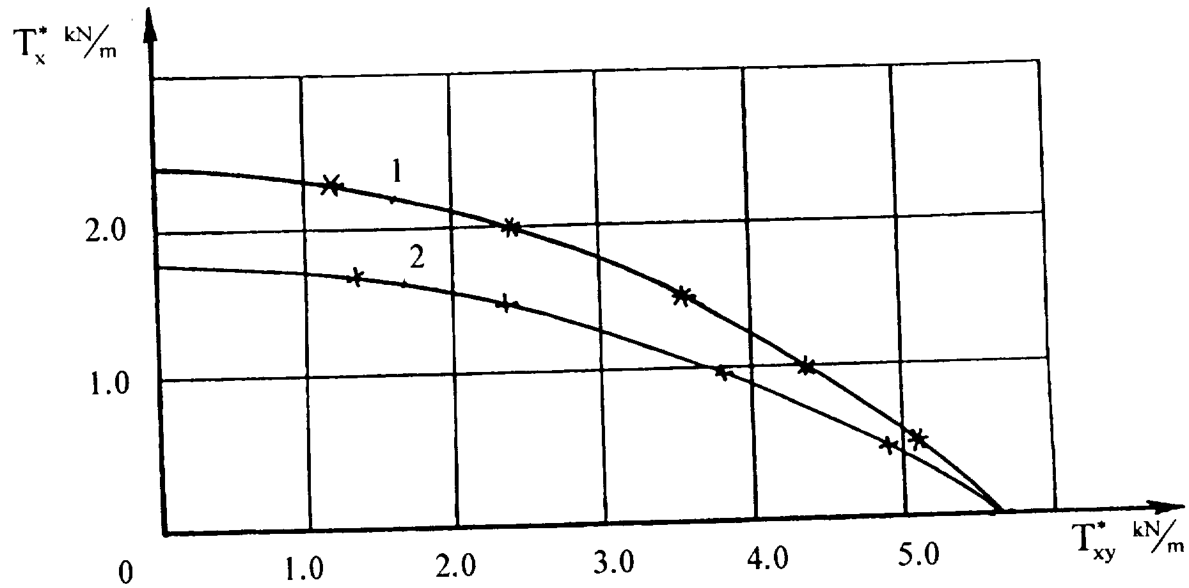

Figure 2.6. "Equal stability" lines for composite plate with (1) freely moving and (2) fixed longitudinal edges

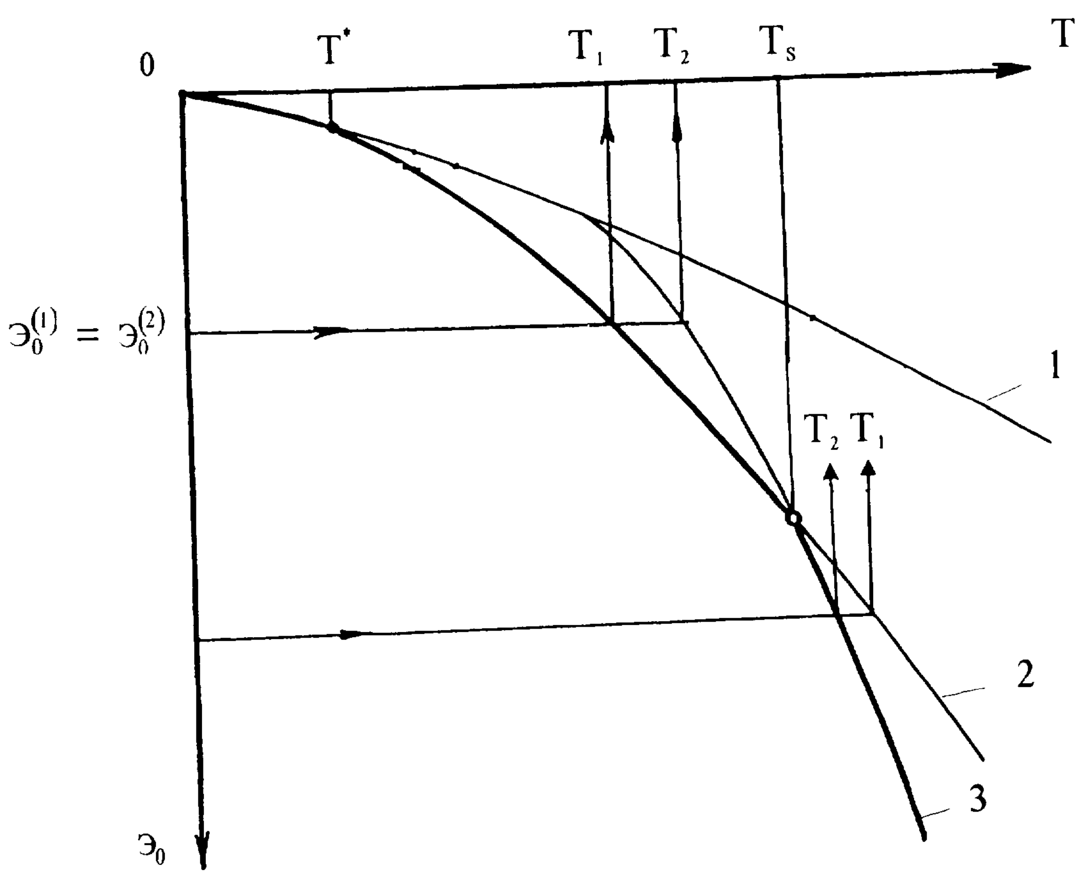

Figure 2.7. Total potential energy corresponding to plate equilibrium modes, as a function of stress resultants

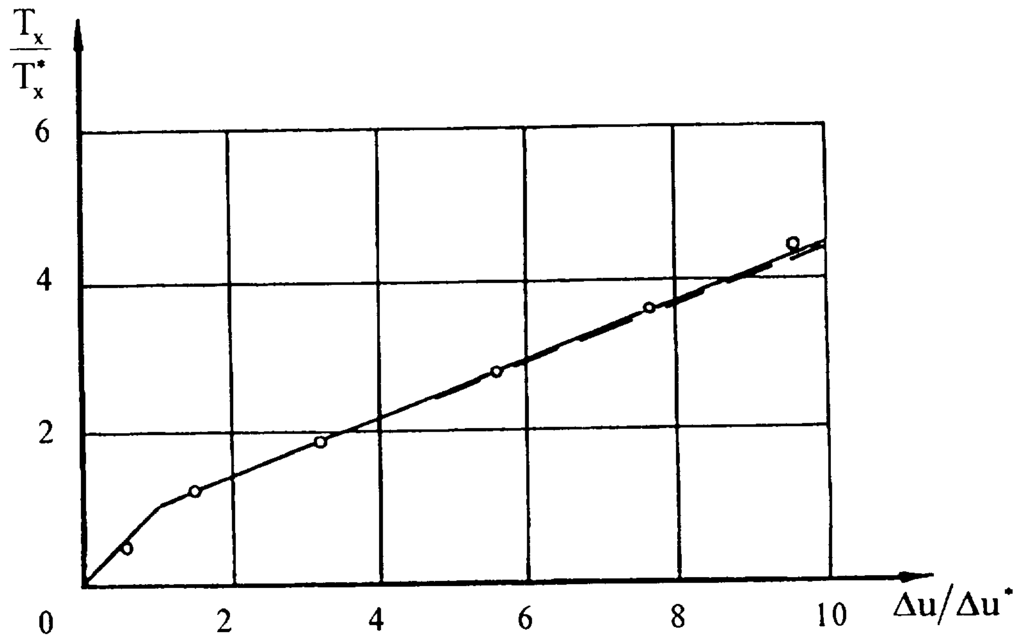

Figure 2.8. Experimental (o) and theoretical displacements of loaded edges of composite plate

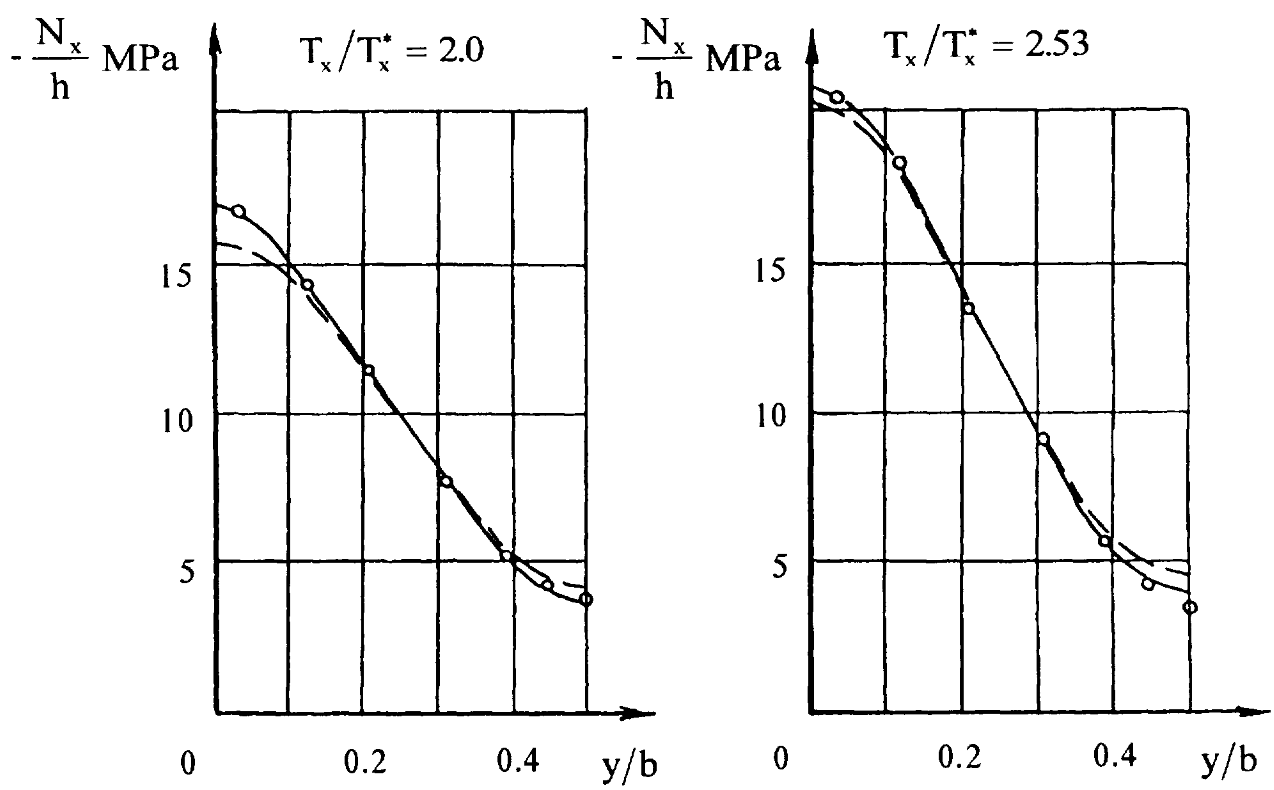

Figure 2.9. Experimental (o) and theoretical stresses in buckled plate

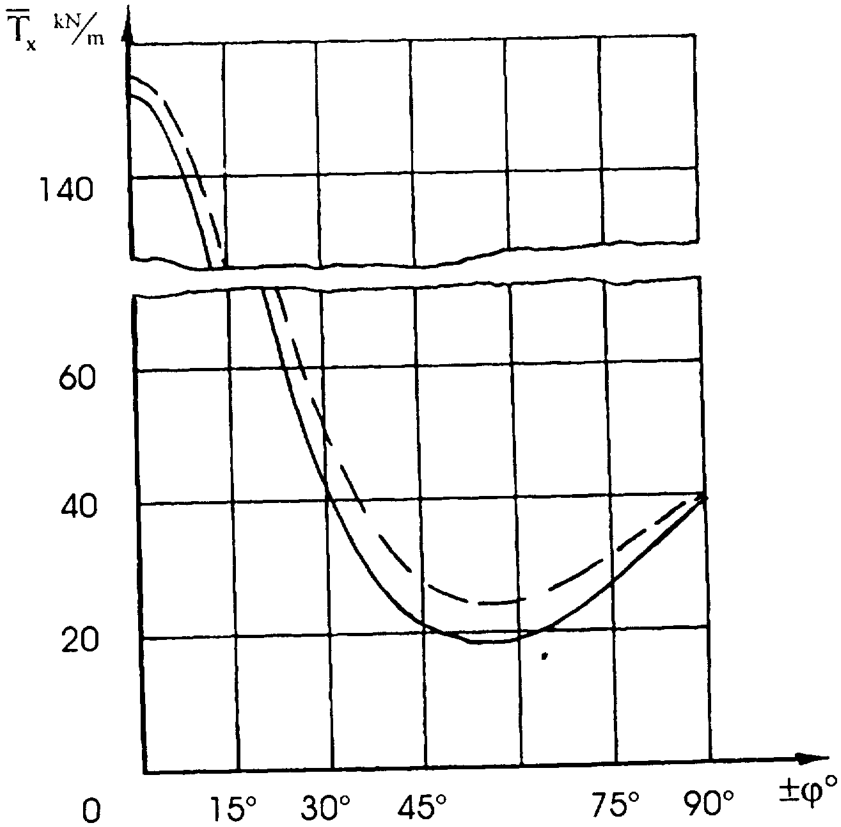

Figure 2.10. Failure stress resultants for compression-loaded plate with freely moving (——) and fixed (– –) longitudinal edges

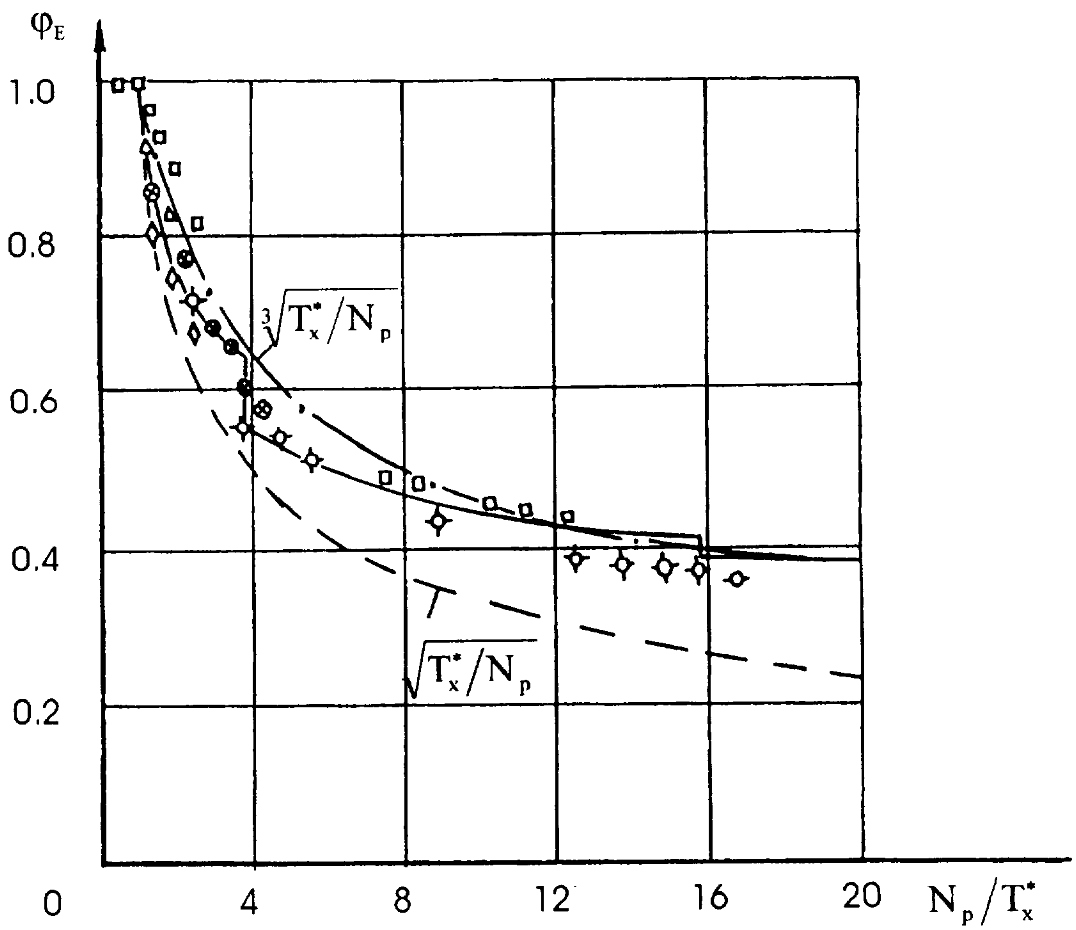

Figure 2.11. Theoretical and experimental values of skin reduction factor for metal plate:
—— new solution
– – – – – von Karman equation

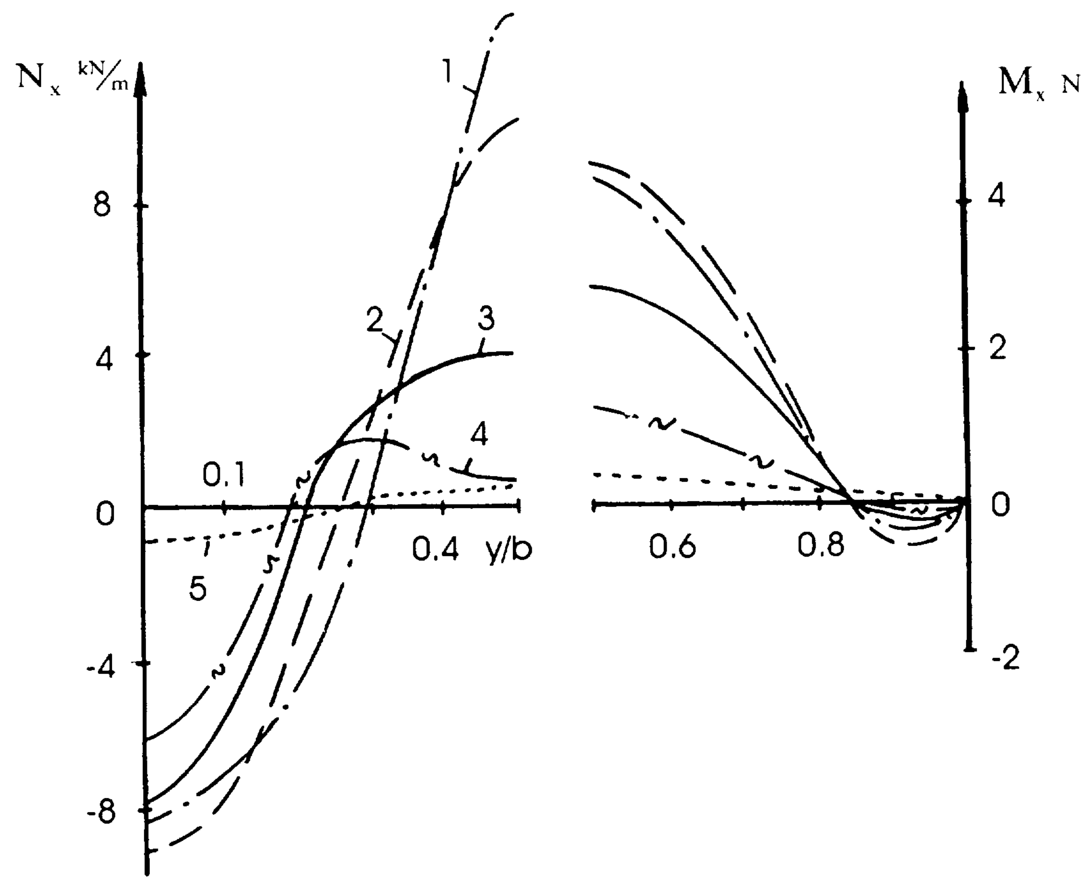

Figure 2.12. Distributions of stress resultants N_x and moments M_x over section {x/b=0.5}

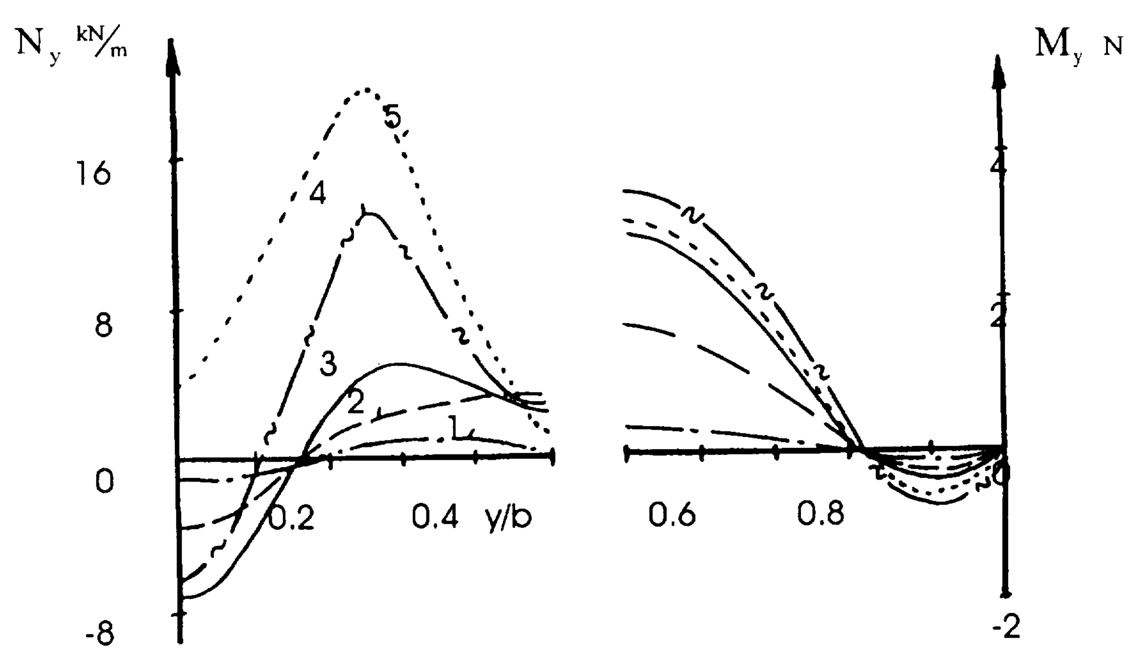

Figure 2.13. Distributions of stress resultants N_y and moments M_y over section {x/b=0.5} of a plate

1, $\varphi=0$; 2, $\varphi=\pm 30°$;
3, $\varphi=\pm 45°$; 4, $\varphi=\pm 60°$;
5, $\varphi=90°$

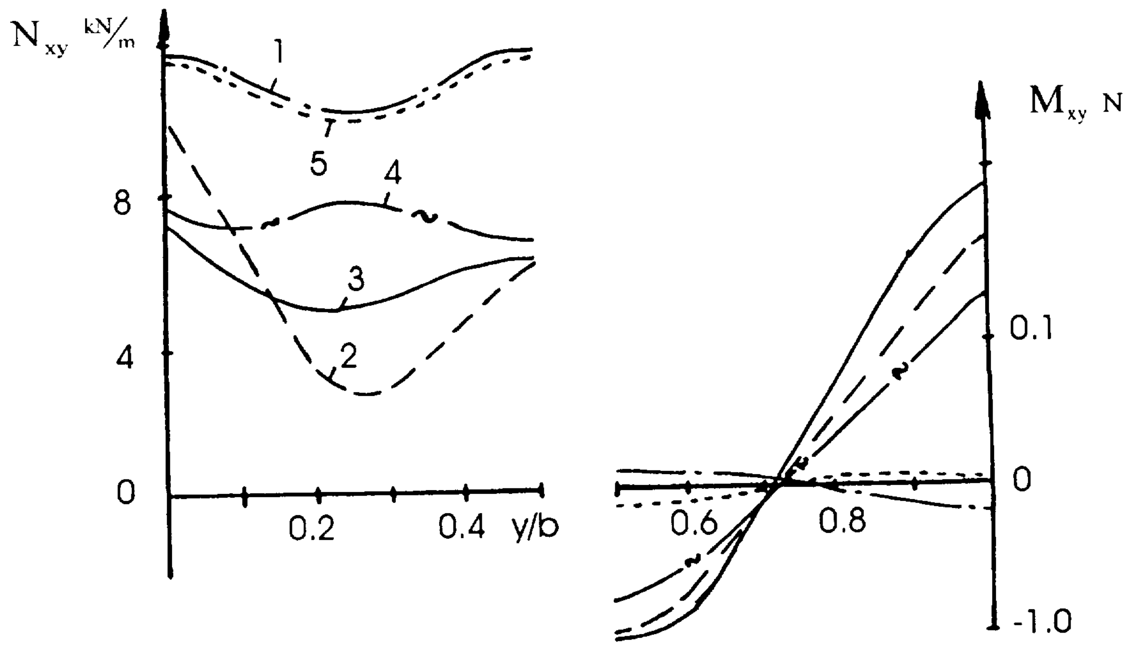

Figure 2.14. Distributions of stress resultants N_{xy} and moments M_{xy} over section {x/b=0.5}

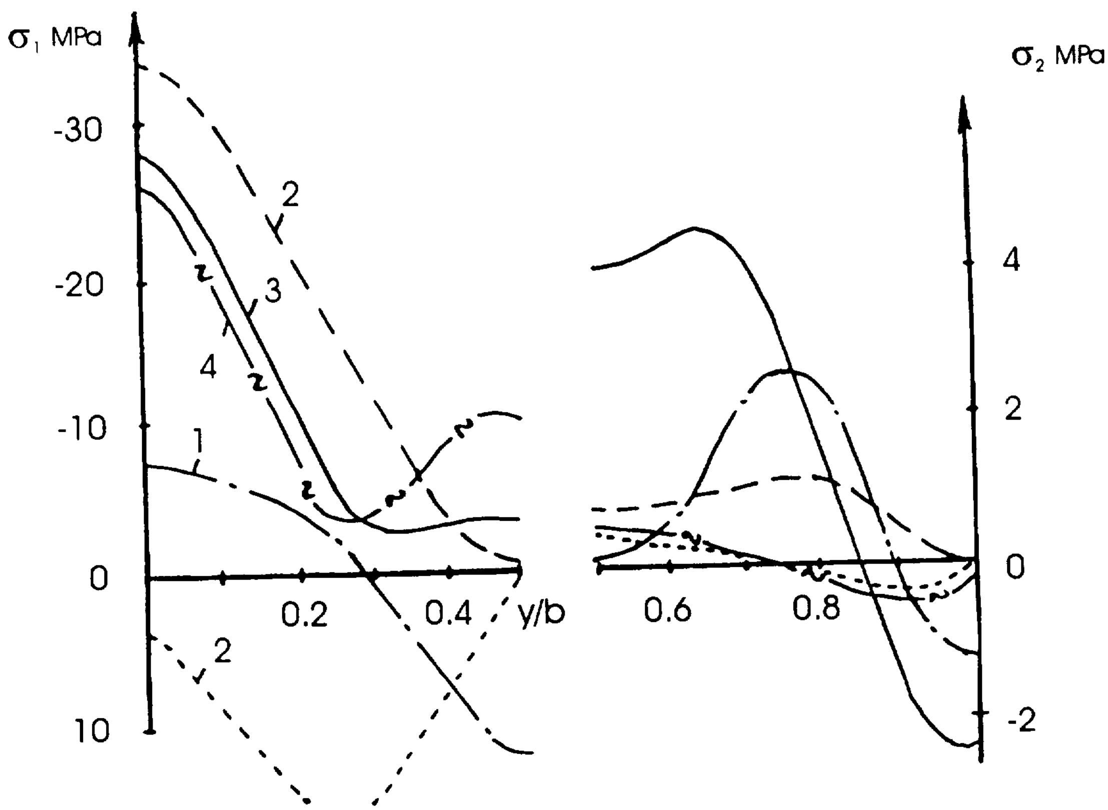

Figure 2.15. Distributions of stresses σ_1 and σ_2 over section {x/b=0.5}
1, $\varphi=0$; 2, $\varphi=\pm 30°$;
3, $\varphi=\pm 45°$; 4, $\varphi=\pm 60°$;
5, $\varphi=90°$

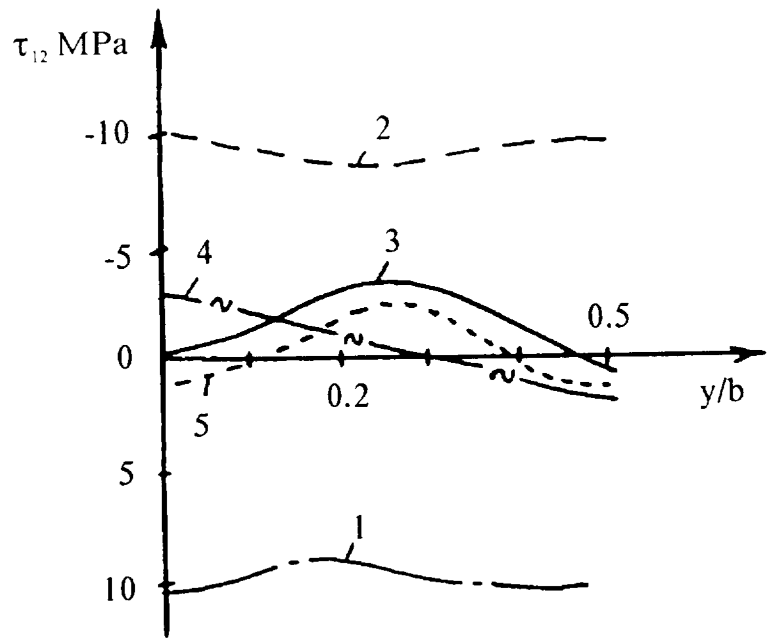

Figure 2.16. Stress τ_{12} profile over section {x/b=0.5}

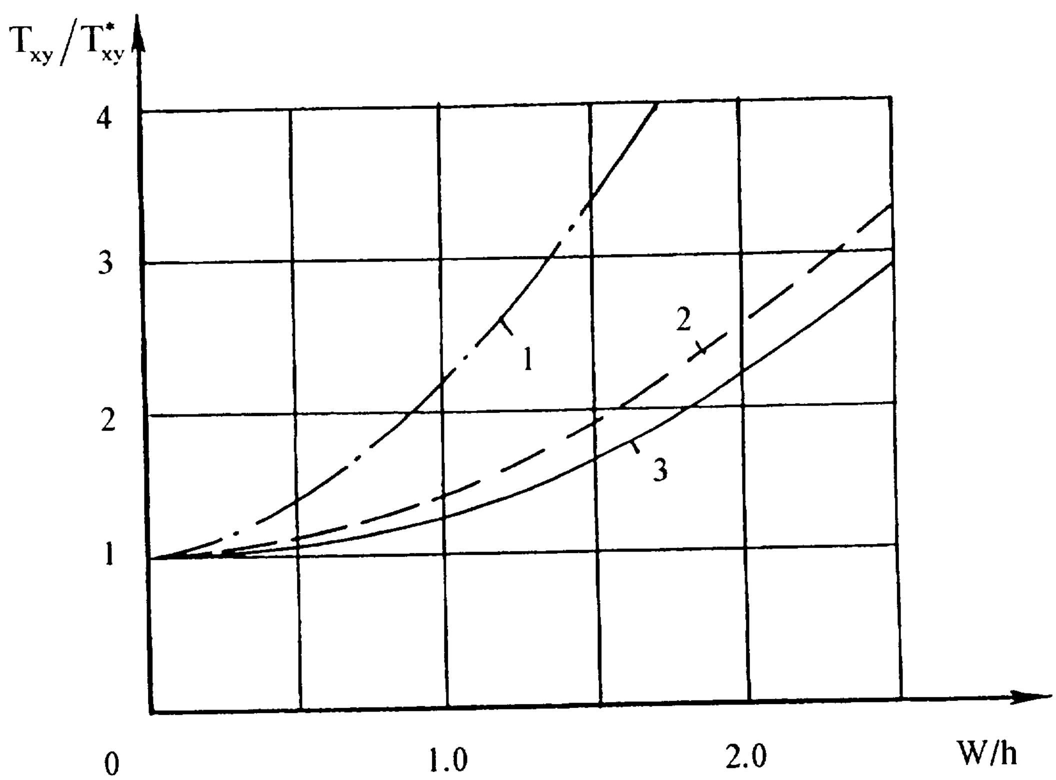

Figure 2.17. "Relative stress relative out-of-plane displacement" curves for composite plates with $\varphi=0$ (line 1), $\varphi=\pm30°$ (line 2), and $\varphi=\pm45°$ (line 3)

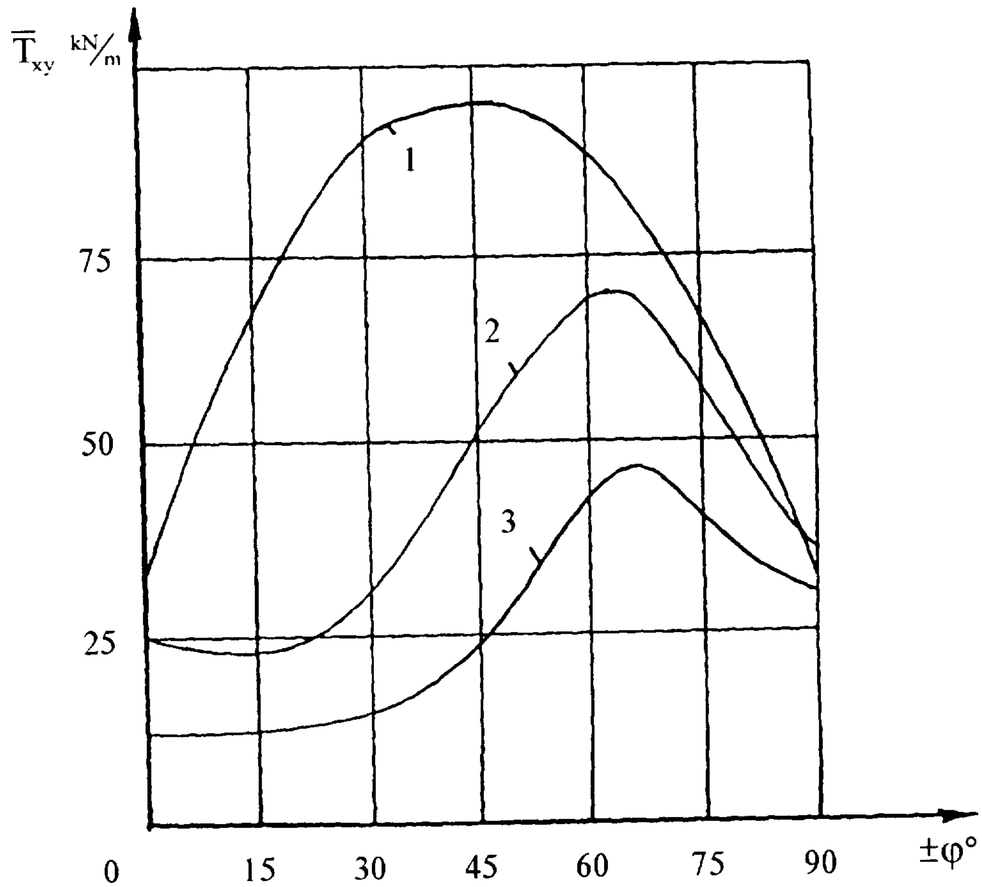

Figure 2.18. Failure shear stress resultant $\overline{T}_{xy}$ for CFRP plates with aspect ratio a/b of 1 (line 1), 2 (line 2), and 3 (line 3)

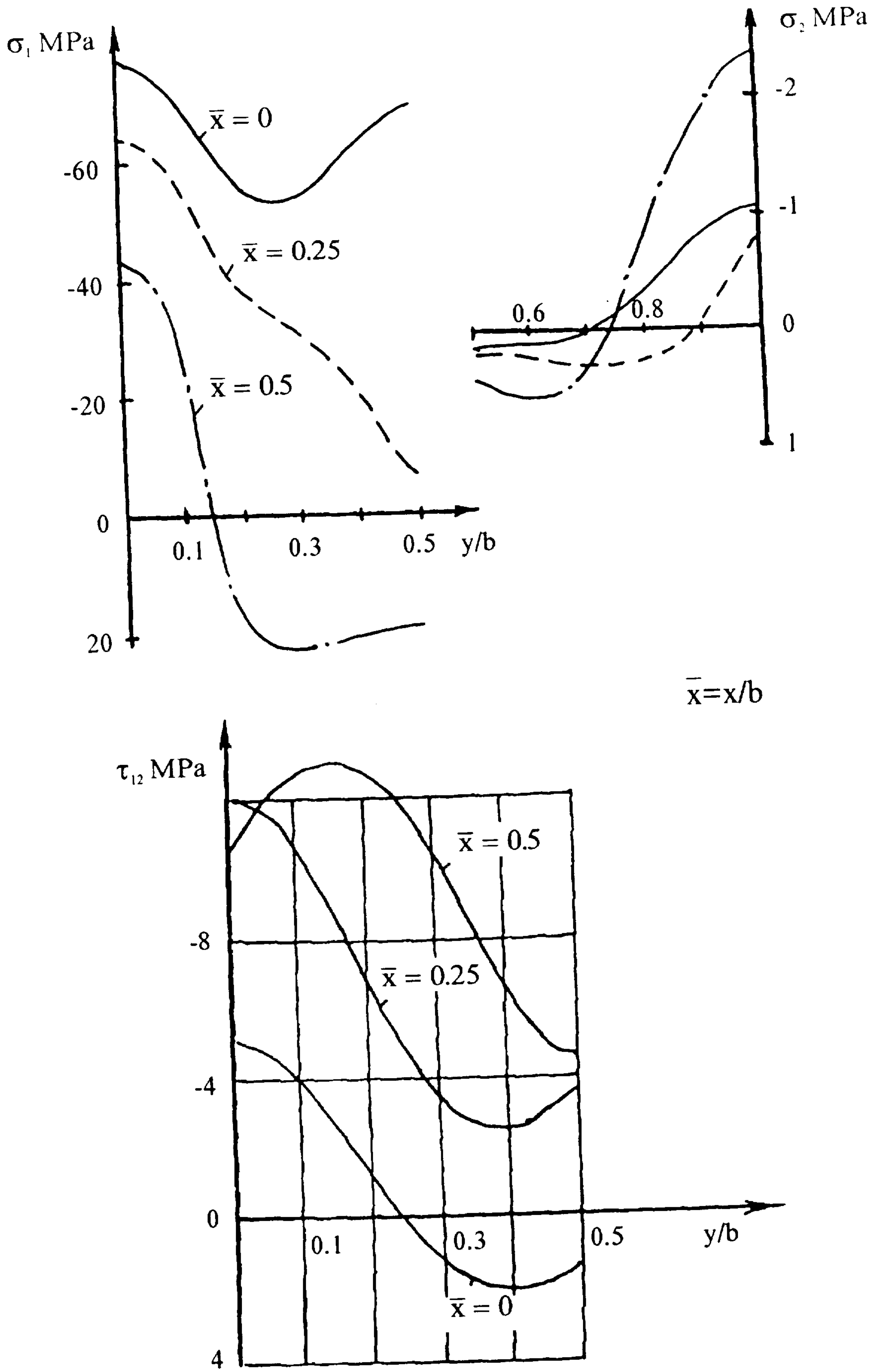

Figure 2.19. Distributions of stresses σ_1, σ_2, and τ_{12} over three sections of plate with $\varphi=\pm45°$ subjected to multiaxial load

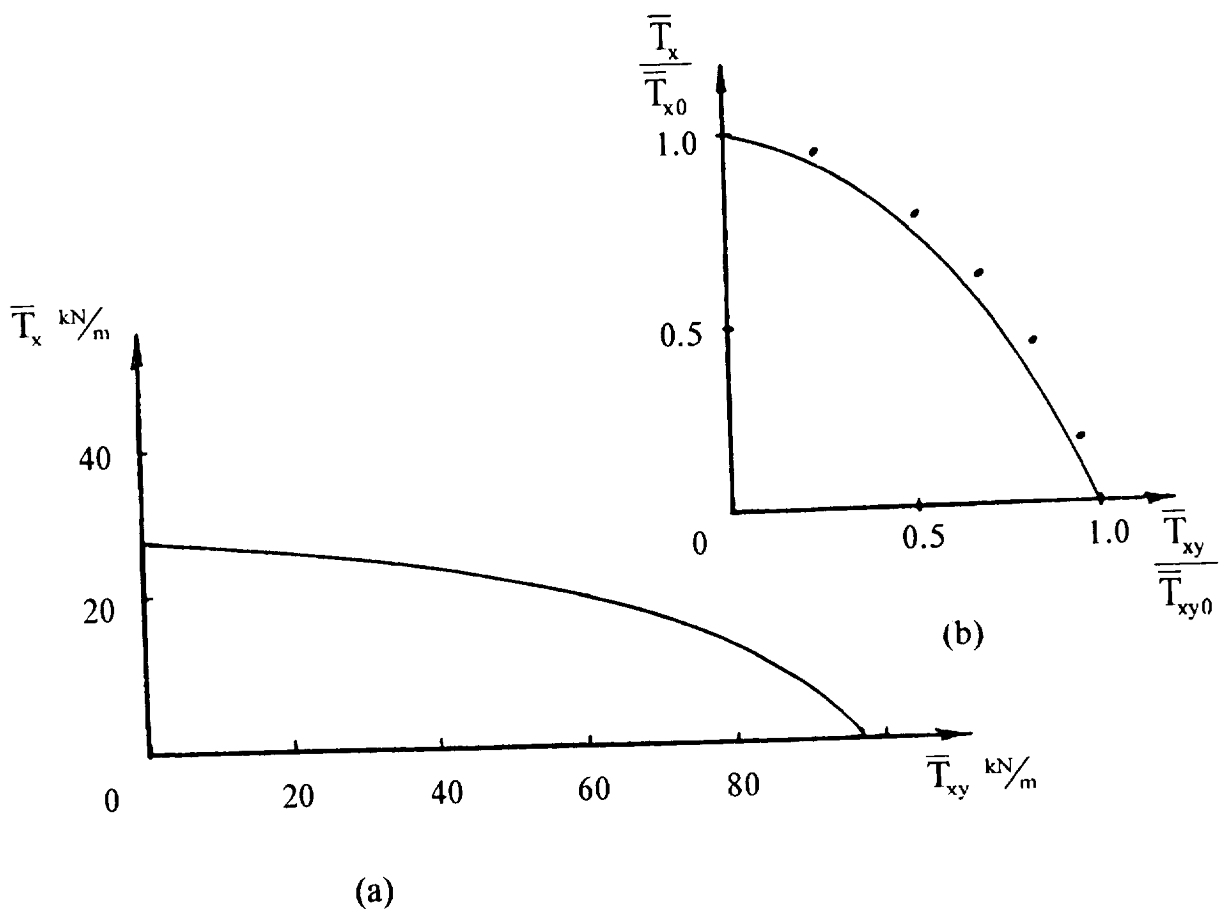

Figure 2.20. Strength surface for CFRP plate under multiaxial load:
(a) in co-ordinates $\overline{T}_x - \overline{T}_{xy}$;
(b) in relative co-ordinates $\overline{T}_x / \overline{T}_{x0} - \overline{T}_{xy} / \overline{T}_{xy0}$

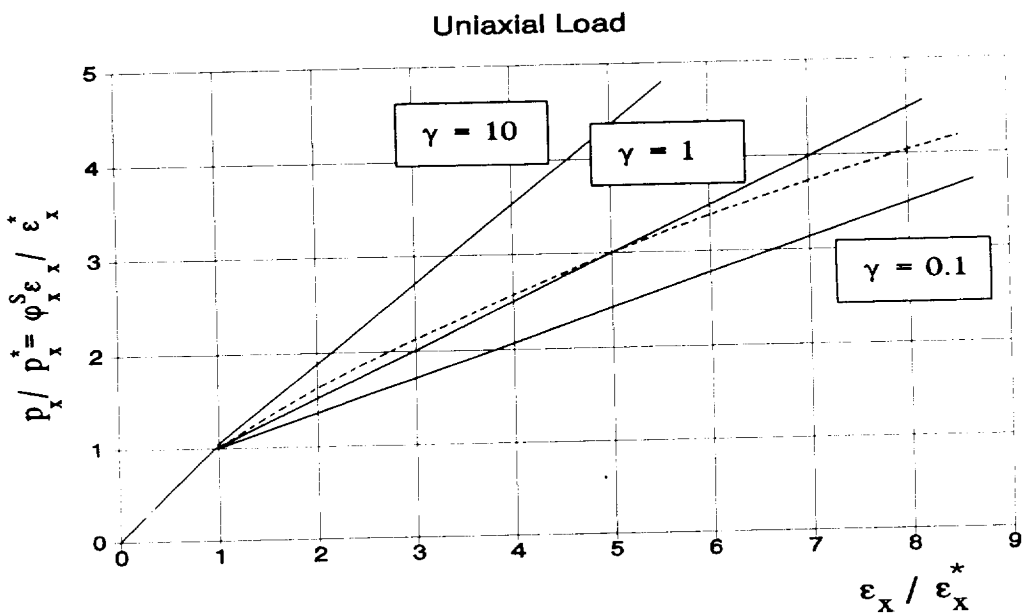

(a)

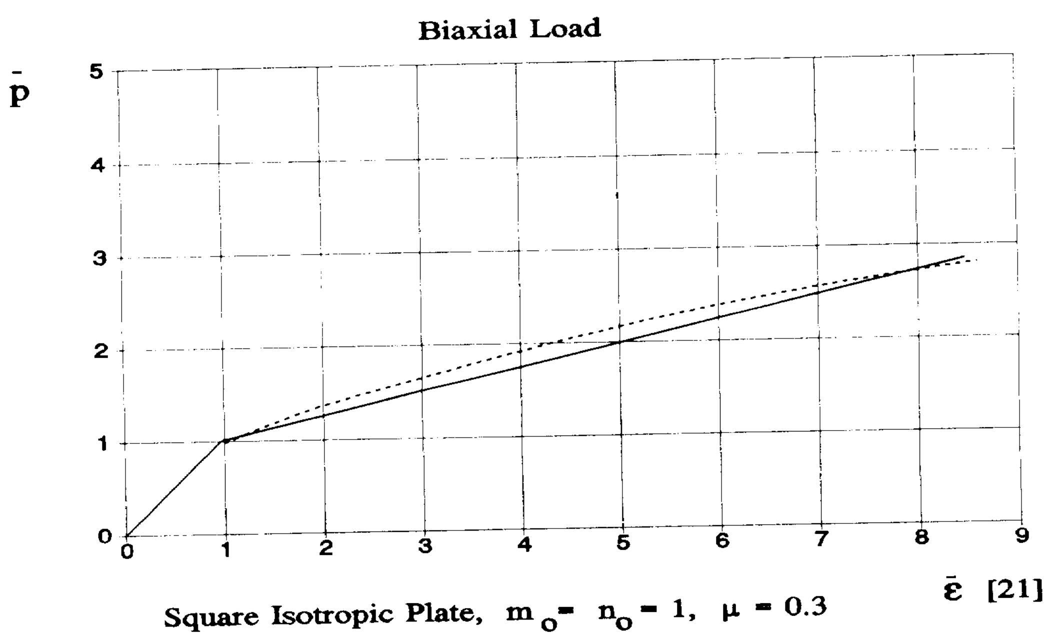

(b)

Figure 2.21 Stress-strain curves for uniaxial and biaxial compression

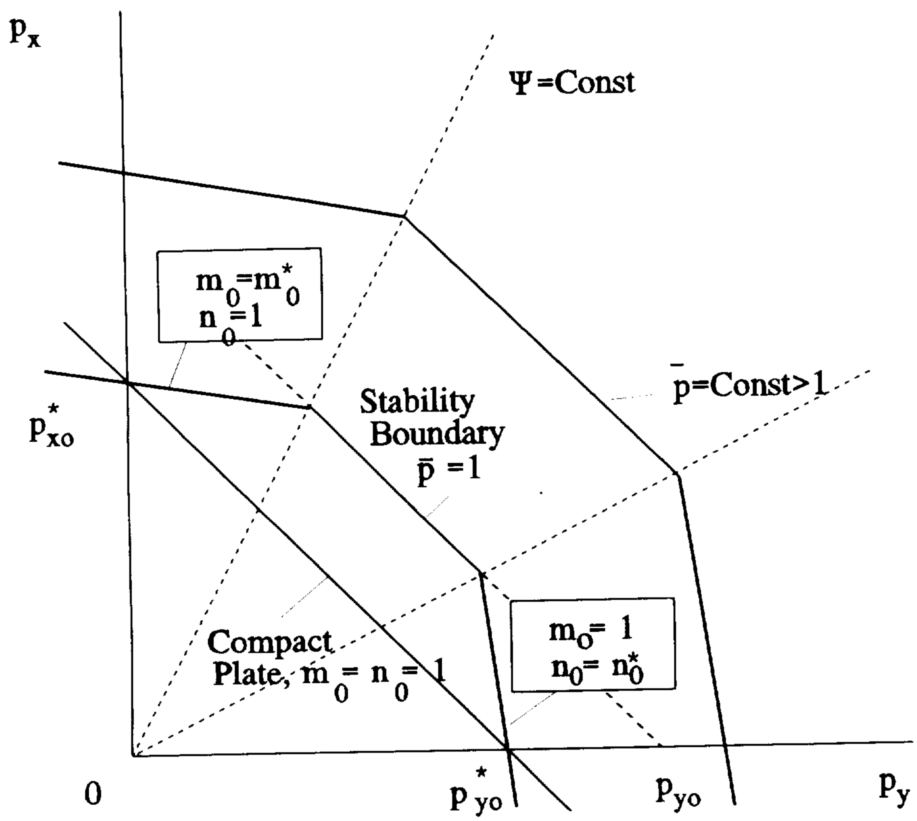

Figure 2.22 Example of stability boundary and postbuckling plate behavior

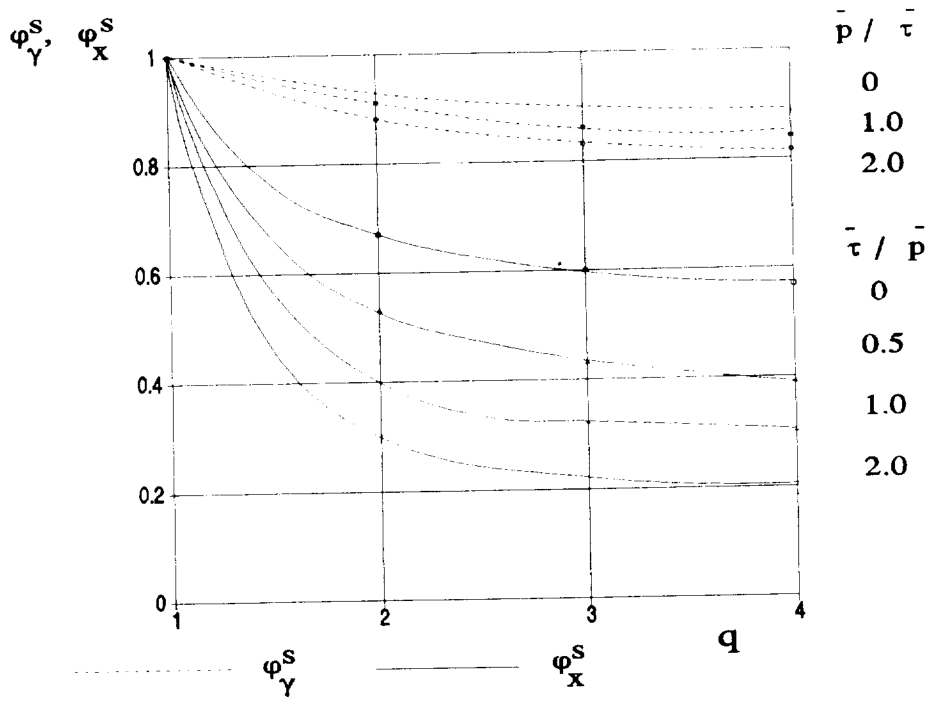

Figure 2.23 Secant reduction factors at $\alpha=1$

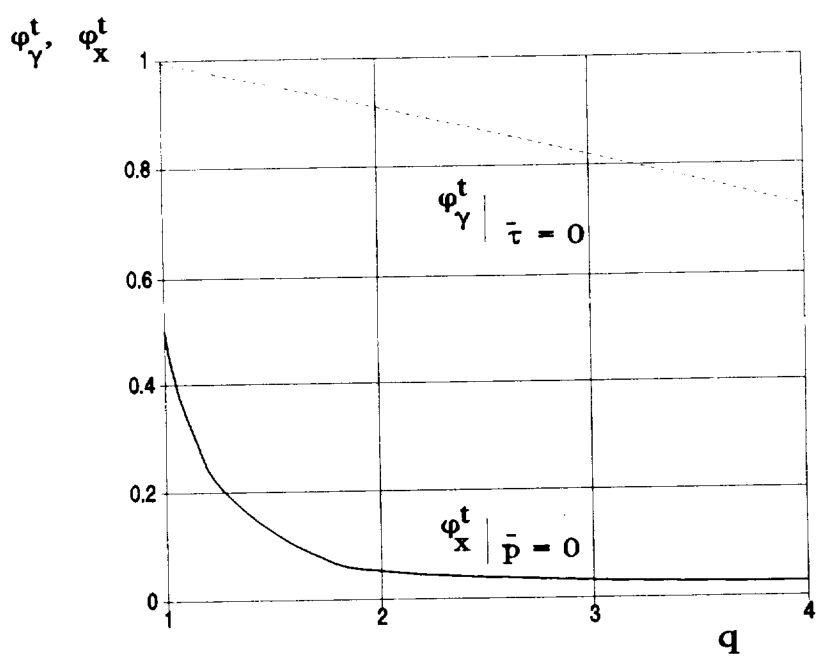

Figure 2.24 Tangent reduction factors at $\alpha=1$

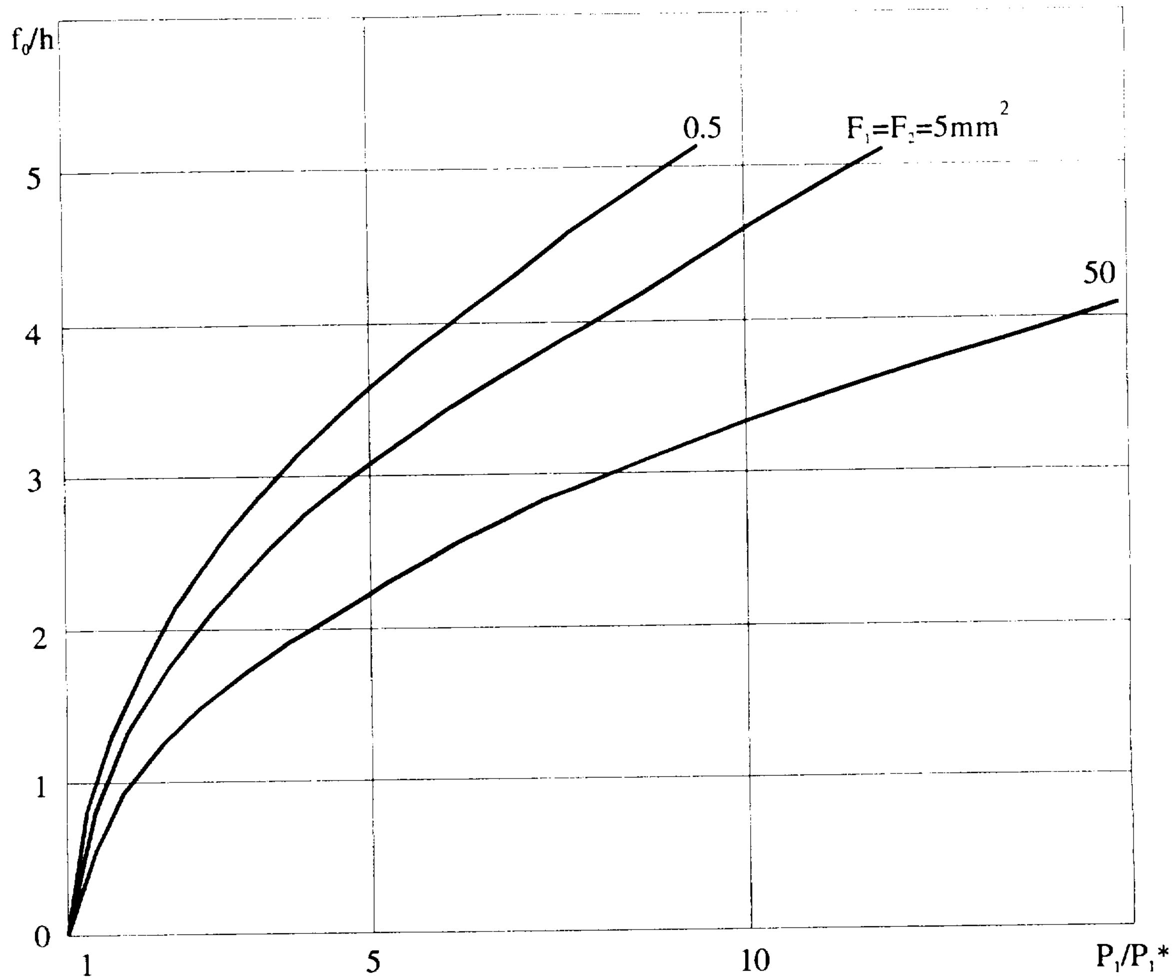

Figure 2.25. Dependence of nondimensional deflection f_0/h on ratio of compressive loads P_1/P_1^*

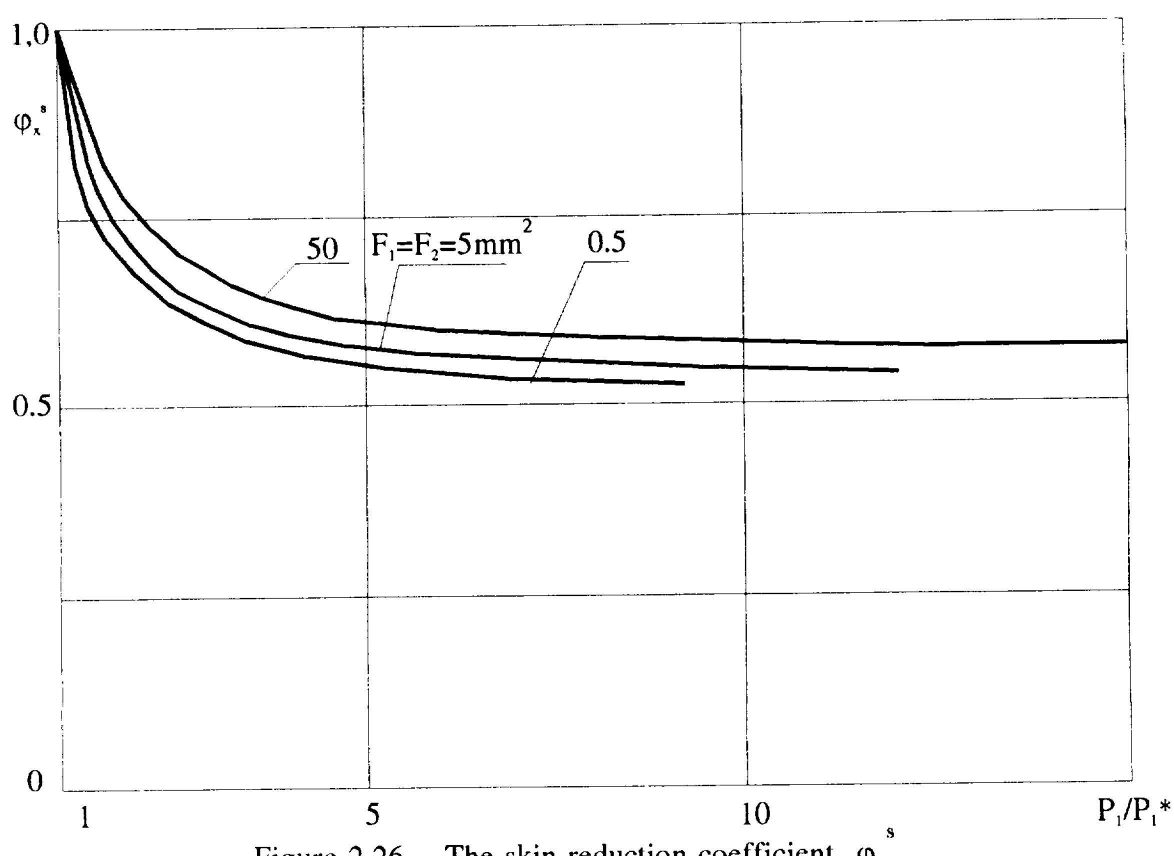

Figure 2.26. The skin reduction coefficient φ_x^s

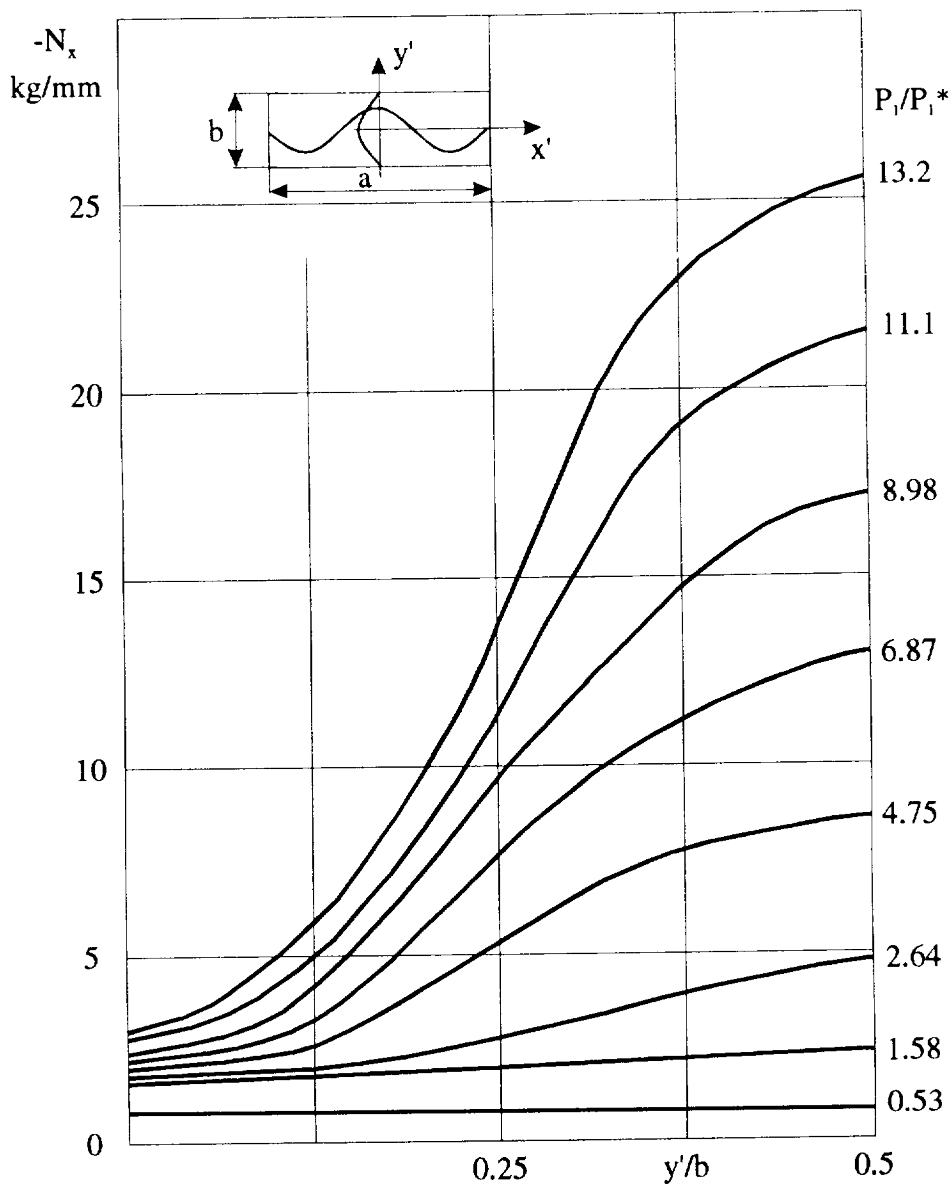

Figure 2.27. N_x distribution over a panel half-wave: dependence on P_1/P_1^* ratio

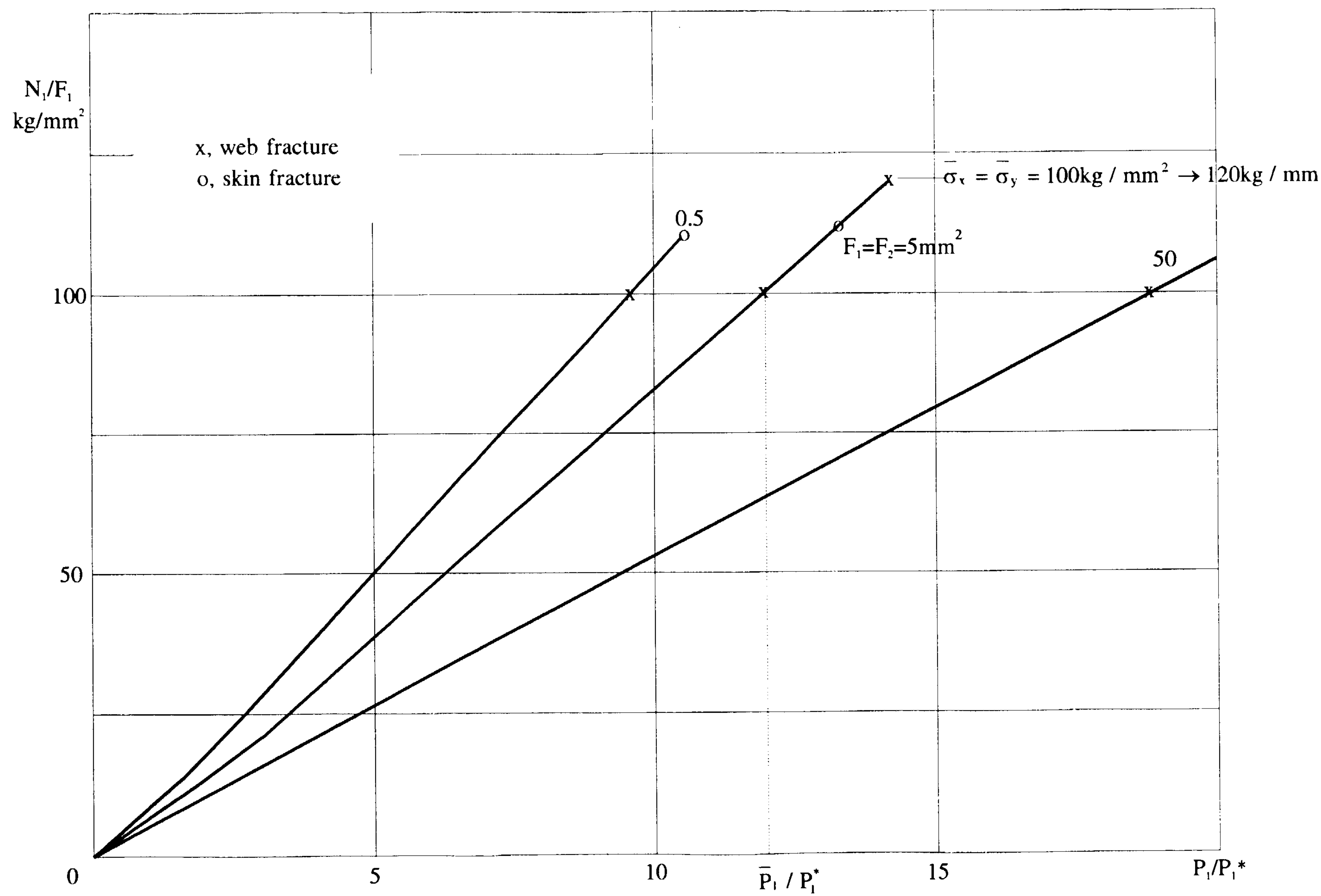

Figure 2.28. Web stress N_1/F_1 as a function of stress resultant ratio P_1/P_1^* ; panel failure mode

Table 3.1. Typical configurations of adhesive joints

№	Type	Schematic	Analytical model	Jumps in elastic line		
1	Simple overlap	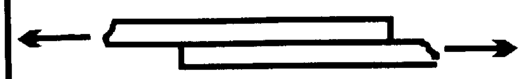	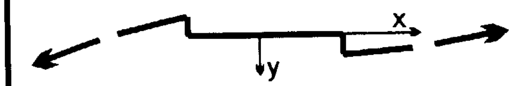	$\Delta\bar{y}_L$	$\Delta y_o=0$	Δy_R
2	One-sided doubler		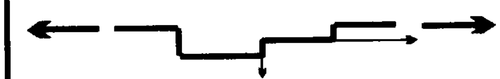	$\Delta\bar{y}_L$	Δy_o	Δy_R
3	One-step joint	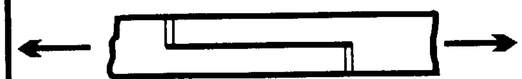		Δy_L	$\Delta y_o=0$	Δy_R
4	Two-step joint		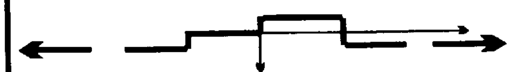	$\Delta\bar{y}_L$	Δy_o	Δy_R
5	One-sided patch	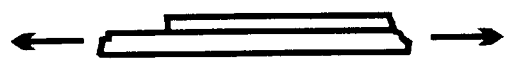	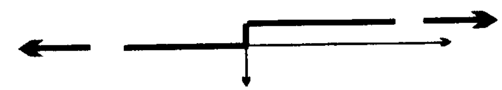	$\Delta y_L=0$	Δy_o	$\Delta y_R=0$
	Symmetric joints					
6	Two-sided doubler	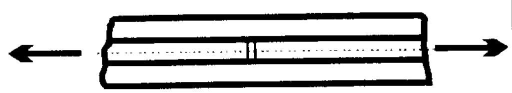		$\Delta y_L=0$	$\Delta y_o=0$	$\Delta y_R=0$
7	Inserted joint	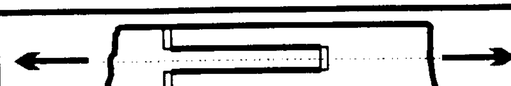		$\Delta y_L=0$	$\Delta y_o=0$	$\Delta y_R=0$
8	Stepped inserted joint	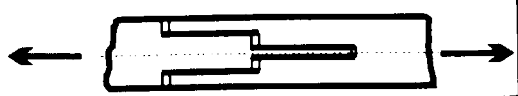		$\Delta y_L=0$	$\Delta y_o=0$	$\Delta y_R=0$
9	Multilayered joint	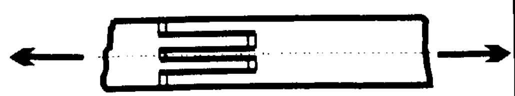		$\Delta y_L=0$	$\Delta y_o=0$	$\Delta y_R=0$

Table 3.2 **Two-sided doubler**

Characteristic	Dimensionality	Sheet	Adhesive layer	Doubler
Thickness	mm	2	0.1	1
Modulus E_x	MPa	$7 \cdot 10^4$	$0.35 \cdot 10^4$	$7 \cdot 10^4$
Modulus E_y	MPa	$7 \cdot 10^4$	$0.35 \cdot 10^4$	$7 \cdot 10^4$
Shear modulus G_{xy}	MPa	$2.7 \cdot 10^4$	$0.25 \cdot 10^4$	$2.7 \cdot 10^4$

Table 3.3 **ONe-sided doubler**

Characteristic	Dimensionality	Sheet (L)	Adhesive layer (a)	Sheet (R)
Material	-	Aluminum	Epoxy resin	Aluminum
Thickness **t**	mm	2	0.1	1
Modulus $\mathbf{E_x}$	MPa	$7 \cdot 10^4$	$0.35 \cdot 10^4$	$7 \cdot 10^4$
Modulus $\mathbf{E_y}$	MPa	$7 \cdot 10^4$	$0.35 \cdot 10^4$	$7 \cdot 10^4$
Shear modulus $\mathbf{G_{xy}}$	MPa	$2.7 \cdot 10^4$	$0.25 \cdot 10^4$	$2.7 \cdot 10^4$

Table 3.4 **Inserted joint**

Characteristic	Dimensionality	Sheet (L)	Adhesive layer (a)	Sheet (R)
Material	-	Aluminum	Epoxy resin	CFRP
Modulus $\mathbf{E_x}$	MPa	$7 \cdot 10^4$	$0.3 \cdot 10^4$	$16 \cdot 10^4$
Modulus $\mathbf{E_y}$	MPa	$7 \cdot 10^4$	$0.2 \cdot 10^4$	$1.4 \cdot 10^4$
Shear modulus $\mathbf{G_{xy}}$	MPa	$2.7 \cdot 10^4$	$0.2 \cdot 10^4$	$0.63 \cdot 10^4$

Table 3.5 **Symmetric overlap**

Characteristic	Dimensionality	Sheet (L)	Adhesive layer (a)	Sheet (R)
Material	-	CFRP	Epoxy resin	CFRP
Thickness $\mathbf{t}$	mm	1	0.1	1
Modulus $\mathbf{E_x}$	MPa	$16 \cdot 10^4$	$0.2 \cdot 10^4$	$16 \cdot 10^4$
Modulus $\mathbf{E_y}$	MPa	$1.4 \cdot 10^4$	$0.15 \cdot 10^4$	$1.4 \cdot 10^4$
Shear modulus $\mathbf{G_{xy}}$	MPa	$0.6 \cdot 10^4$	$0.05 \cdot 10^4$	$0.6 \cdot 10^4$

Table 3.6 **Asymmetric overlap**

Characteristic	Dimensionality	Sheet (L)	Adhesive layer (a)	Sheet (R)
Material	-	Aluminum	Epoxy resin	CFRP
Thickness $\mathbf{t}$	mm	2.0	0.1	1.0
Modulus $\mathbf{E_x}$	MPa	$7 \cdot 10^4$	$0.2 \cdot 10^4$	$16 \cdot 10^4$
Modulus $\mathbf{E_y}$	MPa	$7 \cdot 10^4$	$0.15 \cdot 10^4$	$1.4 \cdot 10^4$
Shear modulus $\mathbf{G_{xy}}$	MPa	$2.7 \cdot 10^4$	$0.05 \cdot 10^4$	$0.6 \cdot 10^4$

Table 3.7.

Characteristic	Symbol	Dimensionality	Layer #	Portion/number of layers			
				2L/1	1L/3	1R/3	2R/1
Length	l	mm	-	530	20	20	530
Material	Brand	-	1	D16	D16	D16	KMU
			2	-	Adhesive	Adhesive	-
			3	-	KMU	KMU	-
Thickness	Δ	mm	1	2.0	2.0	2.0	1.0
			2	-	0.1	0.1	-
			3	-	1.0	1.0	-
Modulus	E_x	MPa	1	70000	70000	70000	160000
			2	-	2000	2000	-
			3	-	160000	160000	-
Modulus	E_y	MPa	1	70000	70000	70000	14000
			2	-	1500	1500	-
			3	-	14000	14000	-
Shear modulus	G_{xy}	MPa	1	27000	27000	27000	6000
			2	-	500	500	-
			3	-	6000	6000	-

Table 3.8 Comparing analytical (C_{an}) and experimental (C_{ex}) compliances

#	t_p mm	t_d mm	d_b mm	E_p N/mm²	E_d N/mm²	E_b N/mm²	C_{an} mm/N	C_{ex} mm/N	γ %
1	10	5	10	210000	210000	210000	0.0345	0.030	15
2	10	3.75	10	210000	210000	210000	0.00347	0.032	8
3	10	2.5	10	210000	210000	210000	0.0384	0.038	1
4	10	5	10	71000	210000	210000	0.0520	0.047	11
5	10	5	5	3600	3600	3600	2.28	2.3	-1

Table 3.9 Local stresses at screw holes in skin (σ_S) and doubler (σ_D)

Bolt #	ΔP, N	K_{1s}	K_{1d}	K_{2s}	K_{2d}	$\left(K_1 \cdot \frac{\Delta P}{d \cdot t}\right)_s$	$\left(K_1 \cdot \frac{\Delta P}{d \cdot t}\right)_d$	$\left(K_2 \cdot \frac{\Delta P}{W \cdot t}\right)_s$	$\left(K_2 \cdot \frac{\Delta P}{W \cdot t}\right)_d$	σ_{Sloc}	σ_{Dloc}
1-5	9.70	1.85	1.85	3.18	3.18	0.375	0.203	0	0.349	0.375	0.552
2-5	8.95	1.85	1.85	3.18	3.18	0.311	0.188	0	0.572	0.344	0.760
3-2	8.75	1.80	1.80	3.15	3.15	0.328	0.178	0	0.667	0.328	0.845
1-1	9.70	1.85	1.85	3.18	3.18	0.375	0.315	0.241	0.190	0.616	0.505
2-4	8.70	1.85	1.85	3.18	3.18	0.335	0.287	0.190	0.445	0.585	0.732
3-1	8.22	1.80	1.80	3.15	3.15	0.308	0.264	0.182	0.522	0.490	0.786
1-3	9.22	1.85	1.85	3.18	3.18	0.355	0.304	0.349	0.381	0.704	0.685
2-3	8.47	1.80	1.80	3.15	3.15	0.317	0.272	0.308	0.409	0.625	0.681
1-2	10.20	1.85	1.85	3.18	3.18	0.393	0.393	0.451	0.254	0.844	0.647
2-2	9.32	1.80	1.80	3.15	3.15	0.349	0.349	0.441	0.277	0.790	0.626
1-1	11.45	1.85	1.85	3.18	3.18	0.441	0.529	0.585	0	1.026	0.529
2-1	10.60	1.80	1.80	3.15	3.15	0.397	0.477	0.607	0	1.004	0.477

Table 3.10 **Experimentally obtained values of radial interference (in microns)**

Collar	Radial displacements, mum								
	Load, $P \times 10^{-4}$, N								
	0	5	10	15	20	25	30	35	40
With rubber layer									
1	0 0 0	+10 -10 0	0 +10 0	+10 +10 0	0 +30 +20	+20 +30 +10	+20 +40 0	+50 -20	+50 +70
2	0 0 0	-10 +10 0	0 +40 0	+10 +60 +50	+40 +150 +60	+70 +110 +50	+80 +140 +110	+140 +130	+180 +210
3	0 0 0	-10 +20 -10	+20 +40 -10	+50 +80 +120	+80 +110 +140	+140 +150 +170	+160 +200 +230	+230 +210	+260 +180
4	0 0 0	+20 +50 +50	+50 +110 +130	+130 +150 +200	+180 +220 +260	+250 +270 +260	+260 +300 +350	+350 +370	+380 +420
Without rubber layer									
1	0	+20	+10	-30	-40	-50	-50	0	-10
2	0	+10	0	-10	-10	-10	+10	-10	+20
3	0	0	-30	+50	+30	+80	+80	+90	+110
4	0	+10	+40	-120	+140	+180	+200	+210	+240

Table 3.11 **Distribution of contact forces over the collars**

Contact nodes	N_i	$\sin \alpha_i$	$N_i \sin \alpha_i$
5	97030	0.510	49485.3
Total load on collar 1			49485.3
10	33100	0.419	13868.9
11	11800	0.416	4908.8
12	46030	0.433	19931.0
13	12900	0.379	4889.1
Total load on collar 2			43597.8
18	36640	0.385	14106.4
19	25610	0.390	9987.9
20	40430	0.394	15929.4
21	19010	0.362	6881.6
Total load on collar 3			46905.3
28	32520	0.394	12812.9
29	59650	0.447	26663.6
30	79550	0.447	35558.9
Total load on collar 4			75035.4
Gross total			215023.8

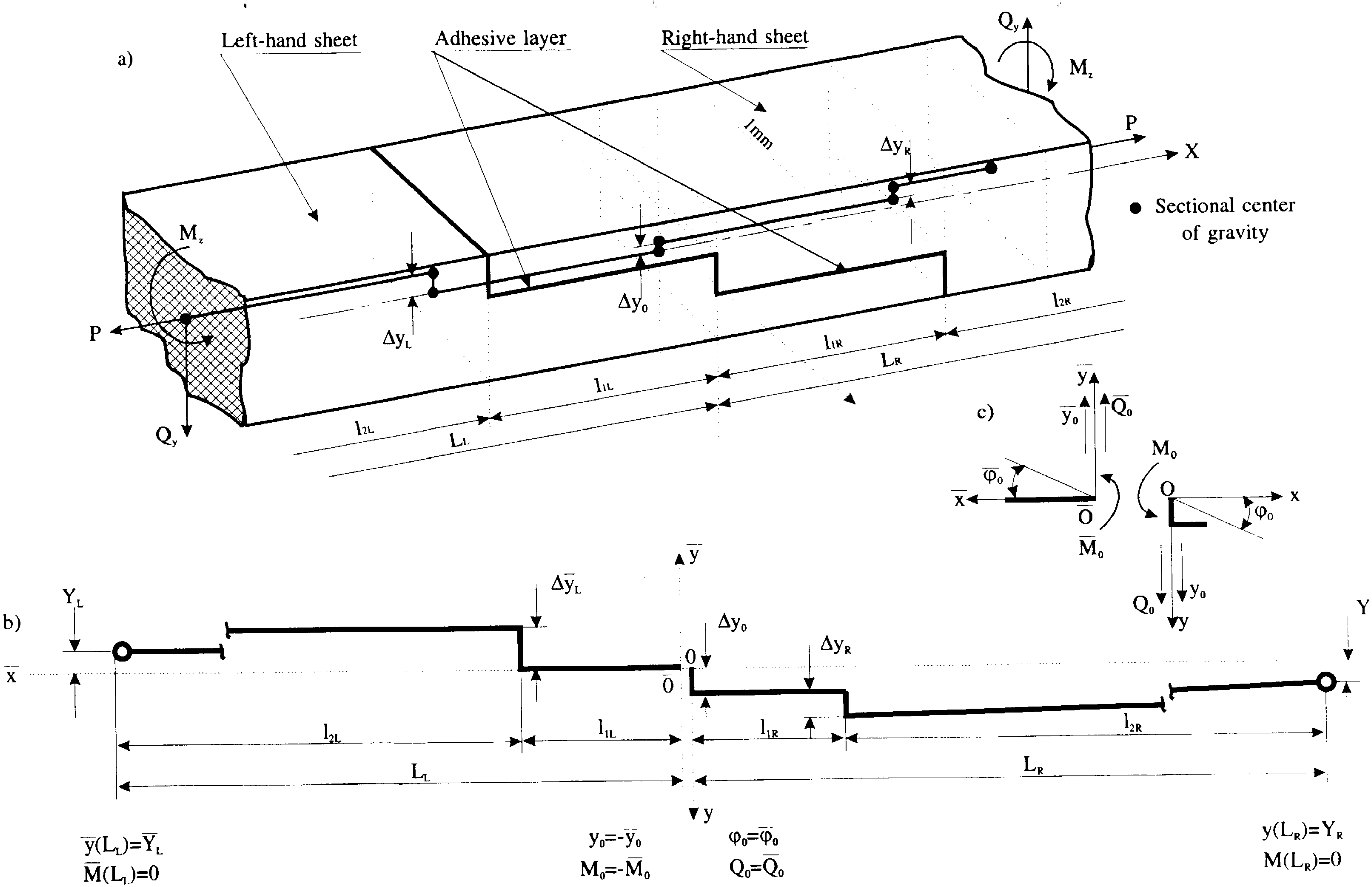

Figure 3.1. Model of adhesive joint of two sheets

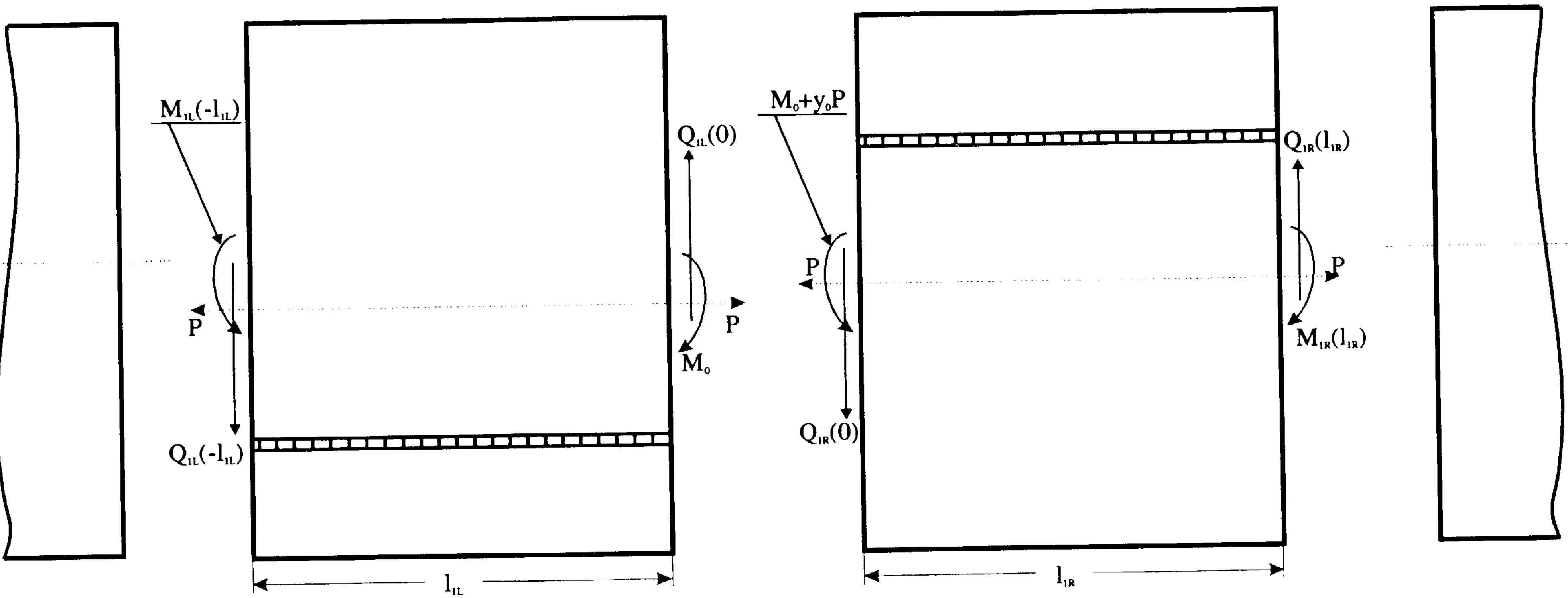

Figure 3.2. Loads on portions of adhesive joint

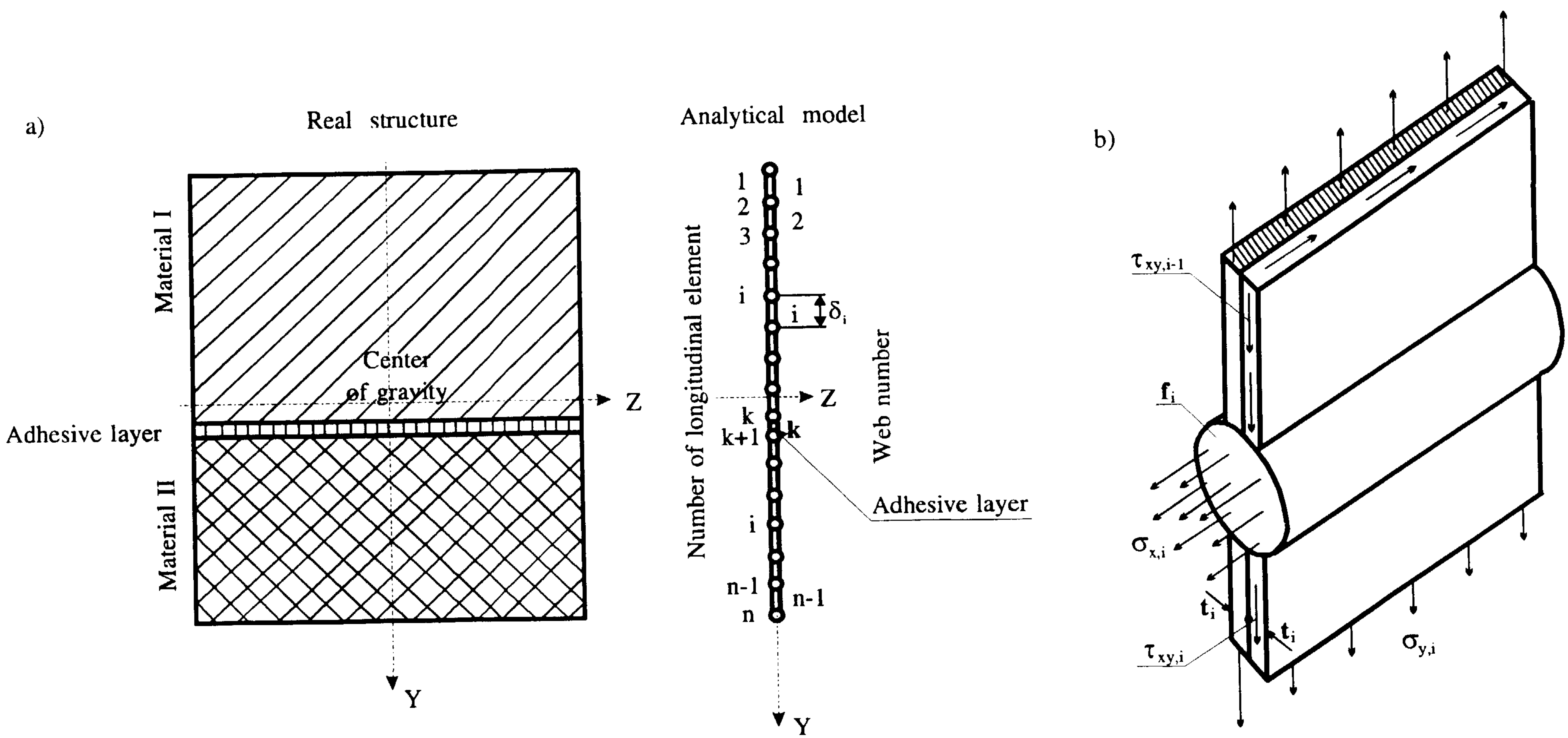

Figure 3.3. Analytical model of adhesive joint

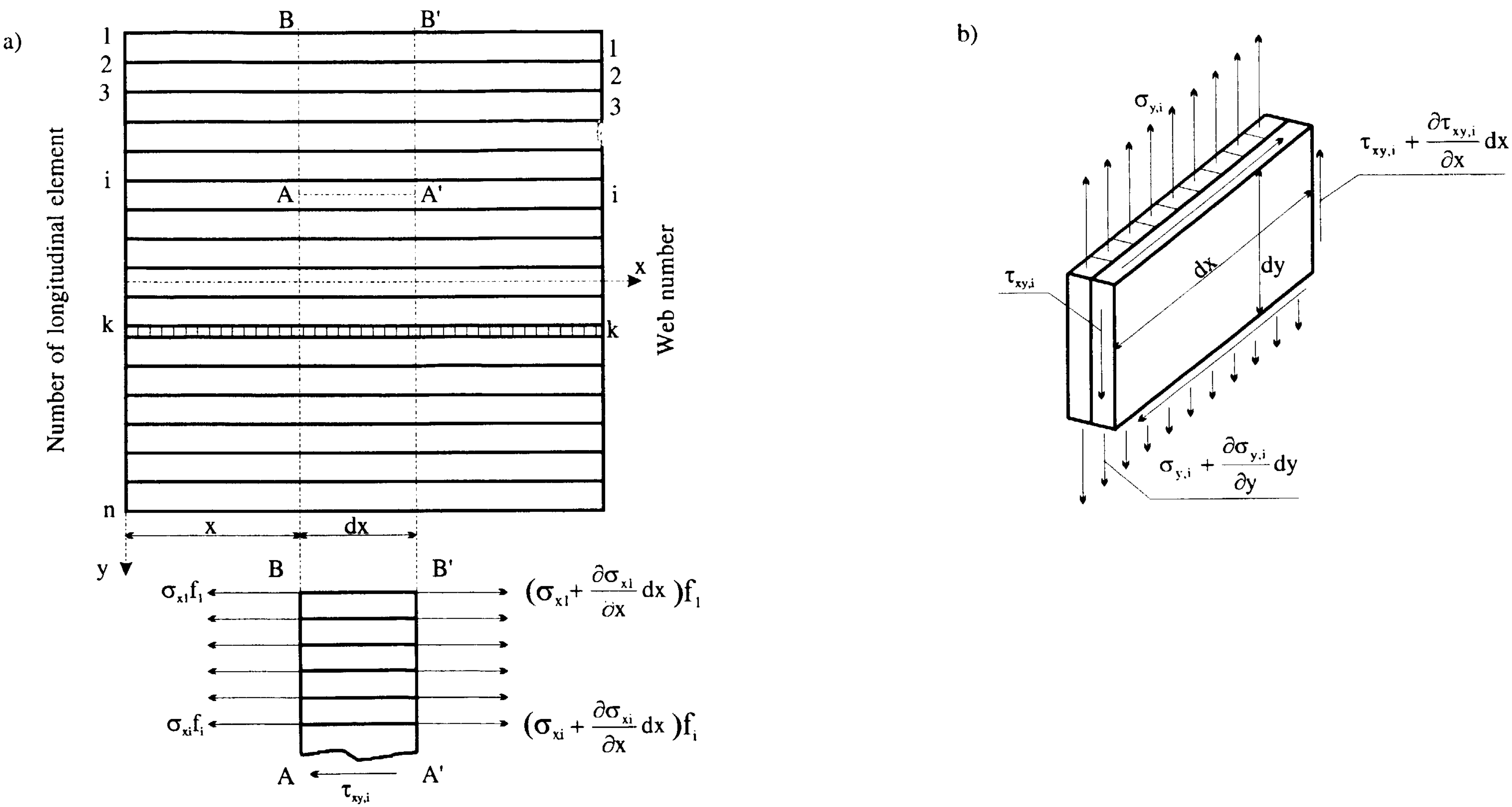

Figure 3.4. Equilibrium of elements in adhesive joint

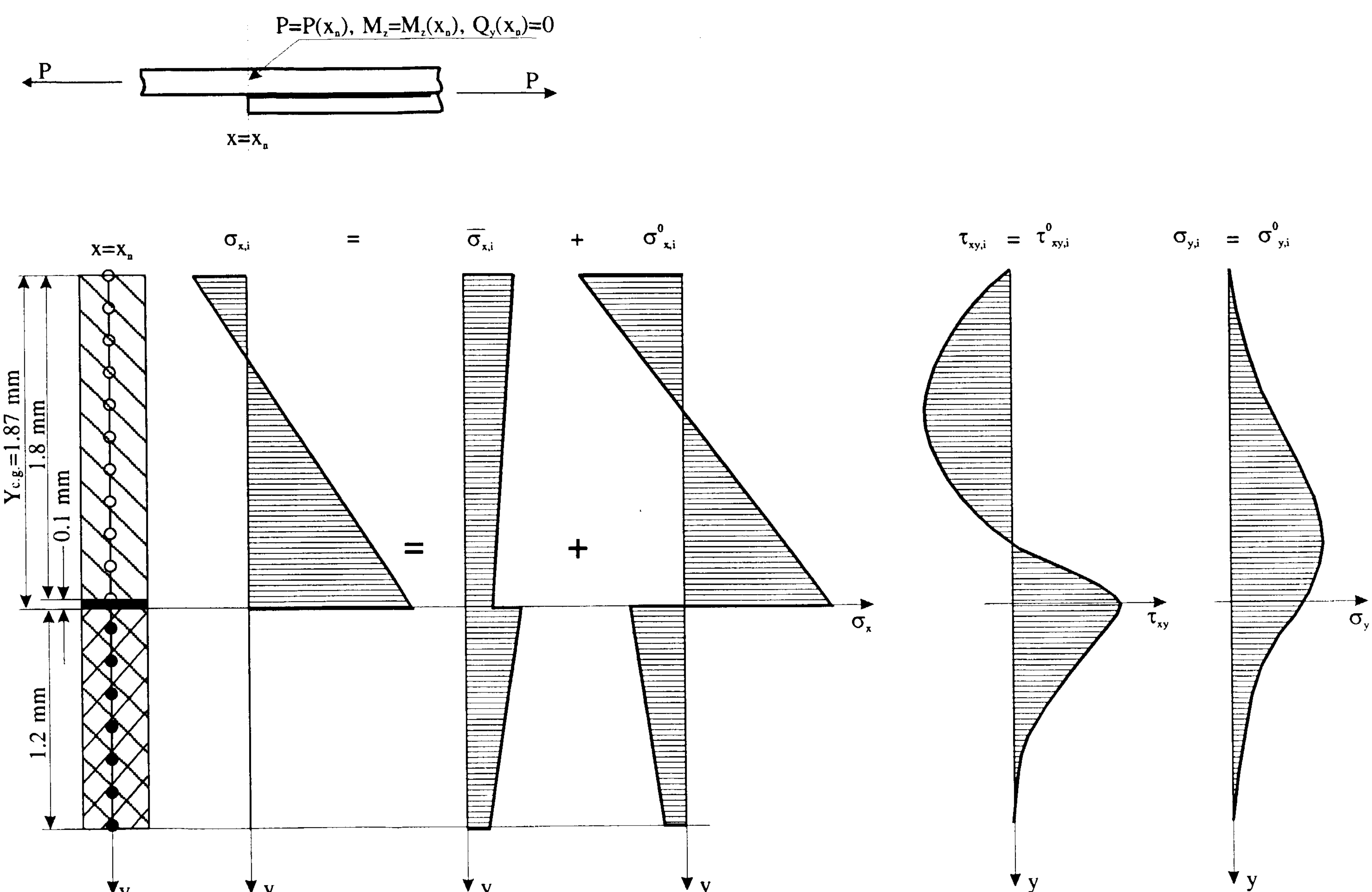

Figure 3.5. Fundamental and correction solutions for section $x=x_n$

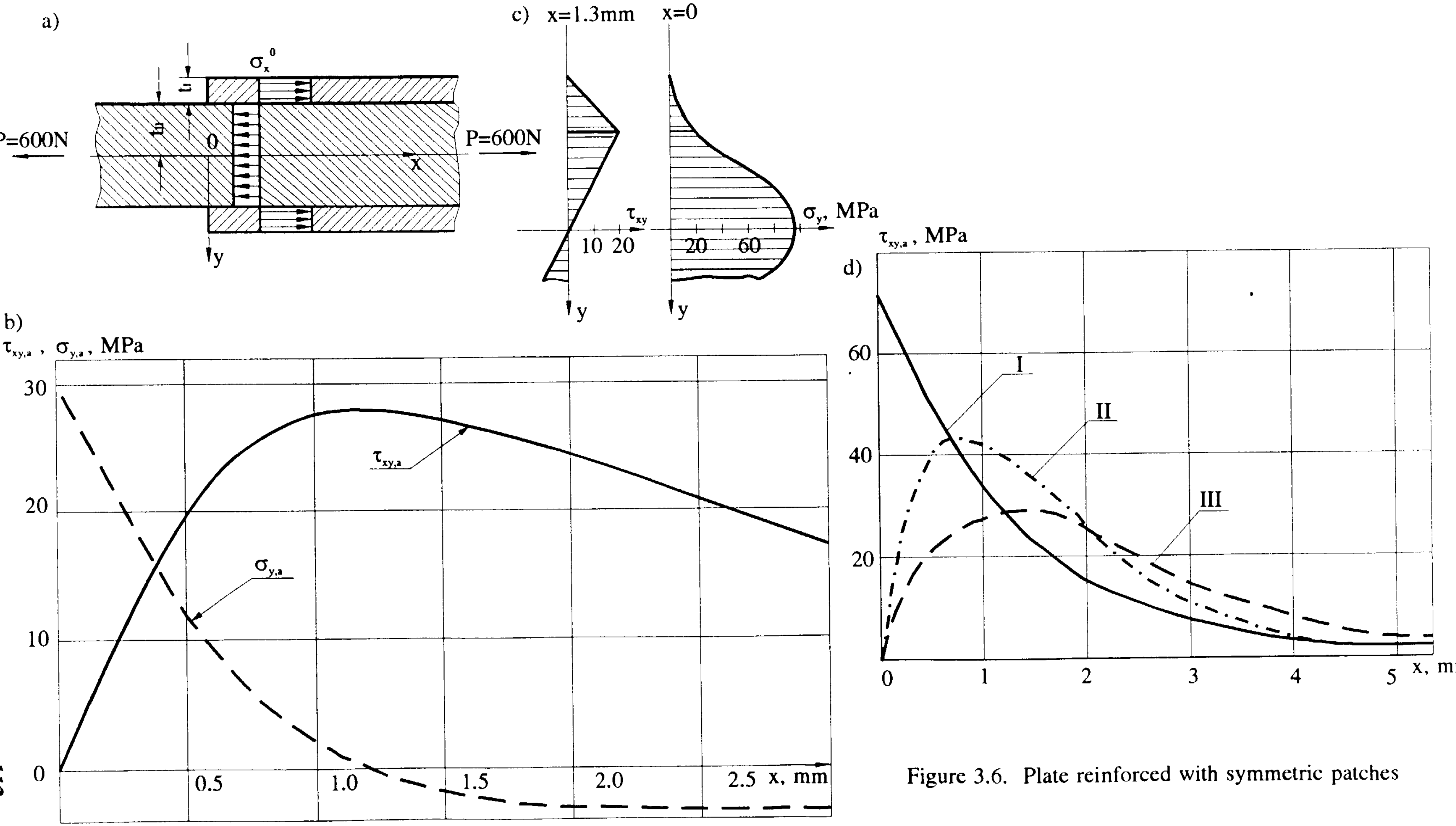

Figure 3.6. Plate reinforced with symmetric patches

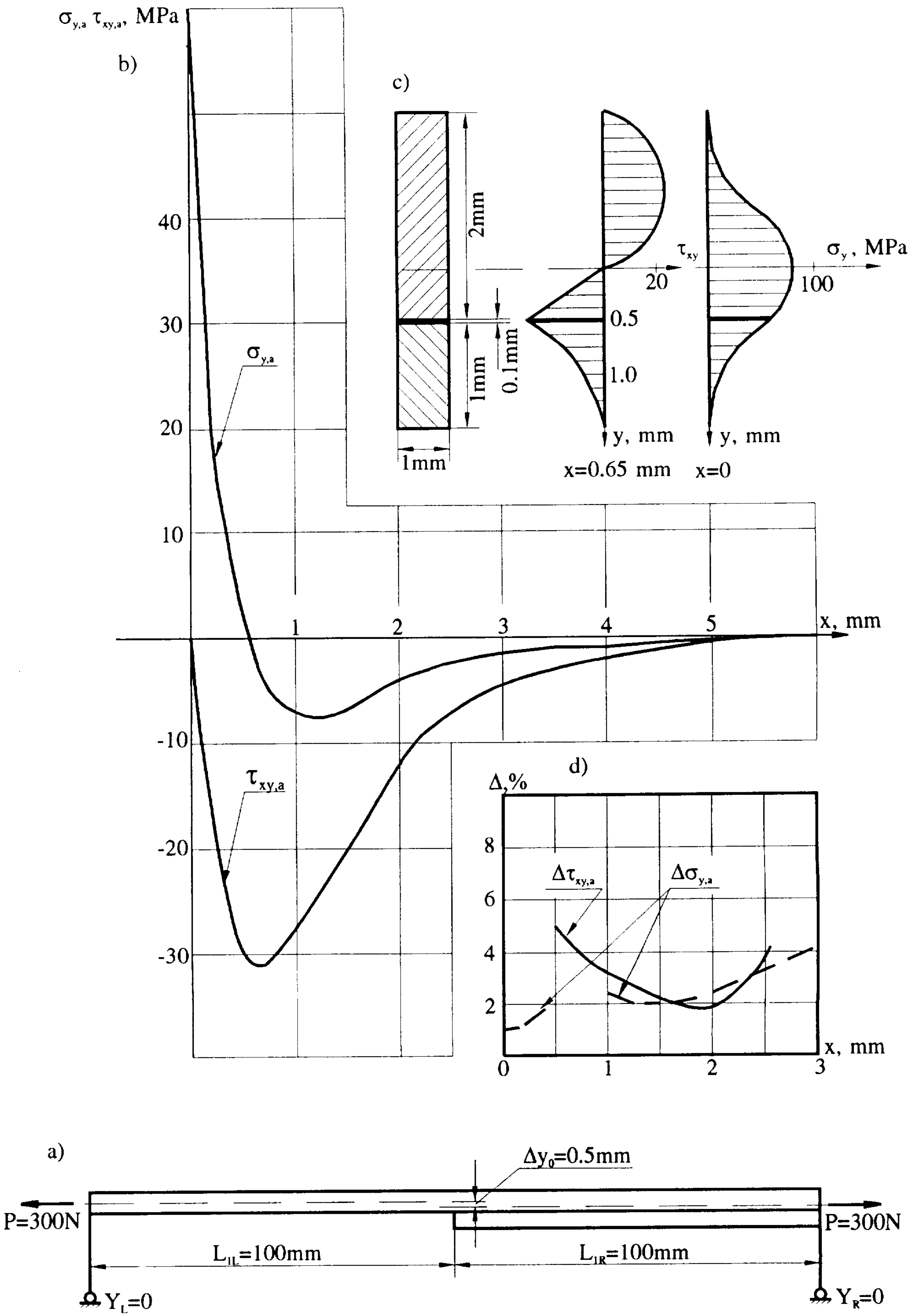

Figure 3.7. Plate a one-sided doubler

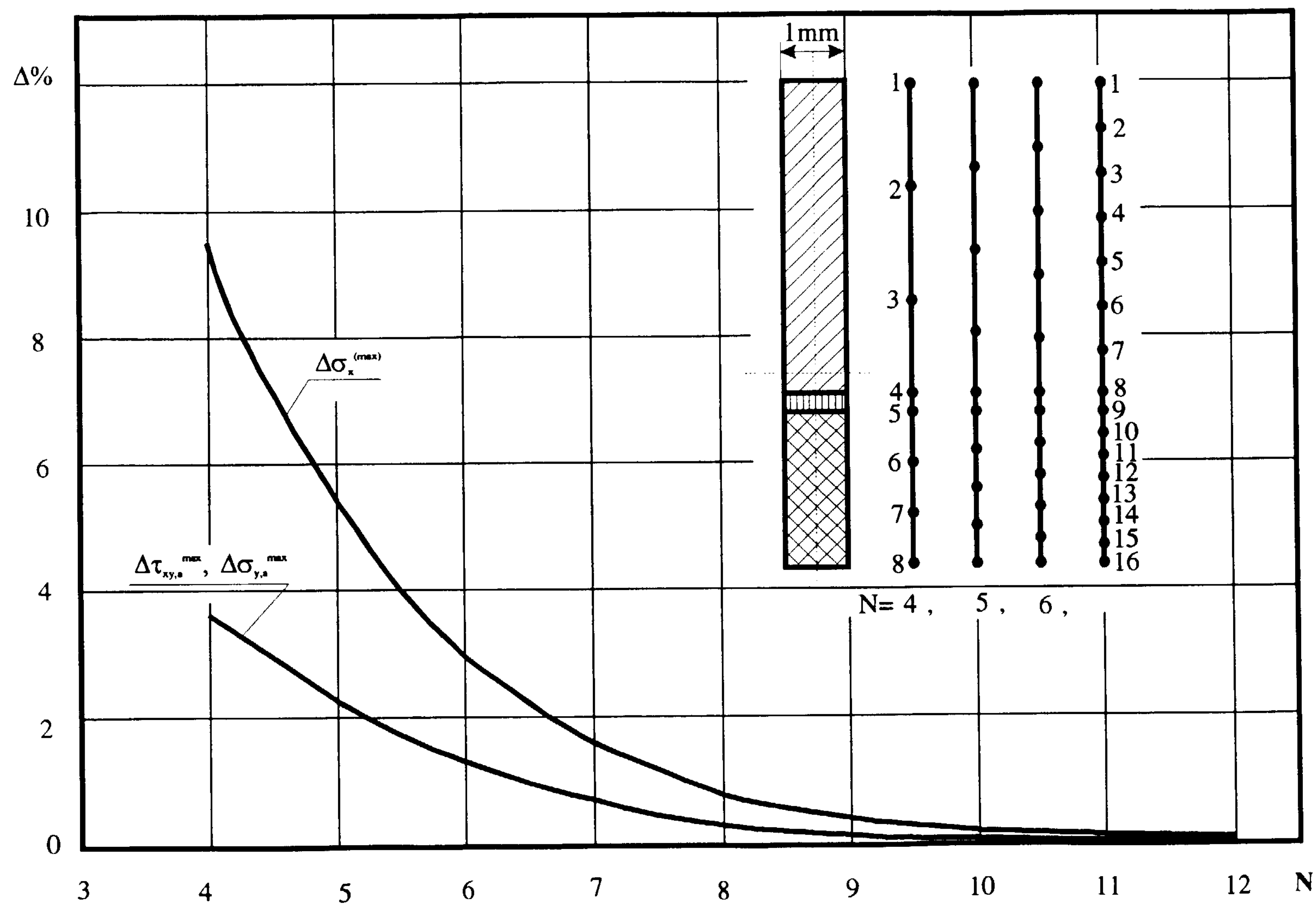

Figure 3.8. The influence of model discretization degree on accuracy of analyses

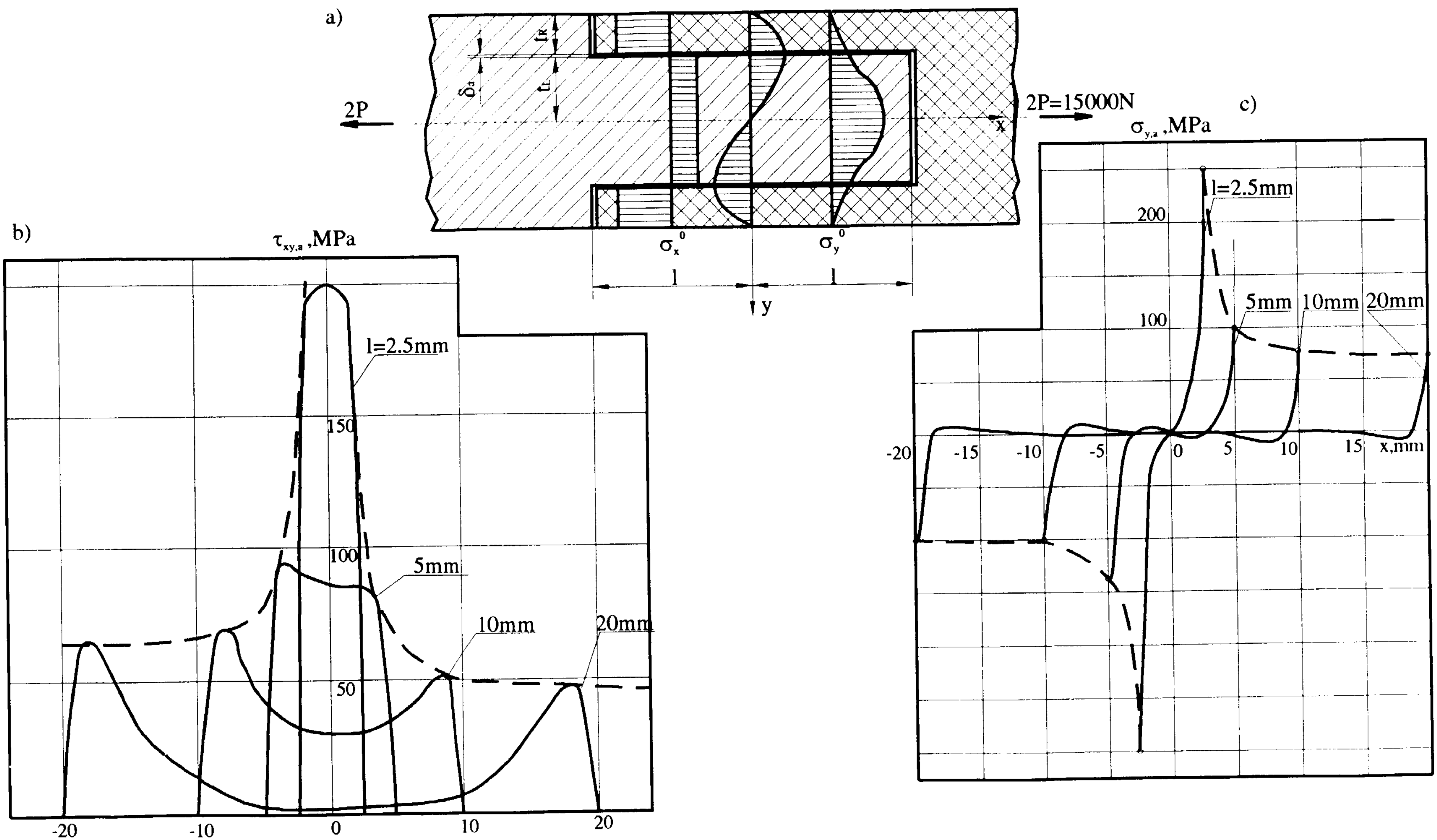

Figure 3.9. Inserted adhesive joint

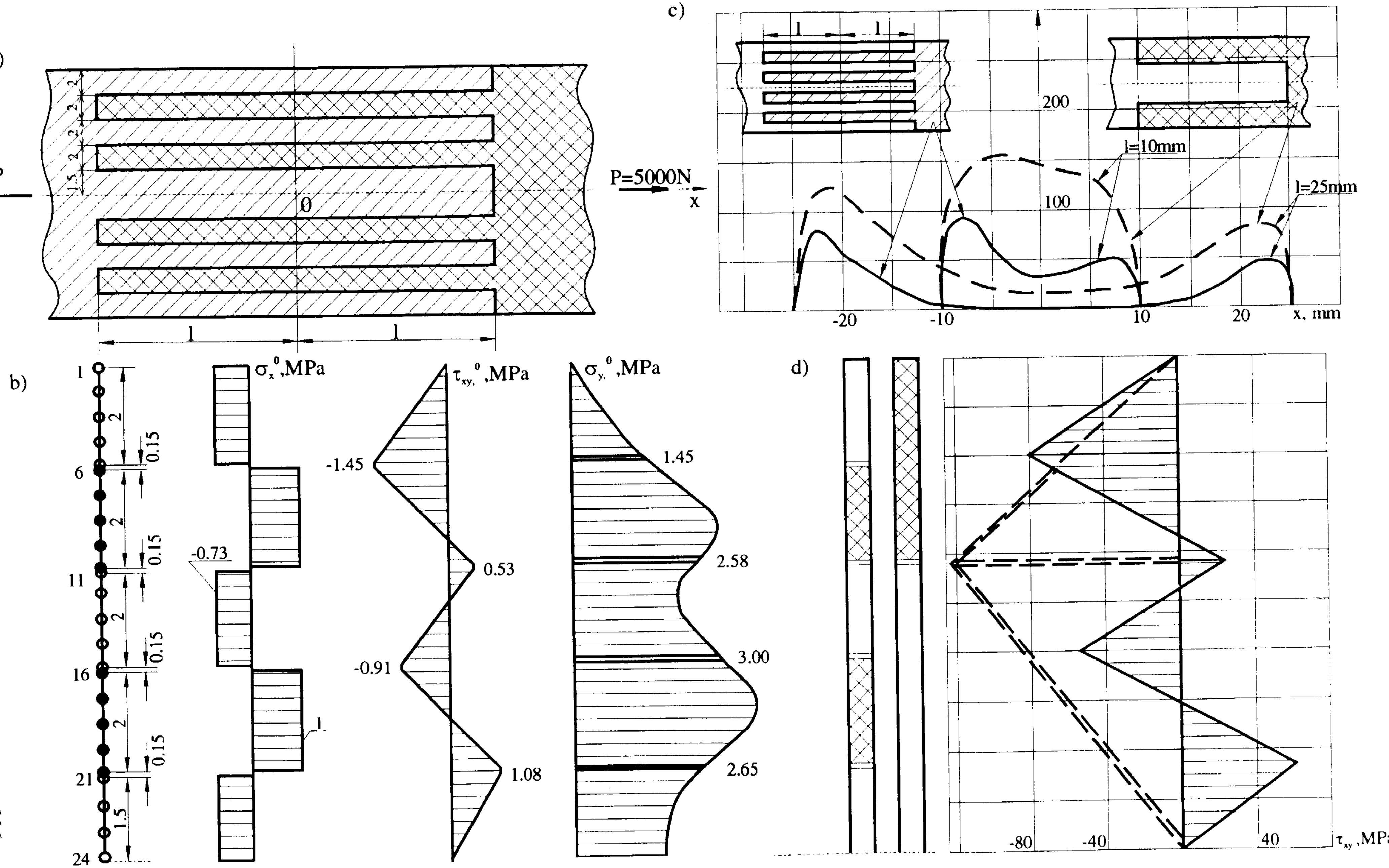

Figure 3.10. Multilayered adhesive joint

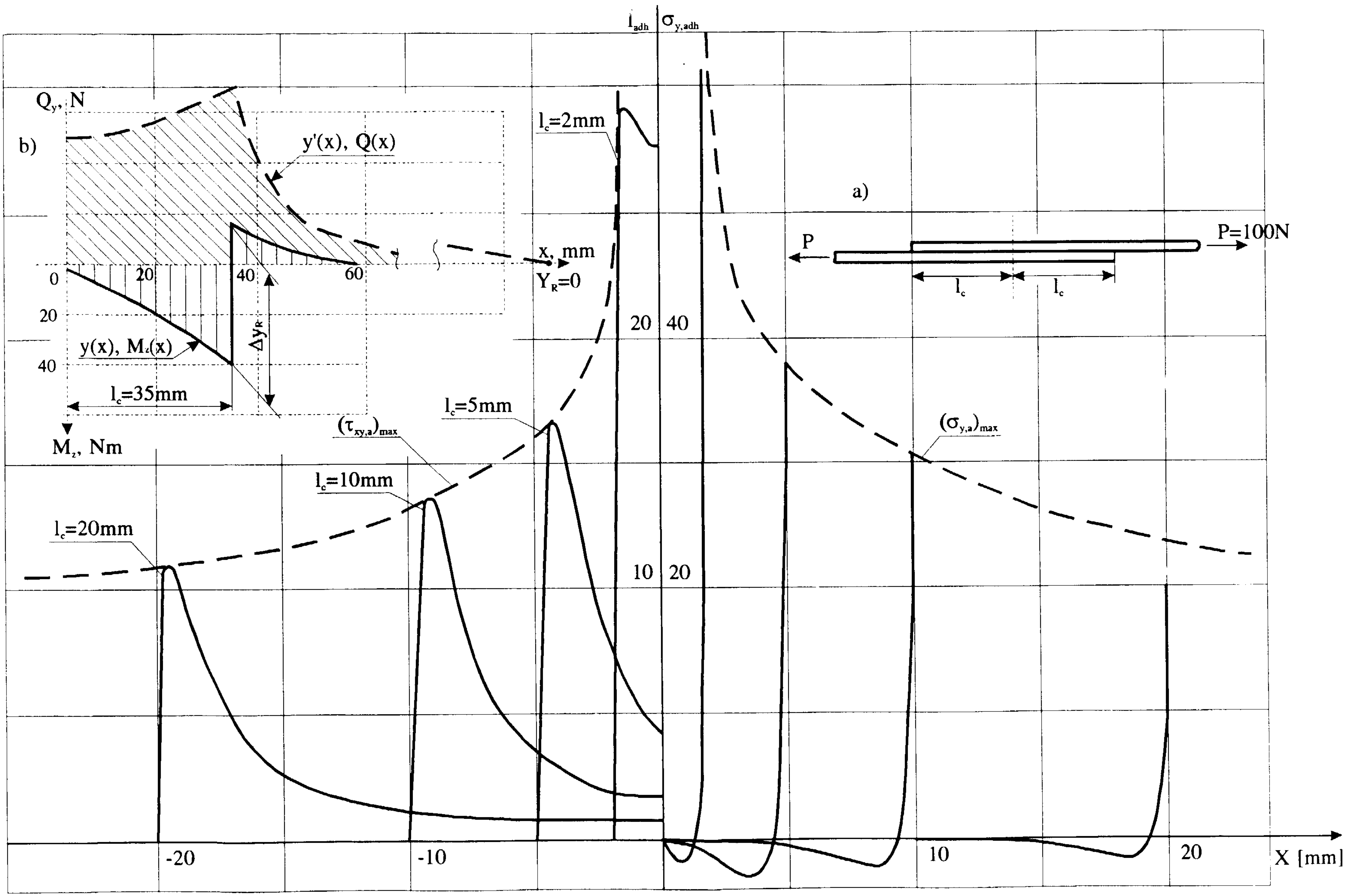

Figure 3.11. The effect of overlap area length on stresses

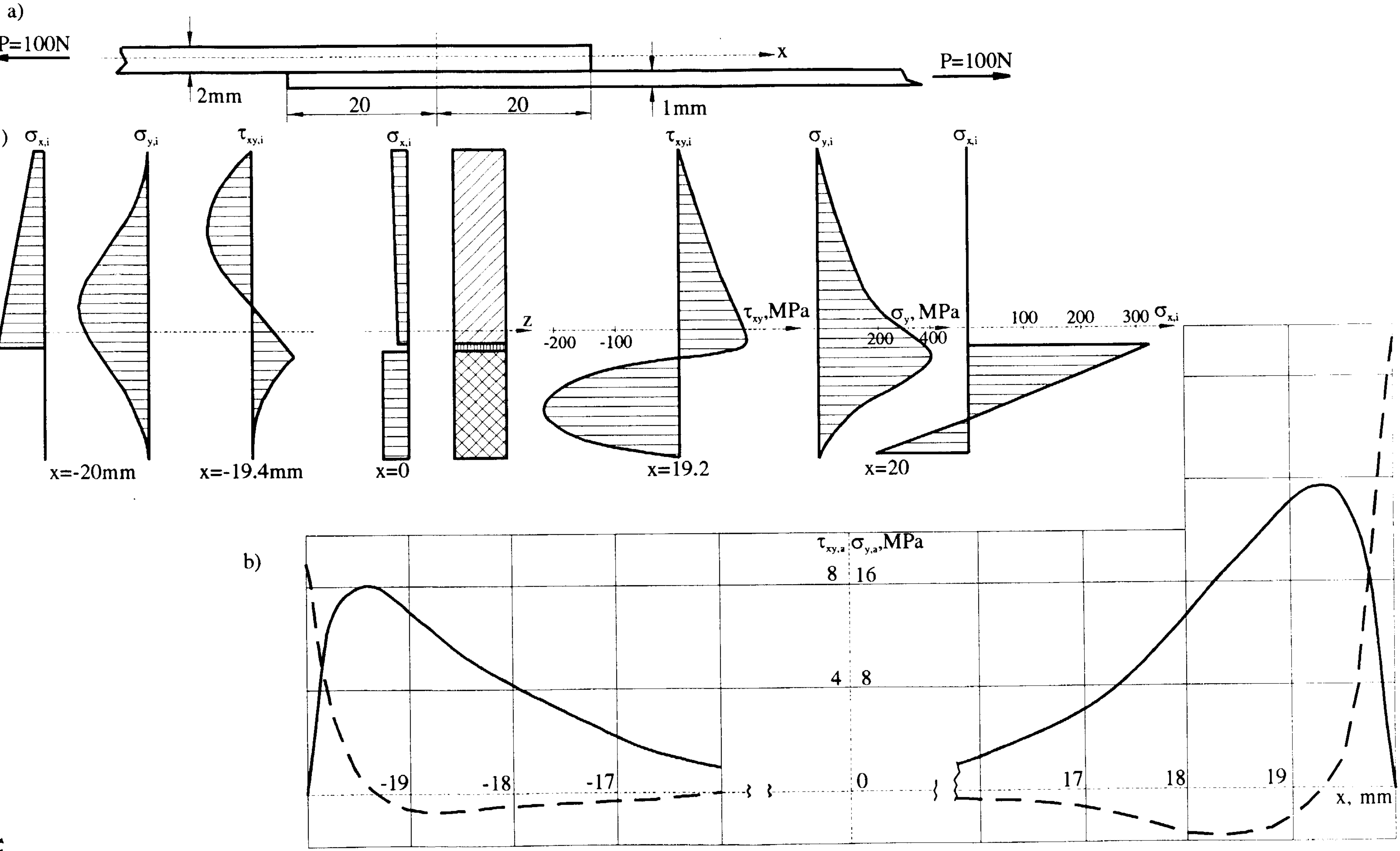

Figure 3.12. Two general sheets with overlap joint

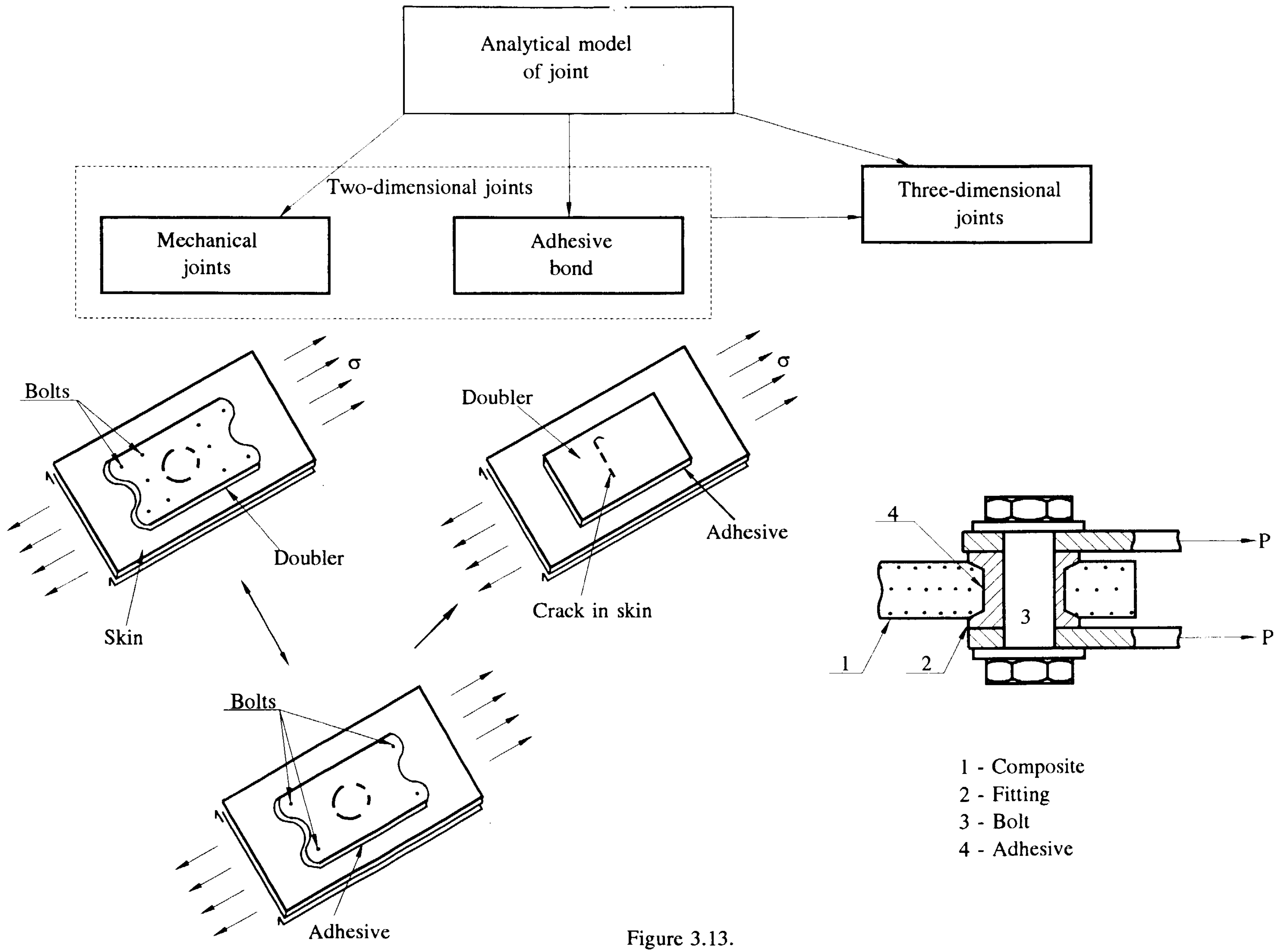

Analytical model of joint
Two-dimensional joints
Mechanical joints
Adhesive bond
Three-dimensional joints
Bolts
Doubler
Skin
σ
Doubler
Adhesive
Crack in skin
σ
Bolts
Adhesive
4
1
2
3
P
P
1 - Composite
2 - Fitting
3 - Bolt
4 - Adhesive

Figure 3.13.

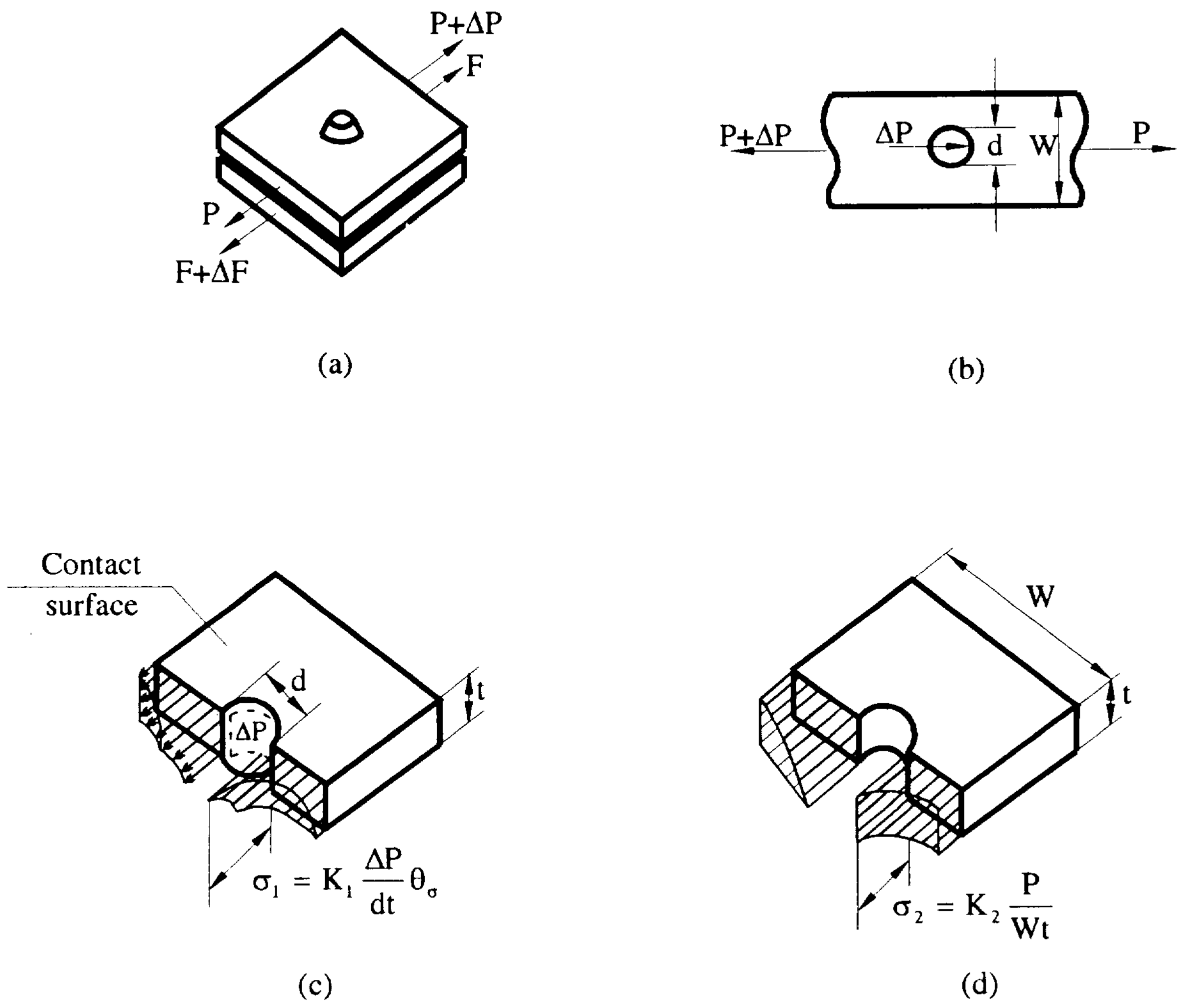
P+ΔP
F
P
F+ΔF
(a)
P+ΔP
ΔP
d
W
P
(b)
Contact
surface
d
ΔP
t
$\sigma_1 = K_1 \frac{\Delta P}{dt} \theta_\sigma$
(c)
W
t
$\sigma_2 = K_2 \frac{P}{Wt}$
(d)

Figure 3.14.

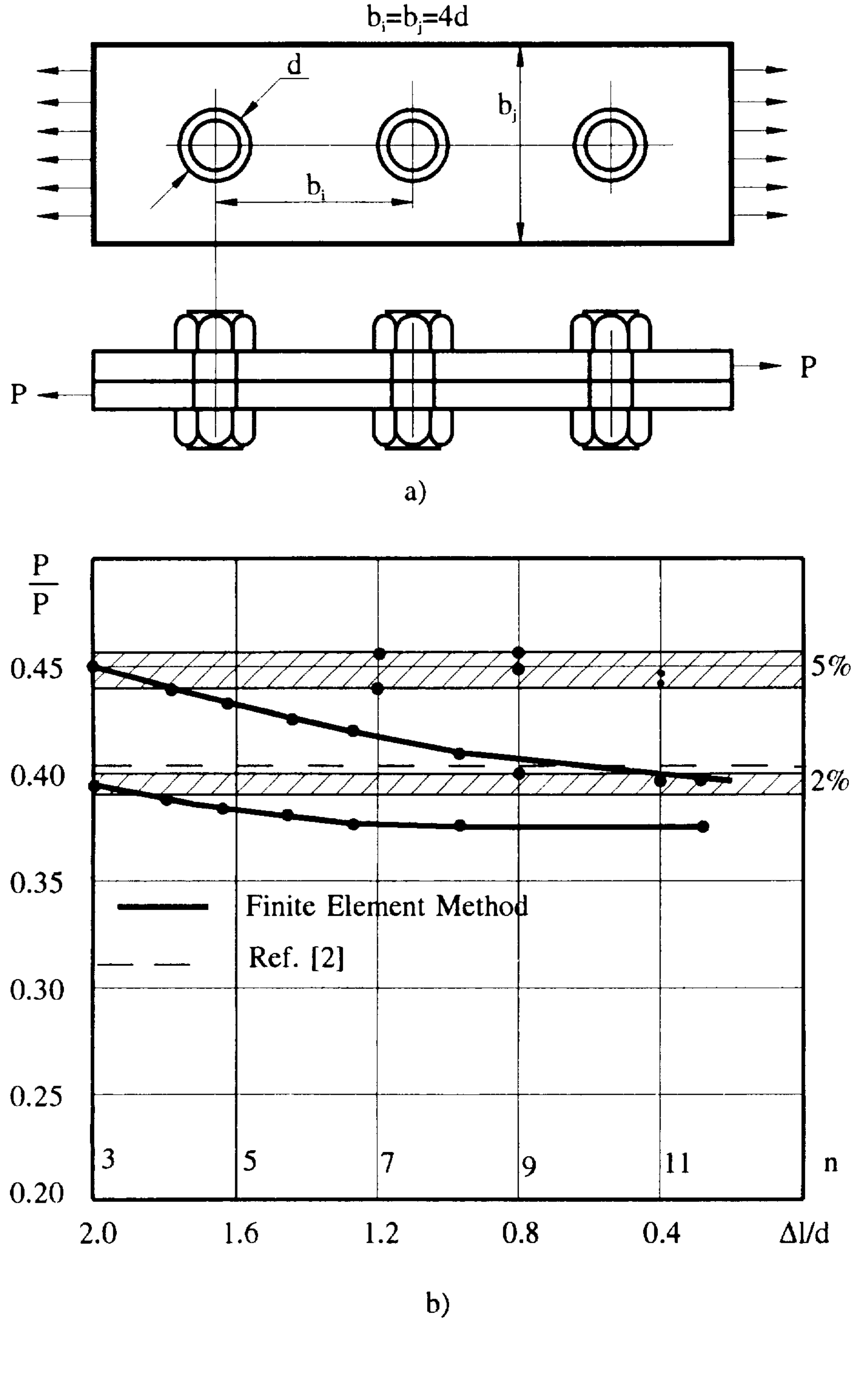

$b_i = b_j = 4d$
d
b_j
b_i
P
P
a)
$\frac{P}{P}$
0.45
0.40
0.35
0.30
0.25
0.20
5%
2%
Finite Element Method
Ref. [2]
3
5
7
9
11
n
2.0
1.6
1.2
0.8
0.4
$\Delta l/d$
b)

Figure 3.15.

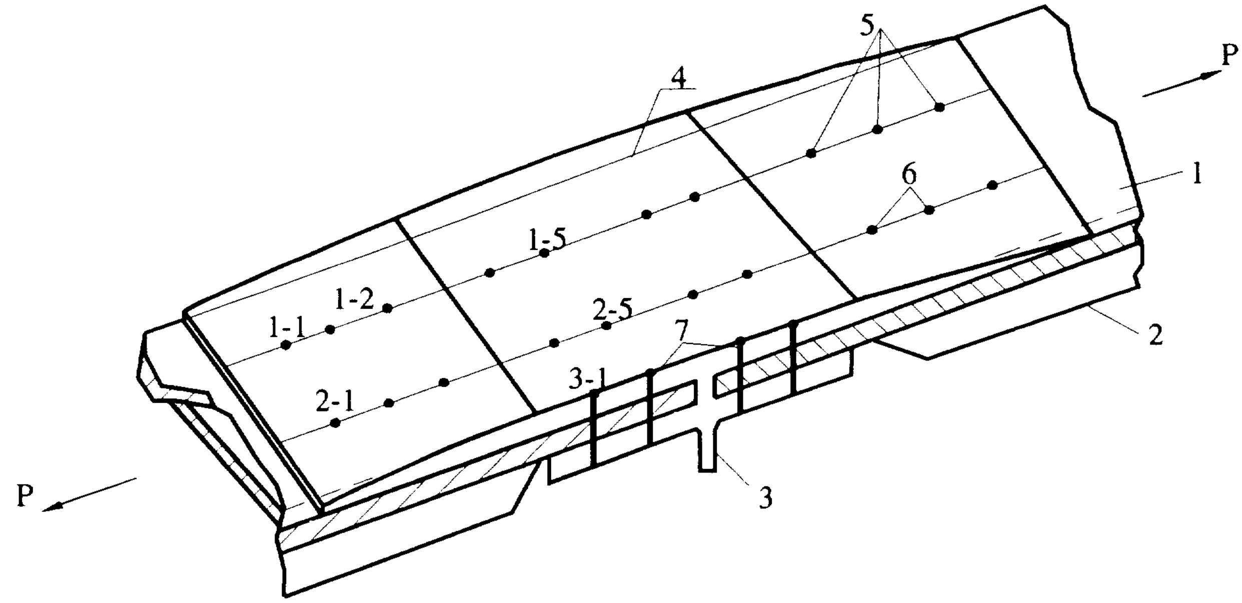

a)

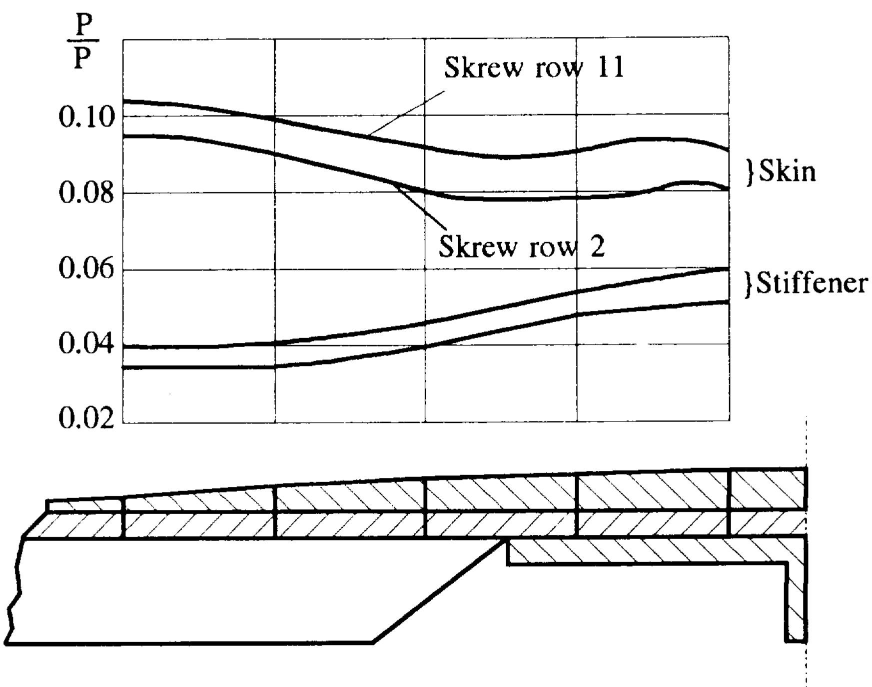

b)

Figure 3.16.

1 - Skin, 2 - Stiffener, 3 - Fitting, 4 - Doubler, 5 - Screw row 1, 6 - Screw row 2, 7 - Screw row 3.

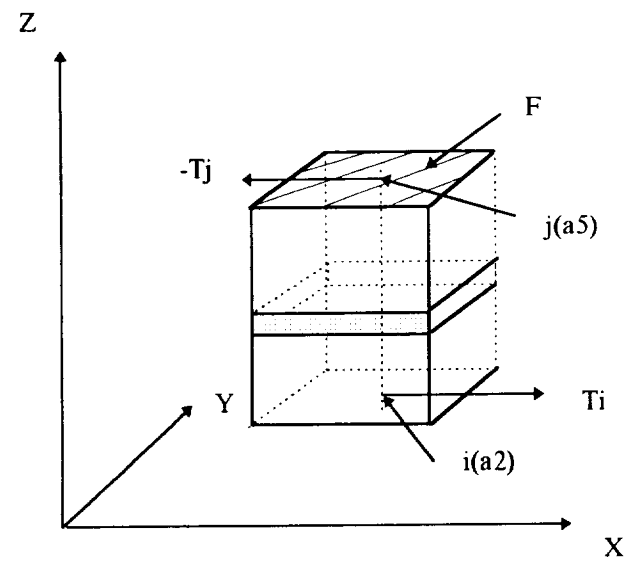

a).

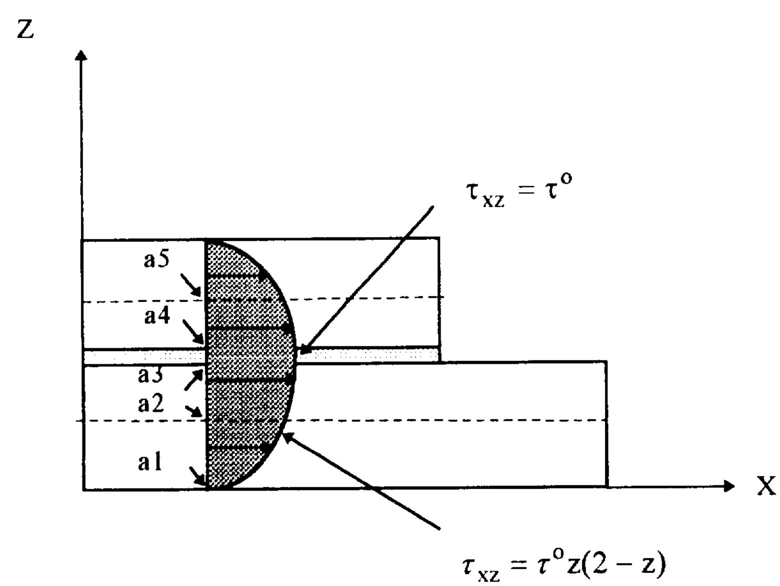

b).

Figure 3.17 Modeling the shear stresses

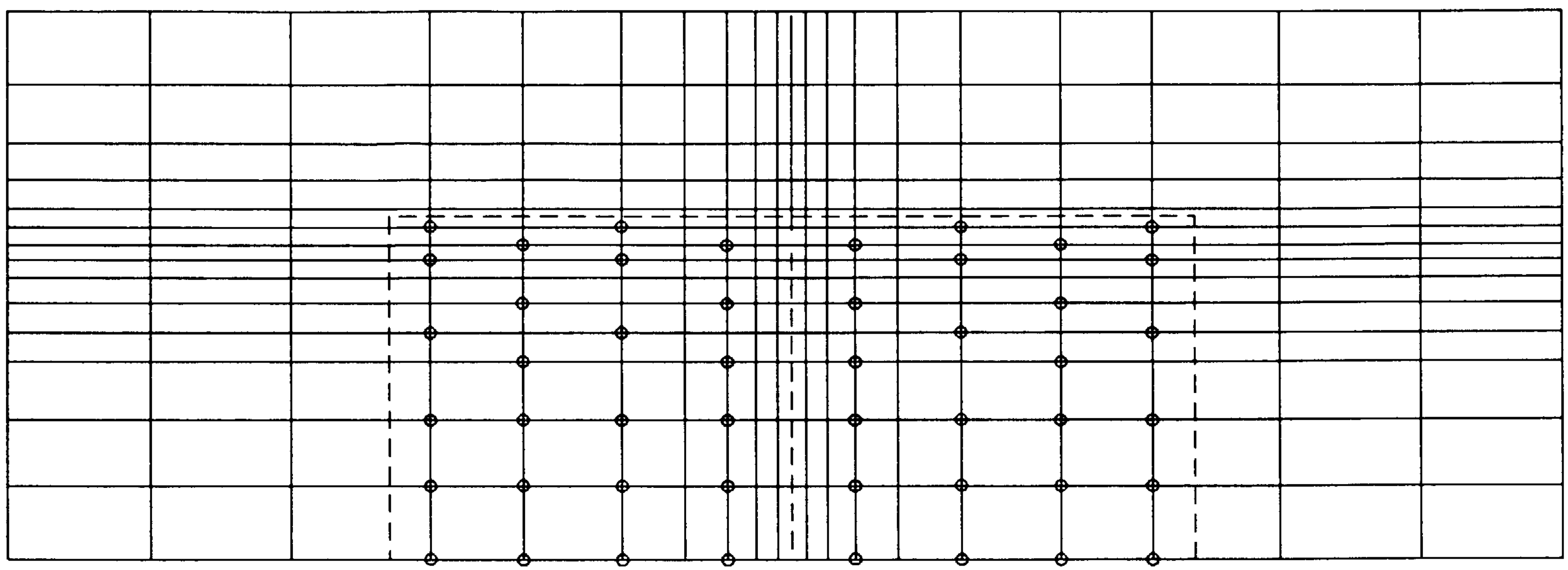

Figure 3.18.

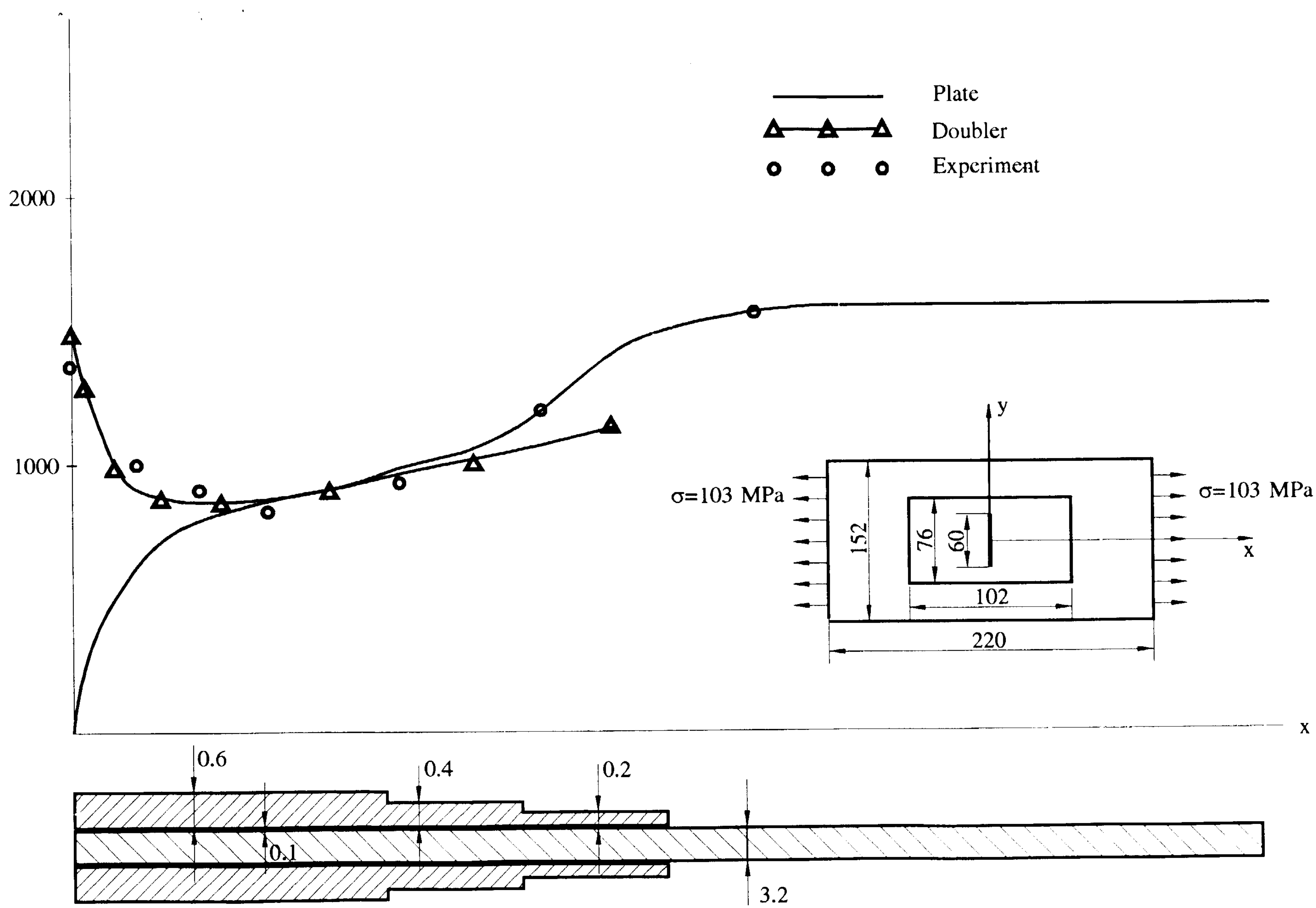

Plate
Doubler
Experiment
2000
1000
x
σ=103 MPa
σ=103 MPa
y
x
152
76
60
102
220
0.6
0.4
0.2
0.1
3.2

Figure 3.19.

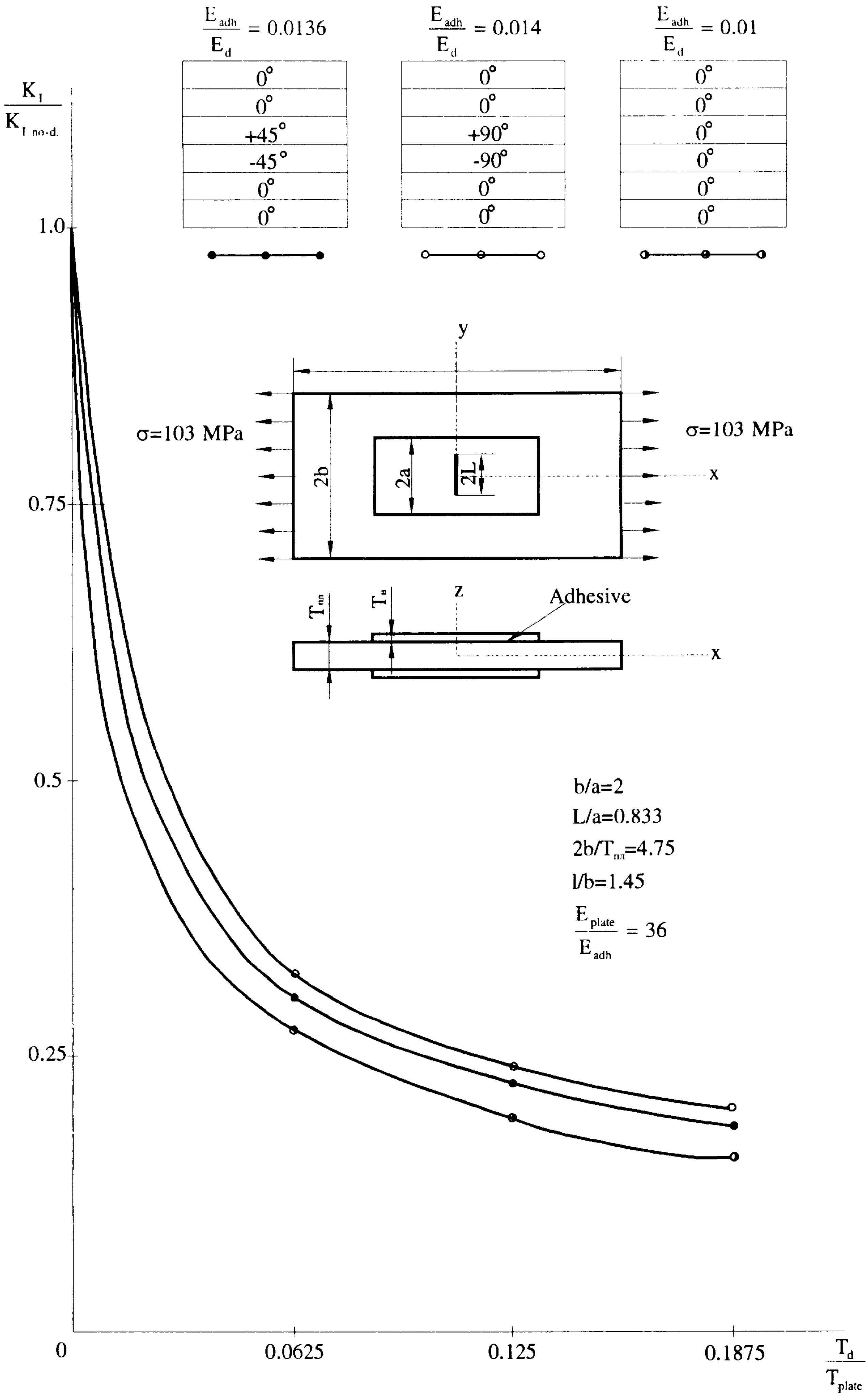

$\frac{E_{adh}}{E_d} = 0.0136$
0°
0°
+45°
-45°
0°
0°
$\frac{E_{adh}}{E_d} = 0.014$
0°
0°
+90°
-90°
0°
0°
$\frac{E_{adh}}{E_d} = 0.01$
0°
0°
0°
0°
0°
0°
$\frac{K_I}{K_{I\ no\text{-}d.}}$
1.0
0.75
0.5
0.25
0
0.0625
0.125
0.1875
$\frac{T_d}{T_{plate}}$
y
x
z
σ=103 MPa
σ=103 MPa
2b
2a
2L
$T_{пл}$
T_{a}
Adhesive
b/a=2
L/a=0.833
$2b/T_{пл}=4.75$
l/b=1.45
$\frac{E_{plate}}{E_{adh}} = 36$

Figure 3.20

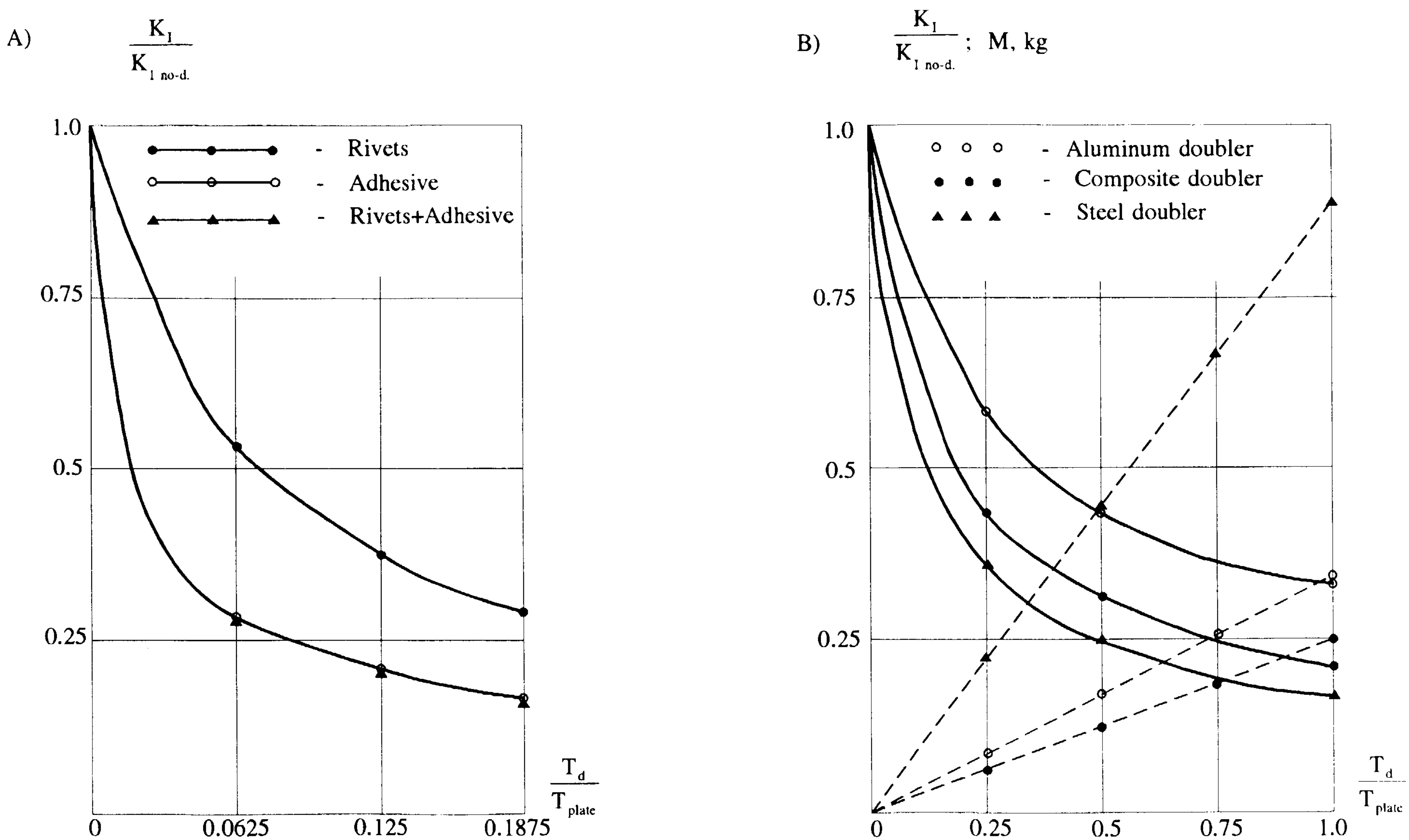
A)
K_I / K_I no-d.
1.0
0.75
0.5
0.25
0
0.0625
0.125
0.1875
T_d / T_plate
- Rivets
- Adhesive
- Rivets+Adhesive
B)
K_I / K_I no-d. ; M, kg
1.0
0.75
0.5
0.25
0
0.25
0.5
0.75
1.0
T_d / T_plate
- Aluminum doubler
- Composite doubler
- Steel doubler

Figure 3.21.

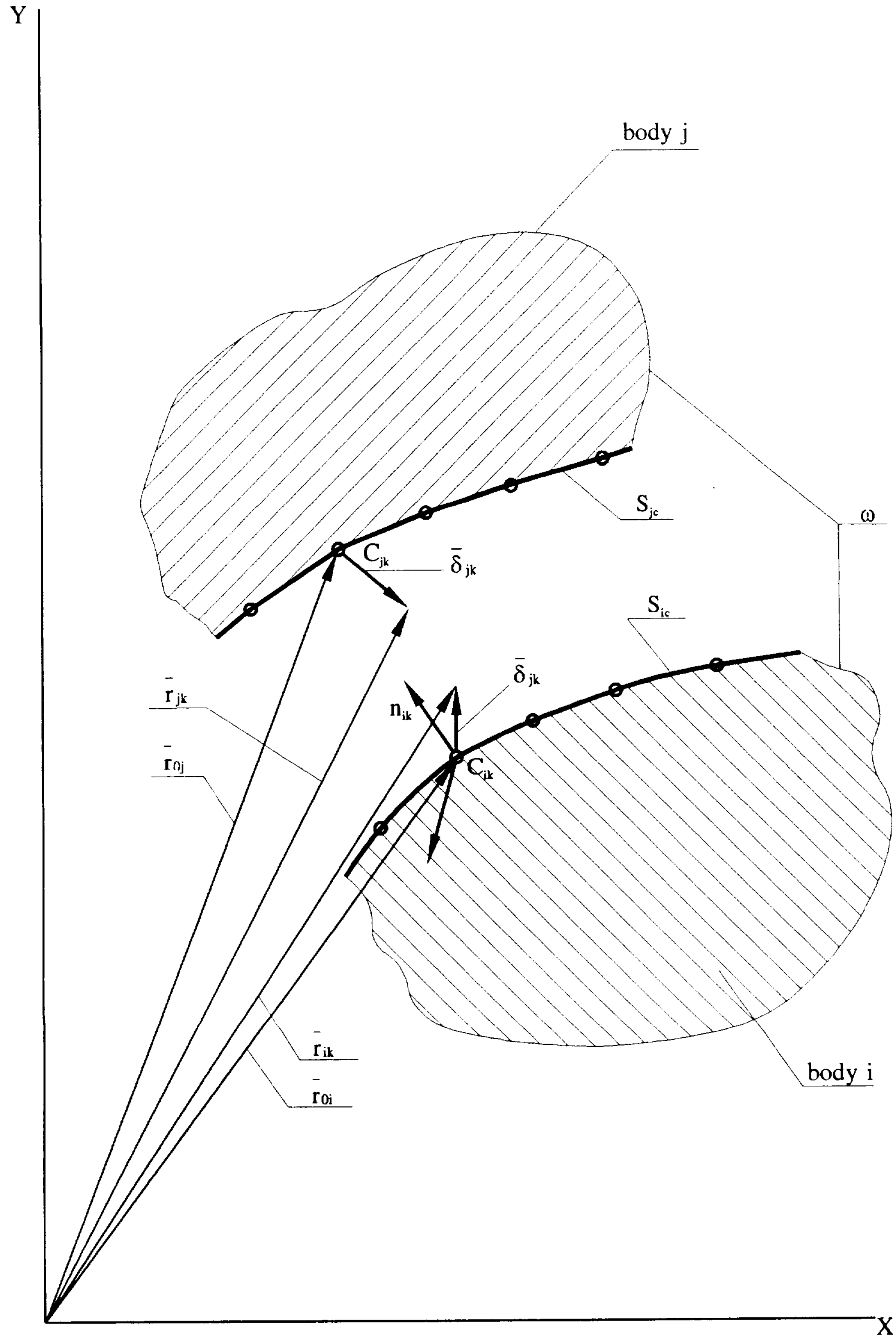

Figure 3.22. Illustration of kinematics

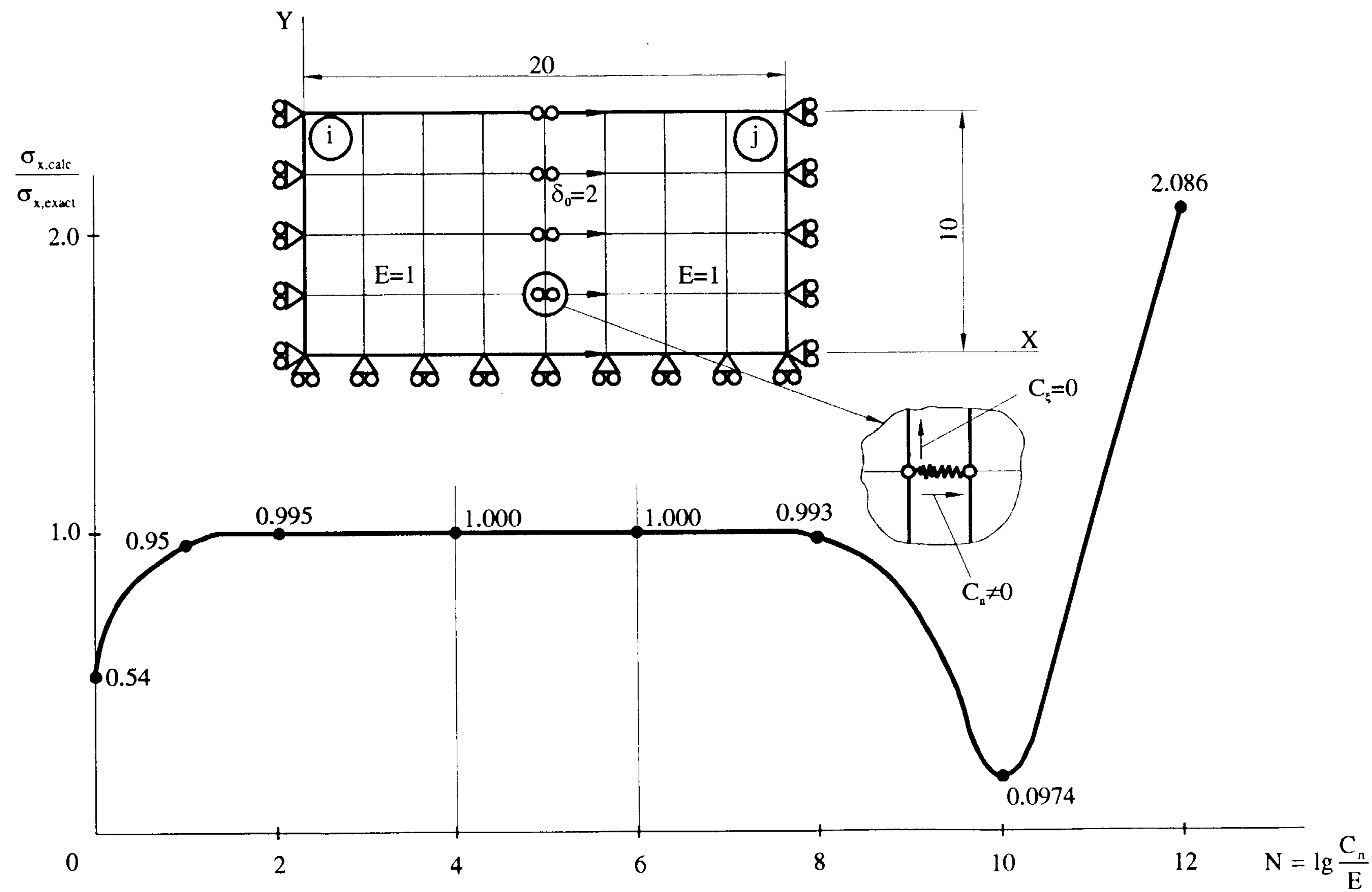

Figure 3.23. Dependence of stresses σ_x on parameter N

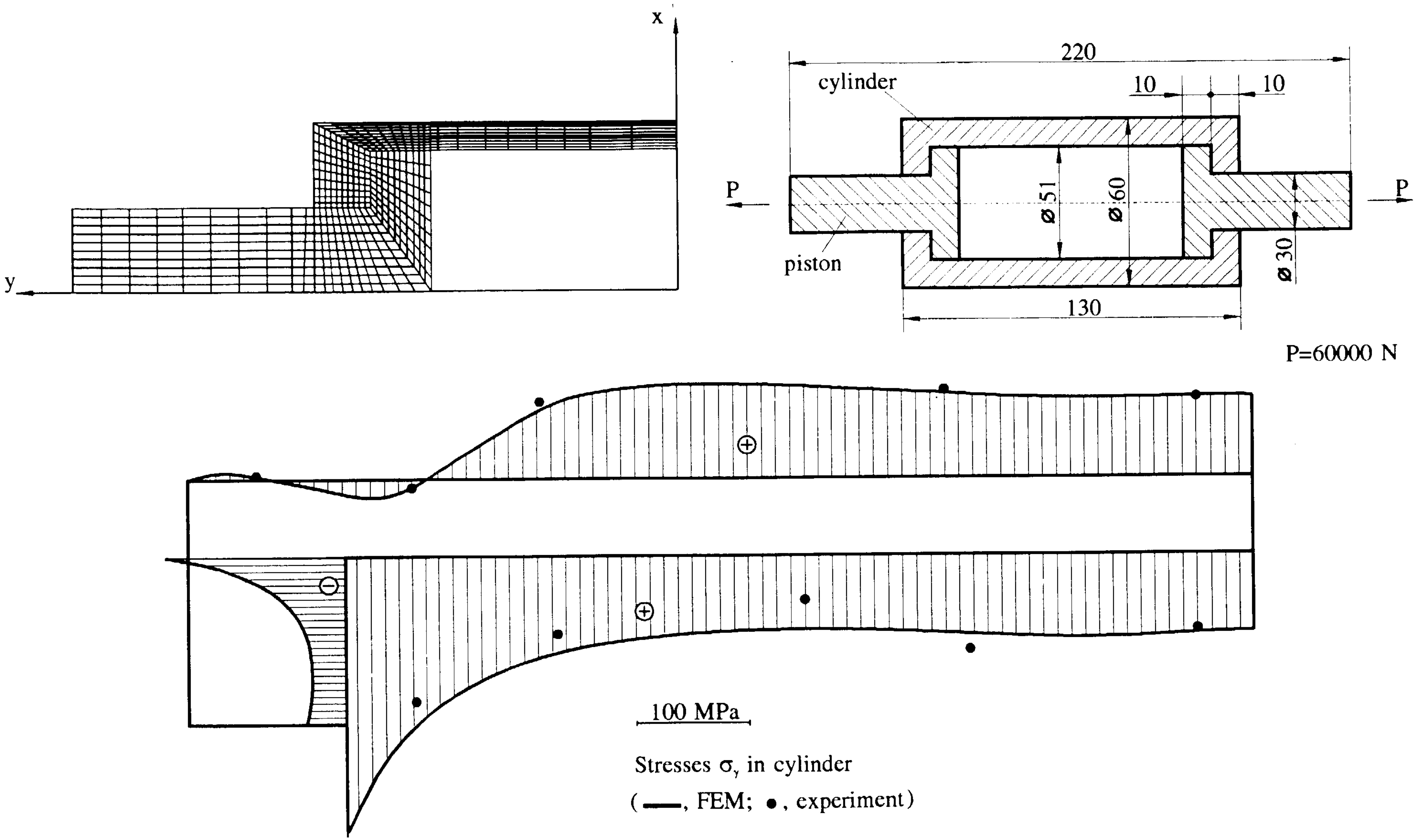
x
y
220
cylinder
10
10
P
P
piston
ø 51
ø 60
ø 30
130
P=60000 N
100 MPa
Stresses σ_y in cylinder
(—, FEM; •, experiment)

Figure 3.24.

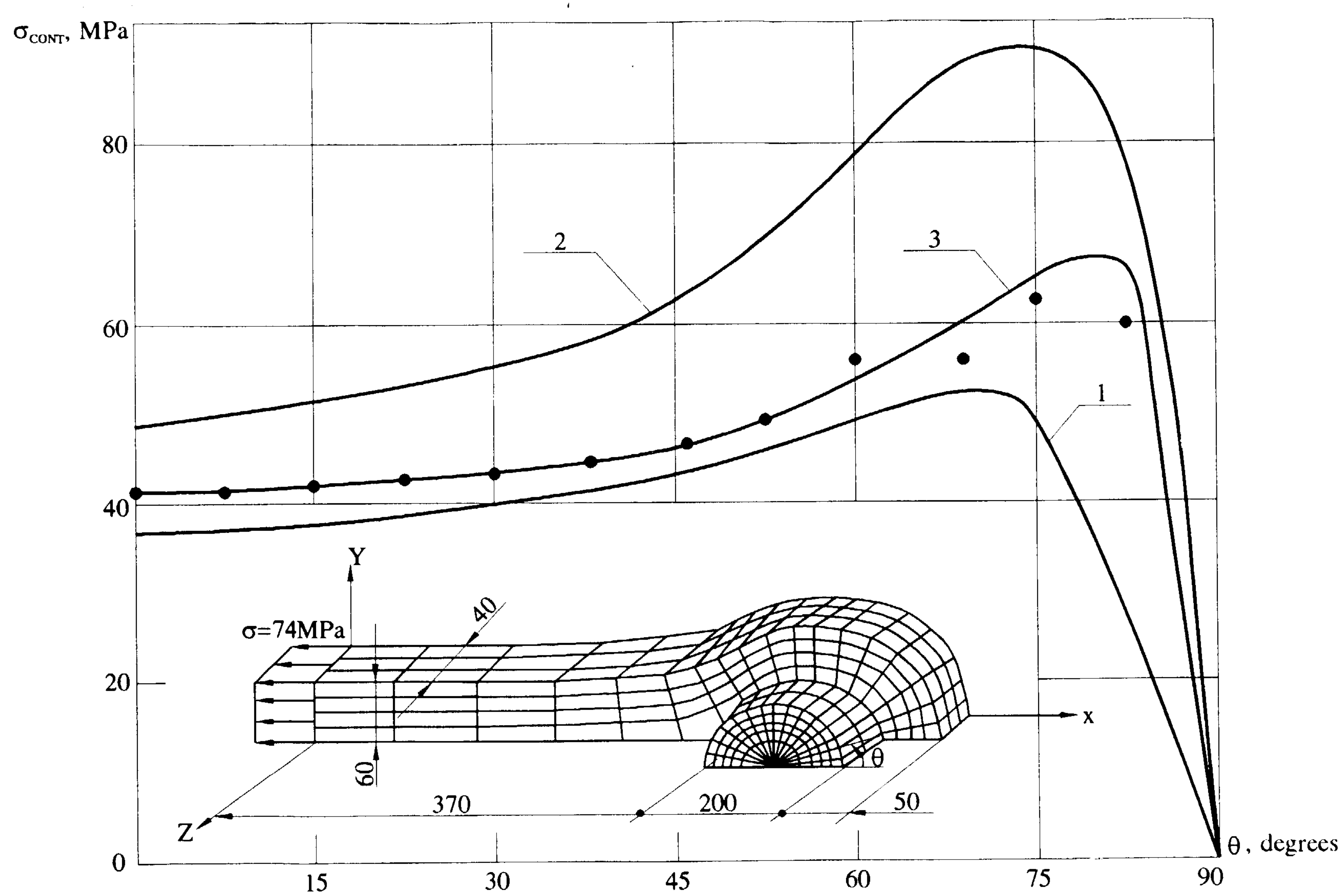

Figure 3.25. Contact interaction of bolt and lug (1, FEM (section Z=0); 2, FEM (section Z=40mm); 3, data from [10]; ●, data from [10])

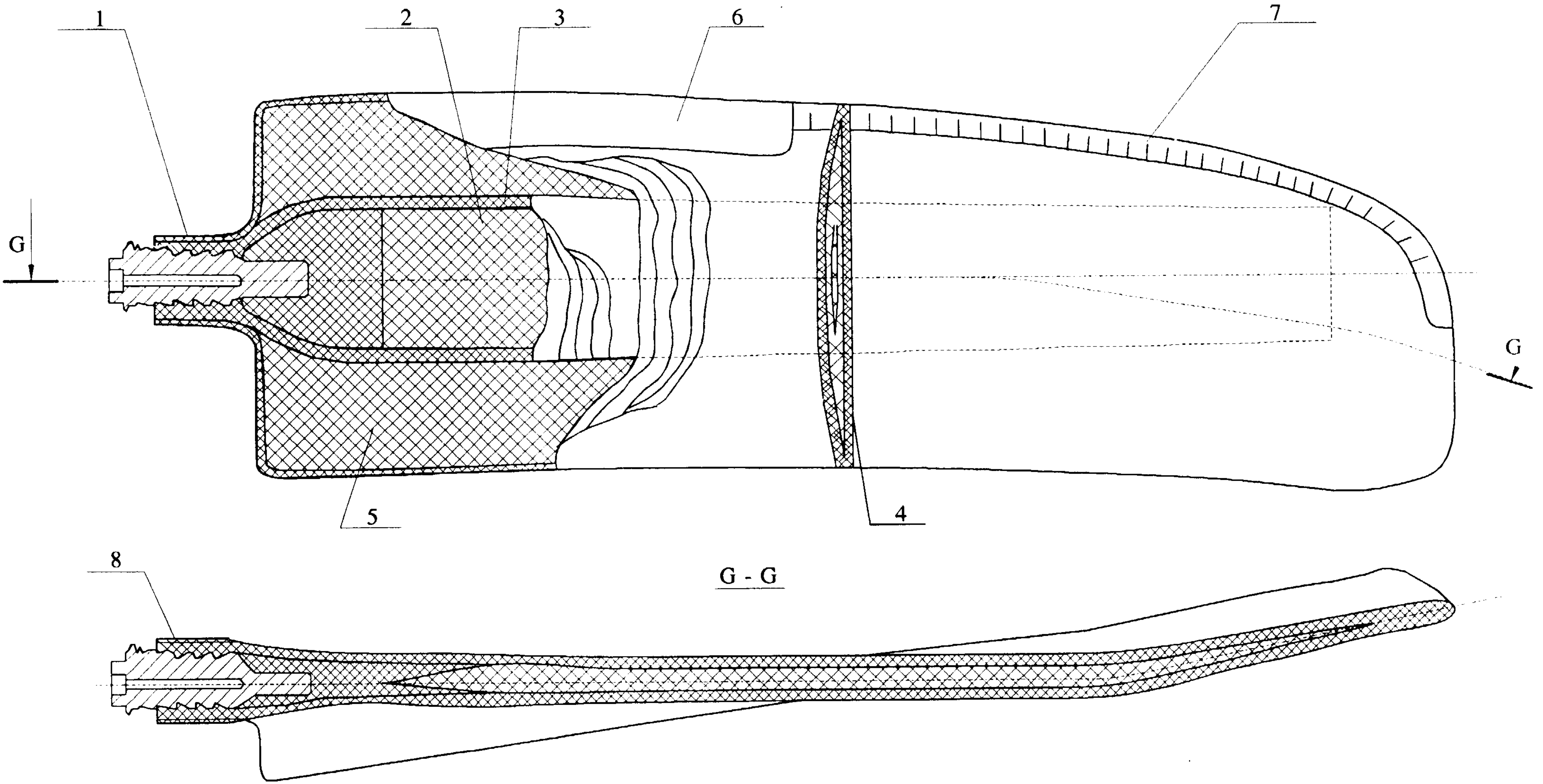

Figure 3.26. Propfan blade (1, metallic fitting; 2, foam core; 3, spar; 4, polymer matrix composite shell; 5, foam inserts; 6, heater; 7, leading edge protector (metal); 8, metallic protector on root).

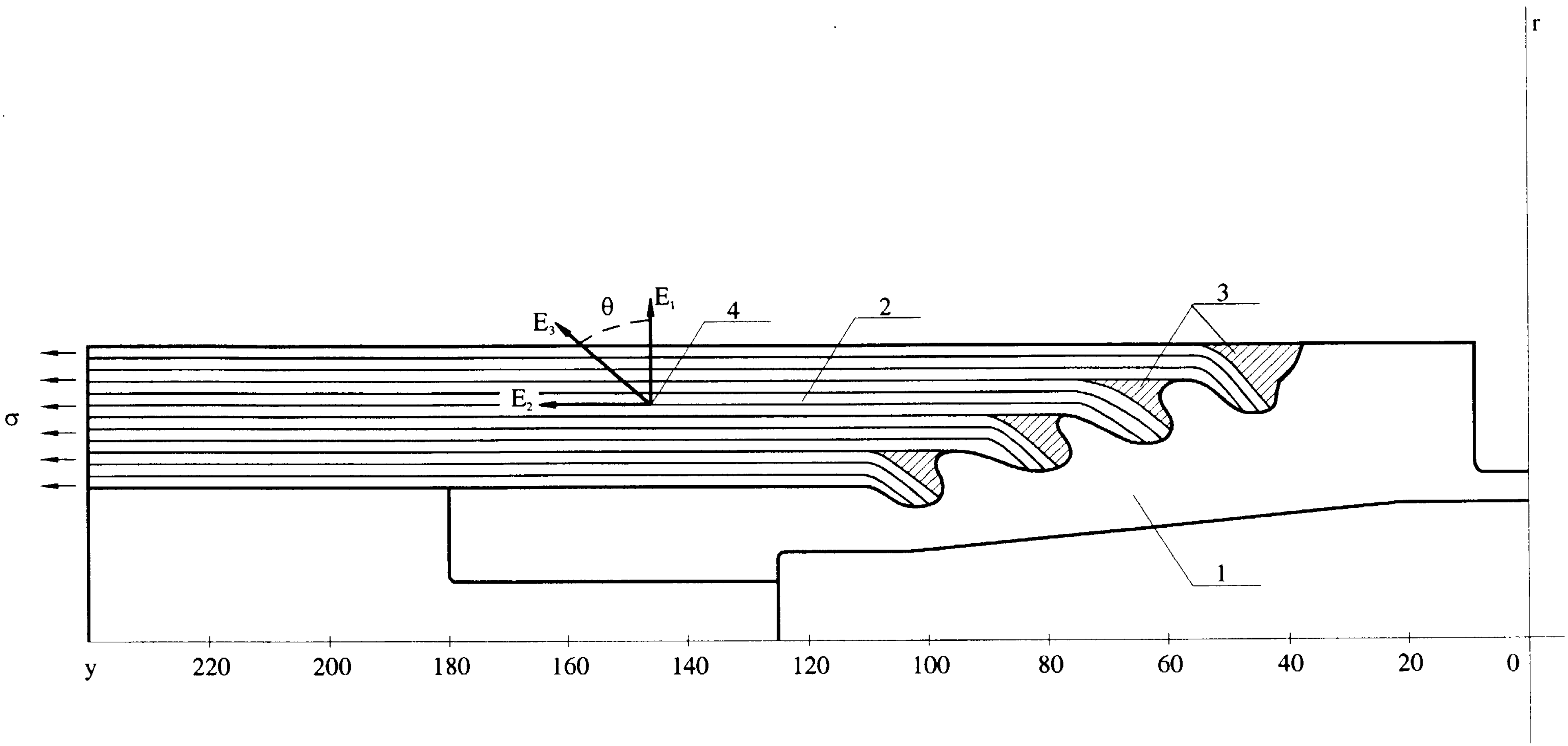

Figure 3.27. Blade/fitting coupling pattern (1, metallic fitting; 2, VPS-20 composite; 3, fiber glass fabric; 4, principal Young moduli)

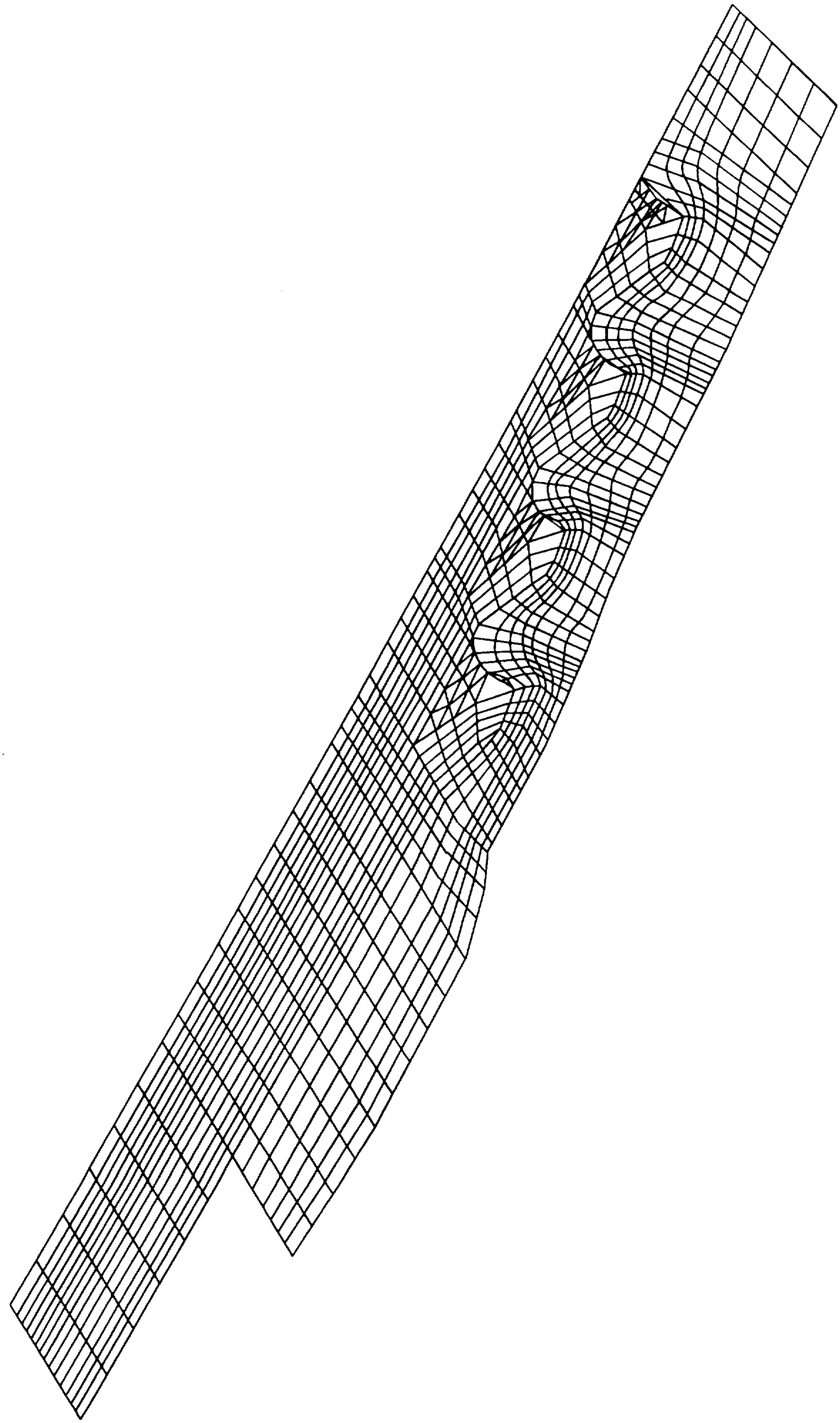

Figure 3.28. Finite element model of propfan blade root

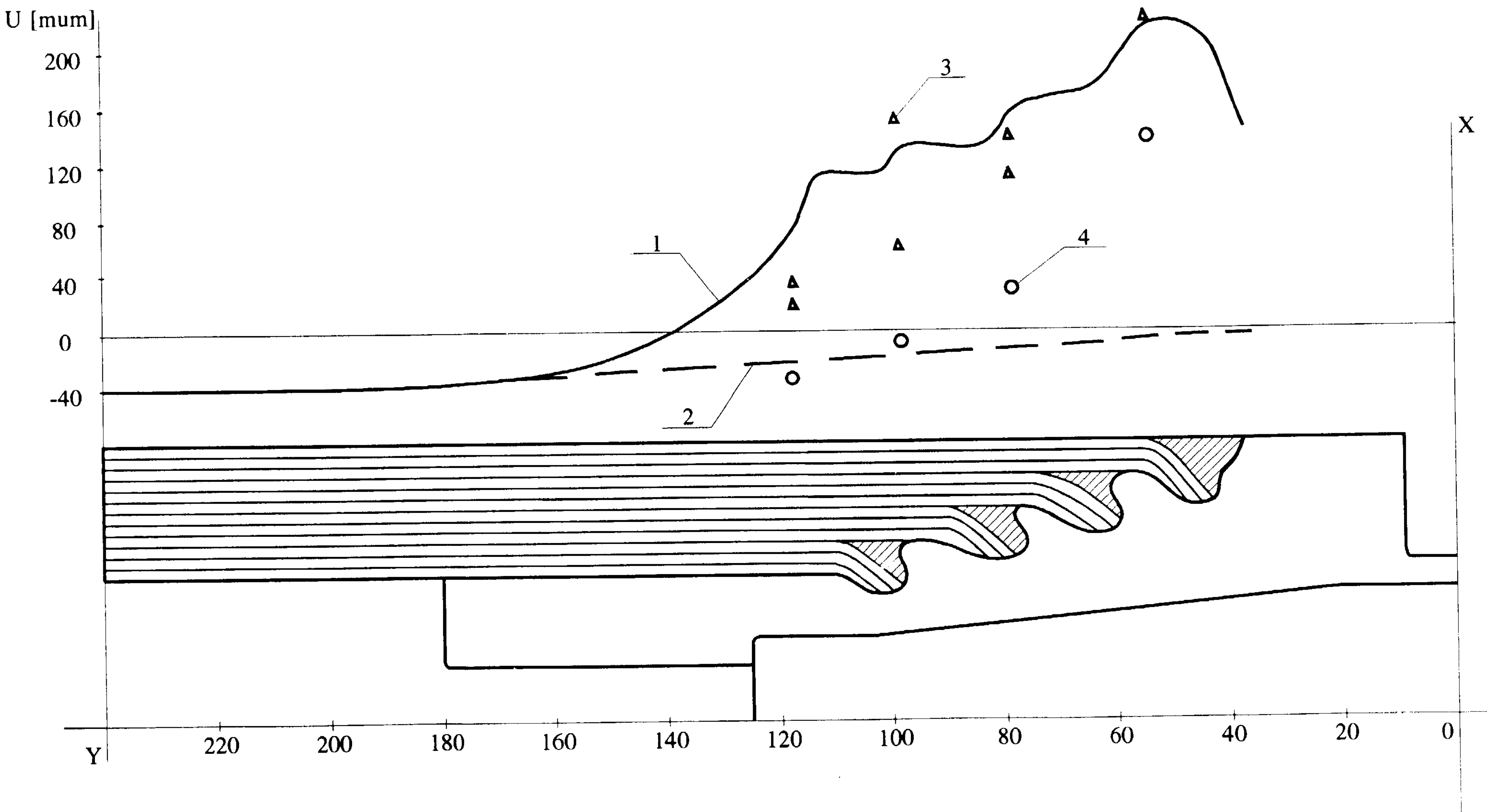

Figure 3.29. Variation of radial displacements U along root axis (1, FEM (rubber layer); 2, FEM (adhesive); 3, experiment (rubber layer); 4, experiment (adhesive))

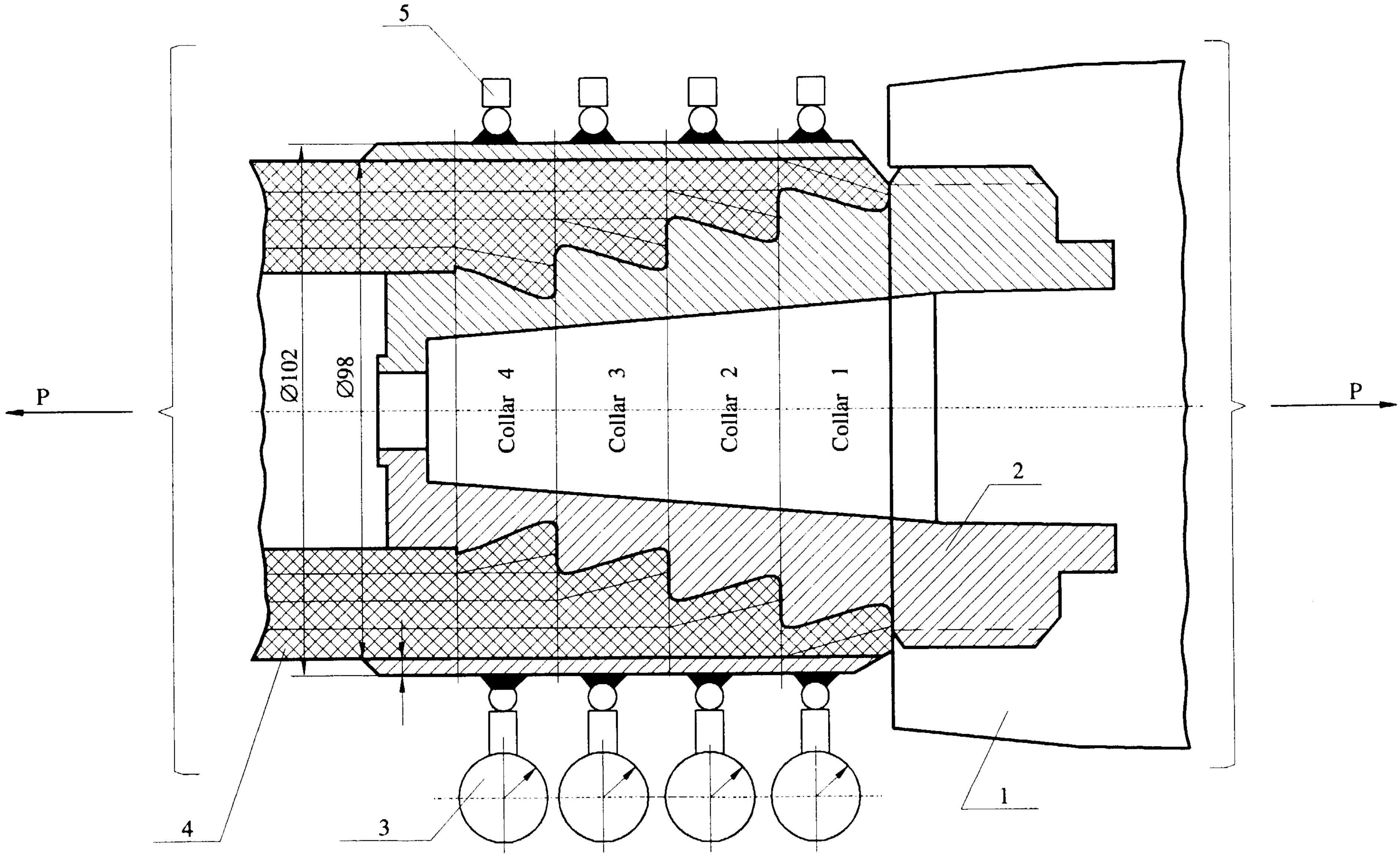

Figure 3.30. Schematic of test set-up (1, load application device; 2, fitting; 3, indicator; 4, composite structure; 5, clamp of indicator)

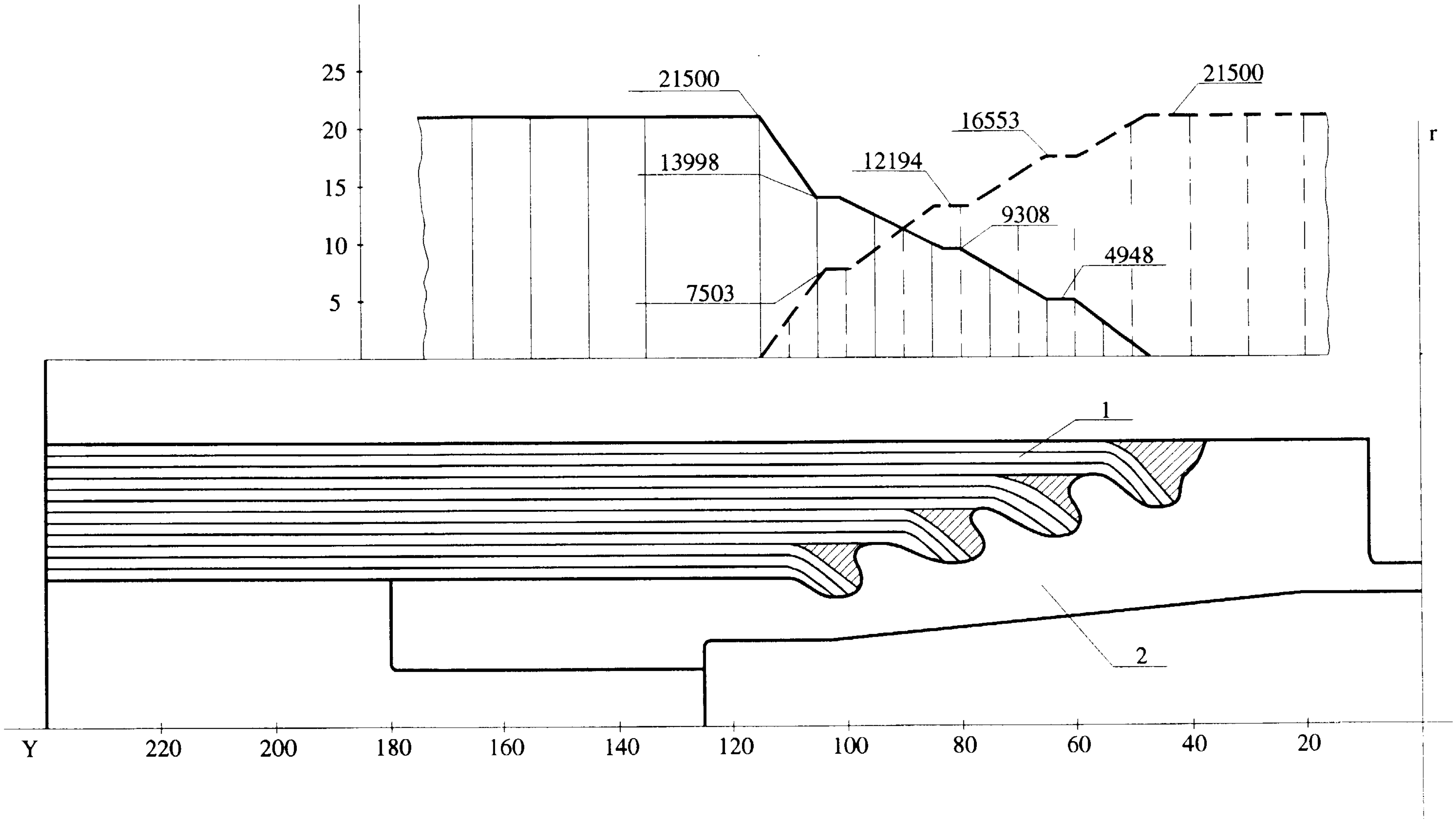

Figure 3.31. Force redistribution in root (1, composite; 2, fitting; ———, effort in composite; – – – –, effort in fitting)

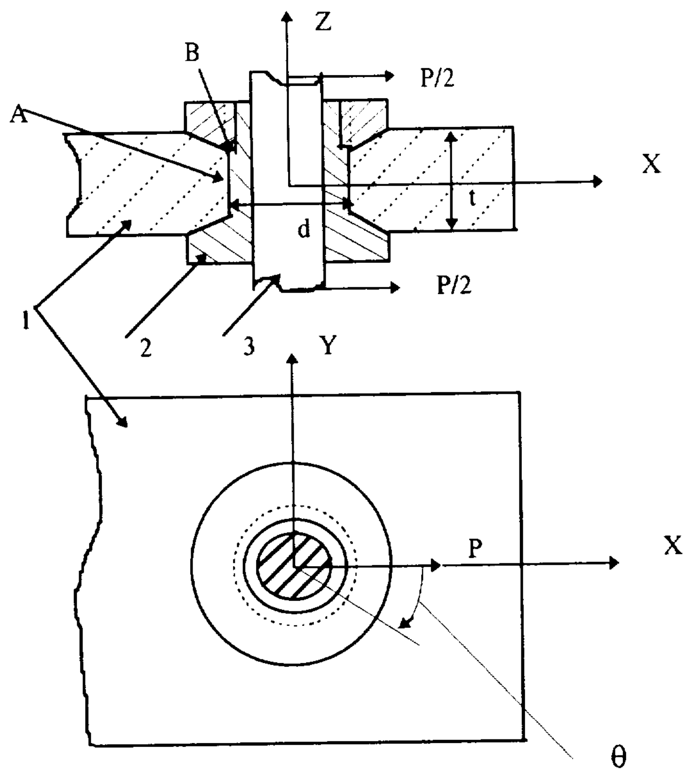

Figure 3.32 Schematic of joint

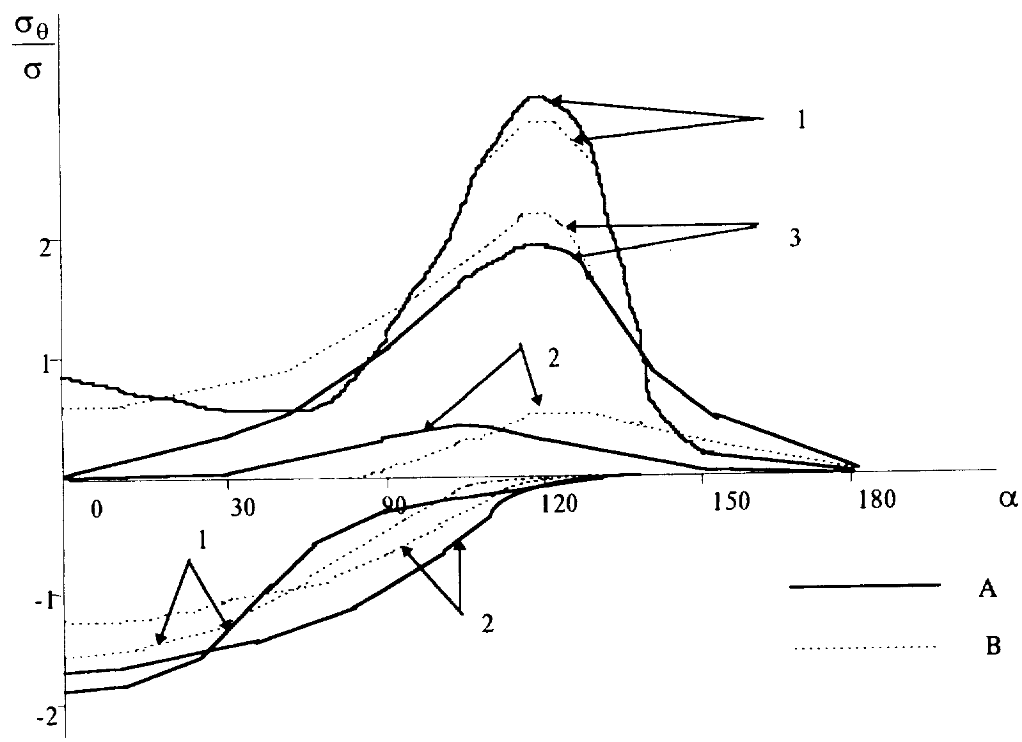

Figure 3.33 Distribution of stress σ_θ over internal surface of hole

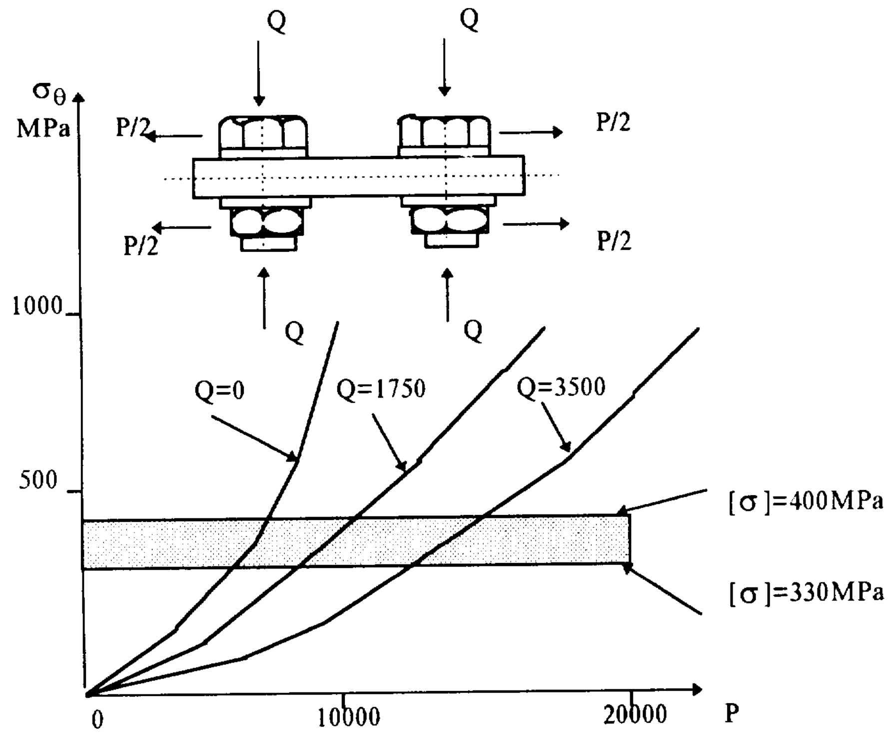

Figure 3.34 Dependence of stress σ_θ on clamp-up force Q

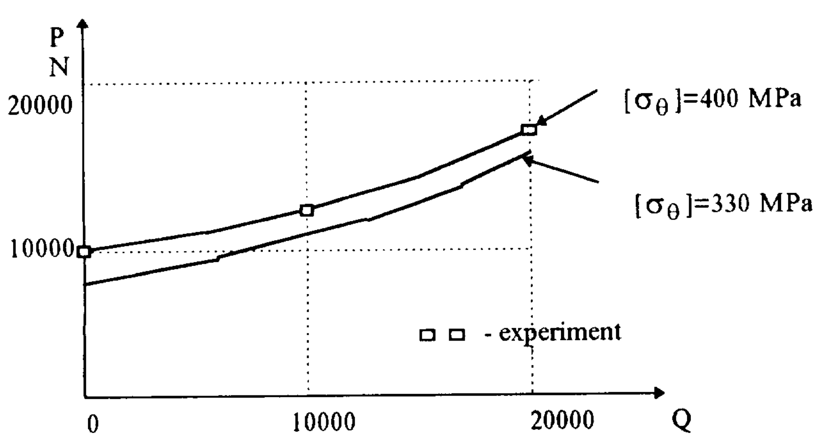

Figure 3.35 Dependence of ultimate force P on clamp-up force Q

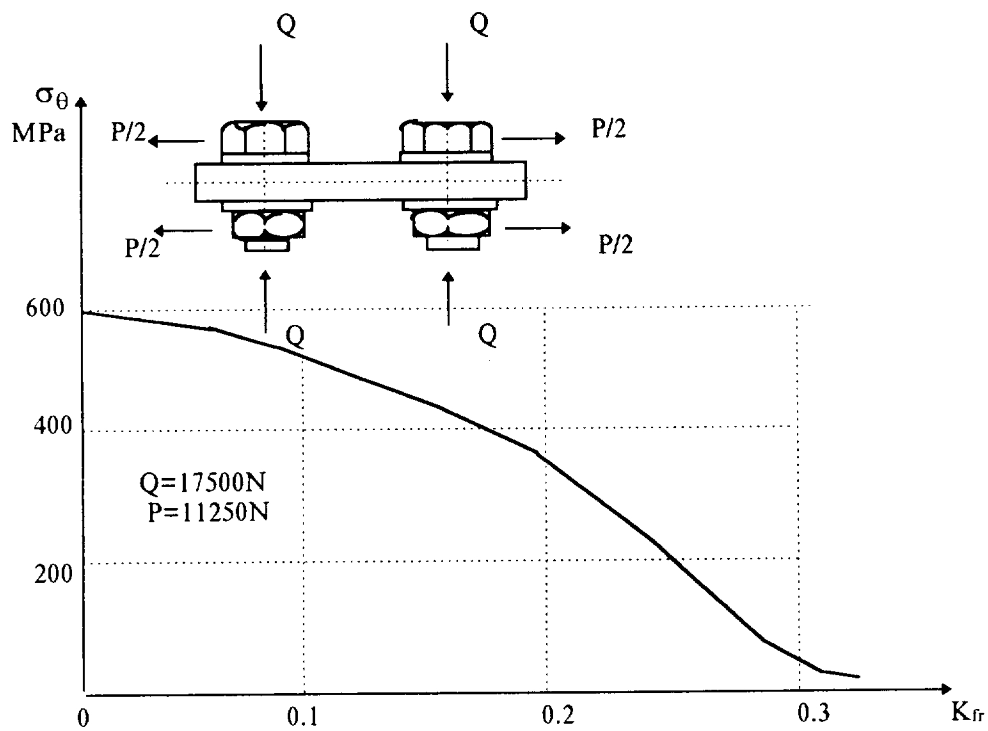

Figure 3.36 The influence of friction coefficient K_{fr} on stress σ_θ.

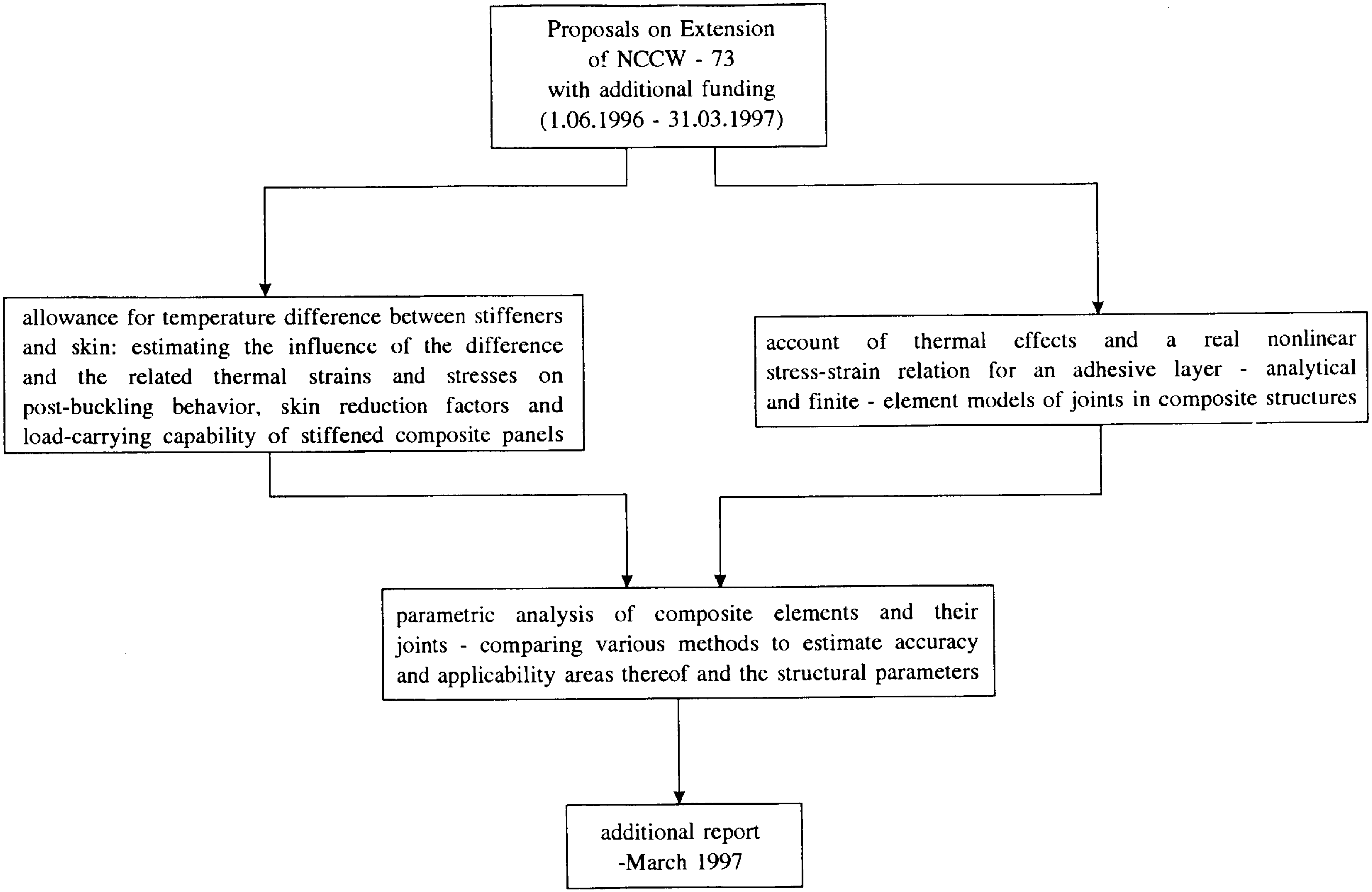

Fig. 3.37. A schematic of the extended studies